Satellite-based Estimates of Sea Ice Volume Flux:

Applications to the Fram Strait Region

Dissertation

Zur Erlangung des Doktorgrades der Naturwissenschaften
im Department Geowissenschaften
der Universität Hamburg.

vorgelegt von

Gunnar Spreen

aus
Georgsmarienhütte

Hamburg
2008

Als Dissertation angenommen vom Department Geowissenschaften der Universität Hamburg

Auf Grund der Gutachten von Prof. Dr. Detlef Stammer
und Prof. Dr. Burghard Brümmer

Hamburg, den 3. Juli 2008

Prof. Dr. Jürgen Oßenbrügge
Leiter des Department Geowissenschaften

Abstract

The sea ice export out of the Arctic Ocean through Fram Strait into the Greenland Sea is the single largest source of freshwater in the Nordic Seas and therefore of special importance for the hydrological cycle of the North Atlantic. On its way south, the exported sea ice melts and thereby modifies the stratification of the ocean surface mixed layer, which in turn influences oceanic deep convection and water mass transformation processes in the Nordic Seas and thus impact global ocean thermohaline circulation. The lack of spatial sea ice thickness information has been one of the weaknesses for previous existing methods to determine the sea ice export. In this study a new method to obtain the sea ice volume flux exclusively from satellite measurements is presented. Previous estimates of the sea ice volume flux relayed on ice draft measurements of a single Upward Looking Sonar (ULS) in the Greenland Sea. The GLAS laser altimeter onboard the ICESat satellite launched in 2003 offers for the first time the opportunity to obtain the spatial sea ice thickness distribution up to 86°N latitude. In this study a method to determine the sea ice freeboard from ICESat altimeter data is developed and applied to nine ICESat measurement periods between 2003 and 2007. Assuming hydrostatic balance and by utilization of further satellite, in situ and climatological data these sea ice freeboard measurements are converted to sea ice thickness maps of the Fram Strait region. The satellite-based ice thickness estimates are combined with sea ice area and sea ice drift, as retrieved from AMSR-E microwave radiometer measurements at 89 GHz, to obtain the sea ice volume flux. The errors of the input quantities and the final sea ice volume flux are assessed. Using this method the spatial sea ice volume flux distribution is obtained from satellite observations for the first time. The Fram Strait sea ice volume flux is further investigated by calculating a monthly sea ice volume flux time series between January 2003 and April 2007. Summer months have to be disregarded due to missing sea ice drift data. The sea ice volume flux shows large inter-annual and -seasonal variability. A mean monthly Fram Strait sea ice volume flux of (248 ± 90) km^3/month with respective minimum and maximum values of 112 km^3/month (May 2003) and 484 km^3/month (December 2004) was found. These satellite-based sea ice volume flux estimates from the years 2003 to 2007 are compared to previous sea ice volume flux estimates obtained for the period 1990 to 1999 and can be used as extension of these previous time series. Finally, a comparison of sea ice volume flux estimates from this study with oceanographic salinity measurements shows good coincidence of summer melting events. A comparison to model results reveals large differences in the lateral distribution of the sea ice volume flux. The presented method does not just allow, as previously, to determine the sea ice export through Fram Strait but has the potential to investigate and better understand the dynamics of sea ice volume changes north and south of Fram Strait.

Zusammenfassung

Der Export von Meereis aus dem Arktischen Ozean durch die Framstraße in die Grönlandsee stellt die größte Quelle von Süßwasser im Europäischen Nordmeer dar und ist daher von zentraler Bedeutung für den Süßwasserhaushalt des Nordatlantiks. Auf dem Weg nach Süden schmilzt das exportierte Meereis und bestimmt so maßgeblich die oberflächennahe Schichtung der Wassermassen, die wiederum die ozeanische Tiefenkonvektion im Europäischen Nordmeer und dadurch auch die globale thermohaline Zirkulation beeinflusst. Einer der bisherigen Schwachpunkte bei der Bestimmung dieses Eisexports ist das Fehlen flächendeckender Beobachtungen der Meereisdicke. In dieser Studie wird ein neues Verfahren vorgestellt, den Meereisvolumenfluss alleinig aus Satellitenbeobachtungen abzuleiten. Bisher beruhten Abschätzungen des Eisvolumenflusses in puncto Eisdicke auf den Eistiefgangsmessungen eines einzelnen Sonars in der Grönlandsee. Mit den seit 2003 gemessenen Daten des Laseraltimeters GLAS auf dem Satelliten ICESat ist es erstmalig möglich, die flächenhafte Eisdickenverteilung bis zu einer geographischen Breite von 86°N zu erfassen. In dieser Arbeit wurde ein Verfahren zur Bestimmung des Eisfreibords aus ICESat Laseraltimeterdaten entwickelt und auf neun ICESat-Messperioden zwischen 2003 und 2007 angewendet. Unter Annahme hydrostatischen Gleichgewichts und mit Hilfe von weiteren Satelliten-, vor Ort gemessenen und klimatologischen Daten werden aus diesen Eisfreibordmessungen Eisdickenkarten der Framstraßenregion erstellt. Diese Meereisdickendaten werden mit Satellitenmessungen der Eisbedeckung und Eisdrift zum Meereisvolumenfluss kombiniert. Für die Bestimmung der Eisbedeckung und Eisdrift werden jeweils AMSR-E Mikrowellenradiometermessungen bei 89 GHz verwendet. Die Fehler der Eingangsdaten und des Meereisvolumenflusses werden abgeschätzt. Mit dieser Methode kann erstmals die flächenhafte Verteilung des Meereisvolumenflusses aus Satellitendaten beobachtet werden. Der Meereistransport durch die Framstraße wird mit Hilfe einer monatlichen Zeitreihe zwischen Januar 2003 und April 2007 ausführlicher untersucht. Hierbei werden die Sommermonate aufgrund fehlender Eisdriftmessungen nicht berücksichtigt. Der Eisvolumenfluss unterliegt großer jährlicher und zwischenjährlicher Variabilität. Der mittlere monatliche Meereisvolumenfluss durch die Framstraße betrug (248 ± 90) km^3/Monat und erreichte minimale und maximale Werten von 112 km^3/Monat (Mai 2003) und 484 km^3/Monat (Dezember 2004). Der erhaltene Meereisvolumenfluss der Jahre 2003 bis 2007 wird mit früheren Meereisvolumenflussbeobachtungen verglichen und kann als Verlängerung dieser früheren Zeitserie verwendet werden. Ein Vergleich der Volumenflussabschätzungen dieser Studie mit ozeanographischen Salzgehaltsmessungen zeigt eine gute Übereinstimmung der sommerlichen Eisschmelzperioden. Ein Vergleich mit Modellergebnissen läßt große Unterschiede in der räumlichen Verteilung des Volumenflusses erkennen. Die vorgestellte Methode erlaubt nicht nur, wie bisher, die Bestimmung des Meereisvolumenexports durch die Framstraße, sondern bietet auch die Möglichkeit, die Dynamik von Meereisvolumenänderungen nördlich und südlich der Framstraße zu untersuchen und besser zu verstehen.

Contents

Chapter 1

Introduction

Arctic sea ice: Where does it come from? Where does it go? The most fundamental answers to these questions were already given by Fridtjof Nansen in 1896. His vessel *Fram*, which entered the Arctic pack ice in the Laptev Sea near the New Siberian Islands in 1893, left the ice again in August 1896 in the Fram Strait after three years of ice drift (*Nansen*, 1897). Since then we know that the main transport of sea ice out of the Arctic Ocean is taking place via Fram Strait and that the source regions for this ice are as far away as the East Siberian Sea on the opposite side of the Arctic Ocean. Nansen also anticipated the importance of sea ice for the Earth's climate system when he described sea ice ocean interactions (*Nansen*, 1902). However, an accurate knowledge of sea ice dynamics and "where the ice goes" still remains an open question and is also the main topic of this work. Sea ice was realized to be one of the key components of the climate system and its interaction with the ocean and atmosphere has not only local but global relevance (*ACIA*, 2004, 2005). Thus here the variability of the Arctic sea ice mass exchange with the Greenland Sea and the possibilities of regularly monitoring it are in the focus. Anyhow, times have changed since Nansen's *Fram* drift. The 2007 *Tara* ice drift following Nansen's trace as part of the International Polar Year (IPY) about 110 years after the *Fram* drift, took only about 15 months for the same distance in a by extent significantly decreased sea ice cover (*Gascard et al.*, 2008). While the Arctic by exploitation of modern technique is not as hostile, dangerous and lonesome anymore as during Nansen's time, still the number of in situ measurements taken there is below the world average. Therefore, observations from space are of special importance.

In this study a technique to derive the sea ice volume transported out of the Arctic Ocean through Fram Strait entirely from satellite measurements is described. It is a multi-sensor study, where different data products from different satellites are combined. For the observation of the sea ice thickness a new method was developed. This is of special importance as before sea ice thickness could only be measured by in situ campaigns and moorings. Finally a time series of the ice volume transport through Fram Strait for 2003 to 2007 is presented. Monitoring anomalies in the Fram Strait sea ice volume flux is of special importance, as they can influence watermass transformation processes in the Greenland Sea and further downstream in the Atlantic Ocean. With the presented technique the lateral distribution of the sea ice volume flux can be directly observed, which was not possible with previous measurement techniques. The retrieval of sea ice volume is demonstrated for the Fram strait region but the used method can be easily adapted to other regions or applied globally.

1.1 Aims

The main aims and questions addressed in this study can be described as follows:

- Development of an exclusively satellite based method to monitor the sea ice volume flux.
- What is the amount and variability of the Fram Strait sea ice volume flux between 2003 and 2007? How does the Fram Strait ice volume transport change inter-annually and inter-seasonally?
- Calculation of a monthly Fram Strait sea ice volume flux time series between January 2003 and April 2007. How large is the amount and variability of the sea ice volume flux during these years in comparison to measurements during the 1990s? Can our estimates be used as an extension of the former time series?
- Combination of different satellite datasets to monitor the spatial distribution of the sea ice volume flux. For this purpose sea ice thickness estimates obtained from ICESat laser altimetry are combined with sea ice area and drift measurements obtained from satellite microwave radiometry (AMSR-E) to retrieve the spatial distribution of the sea ice volume flux.
- Validation of the used sea ice concentration, drift, and thickness datasets to assure their quality for the sea ice volume flux retrieval. Error assessment of these quantities and the sea ice volume flux.
- How does the satellite based sea ice volume flux compare to oceanographic measurements? To get further insight in the sea ice – ocean interactions the sea ice volume flux observations will be compared with in situ ocean salinities measurements obtained from a mooring in the Greenland Sea.
- How does satellite based and modeled sea ice volume fluxes compare? Our sea ice volume flux observations will be compared with results from two coupled sea ice – ocean models.

How long ICESat will continue to operate is unsure, as its designed lifetime of three years with a five-year goal is already exceeded. But plans for ICESat-II are underway and the radar altimeter satellite CryoSat-2 is scheduled for launch in 2009. It is anticipated that the presented sea ice volume flux retrieval method can be easily adapted to CryoSat-2 measurements. Thus, there is good hope that the time series can be continued in future and will help to understand climate relevant processes.

1.2 Structure

This work is organized as follows:
First, in Chapter 2 an introduction to the Arctic climate system and the main processes relevant for this study are given. In the second part of Chapter 2 the used data and sensors are described. The main quantities to retrieve the sea ice volume flux are the

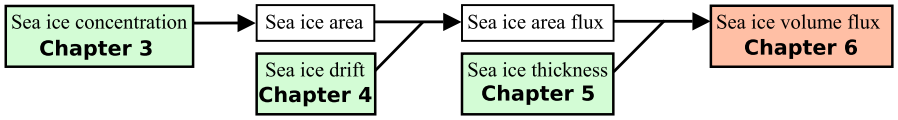

Figure 1.1: Schematic flow diagram of how the quantities involved (green boxes) have to be combined to get the sea ice volume flux. In the lower part of each box the belonging chapter is listed.

sea ice concentration (area), sea ice drift, and sea ice thickness. These quantities are described one after the other in Chapters 3, 4, and 5. The volume flux finally is described in Chapter 6. Figure 1.1 shows a flow diagram how the quantities have to be combined and in which chapter they are described.

The sea ice concentration and drift are derived from passive microwave AMSR-E data using existing methods. The focus for these two quantities therefore lies on the evaluation of the quality of the datasets by comparing them with reference data. This is a prerequisite to estimate the uncertainty of the final ice volume flux data. For the ice thickness a new method was developed to obtain the ice freeboard from ICESat laser altimeter measurements and afterwards convert them to ice thicknesses using additionally QuikSCAT radar backscatter data for sea ice type discrimination. Finally, all three datasets have to be combined to derive the sea ice volume flux. The meridional Fram Strait sea ice volume transport is calculated and compared with model data and oceanographic salinity measurements in the Greenland Sea. *Holfort and Meincke* (2005) state that "the measurements of liquid freshwater flux are of minor value if not the information on freshwater fluxes with the ice are available in parallel". Here a first step in that direction is made. Finally, a conclusion and outlook is given in Chapter 7.

1.3 Publications

Parts of this thesis were published in the following journals and book:

- A first version of sea ice volume flux retrieval method presented in Chapters 5 and 6 and first results were published in:

  Spreen, G., S. Kern, D. Stammer, R. Forsberg, and J. Haarpaintner (2006), Satellite-based Estimates of Sea Ice Volume Flux through Fram Strait, *Ann. Glaciol.*, *44*, 321–328.

  Spreen, G., S. Kern, and D. Stammer (2006), Utilization of Multiple Satellite Sensors to Estimate Sea Ice Volume Flux through Fram Strait, in *Arctic sea ice thickness: past, present & future, Climate Change and Natural Hazards Series 10*, vol. EUR 22416, edited by P. Wadhams and G. Amanatidis, chap. 16, pp. 176–192, European Commission, Brussels.

- Sea ice volume flux estimates using sea ice drift data retrieved from QuikSCAT instead of AMSR-E measurements (Chapter 6, Section 6.5.1) were presented in:

  Haarpaintner, J. and G. Spreen (2007), Use of Enhanced-Resolution QuikSCAT/ SeaWinds Data for Operational Ice Services and Climate Research: Sea Ice

Edge, Type, Concentration, and Drift, *IEEE Trans. Geosci. Remote Sens.*, *45*(10), 3131–3137.

- Parts of the AMSR-E 89 GHz sea ice concentration retrieval and validation (Chapter 3) were published in:

  Spreen, G., L. Kaleschke, and G. Heygster (2008), Sea ice remote sensing using AMSR-E 89-GHz channels, *J. Geophys. Res.*, *113*, C02S03, doi:10.1029/2005JC003384.

Chapter 2

Fundamentals: The Arctic Climate System, Instruments and Data

In the first part (Section 2.1) of this chapter an introduction to the main climate components of the Arctic climate system important for this study are given. In the second part (Section 2.2) the used satellite sensors and datasets will be introduced.

2.1 The Arctic Climate System

2.1.1 The Arctic

Different definitions for the Arctic geographical coverage exist. The Arctic region can be defined by the July 10°C isotherm of the air temperature at the surface. The thereby defined area covers the complete Arctic Ocean including all marginal seas and the Greenland, Bering and Labrador Sea. On land Greenland and parts of Iceland, Canada, Alaska, and Russia are covered. The 10°C isotherm in large parts lies near the Arctic Circle at 66°33′ N latitude, which can be taken as an alternative border definition for the Arctic. Figure 2.1 on the following page shows a geographical overview including topography and bathymetry of the Arctic and surrounding areas including geographical names used throughout this study. The inset shows in detail the concrete study region around Fram Strait and the Greenland Sea. The majority of the northern hemisphere cryosphere is located in the Arctic with its most prominent features, the Greenland Ice Sheet and the Arctic sea ice cover.

The Arctic is a "hot-spot" of the global climate change occurred during the last hundred years, which means the Arctic is one of the most responsive regions to climate change. The Intergovernmental Panel on Climate Change (IPCC) reported in its 4th assessment (*IPCC*, 2007) that the Arctic surface temperature increase of about 1.5°C was twice as high during the last century (1906 to 2005) as the global surface temperature increase (*Trenberth et al.*, 2007). For western Canada, Alaska, and Siberia an even higher warming of 2–3°C during the last 50 years (1954–2003) was reported (*ACIA*, 2004, 2005). The Arctic sea ice cover decreased by about 3% per decade since 1978. The Greenland Ice Sheet has been shrinking with a rate of about 50 to 100 Gt/yr (equivalent to about 0.2 ± 0.1 mm/yr sea level rise) at least for 1993 to 2003. Before that date estimates are uncertain (all from *Lemke et al.*, 2007). The land to sea distribution in the Arctic is completely different from the Antarctic. The mediterranean Arctic Ocean is completely surrounded by land masses. The ground is frozen all year around (permafrost) down to depths of several hundred meters to kilometers, but the surface is not permanently

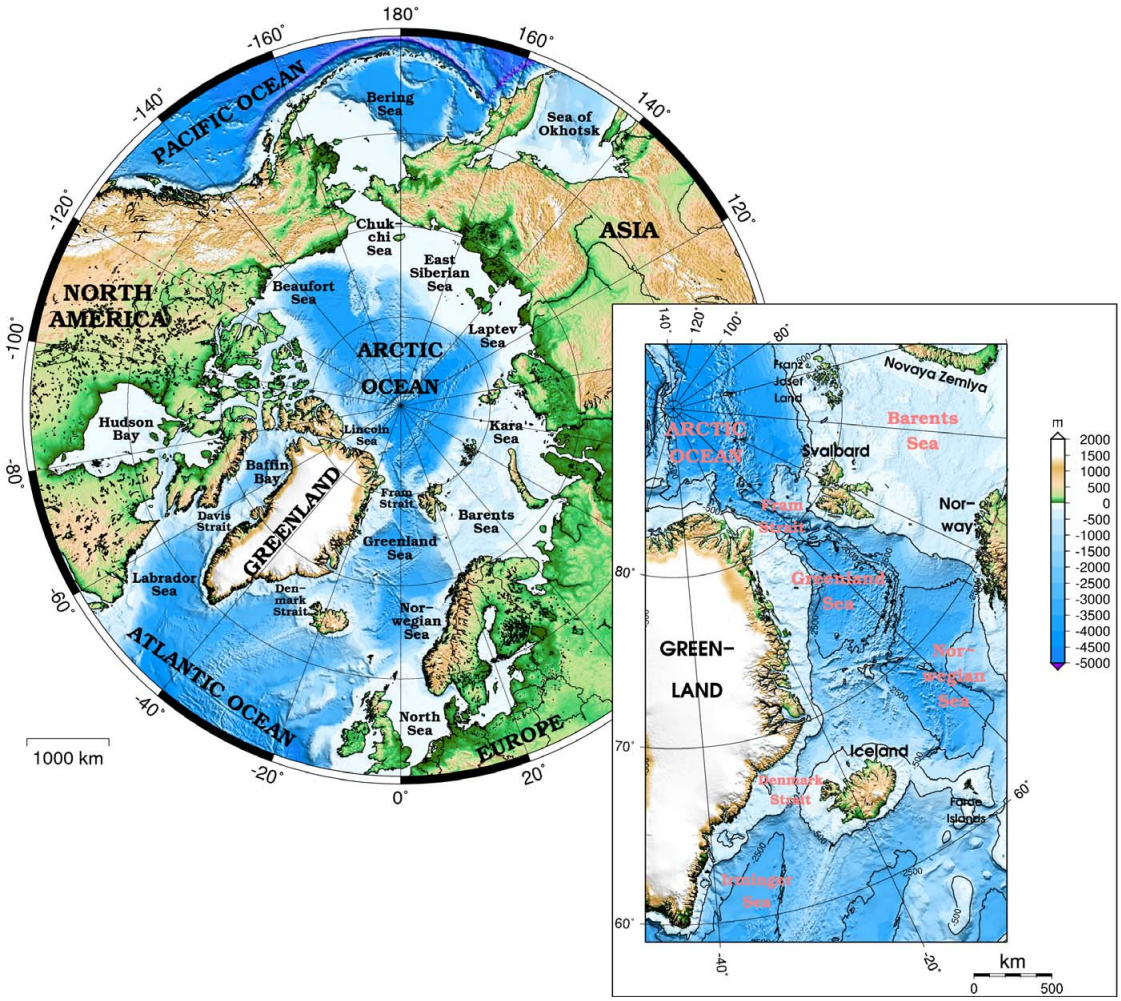

Figure 2.1: Overview of the Arctic (left) and the study region around Fram Strait (right) including topography, bathymetry and names of geographical places used. In the Fram Strait map the 500 and 2500 m depth isolines are marked in black.

covered by ice or snow and thus exhibits the darker soil with larger absorption to the sun light during summer. Therefore, the winter to summer temperature differences on land are large. All this leads to the larger temperature increase on land compared to the ocean during the last decades.

2.1.2 The Arctic Ocean

The Arctic Ocean is a mediterranean sea with a depth of more than 4000 m over large parts of the Amundsen basin. Enclosed are several shallow marginal seas with depths below 500 m. These are the Barents, Kara, Laptev, East Siberian, Chukchi, Beaufort, and Lincoln Sea (see Figure 2.1). The Arctic Ocean has only one deep passage, the Fram Strait, where the majority of water mass exchange with the world oceans takes place. The Fram Strait is approximately 440 km wide and 3000 m deep. Other connections are

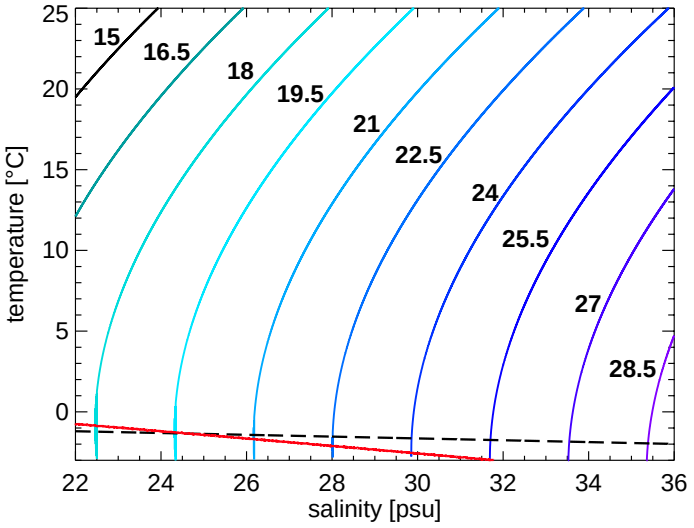

Figure 2.2: Seawater density ρ as a function of temperature and salinity. A value of $1000\,\mathrm{kg/m^3}$ has to be added to the annotations of the colored density isolines to get the full density value. The black dashed line is showing the sea water freezing point and in red the maximum density line is marked. For salinities above 24.7 psu the maximum density lies below the freezing point. Calculation of densities are based on *Fofonoff and Millard Jr.* (1983) using surface pressure.

the Bering Strait, the Barents Sea and the Canadian Archipelago.

The circulation in the Arctic Ocean is dominated by thermohaline forcing. This is in contrast to the major ocean basins Pacific, Atlantic, and Indian Ocean, where most currents are wind driven and only modified by thermohaline effects. The input of brine and fresh water due to freezing and melting of sea ice, respectively, is one of the major components of the thermohaline forcing. The influence of melting and freezing of sea ice on the ocean is enhanced by the fact that in the cold arctic regions changes of the salinity of seawater have a larger effect on the seawater density than they would have in warmer regions. Figure 2.2 shows the seawater density in dependence of its temperature and salinity. For example at -1°C a change of salinity from 32 to 34 psu causes a density change of $1.6\,\mathrm{kg/m^3}$, while at 20°C for the same salinity change the density would only change by $1.5\,\mathrm{kg/m^3}$. This is only a slight difference but nevertheless important for the role of sea ice in enhancing or hampering ocean convection due to ice formation or melting, respectively. As can be seen from Figure 2.2 for low temperatures the water density is getting almost independent of the temperature. Further cooling is not increasing the density anymore. Therefore, changes in salinity are the main driver for density changes at low temperatures. Figure 2.2 also shows the freezing temperature and line of maximum water density in dependence of temperature and salinity. For salinities below 24.7 psu the maximum density is laying above the freezing point. This is also the separation point between brackish water and true sea water. Sea ice can be formed more easily under brackish conditions, as water near the freezing point stays on top the denser but warmer water. Brackish water in the Arctic only exists near the coast in the large river outflow regions in the Kara, Laptev and East Siberian Sea. In the rest of the Arctic first the upper water layer has to be completely cooled near the freezing point before ice formation can start (see also next Section 2.1.3 on the next page).

Figure 2.3 on page 9 shows the main ocean currents in the Arctic together with the two

main sea ice drift patterns, the Transpolar Drift and the Beaufort Gyre. Warmer Atlantic water (dark red arrows) enters the Arctic Ocean in the West Spitzbergen Current via Fram Strait. There it recirculates following the bathymetry in the main oceanic basins, the Nansen, Amundsen, Makarov and Canada basin. Another branch of Atlantic water enters the Arctic Ocean through the Barents Sea and Kara Sea and some Pacific waters enter via Bering Strait. In the Arctic Ocean the Atlantic water gets colder and partly sinks down (especially in ice growth regions due to additional brine input). Finally, it leaves the Arctic Ocean again via Fram Strait into the Greenland Sea. It is now colder and fresher than the surrounding waters and the main transport takes places in the upper 500 m along the shelf break and called East Greenland Current (EGC). A smaller part is also leaving via the Canadian Archipelago and then through Baffin Bay and Davis Strait. These cold waters flowing out of the Arctic are of crucial importance for the global thermohaline circulation. If the arctic water in the Greenland Sea is getting heavier by cooling from the Atmosphere and brine input from ice formation, it can sink down driven by convection and after passing the Denmark Strait overflow feed in the dense waters of the Atlantic Ocean. But on the other hand melting of sea ice can hamper this deep convection and thereby is one of the major processes which can alter the deep convection in the Greenland Sea.

The Arctic Ocean seems to be in a transition phase to a warmer state mainly due to a change of strength and location of the subpolar gyre (*Polyakov et al.*, 2005; *Polyakov*, 2007). Especially, the Atlantic inflow in the upper layers is getting warmer. A part of the recent decrease of sea ice can be attributed to this ocean warming. But it is most likely contributing only to a small part to the sea ice shrinkage, as the sea ice is thermally insulated by the cold halocline layer to the warmer Atlantic waters. The cold halocline layer is formed by surface waters and waters from the large rivers flowing into the marginal seas of the Arctic Ocean. There the cold water is enriched with salt released from ice formation and thus is incorporated between the fresh surface layer and the even saltier but warmer Atlantic waters. The heat exchange between the Atlantic water and the sea ice thus is hampered by the cold halocline layer. The existence of this layer is one of the major differences between the Arctic and Antarctic sea ice to ocean interactions. On the other hand, also the upper ocean heat content is increasing during recent years due to enhanced summer short wave radiation in combination with larger open water areas during summer (*Steele et al.*, 2008; *Kay et al.*, 2008). This warming is causing in particular enhanced lateral melting of sea ice and can result in a positive feedback mechanism ("sea ice-albedo-feedback", see below).

2.1.3 Sea Ice

A Short Introduction to Sea Ice Formation and Growth

Sea ice is formed by freezing of sea water. Its characteristics are due to the salt in the sea water, which influences the freezing process, and are significantly different from fresh water ice. The different forms of sea ice are defined in *WMO* (1989) by the World Meteorological Organisation (WMO). Table 2.1 on page 10 summarizes the most common sea ice types. Frazil ice is the first form of ice which forms when the temperature of the upper ocean drops below its freezing point, which is about -1.8 to -1.9°C. To achieve

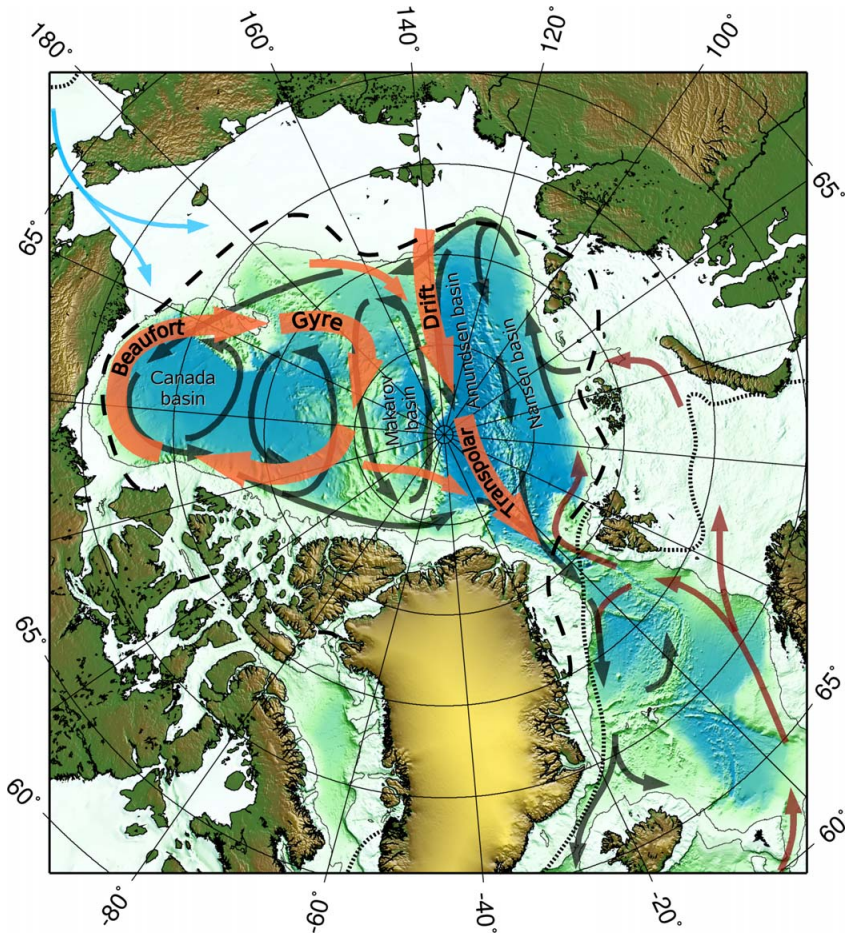

Figure 2.3: Scheme of the main sea ice drift pattern (orange arrows) and circulation in the Arctic Ocean and Greenland Sea. Atlantic waters are shown in dark red (warm) and gray, Pacific inflow via Bering Strait is shown in blue. The typical extent of the summer and winter sea ice cover of recent years are shown as black dashed and dotted lines, respectively. The depth of 500m is marked as black isoline.

this, the upper mixed ocean layer has to be cooled, because in contrast to fresh water the maximum density of sea water with a salinity above 24.7 psu lies below the freezing point (see Figure 2.2 on page 7). Cooling from the atmosphere thus is causing convection in the upper water layer, which first has to be completely mixed and cooled before freezing can start. Frazil ice consists of small ice needles and plates suspended in the water. The immediate salt release to the ocean, when the first ice crystals are formed, lowers the freezing point of the surrounding water and increases the water density. Due to this, convection of the upper water layer including the frazil ice starts. Even under quiet ocean conditions this is hampering the growth of a solid, crystalline ice layer, like on lakes. If the freezing from on top continues and more and more frazil ice is produced, the ice needles and plates coagulate to a soupy layer called grease ice. Grease ice is damping the small scale surface waves and is reflecting less light, giving the sea surface a matt appearance. The next form of ice growth depends on the ocean swell. Under quiet

Table 2.1: Sea ice types for different stages of development after *WMO* (1989). Only the most common sea ice types are listed.

Development	Ice Type	Ice Thickness
new ice/nilas	frazil ice, grease ice, dark nilas	$< 5\,\mathrm{cm}$
	light nilas	$5 - 10\,\mathrm{cm}$
	pancake ice	up to $10\,\mathrm{cm}$
young ice	grey ice	$10 - 15\,\mathrm{cm}$
	grey-white ice	$15 - 30\,\mathrm{cm}$
first-year ice	thin first-year ice	$30 - 70\,\mathrm{cm}$
	medium first-year ice	$70 - 120\,\mathrm{cm}$
	thick first-year ice	$1.2 - 2\,\mathrm{m}$
old ice	second-year ice	$\sim 2.5\,\mathrm{m}$
	multi-year ice	$3\,\mathrm{m}$ or more

conditions like in leads (opening of a fracture in the sea ice cover) a thin, closed ice cover called nilas forms. Nilas damps smallscale surface waves (centimeter scale) but is still elastic enough to follow longer scale waves. If stronger ocean swell is prevailing, small ice floes (30 cm to 3 m diameter) with raised rim, called pancake ice, form from grease ice or nilas. Under continued freezing conditions a solid ice cover forms and the sea ice can grow thermodynamically up to a thickness of up to 2 m during the first winter, but growth to a thickness of about 1 m during the first winter is more common in the Arctic. Sea ice which has not survived one summer melt is called first-year ice. After the first summer it is called residual first-year ice until 31 December of that year. The next year it is called second-year ice and all following years multi-year ice. These are the formal definitions by the WMO (*WMO*, 1989). For sea ice remote sensing beside young and new ice only two ice classes are commonly used: first-year ice and multi-year ice sometimes also called perennial ice. All sea ice, which survived one summer melt is directly called multi-year ice (according to the WMO definition it should be called old ice). The flushing of the sea ice and drainage of brine out of the ice during summer melt is causing a change of the radiometric properties of the sea ice, which can be distinguished by remote sensing. Also in this study only the two classes first-year and multi-year ice are distinguished. More classes of thick ice can not be reliably separated by spaceborne radiometry and the thickness of new ice lies below the error margins of laser altimeter measurements from space.

During ice formation most salt from the sea water is directly released to the ocean, but some salt is incorporated as brine in pockets in between the ice structure. The older the ice gets the less saline it is. During the aging of the ice more and more brine pockets get connected and thereby brine channels are building, through which the brine is draining out of the ice. This is caused mainly by gravity but also other mechanisms exist (*Wadhams*, 2000). After the first heavy brine release during the first days of ice growth the salinity of the ice is decreasing only slowly until the next summer. Then melt water from on top of the ice can flush through the brine channels and remove most of the brine. Thus multi-year ice is less saline than first-year and young ice, particularly in its top few ten centimeters. The strength properties of sea ice are controlled by the

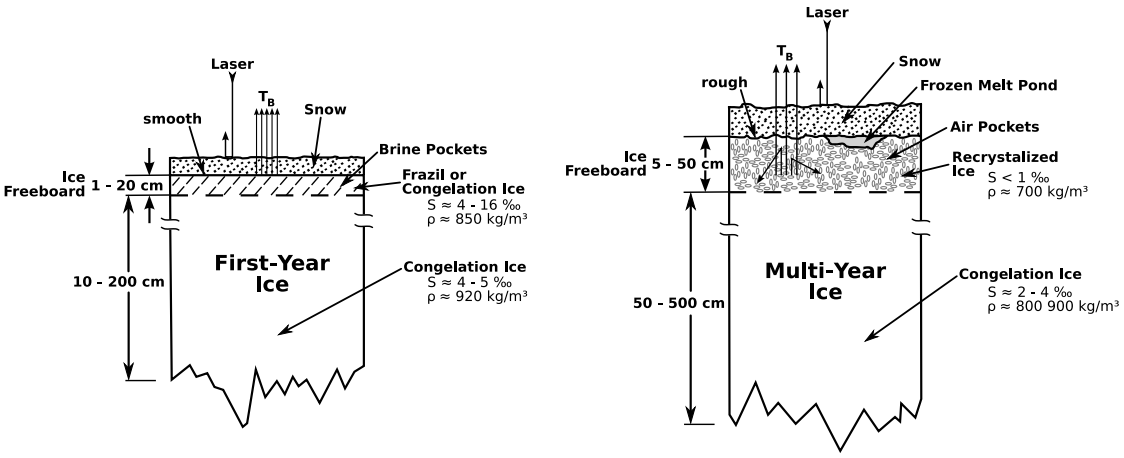

Figure 2.4: Schematic diagram of first-year and multi-year ice (after *Comiso* (1983)). Typical values for some ice characteristic parameters are given. T_B is the emitted brightness temperature in the microwave spectrum, the optical path length of a laser altimeter is also marked.

brine volume. Therefore, the ice after surviving one summer has a greater strength than before (*Wadhams*, 2000). Figure 2.4 shows a scheme of typical first-year and multi-year ice together with their most important parameters.

During winter, snow can accumulate on sea ice. Thus the maximum in snow depth on Arctic sea ice occurs at the end of winter in May and June. During July and August the snow melts almost completely or transforms to slush on top the sea ice. The snow depth is not evenly distributed throughout the Arctic. Largest snow depths appear north of Greenland with a snow depth up to 45 cm during winter. From there the snow depth gradually decreases towards the Eurasian marginal seas and the Chukchi Sea, where the maximum snow depth is about 25 cm (*Warren et al.*, 1999). In general the Arctic Ocean is a cold desert with little snow fall compared to the Antarctic.

After an ice cover has been formed, it is moved around mainly by the drag exposed to the wind, especially on shorter time scales as hours and days. On longer time scales also the ocean currents below the ice are affecting the ice movement, as they are more steady then the atmospheric pressure. Inbetween these time scales lies the forcing by tides, which is larger in the marginal seas than in the central Arctic Ocean. In most areas the semidiurnal tides (M_2 and S_2) dominate the forcing but there are also places like the Yermak Plateau north west of Svalbard where the diurnal tides (K_1 and O_1) play an important role (*Kowalik and Proshutinsky*, 1994).

If these outer forces cause a convergent ice drift situation, the ice gets deformed. Under the outer pressure the ice gets piled up, parts of the floes get pushed upward (and downward) and thereby ridges are formed. This is the dynamic way of ice thickness increase. Thermodynamical sea ice growth general leads to ice not thicker than 2 m (*Wadhams*, 2000). Therefore the thick old ice in the western part of the Arctic Ocean with thicknesses of 5 m and more is formed by a combination of ridgin of ice floes due to dynamic forcing and thermodynamical ice growth. Ridges strongly increase the drag coefficient of the ice and it is "sailing" more efficiently with the wind. Under divergent

drift conditions cracks and leads in the ice are opened.

Continuous offshore blowing winds, e.g. katabatic winds along the coast, can open up large ice free areas, called polynyas. Alternative to these wind driven latent heat polynyas, polynyas can also be kept ice free by continued source of heat from the ocean below and then are called sensible heat polynyas. Sensible heat polynyas are less common. In the Northern Hemisphere the Kashevarov Bank polynya in the Sea of Okhotsk and the Whaler's Bay polynya north of Svalbard are mainly sensible heat driven. Many polynyas like the North Water polynya in the northern Baffin Bay are maintained by a combination of both processes (*Martin*, 2001; *Morales Maqueda et al.*, 2004). Under freezing conditions latent heat polynyas are areas of continuous ice growth, they are therefore sometimes called "ice factories". Polynyas and leads are also important for the ocean to atmosphere heat flux. For low surface temperatures during winter the heat flux from the about -1.8°C warm ocean to the atmosphere in leads and polynyas can reach $1000\,\mathrm{W/m^2}$, while already a 0.2 m thick ice cover reduces the heat flux by one dimension to less than $200\,\mathrm{W/m^2}$ (*Martin et al.*, 2004).

Sea Ice in the Climate System

Up to 7% of the worlds oceans are covered by sea ice (*Cavalieri and St. Germain*, 1995). In winter the extent of Arctic sea ice can reach up to $16 \cdot 10^6\,\mathrm{km^2}$ and in summer it is reduced to about $7 \cdot 10^6\,\mathrm{km^2}$, but in recent years the maximum coverage was reduced to about $14 \cdot 10^6\,\mathrm{km^2}$ and the minimum coverage during summer to about 4 to $5 \cdot 10^6\,\mathrm{km^2}$. The amplitude of the seasonal cycle of the Antarctic ice cover is larger with $18 \cdot 10^6$ and $3 \cdot 10^6\,\mathrm{km^2}$ for the respective winter and summer ice extent. The sea ice area makes up more than one quarter of the surface of the cryosphere and together with the snow on land has the highest variability in its extent.

In contrast to the surrounding water, sea ice has a high mean albedo of about 0.7 to 0.8. A new snow cover can even increase the albedo to more than 0.9, while melt ponds during summer and soot can reduce the ice albedo down to 0.2 (*Gloersen et al.*, 1992; *Hansen and Nazarenko*, 2004). The mean summer albedo of the Arctic Ocean is about 0.5 (*Laine*, 2004). Water has an albedo of 0.04 to 0.15 and thus is absorbing most of the incoming shortwave radiation. The ratio between the sea ice cover and open water fraction is therefore ruling the radiation budget of the high latitude seas. Changes of this ratio cause the positive sea ice-albedo-feedback to come into account. For example if the sea ice cover decreases like during the last decades in the Arctic the amount of energy absorbed by the ocean is increasing. The upper ocean temperature consequently is increasing, which hampers sea ice formation, leading again to a reduction of the ice cover. The ice-albedo-feedback likely has supported the above-average strong warming of the Arctic compared to the mean global warming of the recent decades (*ACIA*, 2004, 2005). Satellite measurements of the global ice cover are therefore an important contribution to global climate monitoring.

It became evident from this, now about 35 year long time series of the satellite sea ice extent measurement that the sea ice area of the Arctic Ocean is currently shrinking (e.g. *Comiso et al.*, 2008; *Serreze et al.*, 2007; *Stroeve et al.*, 2005; *Cavalieri et al.*, 2003). The trend in sea ice extent reduction amounts to -3.7% per decade for the years 1978 to 2007, but increased to -10.1%/decade for 1996 to 2007 while during the period 1978

to 1996 the trend was only -2.2%/decade (*Comiso et al.*, 2008). The reduction of the perennial ice cover (multi-year ice) is even stronger, as additional to the thermodynamical melting large fractions of old ice were transported out of the Arctic Ocean via Fram Strait (*Nghiem et al.*, 2007; *Comiso*, 2002). The Arctic ice cover is expected to further decrease in response to accelerated Arctic climate warming (e.g. *IPCC*, 2007; *Holland et al.*, 2006; *Johannessen et al.*, 2004).

Our knowledge about the sea ice thickness in the Arctic is much poorer because in situ data are very sparse. Therefore, satellite observations are very critical for obtaining information about this quantity. Nevertheless, all available ice thickness measurements from submarines, drilling, and electromagnetic sounding reveal that the Arctic sea ice has thinned substantially since the late 1950s (*Rothrock et al.*, 2008, 2003, 1999; *Wadhams and Davis*, 2000; *Haas*, 2004a,b; *Tucker et al.*, 2001). Together with the shrinking ice area during the same time period, this means a significant reduction of the Arctic sea ice volume. Whether this reduction will continue towards an ice free Arctic Ocean in the future, or whether the downward trend can be attributed to a multi-decadal oscillation (e.g. *Divine and Dick*, 2006), which will reverse into an upward trend in the future, has to be carefully monitored. There is no evidence or explanation for a possible recovery of the sea ice cover in the near future and many climate models predict a summer ice free Arctic Ocean before the end of this century (*IPCC*, 2007; *Zhang and Walsh*, 2006). However, in most climate models the sea ice area decline during the recent decades is not well represented and thus the Arctic might be ice free during summer even earlier (*Stroeve et al.*, 2007).

Sea ice also might play an important role in triggering the transition between glacials and inter-glacials (*Stott et al.*, 2007; *Gildor and Tziperman*, 2003, 2001). Besides the increased direct warming of the upper ocean due to the sea ice-albedo-feedback, a retreat of the sea ice cover enhances the ocean to atmosphere CO_2 flux and such leads to atmospheric CO_2 rise. If the sea ice cover decreases, Ekman transport in the new open ocean areas increases, which leads to a decrease in stratification and by this to a ventilation of the ocean. This causes an enhanced CO_2 flux to the atmosphere, which as result is warming (greenhouse effect). These positive feedbacks are likely important for the fast transition between glacials to inter-glacials.

In the context of this study the dynamic sea ice processes relevant for the climate are of greater importance. The complete global sea ice volume amounts to about $0.05 \cdot 10^6\,\mathrm{km}^3$. This is small in comparison to the ice volume stored in ice sheets and shelfs of about $33 \cdot 10^6\,\mathrm{km}^3$. But due to its high dynamic and variability in comparison to ice sheets the sea ice volume has despite its small amount strong climate relevance. In general, sea ice formation and melting take place at different locations of the ocean. Most of the sea ice in the Arctic is formed in the Eurasian marginal seas (East Siberian, Laptev, Kara, and Barents Sea; see Figure 2.1) and is then transported elsewhere, e.g. through Fram Strait into the Greenland Sea, where it melts (see Figure 2.3 on page 9). This triggers two important climate relevant processes:

Transport of latent heat Heat is released to the ocean when sea ice forms and absorbed from the ocean again when the ice melts at a different location. Therefore, sea ice transport is an energy transport.

Transport of fresh water When sea ice forms salt is released to the ocean surface waters

and when it melts fresh water is released, respectively. Sea ice transport therefore is a fresh water transport.

Especially the second point can impact the larger scale oceanic circulation. The input of fresh or dense water to the ocean (corresponding to melting and forming of sea ice) enhances or weakens ocean stratification, respectively. For example, a positive anomaly of sea ice fresh water export out of the Arctic Ocean through Fram Strait causes a freshening of the surface waters in the Greenland Sea and this hampers convective overturning and water mass formation there. This in turn can result in significant changes in the export of dense water from the Nordic Seas (Greenland, Iceland, and Norwegian Sea) into the Atlantic Ocean and then impact the global ocean thermohaline circulation (*Dickson et al.*, 1988, 2007; *Karstensen et al.*, 2005). Also several modelling studies, e.g. *Komuro and Hasumi* (2007); *Stössel et al.* (1998); *Hasumi and Suginohara* (1995), suggest that sea ice transport affect the global thermohaline circulation. The largest known fresh water anomaly event in the North Atlantic during the last century was the "Great Salinity Anomaly" from the late 1960s to the early 1980s (*Dickson et al.*, 1988), which probably was due to an increased ice transport through Fram Strait. An overview of the various ways how changes in the mass balance of Arctic sea ice influence the global climate is given in *Bamber et al.* (2004).

On short timescales the main driver for the ice drift is the atmosphere. Under free drift conditions, i.e. an open ice cover or divergent drift, the geostrophic wind accounts for more than 70% of the ice drift velocity variance, but on long-term scales (several months) the ice movement can be attributed half to the wind and half to the mean ocean circulation (*Thorndike and Colony*, 1982). As a rule-of-thumb the local ice velocity is 2% of the surface wind speed and tilted about $\Theta_w = 30°$ to the right of the surface wind direction in the northern hemisphere. This relationship was already observed by Nansen during the *Fram* drift (*Nansen*, 1902). The turning angle between the geostrophic wind and the surface wind Θ_a is of similar amount but opposite to the turning angle between the surface wind and the ice drift Θ_w. Thus in absence of ocean currents sea ice drifts almost parallel to the geostrophic wind ($\Theta_0 = \Theta_w - \Theta_a \approx 10°$ to $15°$ for wind speeds $> 5\,\mathrm{m/s}$; *Wadhams*, 2000; *Hibler, III and Flato*, 1992). Sea ice reacts rather quickly to changes of the local wind. After wind forcing starts sea ice reaches a steady drift state after about an hour (*Hibler, III and Flato*, 1992). When the wind starts sea ice is not moving straight but in oscillating inertial loops due to the Coriolis force (the inertial period is 12 hours at the pole). Due to these reasons the sea ice cover is strongly influenced by cyclones passing by the ice edge, what frequently happens in the Greenland Sea (*Brümmer et al.*, 2000; *Zhang et al.*, 2004). These cyclones cause regions of convergent and divergent sea ice drift along the ice edge and to a lesser extent also in the solid ice cover (*Brümmer et al.*, 2003, 2008).

In the Arctic the mean field of sea ice motion shows two main patterns: the Beaufort Gyre and the Transpolar Drift. A typical location and dimension of both are shown in Figure 2.3 on page 9. The stream of ice, which originates from the Laptev and East Siberian Sea in the Eurasian part of the Arctic, and then crosses the Arctic Ocean near the North Pole and ends at Fram Strait is called the Transpolar Drift Stream. In contrast, the Beaufort Gyre is an anticyclonic circulation of ice typically covering the Beaufort Sea and parts of the central Arctic Ocean. These two drift regimes are not completely

separated. Ice from the Beaufort Gyre can flow along the North coast of Greenland and incorporates multi-year ice into the Transpolar Drift Stream (see Figure 2.3 on page 9). Also ice from the Kara and Barents Sea can contribute to the Transpolar Drift. Sea ice which is caught by the Beaufort Gyre can recirculate there for up to 7 to 10 years and gets 5 to 7 m thick due to thermodynamical growth and deformation. Ice originating from the Eurasian part of the Arctic and being transported by the Transpolar Drift Stream is not getting older than 5 years but in general not older than 3 years. Due to the large outflow of old ice from the Canadian part of the Arctic during the recent years today only 10% of the perennial ice in the Arctic is five or more years old (*Maslanik et al.*, 2007b).

The location, extent and strength of the Beaufort Gyre and Transpolar Drift change due to the variability of long-term atmospheric pressure patterns. It can be distinguished between a cyclonic and anticyclonic wind drift regime. These can be connected with the phase of the North Atlantic Oscillation (NAO) and Arctic Oscillation (AO) (*Kwok*, 2000; *Rigor et al.*, 2002; *Martin and Martin*, 2006). During NAO− phases there is a well defined high pressure cell over the Beaufort Sea (anticyclonic phase), while during NAO+ phases this high pressure system is weakend and not showing closed isobars anymore (cyclonic phase), which reduces the strength of the Beaufort Gyre and restricts its location to the Beaufort Sea nearer to the Canadian coast. The Transpolar Drift as consequence of NAO+ is bended more into the direction of the North Pole. The cyclonic and anticyclonic regimes also change inter-seasonal with a more anticyclonic regime dominating during winter and the cyclonic during summer. Which of the two regimes is dominating has also influence on the source region of the ice which is exported through Fram Strait. During a cyclonic phase (NAO+, AO+) more thick ice from north of Greenland and the Canadian Archipelago is transported through Fram Strait and thus enhances the ice volume transport during those years. During the anticyclonic phase the ice is recirculated in the Beaufort Gyre and thus is getting older and thick. During the cyclonic regime the total Arctic sea ice mass is therefore reduced while during the anticyclonic more sea ice mass can build up, if air temperatures allow thermodynamical growth. Between the late 1980s and mid 1990s a strong positive AO phase caused an enhanced outflow of thick old ice from the Arctic. Since then the AO is in a more neutral phase but in spite of that the extent and thickness of old ice have continued to decrease. This shows that AO and NAO can not explain all of the existing ice drift and export variability. Regional atmospheric circulations and internal Arctic processes are of great importance for the variability of both thickness and extent of the Arctic ice cover (*Maslanik et al.*, 2007a,b; *Overland and Wang*, 2005).

To conclude, sea ice is an important climate player in several aspects and *Lenton et al.* (2008) identified the Arctic sea ice as one of nine potential tipping elements in the Earth's climate system and the one which already may have passed a tipping point due to its recent decline.

Fram Strait Sea Ice Volume Flux

Two main processes can be identified for a change in Arctic sea ice mass: a change in the net amount of sea ice production and in the export of sea ice out of the Arctic Ocean. The first process depends on the length of the freezing period, snow accumulation, ice production in polynyas and surface air temperatures. The second process is largely

determined by the sea ice export through Fram Strait into the Greenland Sea, since export through Fram Strait is by far the largest portion of the total Arctic sea ice export. Currently the net annual sea ice volume exported through Fram Strait into the Nordic Seas amounts to about 10% of the total sea ice mass of the Arctic Ocean and is the single largest source of freshwater in the Nordic Seas (*Dickson et al.*, 2007; *Serreze et al.*, 2006; *Aagaard and Carmack*, 1989). Only the liquid freshwater flux through Fram Strait is of the same order. As explained before, interannual perturbations in the sea ice transport through Fram Strait can modify the major water mass formation processes in the Greenland Sea and further downstream with consequences for the deep water formation and global ocean circulation. The amount of the Fram Strait sea ice volume flux is determined by the sea ice thickness at the northern entrance of the Fram Strait and mainly the wind forcing. It was shown by *Pfirman et al.* (2004) that sea ice export through Fram Strait can occur in surge-like events, where large portions of the old, thick ice leave the Arctic Ocean. Depending on the strength and location of the Beaufort Gyre and the Transpolar Drift, it takes several years until ice of similar thickness has formed again (see previous Section).

While in sea ice model studies the ice volume or ice mass flux is one of the quantities of the most interest (e.g. *Koenigk et al.*, 2006, 2007), it is difficult to get this flux from observations. Sea ice area, motion, thickness and ice density have to be known to derive the sea ice volume flux, and it is not possible to obtain all these quantities with any one measurement technique. A multi sensor approach has therefore been chosen by other groups (e.g. *Kwok et al.*, 2004a) and is also chosen for this study, with the goal to utilize only satellite measurements. Existing estimates of the sea ice volume flux through Fram Strait (1950s to 1990s) range from 1600 km^3/year to 5000 km^3/year and show high interannual variability (*Vinje*, 2001; *Vinje et al.*, 1998). During 1991–1999, averaged transports amount to (2218 ± 497) km^3/year, with individual annual values ranging from 1792 km^3 (1998/99) to 3364 km^3 (1994/95) (*Kwok et al.*, 2004a). From the three for the volume flux determination needed parameters sea ice area, motion, and thickness the first two are available on a daily basis (area) or every other day (motion), based on all-weather and daylight independent spaceborne passive (e.g. Special Sensor Microwave/Imager (SSM/I)) and/or active (e.g. SeaWinds on QuikSCAT) microwave sensors since late 1978 (e.g. *Agnew et al.*, 1997; *Kwok et al.*, 1998; *Cavalieri et al.*, 2003). In this study data from the Advanced Microwave Scanning Radiometer for EOS (AMSR-E) are used to obtain sea ice concentration and motion. For comparison also QuikSCAT data are used for ice motion determination.

In contrast, knowledge about the sea ice thickness was limited in the past to a few, sparsely distributed measurements, obtained, e.g. by drilling, moored ULS (*Vinje et al.*, 1998), submarine-based sonar (e.g. *Wadhams*, 2000; *Rothrock et al.*, 1999), and ground-based or air-borne electromagnetic thickness sounding (*Haas*, 2004b,a). Furthermore, all these thickness measurements are obtained on a quite different spatial scale than the ice area and motion measurements. Previous ice volume transport estimates through Fram Strait were obtained primarily using data from moored ULS by extrapolating local thickness estimates across the entire Fram Strait to obtain a complete cross-strait ice thickness profile (e.g. *Vinje et al.*, 1998).

In 2003 *Laxon et al.* (2003) obtained the first satellite-based estimate of the Arctic sea ice thickness distribution from spaceborne radar altimetry, although severe limitations

apply concerning the covered area, the minimum observable ice thickness, and the temporal resolution. Progress was obtained in ice thickness observations after the launch of the Ice, Cloud, and land Elevation Satellite (ICESat) in 2003. ICESat's Geoscience Laser Altimeter System (GLAS) is the first space-borne instrument, which at least comes close to the needed spatial and temporal resolutions needed to monitor the sea ice thickness globally. GLAS is measuring its height above the Earth's surface, from which the Sea Surface Height (SSH) and the sea ice freeboard height can be inferred. Several only recently published studies (*Kwok et al.*, 2004b, 2006, 2007; *Spreen et al.*, 2006; *Zwally et al.*, 2008) provide first estimates of the sea ice freeboard and thickness distribution obtained from ICESat data for the Arctic and Antarctic. Key problems for all these studies are i) inaccurate SSH estimates, ii) unknown snow depth and ice density, which are needed to convert freeboard to ice thickness, iii) contamination by clouds and due to this low data coverage and/or larger errors of the altimeter measurements. Therefore, best results are expected to be obtained in regions with a stationary sea ice cover, which permits averaging over long/large periods/areas. These conditions are not met in the Fram Strait/Greenland Sea: sea ice is known to drift several kilometres per day, divergence and convergence can continuously change surface roughness, and snow accumulation can be very variable. Therefore careful error estimates are crucial to determine the reliability and accuracy of the estimated quantities – like sea ice freeboard height and volume flux. However, as pointed out before, the sea ice volume flux through Fram Strait is the most important ice export of the Arctic Ocean and can have large influence on the ocean circulation and thus the climate system. Continual monitoring of Fram Strait sea ice volume flux is therefore of particular importance.

2.2 Instruments and Data

After the introduction to the different aspects of the Arctic climate system important for this study given in the last section, in this section a short introduction to the satellites sensors from which measurements are utilized in this study is given. Namely these are ICESat/GLAS (Section 2.2.1), AMSR-E (Section 2.2.2), QuikSCAT (Section 2.2.3), ASAR, and RADARSAT (both Section 2.2.4). The order of the satellite sections reflects their importance for this study. Also the used data products are shortly introduced. More detailed descriptions of the used algorithms and measurement principles are given in the accordant chapters where the data are applied. The last section of this chapter (Section 2.2.5) describes the study region and the map projection used consistently for all datasets.

2.2.1 ICESat/GLAS

The Ice, Cloud, and land Elevation Satellite (ICESat) is the first satellite mission which at least comes close to the needed spatial and temporal resolutions needed to monitor the sea ice thickness globally. The primary purpose of ICESat is to determine inter-annual and long-term changes in volume of the polar ice-sheets, mainly Antarctica and Greenland, and the influence of this changes on the global sea level. The possibility to determine also the sea ice freeboard, as it is done in this study, was already mentioned in the pre-launch studies but only as a secondary aspect, which feasibility was not guaranteed

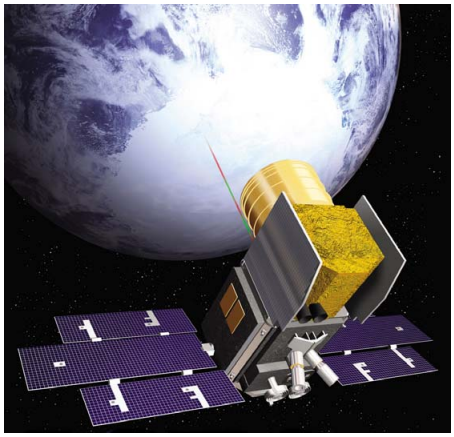

Figure 2.5: Artist's rendering of the ICESat satellite with GLAS transmitting a laser pulse towards the earth surface (courtesy NASA).

(*Zwally et al.*, 2002). Another ICESat application are atmospheric measurements of cloud properties and aerosols height profiles. An artist view of ICESat in space is shown in Figure 2.5.

ICESat was launched on 12 January 2003 by the National Aeronautics and Space Administration (NASA) and carries one main instrument: the Geoscience Laser Altimeter System (GLAS). ICESat is operating in an orbit with 600 km altitude and 94° inclination. This orbit configuration allows altimeter measurements up to 86° North and South. GLAS has three lasers, with only one operating at a time. Each laser produces an 1064 nm and 532 nm wavelength pulse. The 1064 nm pulses are mainly used for altimetry. The 532 nm data are used for the atmospheric products using the LIght Detection And Ranging (LIDAR) principle. In this study only 1064 nm altimetry data is used. The footprint size of the laser beam is about 64 m on the Earth surface. GLAS is transmitting 40 laser pulses per second (40 Hz), which results in a sampling distance of about 172 m on the Earth surface. Table 2.2 is summarizing the main ICESat and GLAS parameters.

The returned laser pulse is captured by a 1 m diameter telescope and the received power spectrum is digitized by 1 GHz sampler. These digitized pulses are referred to as laser waveforms and have a Gaussian shape for flat surfaces. The waveform is now tracked for its maximum (or maxima in case of rough surfaces, different tracking algorithms are used for different surface types). From the traveling time Δt for the identified maximum and the speed of light c the distance $D_{laser} = c\,\Delta t/2$ between laser and Earth surface is calculated (see also Figure 5.1 on page 64).

To get from the measured distance D_{laser} to a surface elevation measurement the exact position of the laser and thus the position of the satellite in space has to be known. For ICESat this Precision Orbit Determination (POD) is done by a Global Positioning System (GPS) tracking system with a radial accuracy < 5 cm.

ICESat was designed to operate continuously for three to five years. Each laser had an expected lifetime of about two years to achieve this goal. Unfortunately the first laser already failed on 29 March 2003 after 37 days of operation. The degradation of the laser pump diodes was much faster than expected due to an improper material usage in manufacture. To obtain a reasonable long time series and to fullfill the mission lifetime the GLAS operating plan was modified. The planed 183 day repeat orbit was changed

Table 2.2: The main parameters of the ICESat satellite and the GLAS instrument.

ICESat	Orbit	
Altitude	600 km	
Inclination	94°	
Validation Repeat Cycle	8 days	
Mission Repeat Cycle	91 days (33 day sub-cycle) (planned: 183 days)	
Time of Circulation	97 minutes	
Launch Date	2003-01-12	
GLAS		
Frequencies	1064 nm near-infrared surface altimetry	532 nm green aerosols and clouds
footprint	≈ 64 m	
measurement distance	≈ 172 m	
pulse repetition frequency	40 Hz	
Start of Operation	2003-02-20	
Ellipsoid	TOPEX/Poseidon (radius = 6378136.3 m, flattening = 1/298.257)	

to a 91 day one and GLAS is operated now three times a year during an identical 33 day subcycle. Table 2.3 on the next page gives the names and dates for all ICESat measurement periods acquired so far. Thus ICESat now is operating longer than its nominal lifetime and how many more measurement periods can be obtained is unknown. Nevertheless, despite the time gaps the ICESat measurement time series now has achieved a length which allows first interpretations of the variability of the obtained geophysical parameters like sea ice thickness.

Further insight in the GLAS's measurement principle and an overview of the ICESat mission are given in *Schutz et al.* (2005); *Schutz* (2002), and *Zwally et al.* (2002).

GLAS Data Product

For this study the "GLAS/ICESat L2 Sea Ice Altimetry Data" product (GLA13, *Zwally et al.* (2003)) in version 28 is used. It contains all ICESat measurements of potentially ice covered regions and GLAS range measurements calculated with a specially for sea ice adapted range offset. Each GLA13 dataset contains data of 14 ICESat orbits a 97 minutes, thus in total approximately 22.5 hours. Figure 2.6 on the following page shows the surface mask used for the ICESat data in the Arctic. The four surface types land, sea ice, ocean, and ice sheet and their combinations are defined. The GLA13 sea ice dataset contains all GLAS measurements falling inside any of the sea ice masks (light gray, turquoise, and purple-gray areas in Figure 2.6). For the sea ice freeboard and thickness calculations in this study only data from the "sea ice + ocean mask" (light gray area) are used.

Table 2.3: Dates of all ICESat measurement periods and indication if the measured data was used for this study.

Period Name	Start Date	End Date	Length [days]	Used
1	2003-02-20	2003-03-29	37	×
2a	2003-09-25	2003-11-19	55	×
2b	2004-02-17	2004-03-21	33	×
2c	2004-05-18	2004-06-21	34	–
3a	2004-10-03	2004-11-08	36	×
3b	2005-02-17	2005-03-24	35	×
3c	2005-05-20	2005-06-23	34	–
3d	2005-10-21	2005-11-24	34	×
3e	2006-02-22	2006-03-28	34	×
3f	2006-05-24	2006-06-26	33	–
3g	2006-10-25	2006-11-27	33	×
3h	2007-03-12	2007-04-14	34	×
3i	2007-10-02	2007-11-05	34	–
3j	2008-02-17	2008-03-21	33	–

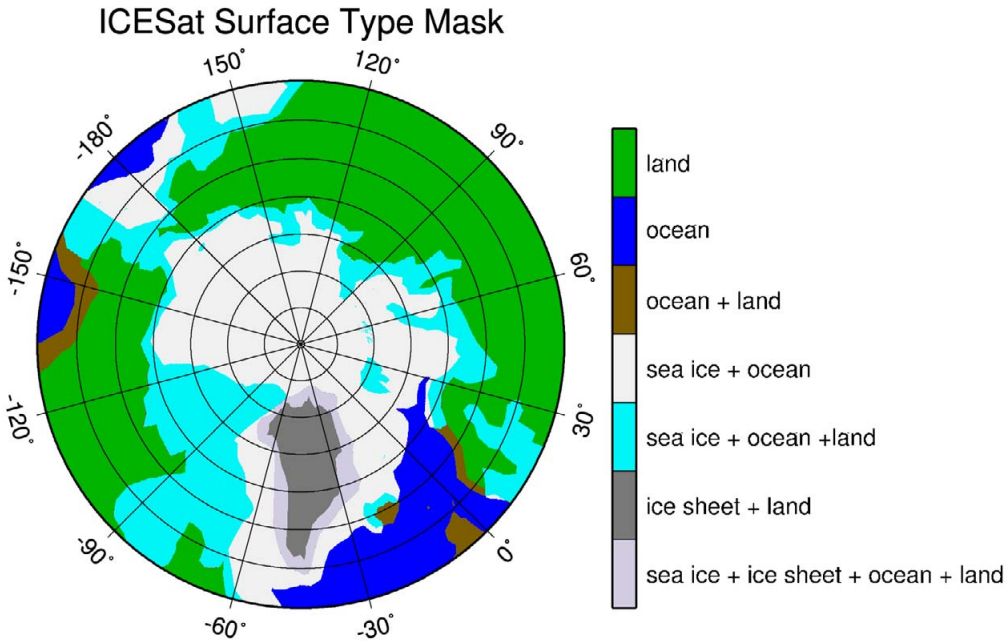

Figure 2.6: The masks for the different surface types used for ICESat data. Areas with different colors denote different surface classes or combinations of surface classes as described by the legend on the right.

The range D_{laser} (see Figure 5.1 on page 64) for every shot is calculated after *Schutz* (2002) by

$$D_{laser} = refRng + siRngOff + dTrop + wTrop \tag{2.1}$$

with $refRng$ as the reference range calculated from the laser pulse runtime, $siRngOff$ the range offset to be added using the algorithm deemed appropriate for sea ice, $dTrop$ the dry troposphere delay range correction, and $wTrop$ the wet troposphere range correction. The troposphere corrections are calculated using surface pressure, temperature, and water vapor interpolated to the laser footprint from the National Centers for Environmental Prediction (NCEP) Global Analysis.

The main data product (beside nearly 90 other data fields with ancillary information) contained in the GLA13 data product is the sea ice surface elevation E defined as

$$E = h_{ellip} - D_{laser} - erElv - ldElv - ocElv\,. \tag{2.2}$$

The ellipsoid height h_{ellip} is the distance between the GLAS and a reference earth ellipsoid, which in the ICESat case is the same ellipsoid as used for the TOPEX/Poseidon radar altimeter mission (equatorial radius = 6378136.3 m and flattening = 1/298.257) in a mean-tide system. Additionally the tides $erElv$ of the solid earth and $ocElv$ of the ocean and the elevation of ocean tidal loading $ldElv$ (*Yi et al.*, 1999) have to be subtracted. The ocean tides $ocElv$ are calculated with the CSR 3.0 global ocean tide model (*Bettadpur and Eanes*, 1994; *Eanes and Bettadpur*, 1995). This is already done for the GLA13 data product and the elevation E as defined in equation 2.2 can be used directly.

The 1064 nm altimetry detector and receiver are able to record returned laser pulses between 0.05 – 13 fJ energy without distortion. Return echos from flat ice or water surfaces under clear atmosphere conditions can have higher energies than 13 fJ at the GLAS detector (*Abshire et al.*, 2005). In these cases the detector is getting saturated, leading to distorted waveforms that are clipped and artificially wide. The standard Gaussian fit processing is getting biased towards longer ranges D_{laser} for such waveforms. *Fricker et al.* (2005) provide a method to recalculate the waveform energy for detector saturation cases and show that this correction significantly improve ICESat's range measurements in the Bolivian salt flat *salar de Uyuni*. This saturation correction is provided as additional data field in the GLA13, v28 dataset. By default the correction is not applied to the elevation measurements, as some slightly saturated cases may not be detected and the correction has a cut-off value of 1.5 m for very strong detector saturations. Nevertheless, as both of these cases are seldom and also in these cases the saturation correction is not deteriorating the final elevations, we decided to apply the saturation correction $satElevCorr$ to the elevation measurements for this study ($E_{corr} = E + satElevCorr$).

Beside the GLAS elevation measurements also the surface reflectivity at the 1064 nm laser frequency can give usefull information to discriminate different surface types and constrain the valid GLAS measurements. The uncorrected reflectivity R_{uncorr} is calculated as the ratio of the received energy P_{receiv} after it has been scaled for range, and the transmitted laser energy P_{transm}:

$$R_{uncorr} = \frac{P_{receiv}}{P_{transm}}\,.$$

Table 2.4: Error budget after *Zwally et al.* (2002) for one ICESat elevation measurement from a single GLAS shot. Last line gives the root mean square (RMS) of all errors, which is the expected single measurement error assuming a Gaussian error distribution.

Error Source	Error Amount
GLAS range measurement precision	10 cm
Radial orbit determination	5 cm
Pointing determination	7.5 cm
Atmospheric delay	2 cm
Atmospheric forward scattering	2 cm
Other (tides, etc.)	1 cm
RMS	13.8 cm

The uncorrected reflectivity R_{uncorr} is contained in the GLA13 dataset for every GLAS measurement. Beside the surface properties, e.g. specular or diffuse (Lambertian) reflection, also the atmosphere influences the ration P_{receiv}/P_{transm}. Therefore R_{uncorr} not always represents the surface reflectivity but a mixture of surface and atmosphere scattering. To obtain the surface reflectivity R the atmospheric effects have to be corrected for:

$$R = R_{uncorr}/e^{-2(tc+ta+tm)} ,$$

where tc is the cloud (column) integrated optical depth, ta is the aerosol (column) integrated optical depth, and tm is the molecular optical depth. The reflectivity R corrected for atmospheric effects is contained in the GLA13 ICESat dataset for every 40th measurement, i.e. in distances of about 7 km. In this study for the comparison to SAR data (Section 5.1.3 on page 72) only the uncorrected reflectivity R_{uncorr} is used as it is available for every GLAS measurement.

Error Budget

Under ideal conditions (cloud free, no detector saturation) ICESat elevation accuracy was found to be < 2 cm and precision < 3 cm over the world largest salt flat the *salar de Uyuni* in Bolivia. The accuracy of ICESat measurements can be heavily derogated by detector saturation caused by high pulse return energy, by forward scattering from clouds, and by higher noise ratios for declining transmitted laser power. These effects may cause biases of up to 1 m for single overpasses (*Fricker et al.*, 2005). Some of the bias caused by detector saturation can be corrected for but nevertheless, for a single ICESat measurement the error can exceed 1 m.

However, the mean error is much smaller. In Table 2.4 the different error contributions to the root mean square (RMS) error of 13.8 cm for a single ICESat elevation measurement according to *Zwally et al.* (2002) are listed. These are theoretically error estimates calculated before the actual ICESat launch. As mentioned above from field comparison the real error can expected to be smaller. Nevertheless, for the error calculations done in this study the conservative error value of 13.8 cm for a single shot ICESat measurement is used. Our expected sea ice freeboard values lie in the decimeter range. Thus, even

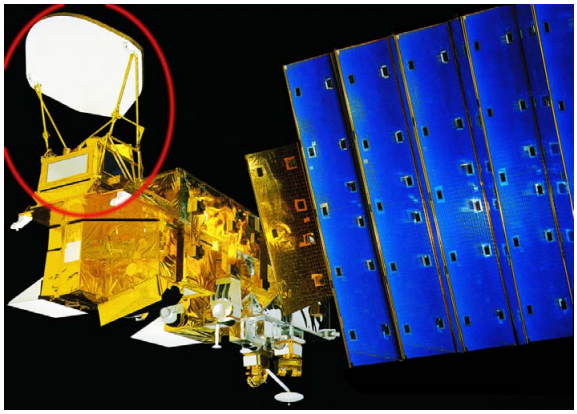

Figure 2.7: Artist's view of NASA's Aqua satellite. The red ellipse marks the AMSR-E microwave radiometer (top: 1.6 m diameter parabolic reflector, bottom: feedhorn unit) (courtesy NASA).

if we would find a perfect ice freeboard algorithm, the reported ICESat error margins would cause large uncertainties for the freeboard estimate from a single ICESat measurement. Therefore, already now it becomes clear, that averaging over several ICESat measurements will be needed to reduce the mean error of the ice freeboard estimates.

2.2.2 AMSR-E

In this study Advanced Microwave Scanning Radiometer for EOS (AMSR-E) data is used to determine sea ice concentration (Chapter 3) and sea ice drift (Chapter 4). Both quantities are together with the ice thickness prerequisites to obtain the sea ice volume flux. The main advantage of observations in the microwave spectrum in comparison to the visual spectrum is the independence of daylight and clouds.

The AMSR-E sensor measures the Earth's electromagnetic emission at six different frequencies between 6.9 and 89 GHz at both horizontal and vertical polarization. AMSR-E is mounted on NASA's AQUA satellite. An artist's view of the Aqua satellite including the AMSR-E sensor is shown in Figure 2.7. Aqua is flying in a sun synchronous, near-polar orbit with an inclination of 98.2°. The orbit altitude is 705 km and the circulation period 99 minutes. AMSR-E is a conical scanning radiometer with 6 feedhorns and a parabolic reflector of 1.6 m diameter. The AMSR-E swath width is about 1450 km and thus daily complete coverage of the Earth surface north and south of ±55° is achieved. Details of the AMSR-E characteristics can be found in Table 2.5 on the following page.

Both the sea ice concentration and drift datasets used for this study exploit brightness temperatures obtained from the vertically and horizontally polarized 89 GHz channels. With a footprint seaice of about 5 km these channels offer todays highest spatial resolution for spaceborne microwave radiometry. The lower frequency channels are only involved as weather filters to detect spurious ice in the open ocean, and for validation purposes. The AMSR-E 89 GHz swath is composed of measurements from two feedhorns, whose footprint locations on the Earth surface is shifted by about 5 km to each other. On 4 November 2004 the 89 GHz feedhorn A (see Table 2.5) failed, what reduced the sampling resolution in flight direction from 5 to 10 km. However, for the polar regions, which are covered by several satellite overflights per day, daily brightness temperature maps with a resolution of about 5 km still can be constructed.

AMSR-E was developed by the Japan Aerospace Exploration Agency (JAXA). The

Table 2.5: Main characteristics of the AMSR-E radiometer on board NASA's AQUA satellite (*JAXA*, 2005). For the footprint size and sampling interval distances are given as sampling versus flight direction. For the temperature resolution the worse one of the two channels (horizontal and vertical) is given.

Center Frequency [GHz]	6.925	10.65	18.7	23.8	36.5	89	
						A Scan	B Scan
Band Width [MHz]	350	100	200	400	1000	3000	3000
3 dB Beam Width	2.2°	1.5°	0.8°	0.92°	0.42°	0.19°	0.18°
Footprint Size [km^2]	43×75	29×51	16×27	18×32	8.2×14.4	3.7×6.5	3.5×5.9
Sampling Interval [km^2]	9×10	9×10	9×10	9×10	9×10	4.5×10	4.5×10
Temperature Resol. [K]	0.33	0.54	0.48	0.45	0.45	0.98	1.12
Integration Time [ms]	2.5	2.5	2.5	2.5	2.5	1.2	1.2
Incidence Angle	55°	55°	55°	55°	55°	55°	54.5°
Dynamic Range	2.7–340 K						
Polarization	Vertical and Horizontal						
Cross Polarization	Less than −20 dB						
Swath Width	1450 km nominal						

National Snow and Ice Data Center (NSIDC) provides AMSR-E data in different processing levels. Level 3 daily gridded brightness temperatures on a 6.25 km polar stereographic grid (see Section 2.2.5) are used to calculate the sea ice concentration (Chapter 3). The sea ice drift is calculated from brightness temperatures on the same grid. Here brightness temperatures are first calculated by the method described in the "AMSR-E Data Users Handbook" (*JAXA*, 2005) from Level 1A swath raw observation counts, which are distributed from NSIDC within hours after acquisition. Afterwards all swath brightness temperatures of one day are interpolated onto a polar stereographic grid (see Section 2.2.5). From these grids sea ice drift is calculated at *Institut français de recherche pour l'exploitation de la mer* (IFREMER) (see Chapter 4).

2.2.3 QuikSCAT/SeaWinds

Data from the Quick Scatterometer Mission (QuikSCAT) satellite are used for two purposes in this study: (1) to obtain the multi-year sea ice fraction (Section 5.2.1 on page 83) and (2) as comparison dataset for the sea ice drift (Section 6.5.1 on page 114).

The SeaWinds instrument on QuikSCAT, launched in June 1999, is an active Ku-band dual-polarized scanning pencil-beam scatterometer. As SeaWinds is the only instrument on board QuikSCAT both will synonymously referred to as QuikSCAT from now on. QuikSCAT measures radar backscatter at 13.4 GHz in horizontal (HH) and vertical (VV) polarization at incidence angles of 46°(1400 km swath-width) and 54°(1800 km swath-width), respectively. The measurements have a footprint of 25×37 km, but subfootprint range resolution is achievable and due to the rotating antenna each point on earth is covered twice for one overflight. All measurements of one day are averaged on a 25 km polar stereographic grid (see Section 2.2.5) for both polarizations covering the complete Arctic and Antarctic (*Ezraty and Piollé*, 2001). The gridded backscatter σ_0 data for both VV and HH polarization are provided by *Centre ERS d'Archivage*

et de Traitement (CERSAT) at IFREMER in Brest, France (`http://www.ifremer.fr/cersat/en/data/download/gridded/psiqscat.htm`). From these daily backscatter maps the multi-year sea ice concentration is calculated with the algorithm described in Section 6.5.1 on page 114. The used QuikSCAT ice drift was calculated from enhanced-resolution (2.225 km) backscatter maps (*Haarpaintner*, 2006) and the drift data were provided by Jörg Haarpaintner.

2.2.4 SAR Data

Due to its high spatial resolution Synthetic Aperture Radar (SAR) data is ideally suited for validation purposes of lower resolving satellite data. In Section 4.3 on page 58 sea ice drift obtained from SAR observations is used as reference for the AMSR-E sea ice drift. In Section 5.1.3 on page 72 ICESat sea ice freeboard heights are validated with SAR data. For both validation comparisons SAR data from two sensors are used: ASAR and RADARSAT. As all measurements in the microwave spectrum SAR observations are independent of daylight and clouds.

Envisat ASAR

The Envisat satellite operated by the European Space Agency (ESA) carries a variety of different sensors for environmental observations (in total nine instruments). One of those is the Advanced Synthetic Aperture Radar (ASAR). It is an imaging microwave radar operating at 5.331 GHz (C-band) in both vertically and horizontally polarization. The ASAR antenna has a size of $10 \times 1.3\,\mathrm{m}^2$. ASAR can acquire data in several different modes offering different spatial resolutions and swath widths. In this study only data from the Wide Swath Mode with a spatial resolution of 150 m and a swath width of 400 km is used. The radiometric resolution lies between 1.5 and 1.7 dB. The incident angle varies between 15° and 45°.

RADARSAT

The second source used for SAR data is the RADARSAT satellite operated by the Canadian Space Agency (CSA). The onboard SAR is as the satellite called RADARSAT and is as ASAR measuring at 5.3 GHz (C-band). In contrast to ASAR RADARSAT is only operating at horizontal polarization for both sending and receiving (HH). The antenna size is $15 \times 1.5\,\mathrm{m}^2$. RADARSAT is operating in different acquisition modes. For this study only data from the ScanSAR mode with a spatial resolution of 100 m and a scene size of $500 \times 500\,\mathrm{km}^2$ is used. The incident angle varies between 20° and 49°.

2.2.5 Polar Stereographic Projection and Study Region

All data are mapped onto a grid using the polar stereographic projection used by the NSIDC for several sea ice products (`http://nsidc.org/data/grids/ps_grid.html`). As only difference for the sea ice thickness and volume flux datasets the World Geodetic System 1984 (WGS84) ellipsoid is used instead of the Hughes ellipsoid used by NSIDC (*Snyder*, 1987). For our grid size of 25 km differences introduced by this are negligible.

The polar stereographic projection is a conformal azimuthal map projection, thus preserving correct projected angles but not the area of all grid cells. The latitude of true scale is set to 70° N. With this projection the distortion in area at the North Pole is about 3% and therefore can be neglected. Different grid resolutions are used for the different datasets but either the grid resolution is 25 km like for the final sea ice volume flux or is an integer factor of this 25 km (e.g. 12.5 or 6.25 km) to guarantee easy data conversion. The region used for this study is covering the Fram Strait, Greenland Sea, and a part of the Arctic Ocean. The corner coordinates are upper-left: 89.54 N/−135.00 E, upper-right: 73.49 N/45.00 E, lower-left: 63.68 N/−45.99 E, and lower-right: 59.22 N/−13.17 E. The complete study region, for which all calculations are done, is for example shown in Figure 5.2 on page 66. Most Figures in this thesis only show the northern, most interesting part of that region (e.g. Figure 6.2 on page 97).

Chapter 3

Sea Ice Concentration

3.1 Introduction

As shown in Figure 1.1 on page 3, the sea ice concentration or respectively the sea ice area is the first quantity to be derived in order to obtain the sea ice volume flux. The sea ice concentration C is defined as the percentage of a given area covered with sea ice. In our case sea ice concentrations are calculated on a grid with 6.25 km × 6.25 km grid cell size. For every grid cell C defines the ice covered percentage of this area of 39.0625 km^2. The rest of the area ($[1 - C]39.0625\,km^2$) consists of open water.

In this study we calculate sea ice concentration data from AMSR-E data using the ARTIST Sea Ice algorithm. It is an enhancement of the sea ice concentration algorithm described by *Svendsen et al.* (1987) for near 90 GHz satellite radiometer data. Within the framework of the Arctic Radiation and Turbulence Interaction STudy (ARTIST), this algorithm was evaluated for SSM/I 85 GHz data and modified to become the ARTIST Sea Ice (ASI) algorithm (*Kaleschke et al.*, 2001). In *Spreen* (2004) the algorithm was adapted to AMSR-E data. Furthermore, the weather filters were refined, an automatic tie-point adaption scheme was introduced, and the ASI data were compared to an ice edge detection algorithm. In this study ASI ice concentrations are further validated to assure the quality of the data and thereby the usefulness for the sea ice volume flux retrieval. Parts of the results presented in this chapter are also published in *Spreen et al.* (2008), but the analysis here goes beyond that.

After a general description of the algorithm in Section 3.2, a tie-point sensitivity analysis is carried out (Section 3.3) and some error estimates are given (Section 3.4). Afterwards AMSR-E ASI data are compared to ship borne observations (Section 3.5) and to two other AMSR-E sea ice concentration algorithms (Section 3.6). The chapter ends with a discussion of the minimum in sea ice coverage during summer 2007.

3.2 ARTIST Sea Ice (ASI) Algorithm

Sea ice concentration has been retrieved by passive microwave sensors since the launch of the Electrically Scanning Microwave Radiometer (ESMR) in December 1972. Since 1987 the SSM/I has been widely used for sea ice concentration determination. A restriction of these instruments is the coarse spatial resolution (approximately 50 km) of the data. In 1992 the 85 GHz channels of SSM/I with a higher spatial resolution of about 15 km have become available.

In 2002 two new and similar microwave radiometers were launched. AMSR-E in May on the AQUA platform and AMSR in October on the MIDORI-II (formerly ADEOS-II)

satellite. Control over MIDORI-II was lost in October 2003. Therefore, only AMSR-E data is used in this study (see also Section 2.2.2 on page 23).

The main advantage of AMSR-E in comparison to SSM/I consists in its improved spatial resolution. For the 89 GHz channels the resolution is improved by factor of three relative to the SSM/I 85 GHz channels (SSM/I footprint size: $13 \times 15\,\mathrm{km}^2$, AMSR-E footprint size: $4 \times 6\,\mathrm{km}^2$). Thereby the elliptical footprint area is reduced from $153\,\mathrm{km}^2$ to $19\,\mathrm{km}^2$. The spatial resolution of ice concentration derived using the widespread NASA-Team and Bootstrap sea ice concentration algorithms is restricted to the resolution of the involved channels with the coarsest resolution, i.e. the 19 GHz channels. They have a footprint size of $43 \times 69\,\mathrm{km}^2$ for SSM/I and $16 \times 27\,\mathrm{km}^2$ for AMSR-E. Thus, the sea ice concentrations presented here represent an improvement in linear spatial resolution of more than a factor of three compared to non-89 GHz AMSR-E based sea ice concentration, and an improvement of more than ten times compared to the resolution of the SSM/I-based ice concentration based on the 37 and 19 GHz channels.

The ice concentration is calculated by the value of the brightness temperature polarization difference P (hereinafter polarization difference or P) of the brightness temperatures T_B measured by the radiometer,

$$P = T_{B,V} - T_{B,H}$$

with V for vertical and H for horizontal polarization. It is known from surface measurements that the polarization difference of the emissivity near 90 GHz is similar for most ice types and much smaller than for open water (Figure 3.1).

This is also valid for the polarization difference P, as the physical temperature is identical for horizontally and vertically polarized brightness temperatures and thus only emissivity differences influence P. For the influence of the atmosphere a_c on the polarization difference we use

$$P = P_s\, a_c = P_s\, e^{-\tau} \left(1.1\, e^{-\tau} - 0.11\right) \tag{3.1}$$

with atmospheric opacity τ and surface polarization difference P_s. This approximation is valid for a horizontally stratified atmosphere under Arctic conditions with an effective temperature replacing the vertical atmospheric temperature profile and a diffusely reflecting surface viewed under an incidence angle of approximately 50° (*Svendsen et al.*, 1987).

The polarization difference in dependence of the ice concentration C can be written as

$$P(C) = \underbrace{\left(C\, P_{s,i} + (1 - C)\, P_{s,w}\right)}_{P_s}\, a_c \tag{3.2}$$

where $P_{s,i}$ and $P_{s,w}$ are surface polarization differences for ice and water, respectively. The atmospheric influence a_c in general is a function of the ice concentration, as both the water vapor content and cloud liquid water decreases from open water to the inner ice pack due to reduced evaporation and cyclones mainly follow the ice edge (*Svendsen et al.*, 1983, 1987; *Brümmer et al.*, 2000). With equation 3.2 the polarization difference P_0 for the ice concentration $C = 0$ (open water) and atmospheric influence a_0 is given by

$$P_0 = a_0\, P_{s,w} \tag{3.3}$$

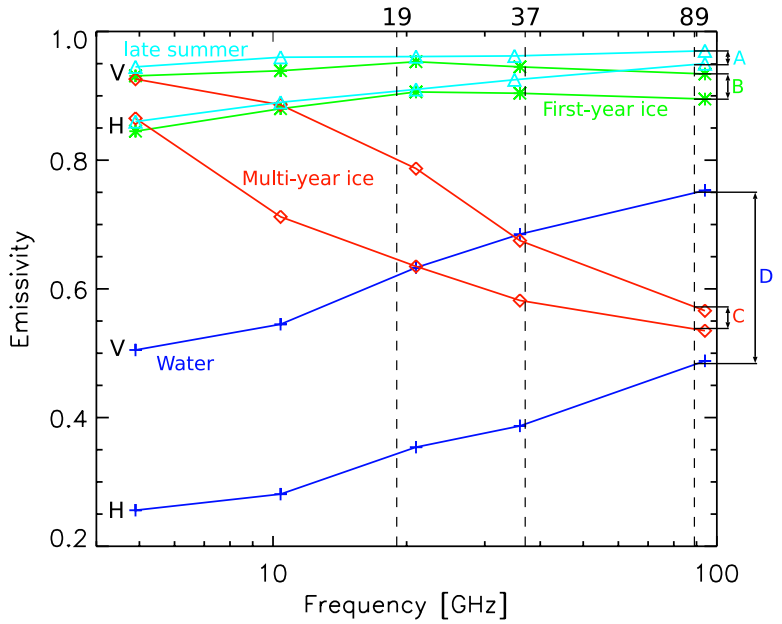

Figure 3.1: Vertical (V) and horizontal (H) emissivity of sea ice and sea water measured at an incident angle of $\theta = 50°$ at different frequencies. The vertical lines show the intersect with the AMSR-E frequencies at 19, 37, and 89 GHz. In winter the *NORSEX Group* (1983) measured first-year (green with stars), multi-year ice (red with diamonds) and open sea water (blue with crosses) at 4.9, 10.4, 21, 37, and 94 GHz. In late summer *Onstott et al.* (1987) measured mixed first-year and multi-year ice (cyan with triangles) at 4.9, 10.4, 21, 35, and 94 GHz. As can be seen from this measurements at 89 GHz the emissivity differences A, B and C for the different ice types are similar and much smaller than the emissivity difference D of water.

and similarly for the ice concentration $C = 1$ (closed ice cover) by

$$P_1 = a_1 \, P_{s,i} \, . \tag{3.4}$$

Taylor expansions of equation 3.2 around $C = 0$ and $C = 1$ lead to

$$P = a_0 \, C(P_{s,i} - P_{s,w}) + P_0 \qquad \text{for} \quad C \to 0 \tag{3.5}$$

$$P = a_1 \, (C - 1)(P_{s,i} - P_{s,w}) + P_1 \qquad \text{for} \quad C \to 1 \tag{3.6}$$

if the derivatives of the atmospheric influence a'_0 for $C = 0$ and a'_1 for $C = 1$ are considered to be zero, assuming the variation of the atmospheric influence to be small for totally ice covered or open water areas. With equations 3.3 and 3.4 the dependence of the atmospheric influence in equations 3.5 and 3.6 can be substituted and the ice concentration is given by:

$$C = \left(\frac{P}{P_0} - 1\right)\left(\frac{P_{s,w}}{P_{s,i} - P_{s,w}}\right) \qquad \text{for} \quad C \to 0 \tag{3.7}$$

$$C = \frac{P}{P_1} + \left(\frac{P}{P_1} - 1\right)\left(\frac{P_{s,w}}{P_{s,i} - P_{s,w}}\right) \qquad \text{for} \quad C \to 1. \tag{3.8}$$

For Arctic conditions $P_{s,w}/(P_{s,i} - P_{s,w}) = -1.14$ is a typical value for sea ice signatures (*Svendsen et al.*, 1987). To be able to retrieve all ice concentration values between 0% and 100% we need to interpolate between the solutions of equations 3.7 and 3.8. Assuming the atmospheric influence to be a smooth function of the ice concentration C we select a third order polynomial for the sea ice concentration between open water and 100% ice cover:

$$C = d_3 P^3 + d_2 P^2 + d_1 P + d_0. \tag{3.9}$$

With equations 3.7 and 3.8 and their first derivatives the unknown coefficients d_i in equation 3.9 can be determined by solving the linear equation system:

$$\begin{bmatrix} P_0^3 & P_0^2 & P_0 & 1 \\ P_1^3 & P_1^2 & P_1 & 1 \\ 3P_0^3 & 2P_0^2 & P_0 & 0 \\ 3P_1^3 & 2P_1^2 & P_1 & 0 \end{bmatrix} \begin{bmatrix} d_3 \\ d_2 \\ d_1 \\ d_0 \end{bmatrix} = \begin{bmatrix} 0 \\ 1 \\ -1.14 \\ -0.14 \end{bmatrix}. \tag{3.10}$$

With the thereby found coefficients d_0 to d_3, equation 3.9 can be used to calculate the sea ice concentration if the tie-points P_0 and P_1 for open water and 100% ice coverage are known. C is set equal to zero for $P > P_0$ and equal to one for $P < P_1$.

The correct choice of the tie-points P_0 and P_1 is important for the retrieval of the sea ice concentration as they also include the mean atmospheric influence. According to the original Svendsen algorithm it was suggested to choose the maxima and minima of the polarization difference of the accordant swath (data of one overflight) as tie points, forming a self-adjusting procedure for different atmospheric conditions (*Svendsen et al.*, 1987). However, it was found that due to changing atmospheric influence within one swath the maximum (minimum) polarization difference often is not the best representation for open water (100 percent ice cover) and is causing non-physical steps in the ice concentration when combining the swaths (*Lomax et al.*, 1995; *Kaleschke et al.*, 2001). Another study successfully used fixed, hand selected tie points for the Svendsen algorithm during the Arctic Ocean Section expedition between 24. July to 9. September 1994 (*Lubin et al.*, 1997). This led to the approach of the ASI algorithm: It uses fixed tie-points that are found by comparing ice concentration of the Svendsen algorithm with well validated reference ice concentration from an independent source, such as an algorithm utilizing the by the atmosphere less influenced lower frequency channels. The tie-points P_0 and P_1 are the two modifiable parameters of the ASI algorithm. They have to be well validated and can be adjusted to changing environmental conditions (e.g. different ice properties due to changing season). Additionally only the weather filter cut-offs for the open ocean can be adjusted (see Section 3.2.1). P_0 and P_1 determine the maximum and minimum polarization difference, respectively. The atmospheric influence on P_1 is small and all ice types even for different seasons have a similar polarization difference (Figure 3.1 on the previous page). P_1 therefore has to be the best representation for all ice types in the dataset. The atmospheric influence on P_0 is larger as cloud liquid water and water vapor reduce the polarization difference above water. Additionally the polarization difference is influenced by the wind driven roughening of the ocean. Thus the choice of P_0 also includes the general atmospheric influence on the polarization difference. The tie-points $P_0 = 47\,\mathrm{K}$, $P_1 = 11.7\,\mathrm{K}$ have been chosen by correlation comparison with AMSR-E Bootstrap ice concentration (*Spreen*, 2004). They are used through the whole year and for

both hemispheres to guarantee a consistent ice concentration from day to day. These tie-points lead to the specific version of equation 3.9:

$$C = 1.64 \cdot 10^{-5}\, P^3 - 0.0016\, P^2 + 0.0192\, P + 0.9710\,.$$

For regional studies adjusted tie-points may yield better results. For example, a different set of tie-points was used during Polarstern expedition ARK-XX/2 ($P_0 = 50\,\mathrm{K}$, $P_1 = 9\,\mathrm{K}$) which visually represented the ice concentration around the ship better in agreement with the helicopter surveys. With the operational tie-points $P_0 = 47\,\mathrm{K}$, $P_1 = 11.7\,\mathrm{K}$ the ice concentration was slightly overestimated, as can be seen in Section 3.5 on page 36.

3.2.1 Weather Filters

One disadvantage of the 89 GHz channels is the pronounced influence of atmospheric cloud liquid water and water vapor on the brightness temperatures. Especially cyclones over open water can reduce the polarization difference to values similarly small as those of sea ice. Therefore, effective filters are necessary to remove spurious ice concentration in open water areas. The weather filtering process consists of three steps. All of them use the lower frequency channels with lower spatial resolution. This in general does not lead to a lower resolution of the marginal ice zone, as the higher resolved ice edge always is covered by non zero ice concentration measurements of the lower frequency channels (see *Kaleschke et al.*, 2001). It only may cause grid points along the ice edge to show too high ice concentrations due to missing weather filters.

The weather filtering steps are:

a) The first weather filter uses the gradient ratio (GR) of the 36.5 and 18.7 GHz channels (*Gloersen and Cavalieri*, 1986), which is positive for water but near zero or negative for ice. This ratio mainly filters high cloud liquid water cases:

$$GR(36.5/18.7) = \frac{T_B(36.5, V) - T_B(18.7, V)}{T_B(36.5, V) + T_B(18.7, V)} \tag{3.11}$$

Fourteen scatter plots $GR(36.5/18.7)$ vs. the 18.7 GHz polarization ratio distributed over all seasons and both hemispheres were analyzed to find an optimal threshold which does not filter out too many low ice concentrations but cuts off all spurious ice (*Spreen*, 2004):

$$GR(36.5/18.7) \geq 0.045 \Rightarrow C(ASI) = 0\,.$$

This threshold keeps all ice concentrations above 15%, which is in general defined as the ice edge contour line (*Gloersen et al.*, 1992; *Cavalieri and St. Germain*, 1995). For conditions with small atmospheric influence also ice concentration below 15% can be observed.

b) The gradient ratio $GR(23.8/18.7)$ is used to also exclude high water vapor cases above open water (*Cavalieri et al.*, 1995). By again analyzing scatter plots analogue to a) a second threshold was found (*Spreen*, 2004):

$$GR(23.8/18.7) \geq 0.04 \Rightarrow C(ASI) = 0\,.$$

After applying this filter almost all spurious ice cases in the open ocean are eliminated.

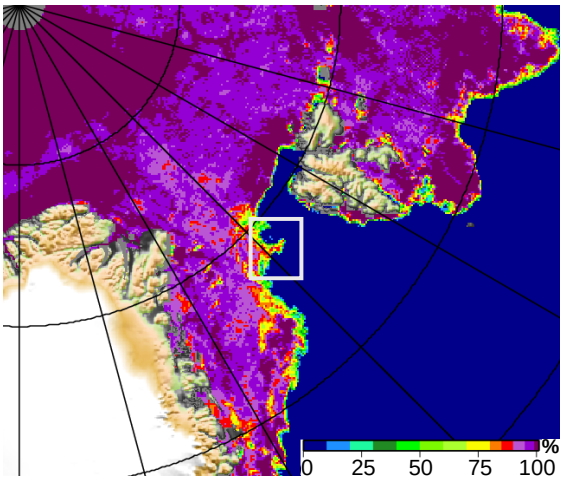

Figure 3.2: Sea ice concentration on 26 February 26 2003 in the Fram Strait region obtained from AMSR-E 89 GHz data (ASI algorithm). Grid spacing is 6.25 km. The corresponding sea ice drift is shown in Figure 4.1 on page 52. The black box marks a region of a dissolving ice edge.

c) Finally, all ASI ice concentrations with corresponding "Bootstrap" ice concentrations (*Comiso et al.*, 2003) equal zero are set to zero:

$$C(Bootstrap) = 0 \Rightarrow C(ASI) = 0\,.$$

After applying these filters only very few extreme weather events may still cause spurious ice in the open ocean, which than also would appear in lower frequency ice concentration algorithms as is assured by weather filter c). But, as mentioned above and as demonstrated in Section 3.4 on page 34, for low to medium high ice concentrations the atmospheric influence can cause an overestimation of the ice concentration.

3.2.2 ASI Results

An exemplary sea ice concentration map showing the complete Arctic on a 6.25 km polar stereographic grid and using the tie-points $P_0 = 47\,\mathrm{K}$ and $P_1 = 11.7\,\mathrm{K}$ is shown in Figure 3.9 on page 44. A color table which mimics the human visual impression of ice is used to visualize the ice concentration for non-scientific users. Figure 3.2 shows an example for our study region, the Fram Strait, on 26 February 2003. The same date is also used as an example for the ice drift in Chapter 4 (Figure 4.1 on page 52). Clearly, this ice concentration map shows the variable ice conditions typical for the Fram Strait during winter, with regions of a very compact but also quite open ice cover along the ice edge. Moreover, the fine spatial resolution of 6.25 km allows discrimination of smaller scale features such as polynyas along the coast or downstream of huge multi-year ice floes, as well as the disintegration of the ice pack into ice patches and fingers in the Marginal Ice Zone (MIZ) (see black box).

An example of the accomplished improvements in the spatial resolution in comparison to more traditional algorithms using the 19 and 37 GHz channels is demonstrated in a section of the Sea of Okhotsk (Figure 3.3), where a region of open water evolved along the south-easterly end of Sakhalin. This region of open water can be clearly identified in the Moderate Resolution Imaging Spectroradiometer (MODIS) false color image (Figure 3.3 right) of that day. It is correctly reproduced as open water in the ASI AMSR-E ice concentration map (middle), but the Bootstrap AMSR-E map only shows a region of

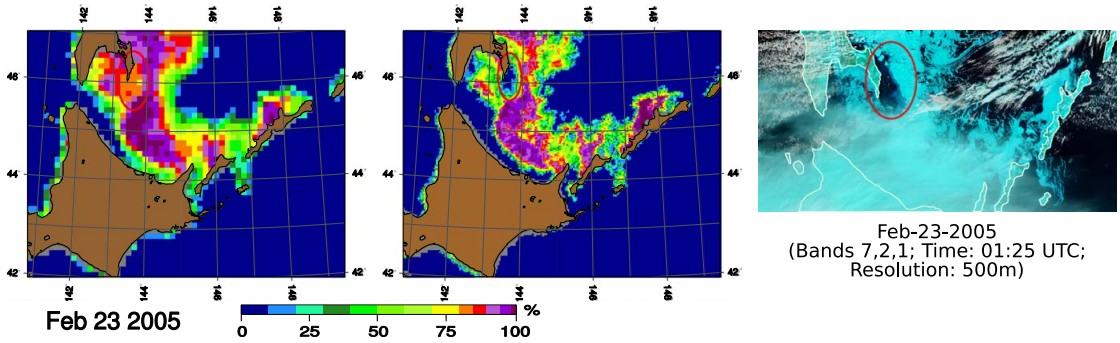

Figure 3.3: Comparison of ice concentration on 23 February 2005 in the Sea of Okhotsk. The left image shows the Bootstrap ice concentration on a 12.5 km grid which matches the spatial resolution of the data. The middle image shows the ASI ice concentrations on a 3.125 km grid. The color code gives the ice concentration between 0 and 100%, missing data is marked gray and land is shown in brown. The red ellipse marks a region of open water which is clearly visible in the ASI ice concentrations and the MODIS false color image of that day (right image; bands 7,2,1 (2155 nm, 876 nm, 670 nm)); image courtesy of MODIS Rapid Response Project at NASA/GSFC) but is not visible in the Bootstrap data due to the lower spatial resolution. In the MODIS image (right) dark areas are open water, while bright and blue colors represent clouds, ice and land. White lines mark land borders.

reduced, non-zero ice concentration (left). The coarse resolution of the 18.7 (≈ 20.1 km) and 36.5 GHz (≈ 10.6 km) channels used by the Bootstrap algorithm and all other low frequency algorithms smears out the open water.

In the following sections the error of the ASI algorithm is evaluated (Sections 3.3 and 3.4) and the ASI algorithm results are compared to in-situ ship data (Section 3.5) and to two other ice concentration algorithms (Section 3.6).

3.3 Tie-point Sensitivity Analysis

The ideal tie-points P_0 and P_1 may vary first with each overflight due to changing direct atmospheric influence (equations 3.3 and 3.4), second on the scale of weeks due to changing radiative properties of the surfaces caused by indirect atmospheric influence (temperature, rain and snow) (e.g. *Voss et al.*, 2003) and third with the seasons (Figure 7 in *Spreen et al.* (2008)). E.g. the fixed tie-points $P_0 = 47$ K and $P_1 = 11.7$ K used here and found by comparison with AMSR-E Bootstrap ice concentration differ from the adaptive tie-points in Section 4.2 in *Spreen et al.* (2008) and the ones used during R/V Polarstern campaign ARK-XX/2. For all these reasons a difference between the true/ideal and the used tie-points is likely.

To estimate the influence of small errors in the tie-points on the sea ice concentration results, a sensitivity analysis has been carried out. The constant tie-points $P_0 = 47$ K and $P_1 = 11.7$ K, which are also used in the operational AMSR-E ASI data product, were chosen as reference. The sea ice concentration C in equation 3.9 on page 30 is a function of the polarization difference P and the tie-points P_0 and P_1, as they are

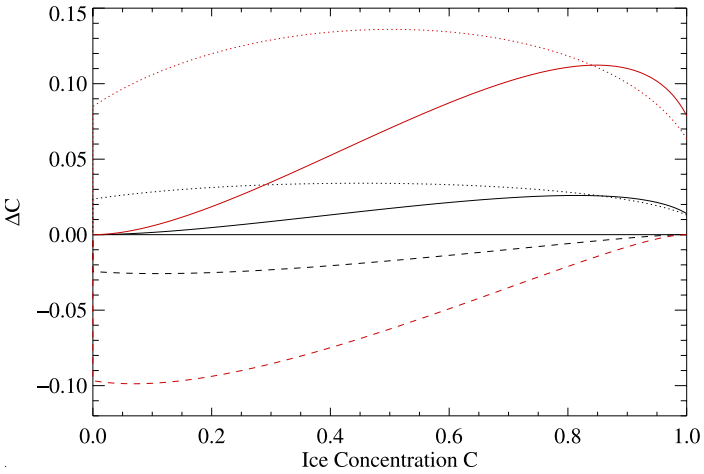

Figure 3.4: Plot of sea ice concentration differences ΔC between original ice concentration (tie-points $P_0 = 47\,\mathrm{K}$ and $P_1 = 11.7\,\mathrm{K}$) and ice concentration where the tie-points were altered by 1 K (black curves) and 4 K (red curves). Dashed: differences for variation of the open water tie-point P_0 by 1 K and 4 K; solid: variation of the ice tie-point P_1 by $-1\,\mathrm{K}$ and $-4\,\mathrm{K}$; dotted: variation of P by 1 K and 4 K, respectively.

needed to determine the coefficients d_i in equation 3.9: $C = C(P, P_0, P_1)$. These three variables P, P_0 and P_1 were varied separately by a value of ΔP between -4 and $+4\,\mathrm{K}$ from their reference values. Then the value of the difference ΔC between the varied and the reference ice concentration was calculated. For example for P_0 follows

$$\Delta C = C(P, P_0, P_1) - C(P, P_0 + \Delta P, P_1)\,.$$

The two dashed curves in Figure 3.4 show example results for $\Delta P = 1\,\mathrm{K}$ (black) and $\Delta P = 4\,\mathrm{K}$ (red), respectively. For P_1 and P, ΔC is calculated accordingly. Additionally P_0 and P_1 were varied simultaneously by $\Delta P = [-4 \ldots 4]$. Some example results are shown in Figure 3.4, where ΔC for $\Delta P = 1\,\mathrm{K}$ and $\Delta P = 4\,\mathrm{K}$ is plotted against the reference ice concentration C.

In all these analyzes the difference ΔC never exceeds $\pm 15\%$ and varies linearly with ΔP. The error of P is given by the radiometric resolution of approximately 1 K of the sensor (Table 2.5 on page 24), the deviation of P_0 and P_1 from the true value is unknown. However, the seasonal variation of the tie-points in Section 4.3. in *Spreen et al.* (2008) indicate that the error in P_1 is of the order of 2 K, leading to an error in C of about 6% at ice concentration near 100%. But for P_0 the deviation may exceed even 4 K and the error near 0% ice concentration therefore may be larger than 15%. These results will be confirmed in the next section.

3.4 Error Estimation

The tie-points P_0, P_1 depend on the near-surface polarizations $P_{s,w}$ and $P_{s,i}$, respectively, and on the atmospheric opacity τ (equations 3.1, 3.2). In order to estimate the errors introduced into the ASI results by these quantities, results from the ship campaigns NORSEX and MIZEX (*Svendsen et al.*, 1987), when all required quantities were measured simultaneously, are used:

$$P_{s,w} = (82 \pm 4)\,\mathrm{K} \qquad P_{s,i} = (10 \pm 4)\,\mathrm{K}$$
$$\tau_w = 0.27 \pm 0.1 \qquad \tau_i = 0.14 \pm 0.035\,.$$

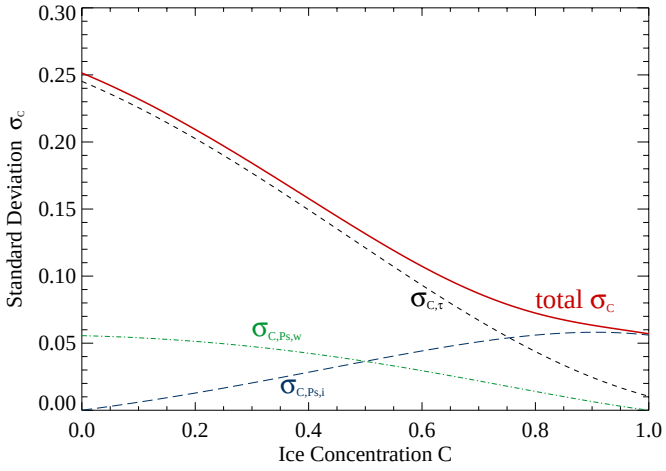

Figure 3.5: The expected standard deviation σ_C (y-axis) in dependence of the ASI ice concentration C (x-axis) using fixed tie-points and standard deviations of τ and P_s obtained during field measurements. The red curve shows the total expected standard deviation of C; the other, not solid curves, show the error contributions of the atmosphere (black dashed, $\sigma_{C,\tau}$), and of the surface polarization differences of open water (green dash-dotted, $\sigma_{C,P_{s,w}}$) and sea ice (blue dashed, $\sigma_{C,P_{s,i}}$).

The optimal tie-points under these circumstances are found as $P_0 = 46\,\mathrm{K}$ and $P_1 = 7.4\,\mathrm{K}$ by using equation 3.1 on page 28. They are kept constant and the standard deviation of the ice concentration σ_C in dependence of C is calculated from equation 3.2 on page 28 assuming τ to decrease linearly between τ_w and τ_i. The standard deviation of P is given as:

$$\begin{aligned}\sigma_P &= \sqrt{\left(\frac{\partial P}{\partial \tau}\right)^2 \sigma_\tau^2 + \left(\frac{\partial P}{\partial P_{s,w}}\right)^2 \sigma_{P_{s,w}}^2 + \left(\frac{\partial P}{\partial P_{s,i}}\right)^2 \sigma_{P_{s,i}}^2} \\ &= \Big[\left(C\ P_{s,i} + (1-C)\ P_{s,w}\right)^2 \\ &\quad \left(-2.2\, e^{-2\tau} + 0.11\, e^{-\tau}\right)^2 \sigma_\tau^2 \\ &\quad + \left(e^{-\tau}(1.1\, e^{-\tau} - 0.11)(1-C)\right)^2 \sigma_{P_{s,w}}^2 \\ &\quad + \left(e^{-\tau}(1.1\, e^{-\tau} - 0.11)C\right)^2 \sigma_{P_{s,i}}^2 \qquad \Big]^{1/2}.\end{aligned}$$

With equation (3.9 on page 30) follows for the standard deviation of C:

$$\sigma_C = \left|\frac{\partial C}{\partial P}\,\sigma_P\right| = \left|(3d_3P^2 + 2d_2P + d_1)\,\sigma_P\right|. \tag{3.12}$$

As can be seen in Figure 3.5, σ_C decreases from 25% for $C = 0\%$ to 5.7% for $C = 100\%$. Above $C = 65\%$, σ_C is smaller than 10%. This gives an impression about the error introduced through average day by day and regional variations of the atmospheric opacity and the surface polarization difference if reliable tie-points are used.

Another error is introduced by the measuring accuracy of the AMSR-E radiometer of about 1 K at 89 GHz (see Temperature Resolution in Table 2.5 on page 24). Additional calculations show that its influence on the ASI ice concentration is below 3.7% (*Spreen*, 2004).

The assumed accuracy of the lower frequency algorithms is approximately 7%, but also cases with discrepancies up to 30% have been observed (*Cavalieri et al.*, 2006; *Comiso et al.*, 1997, (for SSM/I)). For high ice concentration values the ASI algorithm fits well into this range. For low ice concentration the algorithm may significantly overestimate in cases of high cloud liquid water content, especially when cyclones cross the ice edge. On the other hand, the 89 GHz channels are less affected by ice types, refrozen meltponds and snow layering, however they are sensitive to the density and grain size of the snow on top of the sea ice (*Tonboe et al.*, 2006b).

3.5 Comparison to Ship Based Observations

During R/V Polarstern cruise ARK-XIX/1 (28 February to 24 April 2003), the already mentioned cruise ARK-XX/2 (16 July to 29 August 2004), and Polarstern cruise ARK-XXII/2 (28 July to 7 October 2007) sea ice conditions around the vessel were routinely observed from the bridge by the scientists on board by visual surveillance. The winter/spring cruise ARK-XIX/1 started in the Storfjorden and Barents Sea and continued along the west coast of Svalbard up to 82° N in the Fram Strait. Sea ice observations were conducted between 2003-03-06, 09:00 UTC and 2003-04-21, 11:00 UTC. The summer cruise ARK-XX/2 started in Longyearbyen and went through the Greenland Sea through Fram Strait up to 85° N. Sea ice observations were conducted between 2004-07-24, 15:00 UTC and 2004-08-18, 13:00 UTC. The summer to fall cruise ARK-XXII/2 started in Tromsø, Polarstern steamed through the Barents Sea passing East of Svalbard up to 84.5° N. From there the cruise continued to the East covering almost the complete part of the Eurasian and Russian Arctic Ocean. The northern most point was 88.4° N and the eastern most 135° W. Sea ice observations were conducted between 2007-08-01, 17:00 UTC and 2007-09-25, 12:20 UTC in the Laptev Sea. Plots of the cruise track of the three expeditions are shown on the right side of Figure 3.6.

One of the several observed quantities is the total sea ice concentration, which is shown as gray lines in Figure 3.6 for ARK-XIX (top), ARK-XX (middle), and ARK-XXII (bottom), respectively. Details can be found in *Lieser* (2005) and *Hendricks et al.* (2008), the datasets including photos of every observation for ARK-XIX and ARK-XX are available through *Lieser et al.* (2005) and *Lieser and Haas* (2005). As the observations were conducted by up to 16 different persons, errors may be introduced due to different subjective estimates of the ice concentration around the ship. The ice concentration estimates represent the area visible from the vessels bridge. If the observations had been done following the ASPeCt sea ice observation protocol (*Worby*, 1999), like it was done for cruise ARK-XXII, the observed area should have been limited to 1 km radius. However, the observed area depends on the overall visibility (fog, haze etc.) and thus is often considerably smaller than the AMSR-E 89 GHz footprint and certainly smaller than the 36.5 GHz and 18.7 GHz footprints. Still these are valuable in-situ data for validation of sea ice concentration algorithms.

These in-situ observations are compared to three different AMSR-E sea ice concentration data sets: (1) ASI ice concentrations on a 6.25 km grid using the tie-points $P_0 = 47$ K and $P_1 = 11.7$ K, (2) NASA-Team 2 ice concentrations on a 12.5 km grid (*Markus and Cavalieri*, 2000), which is the standard AMSR-E ice concentration data available from

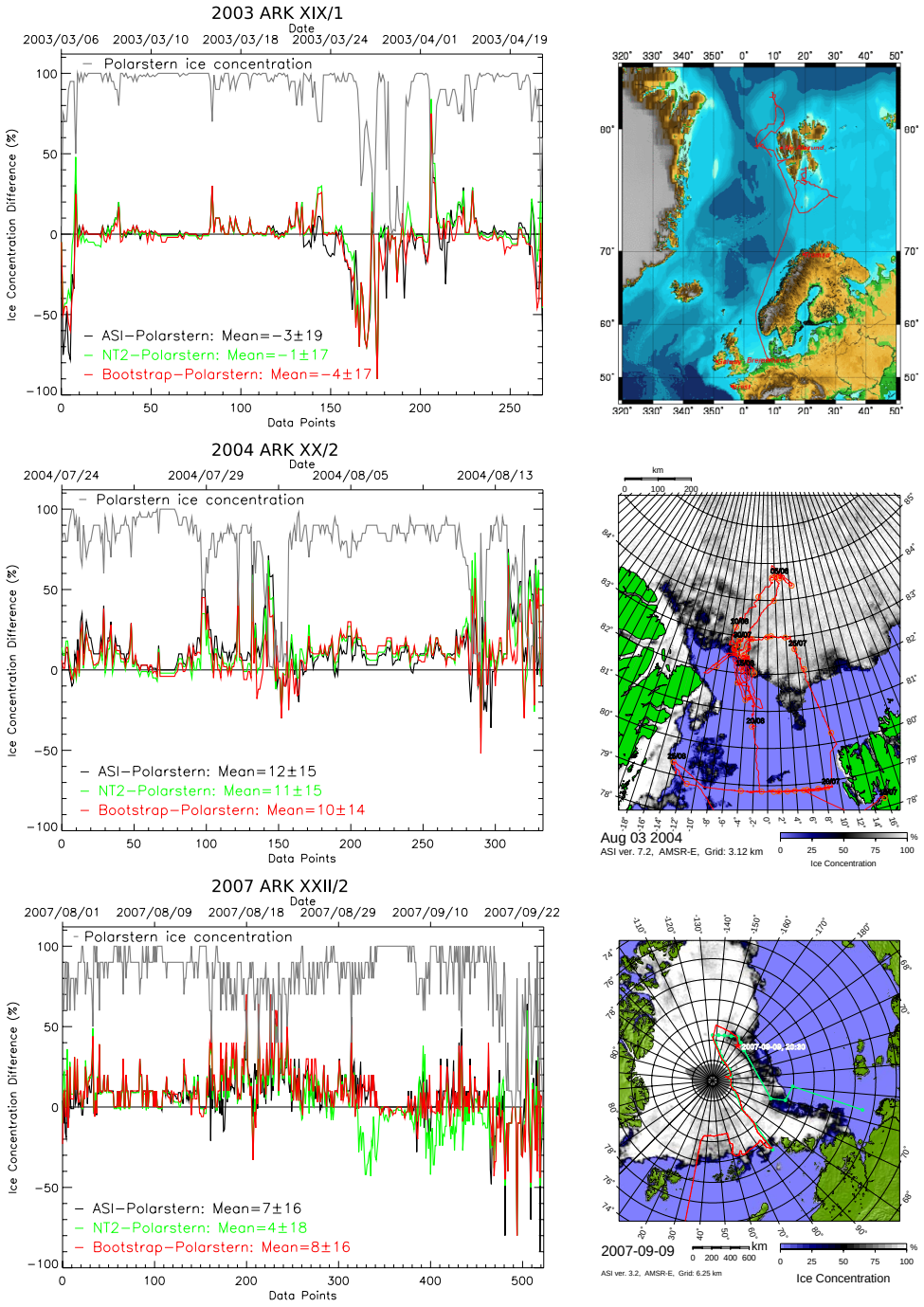

Figure 3.6: Comparison of ice concentrations observed from R/V Polarstern with those obtained from AMSR-E data using three different algorithms. From top to bottom: expedition ARK-XIX/1 (March/April 2003), ARK-XX/2 (July/August 2004), and ARK-XXII/2 (August/September 2007). Gray line: visual Polarstern ice concentrations. The differences between these and the ASI, NASA-Team 2, and Bootstrap algorithm ice concentration are shown in black, green, and red, respectively. X-axes give data point numbers (bottom) and the corresponding dates (top). Right side: respective cruise plots.

Table 3.1: Comparison of visual observations from the bridge of R/V Polarstern with the AMSR-E ASI, NASA-Team 2, and Bootstrap sea ice concentrations. The mean difference (diff.), the standard deviation of the difference (RMS), and the correlation (corr.) between the AMSR-E and Polarstern ice concentrations are given for three expeditions. The dates when the bridge observations started an ended are given in the second and third rows.

expedition	ARK-XIX/1			ARK-XX/2			ARK-XXII/2		
start observ.	2003-03-06			2004-07-24			2007-08-01		
end observ.	2003-04-21			2004-08-18			2007-09-25		
	diff. [%]	RMS	corr.	diff. [%]	RMS	corr.	diff. [%]	RMS	corr.
ASI	−3	19	0.79	12	15	0.80	7	16	0.75
NASA-Team 2	−1	17	0.78	11	15	0.79	4	18	0.66
Bootstrap	−4	17	0.78	10	14	0.83	8	16	0.72

NSIDC (*Cavalieri and Comiso*, 2004), and (3) ice concentrations from the Basic Bootstrap Algorithm (BBA) (*Comiso et al.*, 1997) on a 12.5 km grid, which are provided as differences to NASA-Team 2 concentrations in the NSIDC data set, too. The differences between these three algorithms and the Polarstern data are shown in Figure 3.6 on the preceding page. All three AMSR-E data sets are highly correlated with the Polarstern ice concentrations. The mean difference lays between −4% and 12% with standard deviations of 14% to 19%. The statistical values of the comparisons are summarized in Table 3.1.

During the three Polarstern campaigns all three ice concentration algorithms are performing similar. During the winter campaign ARK-XIX all algorithms reproduce the Polarstern ice concentration estimates quite well with a small overall underestimation, which is small compared to the standard deviation and is caused by outliers during those short periods, when Polarstern mostly operated in the marginal ice zone and the total ice concentration was low (Figure 3.6 on the preceding page). For low ice concentrations the expected error for all algorithms is larger than for high ice concentrations. The main reason for the large differences at low ice concentrations can be attributed to the different spatial resolution and time sampling of the Polarstern and AMSR-E ice concentrations. Polarstern ice concentrations are collected hourly whereas the AMSR-E ice concentrations are calculated from a mean of several satellite overflights of one day. Therefore, the ice concentration seen from the bridge of Polarstern might not be representative for neither the complete area of an AMSR-E grid cell nor the period on which the AMSR-E ice concentration value is based on. This is supported by the fact that spikes (sudden changes) in the Polarstern total ice concentration data (gray curve in Figure 3.6) directly match spikes in all three ice concentration difference data sets (red, green, and black curves).

During the summer campaign ARK-XX and ARK-XXII all three algorithms on average overestimated the Polarstern observations by between 4 and 12%. During ARK-XX the bias is positive for almost the complete time series and all three algorithms are well correlated. This is in agreement with the experience made during the cruise ARK-XX,

where different tie-points were used to better represent the visual inspections from the helicopter. During ARK-XXII until end of August the bias is positive and of the same order as during ARK-XIX for all algorithms. After that, the bias for ASI and Bootstrap drop down to near zero and even gets negative towards the end of the cruise where low ice concentrations were encountered. The second part therefore is more similar to the winter cruise ARK-XIX and the transition of the differences can be explained by the change from summer melting conditions to the start of freeze up in fall. During this second part of the cruise the NASA-Team 2 results are quite different from and often much lower than those of the other two algorithms. Especially at the beginning of September 2007 NASA-Team 2 is heavily underestimating the observed ice concentrations. The reasons for that are not known so far. In total, this underestimation causes the small mean difference of 4% for the NASA-Team 2 algorithm but it can be stated that for the ARK-XII cruise ASI and Bootstrap perform best out of the three algorithms, as the standard deviation of NASA-Team 2 is largest and its correlation is smallest.

Why are all three algorithms overestimating the observed sea ice concentrations during summer? The high fraction of melt ponds should cause an underestimation of sea ice concentration. For the ASI algorithm one main cause is the atmospheric influence. High cloud liquid water and water vapor values in the atmosphere will cause a positive bias for the ice concentrations if this is not corrected by adapted tie-points. The study in *Spreen et al.* (2008) of automatically matching AMSR-E ASI ice concentration values to SSM/I NASA-Team ones showed, that for the ASI algorithm in the Arctic at least two different sets of tie-points would be necessary to imitate the SSM/I NASA-Team ice concentrations. Especially the summer ice tie-point P_1 has to be lower than the winter P_1 tie-point. Thus for the ASI algorithm a summer tie-point for melting conditions of about $P_1 = 9\,\mathrm{K}$ should be a better choice than the here used tie-point $P_1 = 11.7\,\mathrm{K}$, which is constant during all seasons.

Another reason for the positive bias might be caused by the in-situ observations itselves, as the Polarstern's cruise track follows easily navigable ice conditions. During the winter cruise ARK-XIX the ice concentrations mostly were near or at 100%. Than this fact makes not much difference for the ice concentration differences, as the vessel's captain might prefer leads, but which are mostly refrozen and thus 100% ice covered though. In contrast to the winter cruise, the observed ice concentration seldomly exceeds 90% in summer. Now the choice of the vessel's route through the ice also influences the ice concentration differences, as the ship's route might be biased to lower ice concentration compared to the general ice conditions in the AMSR-E footprints. On the other hand, the better representation of the small field of view from the bridge of Polarstern by the higher spatial resolution of the ASI algorithm is not attaining any advantage in comparison to the two other algorithms. Standard deviations and correlations differ only insignificantly for all three algorithms (beside the one already discussed NASA-Team 2 case). This is again presumably caused by the enhanced sensitivity of the 89 GHz channels to atmospheric water vapor and cloud liquid water. However, a quantitative intercomparison of the algorithms is hampered by the different spatial resolution and grid size used for the datasets, which by itself causes different statistical properties. Therefore, in the next section the spatial resolution of the ASI data is reduced to the Bootstrap and NASA-Team 2 one.

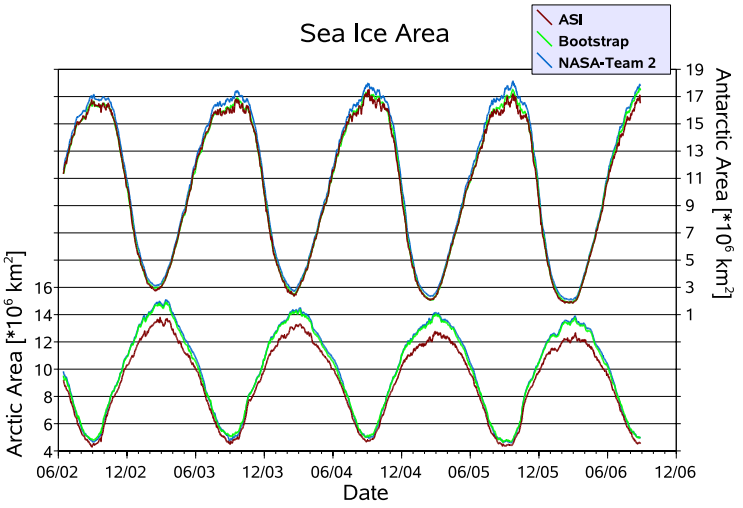

Figure 3.7: Sea ice covered area in the northern (bottom graphs) and southern (top graphs) hemisphere obtained from AMSR-E data by three different sea ice concentration algorithms: ASI (red), Bootstrap (green), NASA Team 2 (blue).

3.6 AMSR-E Ice Concentration Algorithm Intercomparison

To further evaluate the performance of the ASI algorithm in comparison to the Bootstrap and NASA-Team 2 ice concentrations (same data sets as in Section 3.5), the complete available AMSR-E time series from 19 June 2002 to 31 August 2006 is considered. Days with large areas of missing data or with spurious ice caused by strong atmospheric influence in at least one of the datasets were discarded. In total 95% of the 1534 days are considered in the Arctic and 96% in the Antarctic. The sea ice area and sea ice extent are often taken as climate change indicators (e.g. *Comiso*, 2002; *Serreze et al.*, 2003; *Stroeve et al.*, 2005; *Serreze et al.*, 2007; *Comiso et al.*, 2008). Figure 3.7 shows the sea ice area for the northern (bottom) and southern (top) hemisphere calculated with the three algorithms.

All algorithms show similar results. For the Antarctic small differences occur during winter, where NASA-Team 2 gives the largest area. The amount of the Antarctic winter maxima shows a small increase during the AMSR-E measurement period, the four summer minima decrease continuously with about $1 \cdot 10^6\,\mathrm{km}^2$ less ice area in 2006 than in 2003. In the Arctic the ASI results are less or equal to those of the Bootstrap and NASA-Team 2 ice area, with higher differences in winter. The ice area is decreasing in summer and winter for all three algorithms. The decrease of the winter maxima in the four year period is larger than $1.2 \cdot 10^6\,\mathrm{km}^2$. The ASI sea ice extent never exceeds the Bootstrap extent because Bootstrap open water areas are used as mask for the ASI data, as it is part of the algorithm to set ASI to zero where Bootstrap gives zero. For the area differences, additionally, the different grid resolution has to be considered. Spill over effects along the coasts, weather filtering in the marginal ice zone and all other errors which influence a complete grid cell, will affect a larger area for a 12.5 km than for a 6.25 km grid. For instance, the integrated area of polynyas often shows differences on the two grid resolutions, as can be seen in the example in Figure 3.3 on page 33.

To compare the three data sets with a matched resolution, the ASI data are convolved with a Gaussian function with the full width at half maximum set to 21 km, the resolution of the AMSR-E 18.7 GHz channels, and then interpolated on the 12.5 km grid. The spatial

Table 3.2: Sea ice concentration algorithm intercomparison: mean bias, standard deviations (RMS) and correlation between ASI and Bootstrap, and ASI and NASA-Team 2 sea ice concentrations for the AMSR-E period 19 June 2002 to 31 August 2006.

hemisphere	difference	bias	RMS	correlation
north	ASI − Bootstrap	−1.4	8.2	0.95
	ASI − NASA-Team 2	−2.0	8.8	0.93
south	ASI − Bootstrap	1.7	10.8	0.92
	ASI − NASA-Team 2	−1.6	7.2	0.97

distribution of the mean differences during the 2002-06-19 to 2006-08-31 AMSR-E period for ASI minus Bootstrap and ASI minus NASA-Team 2 and the time series of these differences are shown in Figure 3.8 on the next page for both hemispheres.

In the northern hemisphere the mean overall difference for ASI minus Bootstrap is $-1.4\% \pm 8.2\%$ with a mean correlation of 0.95. For ASI minus NASA-Team 2 the mean difference amounts to $-2.0\% \pm 8.8\%$ with a mean correlation of 0.93. In the southern hemisphere ASI minus Bootstrap is on average $1.7\% \pm 10.8\%$ with a correlation of 0.92 and ASI minus NASA-Team 2 is $-1.6\% \pm 7.2\%$ with a correlation of 0.97. The $\pm$ values give again one standard deviation. These results are summarized in Table 3.2.

The spatial patterns in the maps of both differences show a lot of similarities. In the Arctic the largest negative differences occur in the dynamic East Greenland Current and along the west coast of Novaya Zemlya. In the southern hemisphere the by amount largest differences occur along the coast and there are patterns of similar negative differences in both data sets in the Ross Sea ($-145°$ to $-180°$ longitude) and along a zone at $-65°$ latitude starting in the Weddell Sea (30° W) and ranging till 60° W. The latter is an area where the ice edge is rather stable for some months of each year during the investigation period. Also other locations of stable ice edge can be identified in the differences maps in Figure 3.8 on the next page by eather strong positive or negative differences. Thus, the ice edge is another region where large differences occur. The absolute value of the mean difference is not exceeding 2% for any of the four cases. This is within the error estimates of all three algorithms (Section 3.3 and 3.4, and e.g. *Comiso et al.* (1997)). The standard deviations reach 10%, but the larger differences mainly occur along the coast and in the marginal ice zone, what already has been shown in Section 3.4. For three out of the four cases the mean difference is negative and for one it is positive with a similar absolute value. In the Arctic the ASI algorithm seems to slightly underestimate the ice concentration in comparison to the two standard AMSR-E algorithms. In the Antarctic the value of the mean ice concentration of the ASI algorithm lies well in between the two other algorithms.

The bottom graphs in Figure 3.8 show the time series of the Arctic and Antarctic differences smoothed with a 7-day running mean as bright green (ASI − Bootstrap) and red (ASI − NASA-Team 2) lines and smoothed with a 180-day running mean as darker red and green lines. The 7-day smoothed time series shows high variability with a lot of changes on the scale of few days, particularly for the Antarctic difference ASI − Bootstrap. As this is the typical time scale of weather systems we suppose that these changes represent the associated changing atmospheric influence. The 180-day smoothed

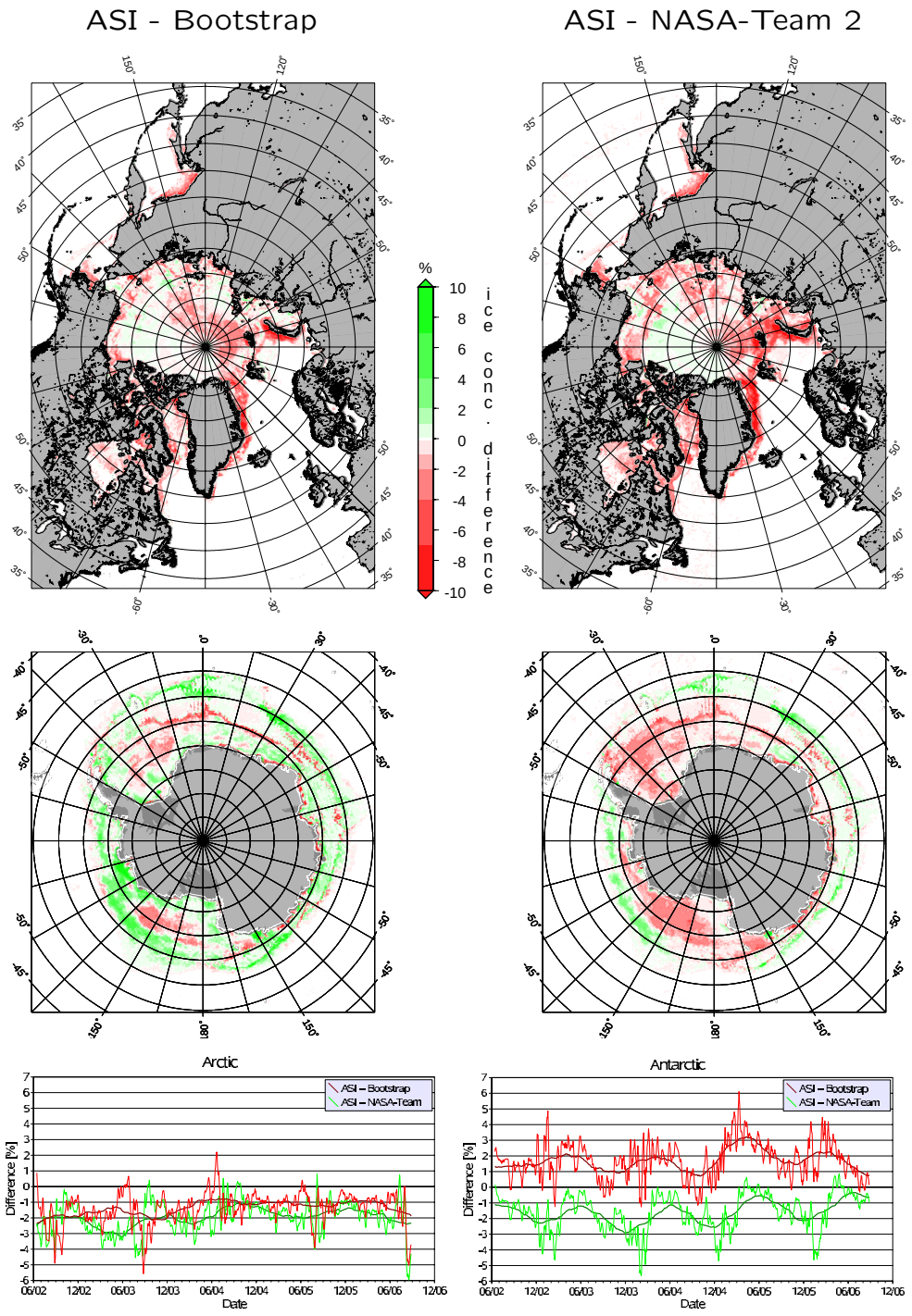

Figure 3.8: Mean daily ice concentration differences (in percent) for the period 2002-06-19 to 2006-08-31. Left maps: ASI minus Bootstrap; right maps: ASI minus NASA-Team 2. Top panels: northern hemisphere; middle panels: southern hemisphere. Bottom graphs: time series of the differences for the northern hemisphere (left) and southern hemisphere (right). Green curves: ASI minus Bootstrap; red curves: ASI minus NASA-Team 2. Thin curves are 7-day and thick 180-day running means.

curves show a clear seasonal cycle, which is more pronounced in the Antarctic, but here also the amplitude of the seasonal change in ice area is much larger (see Figure 3.7 on page 40). For the Antarctic differences it is remarkable that the accordant maxima and minima of the 180-day smoothed (ASI − Bootstrap) and (ASI − NASA-Team 2) time series are shifted by approximately three month to each other, indicating a different behavior for freeze up and melting of the algorithms. The detailed reason for this shift is not known. We expect that by using seasonally changing tie-points as suggested in *Spreen et al.* (2008) the here observed seasonal differences could be reduced. A hemispherical different set of tie-points for Arctic and Antarctic could also reduce the differences. But as we do not know which of the three algorithms is best in representing the true ice conditions, an adaptation based only on differences is questionable. Nevertheless, for applications where not the best representation of the truth but minimal differences between two algorithms is desirable, an adaptation of the tie-points like the one described in *Spreen et al.* (2008) should be used.

3.7 2007 Arctic Sea Ice Minimum and AMSR-E Time Series

For the northern hemisphere the absolute minimum of the 35 year long satellite data derived sea ice extent and area time series occurred in September 2007 (*Comiso et al.*, 2008; *Cavalieri et al.*, 2003). The sea ice extent definition used here is defined by the 15% ice concentration isoline. Figure 3.9 on the next page shows the 2007 minimum sea ice extent as seen with the ASI AMSR-E data. While for example in 1979 the mean September sea ice extent and area were $7.1 \cdot 10^6\,\mathrm{km}^2$ and $6.2 \cdot 10^6\,\mathrm{km}^2$ (Figure 3.9 top right), in 2007 the extent and area only amount to $3.7 \cdot 10^6$ and $3.4 \cdot 10^6\,\mathrm{km}^2$ (Figure 3.9 bottom right), respectively. This is a difference in sea ice coverage of roughly 45%. Note that sea ice extent and area of September 1979 were not particularly high for that time period but resemble rather average conditions. Also in comparison to the absolute minimum sea ice extent and area that has occurred until 2007, which is the minimum of September 2005, when the quantities extent and area had values of $4.8 \cdot 10^6$ and $4.5 \cdot 10^6\,\mathrm{km}^2$, respectively, 2007 was an extraordinary low ice concentration year with again a reduction of more than one million square kilometers in ice coverage compared to 2005.

Figure 3.10 on page 45 shows the daily sea ice extent anomalies of the 2002-06-18 to 2007-12-31 AMSR-E time series for the Arctic (top) and Antarctic (bottom). For each day of a year the mean over all years of the time series for that day is calculated. The anomaly of a specific date is the difference between the ice extent of that date to the mean daily ice extent. For the anomaly time series in Figure 3.10 this means that for dates between 18 June and 31 December six years are taken into account and for all other dates (1 January to 17 June) five years are taken into account for the anomaly calculation. The 30-days running means of the Arctic and Antarctic time series are shown in red and blue, respectively. In summer 2007 between July and October the Arctic ice extent anomalies are strongly negative by more than 1 Million square kilometers. This shows that the arctic summer 2007 had an extraordinary low ice extent even in respect to the last five years. In November/December 2007 the Arctic ice cover recovered fairly fast to an almost neutral state with respect to the conditions of 2002 – 2007. On the other

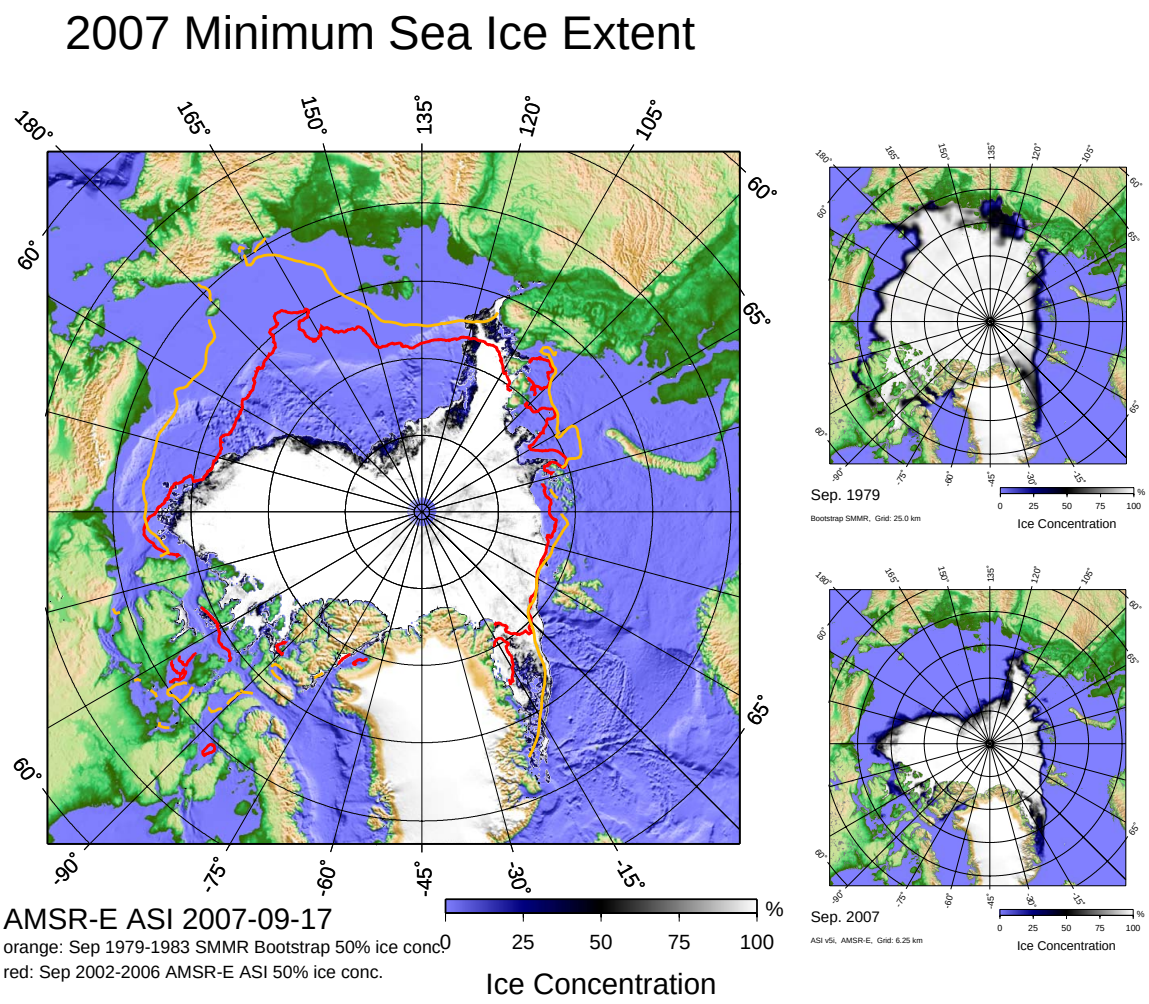

Figure 3.9: The left map shows the sea ice concentration distribution at the time of the minimum Arctic sea ice extent for 2007, which occurred on 17 September. The red contour is the mean 50% ice concentration isoline for the five years 2002 to 2006 and the orange one is the respective isoline for 1979 to 1983. Top right map shows the mean September ice concentration in 1979 and lower right map the mean September ice concentration in 2007. Note the drastic reduction of the sea ice cover in the Eastern Central Arctic, Laptev Sea, East Siberian Sea, Chukchi Sea, and Beaufort Sea (see Figure 2.1 on page 6 for locations of the seas). The 2007 data are ASI AMSR-E ice concentrations, the 1979 data Bootstrap SMMR ice concentrations (see text for explanation of used abbreviations).

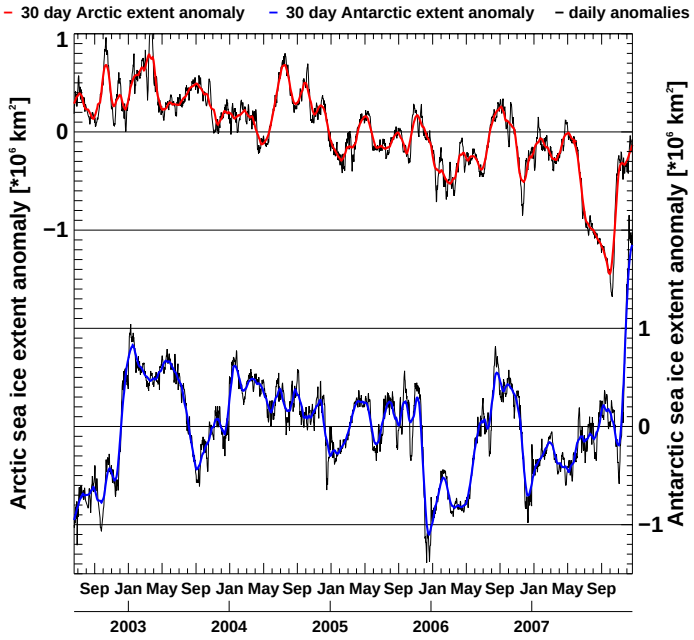

Figure 3.10: Arctic (top) and Antarctic (bottom) daily sea ice extent anomalies for the ASI AMSR-E time series between 2002-06-18 and 2007-12-31 (black lines). 30-day running means are shown in red for the Arctic and blue for the Antarctic. Note the strong negative anomaly for the Arctic and strong positive anomaly for the Antarctic in summer 2007.

hand, the summer ice cover in the Antarctic seems to become extraordinary high in 2007/2008. Until 31 December 2007 a strong positive ice extent anomaly of 1.9 million square kilometers evolved in the Antarctic, which at least means that the summer melting is starting later than usual in 2007/2008 or that e.g. a thicker snow cover is hampering the melting. The first months of 2008 will show if this anomaly can persist until the Antarctic summer sea ice minimum in March. However, as can be seen for the 35-year long sea ice extent time series from satellite data, the sea ice extent in the Arctic shows a clear negative trend, which increases in the last ten years, while the sea ice extent in the Antarctic has no clear trend. The here presented only 5.5 years long ASI AMSR-E time series fits in: the Arctic shows a negative trend while the Antarctic stays stable.

The sea ice concentrations on which the analysis above is based upon are calculated with the ASI algorithm from AMSR-E data described in Section 3.2. Only the 1979 ice concentrations (Figure 3.9 top right and orange contour in Figure 3.9 left) are calculated with the Bootstrap algorithm (*Comiso*, 1995) from Scanning Multichannel Microwave Radiometer (SMMR) data. For the sea ice area calculation the hole around the North Pole, which was not observed by the satellite sensors, was filled up with 99% ice concentration. Note that this hole has a radius of about 6° for SMMR and 1° for AMSR-E. Also the spatial resolution is different (grid resolution 25 km for SMMR and 6.25 km for AMSR-E). Beside the different algorithms used these two facts will cause some difference in the calculated sea ice area. Nevertheless, the sea ice extent should be fairly comparable, only the different grid size might cause a significant difference. The 2007 Arctic sea ice minimum is discussed in more detail in *Comiso et al.* (2008) and *Maslanik et al.* (2007b).

3.8 Sea Ice Concentration Discussion

Today the 89 GHz channels of AMSR-E offer the highest spatial resolution for extraction of daily available, global sea ice concentration data. THE ASI algorithm is on of the few sea ice concentration algorithm using only this channels to retrieve sea ice concentration and therefore benefit from the high spatial resolution. The ASI ice concentration algorithm uses an empirical model to retrieve the ice concentration between 0% and 100%. The atmospheric influence is modeled in dependence of the ice concentration and three weather filters eliminate spurious sea ice in the open ocean. Even if the set of tie-points is not adapted daily to the changing atmospheric and surface conditions, the algorithm shows appropriate results especially at mid and high ice concentrations (above 65%), where the error should not exceed 10%. In areas with low ice concentration, depending on the atmospheric conditions, larger deviations may occur. In general, the comparisons show that the ASI algorithm is performing with a similar quality like the two other AMSR-E sea ice concentration algorithms. The enhanced atmospheric influence is not causing a significantly different sea ice distribution.

This finding is supported by a recent study comparing seven of the most frequently used SSM/I sea ice concentration algorithms (*Andersen et al.*, 2007). Over high concentration sea ice it was found that those algorithms using data acquired at frequencies with shorter penetration depth, i.e. using mainly near-90 GHz information, tend to produce significantly better statistics than the algorithms at 19 and 37 GHz that are most frequently used nowadays. It was found that during winter the root mean square difference of the near-90 GHz ice concentrations with respect to the ship and SAR data used as reference was consistently smaller. *Andersen et al.* (2007) also investigated the influence of using different ice concentration algorithms on the linear trends in time series of Arctic sea ice area and extent for the period 1991 to 2005. The differences in trends were significant between 15% and 20% of the total negative trend in winter. The differences in winter trends are found to be most likely caused by systematic changes of both the atmospheric and sea ice surface properties in the Arctic during this period.

Together with the results of this study it can be stated that using near 90 GHz data some shortcoming arising from stronger atmospheric influence is compensated by less sensibility to sub-surface effects (e.g. snow layering).

Furthermore, systematic sea ice concentration uncertainties affect climate model variables (e.g. the surface air temperature) nearly linearly (*Parkinson et al.*, 2001). However, regional atmospheric models will benefit of the increased horizontal resolution of the ASI AMSR-E ice concentration data, as open water areas and thus the heat transfer is better resolved, see *Kaleschke et al.* (2001) for an example based on SSM/I data.

Additionally, the increased resolution reduces the errors due to mixed coastal pixels. This is particularly useful when mapping coastal polynyas and smaller seas such as the Baltic Sea, Caspian Sea and the Sea of Okhotsk. The polynya area and thus the ocean-atmosphere heat transfer can be estimated with higher accuracy. This is already used for coastal polynyas studies in the Southern Ocean, especially focussing on the dynamics of polynyas (*Kern et al.*, 2007). Polynya areas derived by the Polynya Signature Simulation Method (*Markus and Burns*, 1995) using SSM/I data and from ASI AMSR-E ice concentration show good agreement.

Because of sparse spatial resolution of the ICESat GLAS data and the high uncertainty

of the derived ice thickness for single GLAS measurements, sea ice thickness maps can only be derived on a 25 km grid (see Section 2.2.1 and Chapter 5). Therefore, for the determination of the sea ice volume flux no surplus is obtained from the high spatial resolution of the ASI AMSR-E data for this study. Nevertheless, as has been shown here, it is in terms of accuracy a suitable dataset for this purpose.

3.9 Sea Ice Concentration Summary

The sea ice concentration section can be summarized as follows:

- The for AMSR-E data adapted ARTIST Sea Ice (ASI) concentration algorithm offers sea ice concentration data with about 5 km spatial resolution, which is todays highest resolution available for daily global dataset.
- ASI data was validated
  - by testing the sensitivity of the tie-point selection on the resulting ice concentration (Section 3.3),
  - by comparing ASI data with shipborne observations from three campaigns (Section 3.5),
  - and by comparison of hemispherical ASI data with the results of the two standard sea ice concentration algorithms (Section 3.6).

  In all these surveys the ASI algorithm showed similar good results as the other well validated sea ice concentration algorithms, which utilize the lower frequency channels.
- ASI data is well suited to derive the sea ice area, which is the first quantity needed to obtain the sea ice volume flux (see Figure 1.1 on page 3).

Chapter 4

Sea Ice Drift

In the last chapter we determined the area covered by sea ice using satellite data. In a next step the sea ice drift has to be obtained to get the sea ice area flux (see Figure 1.1 on page 3).

Sea ice drift can be obtained from satellite passive microwave radiometry by the cross-correlation of fields of time-lagged data (e.g. *Kwok et al.*, 1998; *Martin and Augstein*, 2000; *Kwok*, 2008), in which recognizable features are tracked. As these features have to be correlated, the already coarse resolution of passive microwave sensors is further reduced. Like for the sea ice concentration (Chapter 3) again the 89 GHz channel data of AMSR-E are used, because they currently offer the highest spatial resolution for passive microwave remote sensing.

4.1 IFREMER AMSR-E 89 GHz Sea Ice Drift Product

The ice drift data used in this study is provided by IFREMER and the used method is described in *Ezraty et al.* (2007a,b,c). A brief description of the method is given in the following. For comparison (see Section 6.5.1 on page 114) also ice drift data derived from QuikSCAT data is used employing a similar method (*Haarpaintner*, 2006; *Haarpaintner and Spreen*, 2007).

The sea ice drift is calculated from 89 GHz brightness temperature maps with a time gap of two days. The calculation of the ice drift can be split into five steps:

1. Construction of the 89 GHz brightness temperature maps from swath data.
2. Calculation of the fields of Laplacian.
3. Applying a correlation algorithm to these fields.
4. Merging of the sea ice drift derived from the two brightness temperature maps acquired at the two polarizations.
5. Quality check of the ice drift.

(1.) The sea ice drift is first calculated separately from the vertically and horizontally polarized 89 GHz AMSR-E brightness temperatures $T_{B,V}$ and $T_{B,H}$. All 89 GHz $T_{B,V}$ and $T_{B,H}$ measurements of day d_0 are interpolated on grids with 6.25 km spatial resolution, respectively. The used grid is identical to the one used for the sea ice concentration in Chapter 3 (for information about the map projection see Section 2.2.5 on page 25). The same is done for the brightness temperatures of day $d_2 = d_0 + 2$ two days later.

(2.) Next, the second spatial derivative (Laplacian) of the brightness temperature is calculated for all grid cells from the surrounding 5×5 pixel fields:

$$\Delta(T_B)_0 = \frac{1}{9}\sum_{i=0}^{8} T_{B_i} - \frac{1}{16}\sum_{i=9}^{24} T_{B_i}\,.$$

$\Delta(T_B)_0$ is the Laplacian at location $i = 0$, $i = 1$ to 8 are the locations of the neighboring grid cells to $i = 0$, and $i = 9$ to 24 are the outer ring of the 5×5 matrix. The numbering of i is shown in the following sketch:

9	10	11	12	13
24	1	2	3	14
23	8	0	4	15
22	7	6	5	16
21	20	19	18	17

Afterwards, the field of Laplacian is smoothed with a 3×3 median filter:

$$\Delta_S(T_B)_0 = Median(\Delta(T_B)_{i=0\ldots8})$$

The $\Delta_S(T_B)$ fields still have the original grid resolution of 6.25 km and are the source for the following correlation analysis.

(3.) A cross-correlation analysis between the $\Delta_S(T_B)$ map of day d_0 and the one of day d_2 is performed. The correlation analysis is done with $\Delta_S(T_B)$ patterns P of 11×11 pixel size. The correlation analysis is performed for every fifth T_B grid cell, which means every 31.25 km and an overlap of half the size of pattern P. 31.25 km is therefore also the final grid resolution of the ice drift data. As $\Delta_S(T_B)$ patterns are correlated, smaller step sizes than five would not increase the amount of information. First, all patterns $P0_{i,j}$ of day d_0 are checked for the existence of significant structures, which could be found again in the map d_2 two days later. This is done by correlating $P0_{i,j}$ with all patterns $P0$ centered around the neighboring grid cells of $P0_{i,j}$, e.g. $P0_{i-6,j-6}$, $P0_{i-6,j-1}$, $P0_{i+6,j+6}$ etc. A correlation value ≤ 0.6 is assumed as decorrelation, which is indicating the existence of a structure in the pattern $P0_{i,j}$. Next, all patterns $P0$ with identified structures are searched for in the $\Delta_S(T_B)$ map of day d_2. The pattern $P0_{i,j}$ is moved around in a 25×25 pixel large search window around its center location. For each grid cell in this search window the correlation coefficient between $P0_{i,j}$ and the accordant pattern $P2$ of day d_2 is calculated, i.e. $P0_{i,j}$ is correlated with $P2_{i-12,j-12}$, $P2_{i-12,j-11}$, $P2_{i-12,j-10}$ etc. The location of the grid cell with the highest correlation coefficient is selected as the most likely ice drift vector. This also can be the starting grid cell (i, j) itself, which then means no ice motion.

(4.) The correlation analysis described under items (2.) and (3.) is done separately for both the vertically and horizontally polarized T_B fields. Thus at this point two independent ice drift maps D_V and D_H exist, which have to be merged to one consistent ice drift field. A first consistency check is performed using the mean European Centre for Medium-Range Weather Forecasts (ECMWF) wind field during the two day gap. All ice drift vectors with a drift distance > 12.5 km ($D > 0.15$ m/s) and an angular difference $\geq 80°$ to the ECMWF wind are sorted out. All drift vectors with smaller velocity are kept. Afterwards the local consistency of the D_H and D_V fields are checked using the mean + 4 standard deviations and median + 2 standard deviations of the surrounding

drift vectors in a $312.5 \times 312.5\,\mathrm{km}^2$ area as criterion. Now the two drift maps can be merged. a) At the grid points, where both ice drift vectors D_H and D_V are identical, these unambiguous ice drift vectors are used for the final merged ice drift map D. b) At the grid points, where both D_H and D_V are valid ice drift vectors but differ from each other, the most likely ice drift solution has to be found. A cost functions, which additionally to D_H and D_V at the grid point also takes the ice drift D of the surrounding 5×5 matrix into account, is minimized and the solution taken as final drift D. c) At the grid points where only one of the two ice drift maps contains a valid ice drift vector, these vectors are checked for consistency with the ice drift of the surrounding 5×5 matrix. Only ice drift vectors which fullfill the criterion $\mid x_m - x_0 \mid + \mid y_m - y_0 \mid \leq 2$ are kept. x_m and y_m are the mean x and y drift distances in pixel units of the 5×5 matrix and x_0 and y_0 the accordant pixel drift distances at the grid point itself. This criterion enables either each component to differ by at most one pixel or a single component to differ by at most two pixels. Also the angular difference is tested with a similar scheme. The minimization of the cost function (b) and the consistency check (c) is performed iteratively for all ambiguous ice drift grid cells until the ice drift of none of them is changing anymore. This has to be done, as, due to the used 5×5 drift matrix, the result of the minimization or consistency check is also influencing the surrounding grid cells. At this point the final drift field D is found.

(5.) Finally, to each grid point a quality flag consisting of 6 bits (o or 1) is assigned depending on how the two drift solution agreed and which quality criteria were met. In general the final sea ice drift grid contains gaps, where no correlation was found or the quality criteria were failed.

A more detailed description of the sea ice drift algorithm can be found in *Ezraty et al.* (2007a,b,c). The AMSR-E 89 GHz sea ice drift maps on a 31.25 km grid are processed at IFREMER and can be downloaded from their ftp-server: `ftp://ftp.ifremer.fr/ifremer/cersat/products/gridded/psi-drift/`. For our purpose these ice drifts are interpolated on a grid covering the study region using the same projection as for the original ice drift grid but with a grid resolution of 25 km instead of the original 31.25 km. An example of the ice drift between 26 and 28 February 2003 is shown in Figure 4.1 on the next page. In a small band east and south of Svalbard a strong outflow of sea ice is taking place. In the Fram Strait the ice motion increases from west to east. Areas of no ice drift are marked with magenta triangles. But there are also areas where the sea ice drift retrieval failed, e.g. at 85°N, 0°E or in large areas of the Barents Sea. These areas have to be interpolated with ice drift estimates to retrieve the sea ice volume flux (Chapter 6) and are also interpolated for the comparison to SAR ice drift in Section 4.3.

Melting processes at the sea ice surface during summer cause the sea ice surface to look more unique in the microwave spectrum. This hampers the cross-correlation analysis. Less distinct features can be found in the brightness temperature maps, which then could be tracked for the ice drift estimation. Therefore, this ice drift dataset is only available during winter months, i.e. during October to March or October to April.

The error in ice drift speed was estimated by comparison to ice drift speeds from the International Arctic Buoy Program (IABP) and was 3.6 cm/s (3.1 km/day) for the complete Arctic (*Ezraty et al.*, 2007a). However, the error is expected to be larger in dynamic regions such as the Fram Strait. We therefore in the following assess the AMSR-E 89 GHz ice drift in the Fram Strait region by comparing it to ice drift estimates

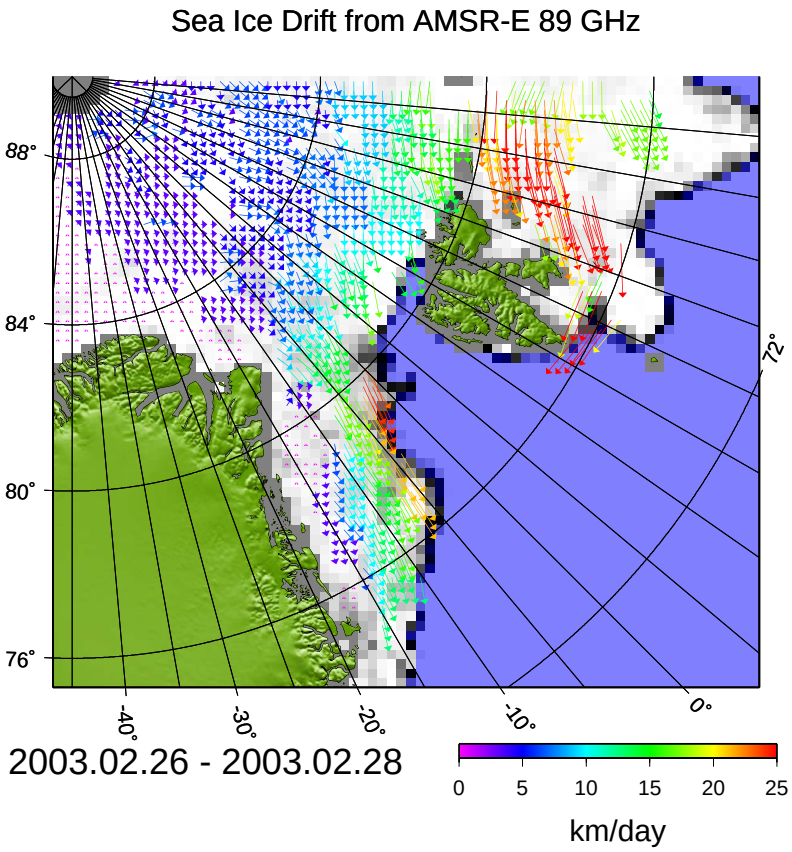

Figure 4.1: Color-coded sea ice drift in Fram Strait region obtained from merged vertically and horizontally polarized AMSR-E 89 GHz data with a time gap of two days: 26–28 February 2003; grid spacing is 25 km (interpolated from 31.25 km grid). Grid points with no ice drift are marked with a magenta triangle. Background: AMSR-E ASI sea ice concentration, see Chapter 3 and Figure 3.2 on page 32 for details.

derived from higher resolving SAR data. Before that, the SAR ice drift is validated with buoy measurements.

4.2 SAR Sea Ice Drift and Comparison to Buoy Ice Drift

By tracking the movement of distinct ice features visible in two consecutive SAR images sea ice drift can be obtained from SAR data. Several methods exist to extract the sea ice drift automatically from SAR images, e.g. *Kwok* (1998); *Kwok et al.* (2003); *Geiger and Drinkwater* (2005). The used methods are similar to the one described in the last Section for AMSR-E data. To achieve highest accuracy in this study we manually analyze the SAR scenes to retrieve the sea ice drift. First, all SAR data are projected on the same polar stereographic grid (see Section 2.2.5 on page 25). Thereafter, pairs of consecutive SAR scenes were analyzed by marking distinctive features, e.g. edges of ice floes, in both images. The distance between the two marked points can be calculated and as the time difference between the two SAR scenes is known the mean ice drift of the marked feature is obtained. About 100 (from 5 to 315) of these drift vectors are identified for every image pair. The large spread of 5 to 315 identified drift vectors per SAR image pair is mainly due to the changing amount of overlap of the SAR scenes and to a lesser extent to the identifiability of surface structures.

26 SAR scenes acquired between 2003-03-03 and 2003-04-21 were available for the manual ice drift estimation. 15 of those 26 scenes were acquired by the ASAR and 11

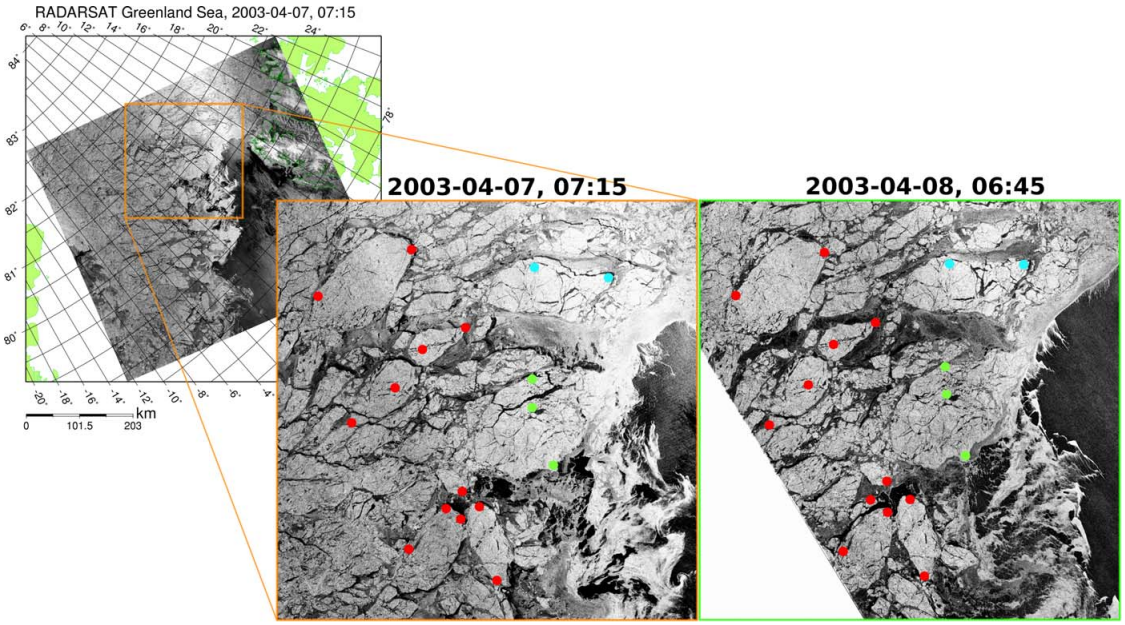

Figure 4.2: Example of SAR scenes pair used for manual ice drift estimation. In the upper left the complete $500 \times 450\,\mathrm{km}^2$ RADARSAT scene from 2003-04-07, 07:15 UTC covering almost the complete Fram Strait is shown. In the bottom part a blow-up of a section of the scene is shown (orange border) together with a blow-up of the same part of the ice cover one day later (green border) extracted from the RADARSAT scene from 2003-04-08, 06:45 UTC. Dots mark examples for points used for the manual ice drift estimation. Green dots mark a convergent zone, blue a divergent one.

by the RADARSAT sensor (see Section 2.2 on page 17). For both sensors the SAR mode with the widest swath was used (ASAR: Wide Swath Mode (WSM), $400 \times 400\,\mathrm{km}^2$, 150 m resolution; RADARSAT: ScanSAR Wide (SCW), $500 \times 450\,\mathrm{km}^2$, 100 m resolution). Based on the 26 scenes in total 37 SAR image pairs with overlapping data coverage and a time difference below 5 days were analyzed. Table 4.1 on the next page gives an overview of the used data.

Figure 4.2 shows an example of two consecutive SAR scenes used for ice drift estimation. In the bottom part a blow-up of the ice cover extracted from the RADARSAT scenes from 2003-04-07, 07:15 UTC and 2003-04-08, 06:45 UTC and thus about one day apart are shown. Red dots mark examples for points which can be used for the manual ice drift extraction. As both scenes are shown in the same geographic projection the location on Earth for the identified points can be extracted and thus ice drift vectors for accordant pairs of points are calculated. In this case already by eye convergent and divergent ice drift zones can be identified, e.g. the leads (dark areas) running through the large flow in the middle and marked with three green dots were closed in the second scene, while for the upper right flow marked with two blue dots the lead area was increasing.

The obtained 37 SAR ice drift datasets (see Table 4.1 on the next page) are to be compared to the two-daily ice drift obtained from AMSR-E data (Section 4.1) to assess

Table 4.1: List of SAR scene pairs used for manual ice drift extraction. Columns 1 and 2: Date and time of the first and second SAR scene, respectively; appended 'A' ASAR and 'R' RADARSAT scene. Column 3: Time difference between the two scenes in days; in brackets the AMSR-E time difference used in Section 4.3. Column 4: Number of identified drift vectors. Column 5: Number of ice drift buoys covered by the SAR scenes.

Start Date and Time	End Date and Time	Time Diff. [d]	Drift Vectors	Buoys
2003-03-03 20:00 A	2003-03-06 11:49 A	2.7 (3)	5	–
2003-04-02 08:00 R	2003-04-04 07:02 R	2.0 (2)	223	2
2003-04-02 08:00 R	2003-04-04 11:36 A	2.1 (2)	96	3
2003-04-02 08:00 R	2003-04-05 16:32 R	3.4 (3)	219	4
2003-04-02 08:00 R	2003-04-05 19:23 A	3.5 (3)	315	4
2003-04-04 07:02 R	2003-04-05 19:23 A	1.5 (2)	36	2
2003-04-04 07:02 R	2003-04-07 07:15 R	3.0 (3)	55	2
2003-04-04 11:36 A	2003-04-05 16:32 R	1.2 (2)	131	3
2003-04-05 16:32 R	2003-04-07 07:15 R	1.6 (2)	59	3
2003-04-05 16:32 R	2003-04-07 20:00 A	2.1 (2)	195	2
2003-04-05 16:32 R	2003-04-08 06:45 R	2.6 (3)	50	3
2003-04-05 19:23 A	2003-04-08 19:29 A	3.0 (3)	130	5
2003-04-07 07:15 R	2003-04-08 06:45 R	1.0 (2)	66	3
2003-04-07 07:15 R	2003-04-08 19:29 A	1.5 (2)	108	3
2003-04-07 07:15 R	2003-04-10 07:27 R	3.0 (3)	32	2
2003-04-07 20:00 A	2003-04-10 20:06 A	3.0 (3)	51	1
2003-04-08 06:45 R	2003-04-10 07:27 R	2.0 (2)	71	3
2003-04-08 19:29 A	2003-04-10 20:06 A	2.0 (2)	55	2
2003-04-08 19:29 A	2003-04-11 19:35:50 A	3.0 (3)	40	2
2003-04-10 07:27 R	2003-04-11 19:35:08 A	1.5 (2)	110	4
2003-04-10 07:27 R	2003-04-11 19:35:50 A	1.5 (2)	115	1
2003-04-10 07:27 R	2003-04-12 19:03 A	2.5 (3)	97	3
2003-04-10 07:27 R	2003-04-13 07:40 R	3.0 (3)	154	3
2003-04-11 19:35:08 A	2003-04-14 19:40 A	3.0 (3)	55	4
2003-04-11 19:35:50 A	2003-04-14 07:10 R	2.5 (2)	98	1
2003-04-11 19:35:50 A	2003-04-14 19:41 A	3.0 (3)	115	2
2003-04-11 19:36 A	2003-04-12 19:03 A	1.0 (2)	15	–
2003-04-12 19:03 A	2003-04-13 07:40 R	0.5 (2)	131	3
2003-04-12 19:03 A	2003-04-15 12:30 A	2.7 (3)	164	4
2003-04-13 07:40 R	2003-04-14 07:10 R	1.0 (2)	139	2
2003-04-13 07:40 R	2003-04-14 19:40 A	1.5 (2)	152	3
2003-04-13 07:40 R	2003-04-15 12:30 A	2.2 (2)	187	–
2003-04-14 07:10 R	2003-04-14 19:40 A	0.5 (2)	198	2
2003-04-14 07:10 R	2003-04-15 12:30 A	1.2 (2)	81	1
2003-04-15 12:30 A	2003-04-20 07:35 R	4.8 (6)	46	2
2003-04-15 12:31 A	2003-04-20 07:36 R	4.8 (6)	30	–
2003-04-20 07:35 R	2003-04-21 07:07 R	1.0 (2)	19	–
Total Records:	37		3843 (Mean 104)	84

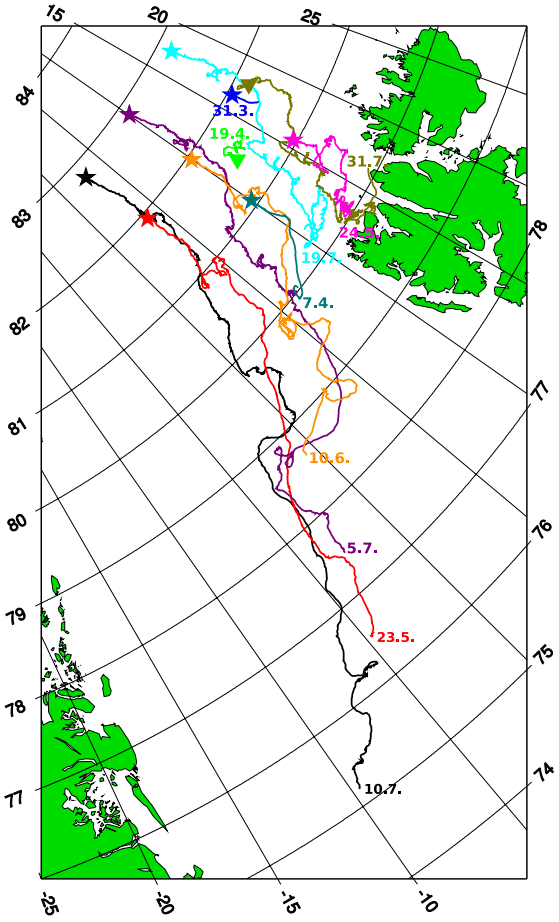

Figure 4.3: Drift of ten sea ice buoys in the Fram Strait region in 2003. Stars mark the starting point of buoys deployed at 2003-03-27. Triangles mark the starting point of the two buoys deployed at 2003-04-04 and 2003-04-05. At the end of the ice drift tracks the dates of the end of the data transmission are given. The last buoy was lost at 2003-07-31.

the quality of the AMSR-E drift in the Fram Strait region. To use the manual SAR drift as reference the accuracy of the dataset has to be assured. Therefore, first the SAR ice drift is compared to sea ice drift obtained from ice buoy measurements. The accuracy of the ice buoy drift integrated about at least 12 hours is assumed to be high but buoy data unfortunately is only available for limited time periods and in a small area.

In the frame of the joint Finish – German 2003 Arctic Systems - Arctic Atmospheric Boundary Layer and Sea Ice Interaction Study (ACSYS-ABSIS) eleven Argos sea ice buoys were deployed north-west of Svalbard (*Launiainen*, 2003). Ten of them worked properly and are used for this study. Figure 4.3 gives an overview of the drift of the ten buoys. Eight of the ten buoys were deployed on 2003-03-27 by parachutes from an aircraft (marked with a star in Figure 4.3). The last two were deployed on 2003-04-04 and 2003-04-05, respectively. The buoy position is transmitted hourly by the Argos satellite system. The lifetime of the buoys ranged from 11 to 118 days. The last buoy was lost at 2003-07-31. The end date of each buoy dataset is written next to the accordant buoy track in Figure 4.3.

From the hourly buoy positions the buoy drift during the time difference of the 37 SAR drift datasets (Table 4.1) were calculated. Only up to five of the ten buoys were covered by one SAR ice drift dataset. Mainly only two or three buoys were covered (see last column in Table 4.1). In five cases no overlap with a buoy was found. Therefore 32

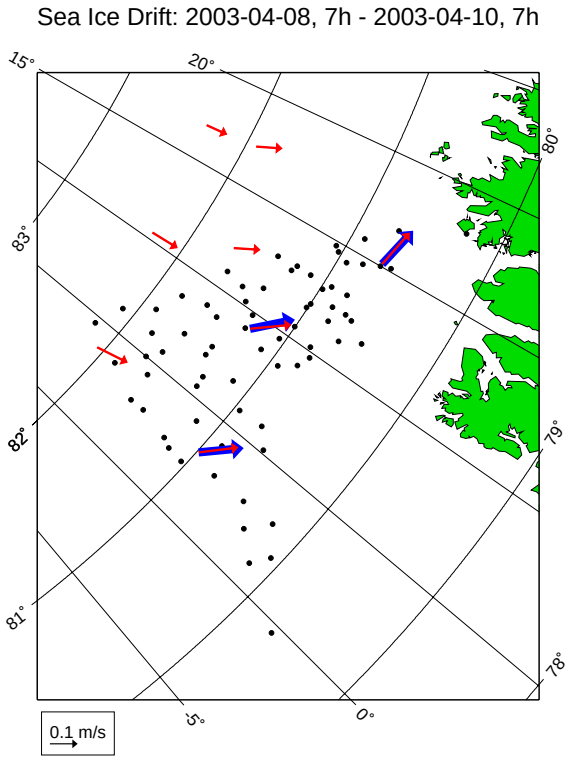

Figure 4.4: Super-imposed sea ice drift obtained from buoy and SAR data. The sea ice drift of eight ice buoys between 2003-04-08, 7 UTC and 2003-04-10, 7 UTC is shown as red arrows. In three cases the SAR ice drift during the same period could be interpolated to the buoy position (blue arrows). The black dots mark the positions of all original SAR ice drift vectors. Buoys outside the SAR drift region were not used for the comparison.

SAR ice drift cases with overlapping buoy drift remain. In total 84 buoy ice drift vectors can be compared with the SAR ice drift (see last column in Table 4.1). For all buoys inside the SAR drift region the SAR drift was interpolated at the buoy positions. No extrapolation for buoys outside this region was done. Figure 4.4 shows an example for the ice drift case 2003-04-08, 7h to 2003-04-10, 7h. Only the three buoys (red and blue arrow) inside the SAR drift region, which is marked by the black spots, are used for the comparison.

Figure 4.5 shows a scatterplot of the buoy ice drift velocity versus the SAR ice drift velocity (left panel) and a scatterplot of the SAR ice drift velocity versus the angle difference between SAR and buoy ice drift (right panel). Table 4.2 lists some statistical values for the SAR – buoy comparison. Both the velocity and direction (angle) of the SAR and buoy drift agree very well. The mean difference between the 84 SAR and buoy velocity observations is (0.0 ± 0.8) cm/s and if the mean absolute difference is taken the deviation increases only to (0.6 ± 0.5) cm/s. The velocity scatterplot in Figure 4.5 shows that all observations are centered around the identity line. There are no outliers for the ice drift velocity. Therefore, also the linear regression $y = mx + b$ reproduces with $m = 0.96$ and $b = 0.00$ almost the identity function. It can be concluded that the accuracy of the manual SAR ice drift velocity is very high. The ice drift velocities are equally distributed between 0 and 0.2 m/s. Surprisingly for these 84 cases no higher ice drift velocities were observed. Velocities above 0.2 m/s are common in the Fram Strait region even for integration intervals of days, as can be seen from the 2-daily AMSR-E drift dataset (e.g. Figure 4.1 on page 52, 25 km/day $\approx$ 0.3 m/s). In this respect our SAR to buoy drift comparison is not ideal, as high drift velocities would have been of special

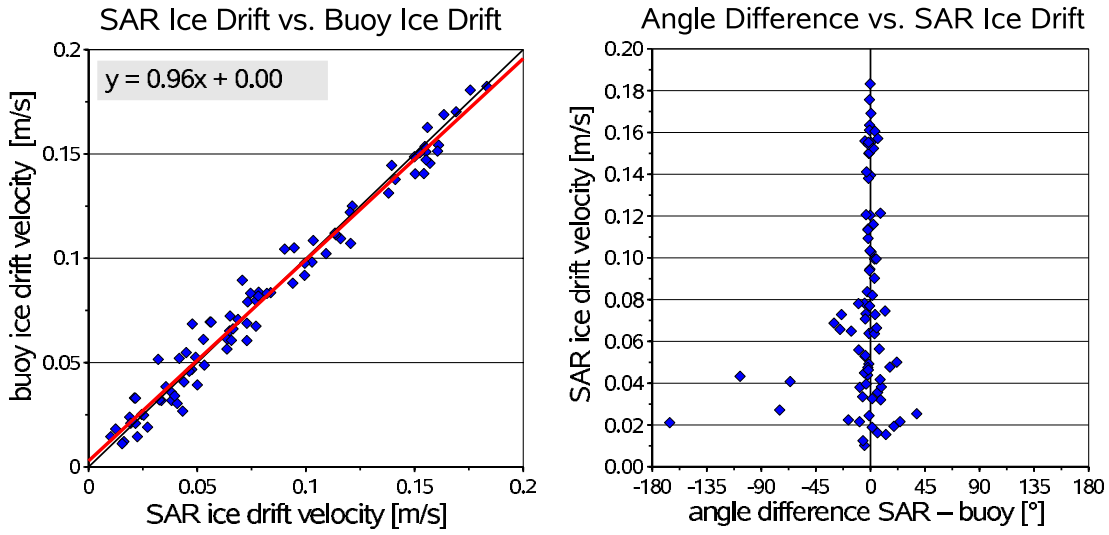

Figure 4.5: Left: Scatterplot of the buoy versus SAR drift velocity. Red line and equation show the linear regression fit, the black line is the identity function. Right: Scatterplot of the SAR drift velocity (y-axis) versus the angle difference between SAR and buoy drift (x-axis). In both plots 84 ice drift vectors obtained between 2003-04-02 and 2003-04-15 in the Fram Strait region are compared.

Table 4.2: Comparison of 84 SAR with 84 buoy ice drift observations between 2003-04-02 and 2003-04-15 in the Fram Strait region.

	mean	standard deviation
SAR drift velocity	8.1 cm/s	4.9 cm/s
buoy drift velocity	8.1 cm/s	4.8 cm/s
velocity difference SAR − buoy	0.0 cm/s	0.8 cm/s
velocity difference |SAR − buoy|	0.6 cm/s	0.5 cm/s
angle difference SAR − buoy	−5°	26°
angle difference |SAR − buoy|	11°	24°
angle difference SAR − buoy without outliers	0°	10°
angle difference |SAR − buoy| without outliers	6°	8°
correlation coefficient drift velocity	0.99	
linear regression drift velocity	$y = 0.96x + 0.00$	

interest.

The mean angle difference between the SAR and buoy drift vectors is with $-5°$ small but has a large standard deviation of $26°$. The angle difference scatterplot in Figure 4.5 shows that this deviation mainly is caused by four outliers with angle differences above $|45°|$, which all occur at small drift velocities below 0.05 m/s. Naturally, the uncertainty for the drift direction increases for low drift velocities and converges infinity for a drift velocity of zero. For example a drift velocity of 0.02 m/s and a time difference of one day between two SAR scenes would only cause a spatial shift of about 10 pixels. A slightly wrong identification of an ice feature in one of the two scenes would thus result in a large drift angle error. The manual feature identification has an accuracy of about ± 3 pixels. For the one observation with and angle difference near $-180°$ (see Figure 4.5, right panel) also an sign error for in the manual SAR ice drift dataset can not be excluded. If the four outliers above $|45°|$ angle difference are removed the standard deviation of the angle differences is reduced to $10°$, less than half the original value and the mean difference reduces to $0°$. Even the mean of the absolute difference stays with $6°$ small.

The good agreement between sea ice drift derived from buoy and SAR observations shows that the manually interpreted SAR drift dataset can be used as a valid reference of the ice drift distribution. Formally, this can only be stated for the observed drift velocity range between 0 and 0.2 m/s. But as these velocities between 0 and 0.2 m/s are mean velocities over 0.5 to 5 days, they also include temporary higher velocities comprehensively. However, in the following the SAR drift dataset is assumed to be a accurate reference for all observed cases.

4.3 Validation of AMSR-E Ice Drift with SAR Ice Drift Data

The in Section 4.1 described AMSR-E sea ice drift data now can be compared to the 37 SAR ice drift cases given in Table 4.1 on page 54. The time gap between two SAR scenes used for ice drift estimation varies between 12 h and 4.8 days (Table 4.1). To compare data with a similar time gap not only AMSR-E ice drift data using a 2 day time gap but additionally AMSR-E data using a 3 and 6 day time gap is used. The identical method as described for the two-daily AMSR-E ice drift data described in Section 4.1 is also used for the 3-daily and 6-daily datasets. For each SAR drift dataset the AMSR-E dataset with the smallest difference for the time gap is used. The number in brackets in column 3 in Table 4.1 indicates which AMSR-E dataset was used for the comparison (2, 3, or 6).

Occasionally gaps of missing data occur in the 31.25 km AMSR-E ice drift grid (see Figure 4.1 on page 52). If for a grid point in the surrounding no adequate pattern with high correlation is found, the grid point is left empty. Thus the ice drift is not defined for all ice covered regions. To achieve a high agreement between the SAR and AMSR-E ice drift only regions with coexistent SAR and AMSR-E ice drift could be compared, as it was done for the buoy and SAR ice drift. This would cause a lot of SAR ice drift vectors not to be used for the comparison in the MIZ, where gaps with missing data in the AMSR-E ice drift frequently occur. For the calculation of the sea ice volume flux through Fram Strait (Chapter 6) the sea ice drift has to be defined for all ice covered regions. To achieve this the AMSR-E sea ice drift is inter- and extrapolated for the complete ice cover, which causes inaccuracies for the sea ice drift estimates. To account

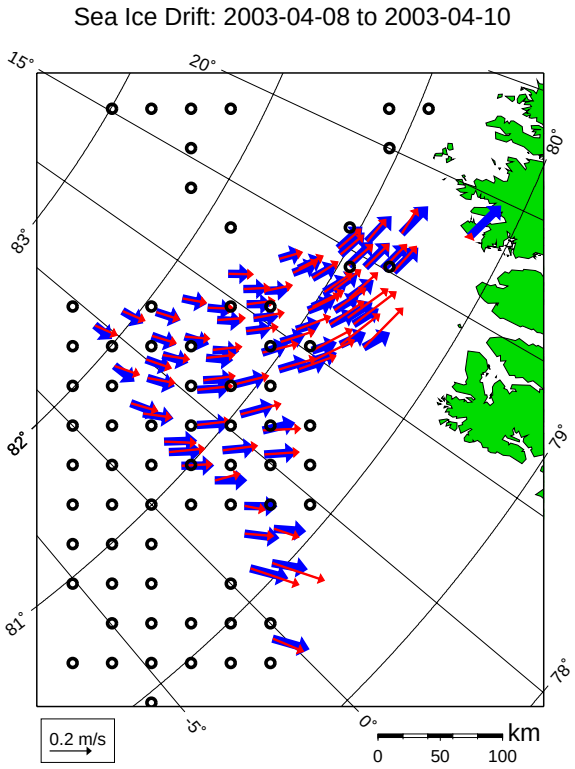

Figure 4.6: Super-imposed sea ice drift obtained from AMSR-E and SAR data. The 71 sea ice drift vectors obtained from two SAR scenes between 2003-04-08, 06:45 UTC and 2003-04-10, 07:27 UTC are shown in red. The sea ice drift obtained from AMSR-E data from 2003-04-08 and 2003-04-10 was inter- and extrapolated to the SAR drift vector positions and is shown as blue arrows. The black circles mark the original AMSR-E ice drift vector positions on a 31.25 km grid. For empty grid nodes the AMSR-E ice drift algorithm failed in estimating the ice drift.

also for these inaccuracies, the AMSR-E ice drift is inter- and extrapolated to all SAR ice drift locations. A continuous curvature splines in tension interpolation (*Smith and Wessel*, 1990) with a tension factor of 0.25 is used for this purpose. For all 3843 SAR ice drift vectors (see Table 4.1 on page 54) the accordant AMSR-E ice drift is interpolated from the surrounding AMSR-E ice drift field.

It is valid to interpolate the spatial lower resolved AMSR-E ice drift to the higher resolved SAR ice drift vectors, as the small scale motion of the floes, e.g. rotation, is small compared to the large scale motion of the ice pack.

Figure 4.6 shows as an example the mean SAR ice drift between 2003-04-08, 06:45 UTC and 2003-04-10, 07:27 UTC together with the AMSR-E ice drift between 2003-04-08 and 2003-04-10 (the same case as shown for the comparison of SAR and buoy ice drift in Figure 4.4 on page 56). The red arrows show the 71 SAR ice drift vectors obtained in the overlapping region of the two SAR scenes. The blue arrows show the interpolated AMSR-E drift for the same location and the black circles mark the original locations of the AMSR-E ice drift vectors on the 31.25 km grid. In the inner ice pack the SAR and AMSR-E ice drift agree very well both in direction and amount. Closer to the ice edge and if the distance between the original AMSR-E drift (black circles) and SAR drift vectors increases, the deviation between the two drift datasets increases.

While for the SAR drift the time difference between the two scenes is exactly known, the exact time difference for the AMSR-E data is unknown, as the drift algorithm described in Section 4.1 is using daily brightness temperature maps and not swath data. Only the mean time difference for all drift vectors of 48 h is known and can be used for the drift velocity calculation. As the real time difference for individual drift vectors

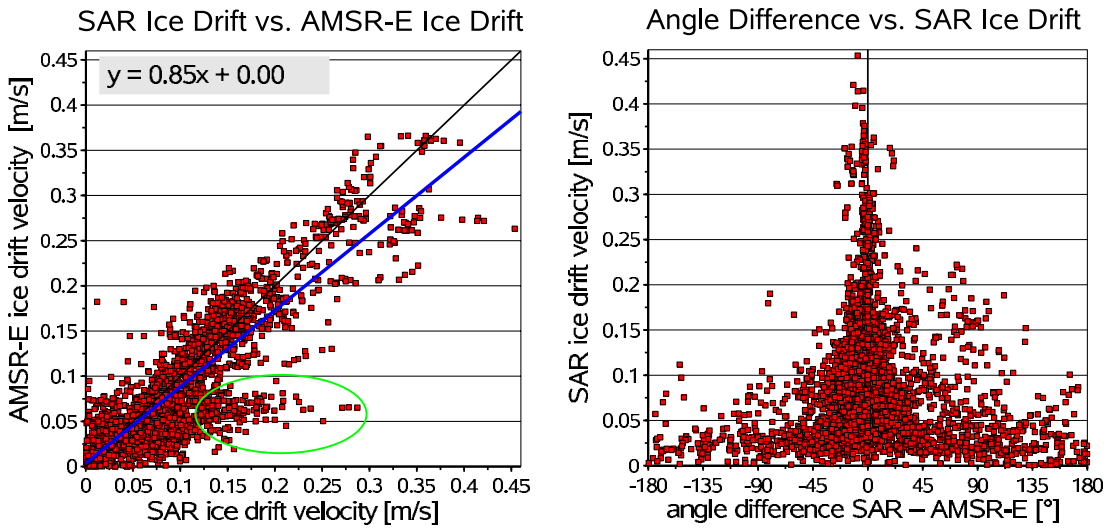

Figure 4.7: Left: Scatterplot of the AMSR-E versus SAR ice drift velocity. The blue line and equation show the linear regression fit, the black line is the identity function. The green ellipse marks a region of too small AMSR-E ice drift velocities. Right: Scatterplot of the SAR drift velocity versus the angle difference between SAR and AMSR-E drift. In both plots 3843 ice drift vectors obtained between 2003-03-03 and 2003-04-20 in the Fram Strait region are compared.

theoretically may differ by ±24 h this can cause substantial errors for the drift velocity calculation. Fortunately the Aqua satellite overpasses the same region on Earth at similar times of the day everyday, as Aqua is in a sun-synchronous orbit. For the Fram Strait region the AMSR-E descending overpasses occur at about 4 UTC (between 2 and 6 UTC) and the ascending overpasses at about 14 UTC (between 11:30 UTC and 15:30 UTC). In total the region is covered 4 or 6 times per day (2 or 3 descending and ascending overpasses respectively). Thus the inaccuracy introduced by using daily brightness temperature maps is not as large as the ±24 h might suggest.

Such drift comparison as shown in Figure 4.6 on the preceding page is done for all 37 SAR ice drift cases. Figure 4.7 shows (similar to Figure 4.5 on page 57) the scatterplot of the interpolated AMSR-E ice drift velocity versus the SAR ice drift velocity (left panel) and a scatterplot of the SAR ice drift velocity versus the angle difference between SAR and AMSR-E ice drift (right panel). In Table 4.3 the statistical values for the SAR with AMSR-E ice drift comparison are summarized.

The mean difference between the SAR and AMSR-E ice drift velocity for the 3843 compared cases is (1.1 ± 3.4) cm/s. This difference of about 1 cm/s, where the AMSR-E drift is smaller than the SAR drift, can be mainly attributed to a branch of AMSR-E observations at a velocity of about 0.05 m/s marked with a green ellipse in Figure 4.7. For AMSR-E velocities of about 0.05 m/s SAR velocities of more than 0.25 m/s can be found. This branch is also causing the linear fit of $y = 0.85x + 0.00$ in Figure 4.7 to deviate from the identity line. It is likely that this branch is caused by interpolating smaller AMSR-E ice drift velocities from the ice pack to SAR drift locations in the MIZ,

Table 4.3: Comparison of 3843 SAR with 3843 AMSR-E ice drift vectors obtained for 37 pairs of SAR scenes acquired between 2003-03-03 and 2003-04-20 in the Fram Strait region.

	mean	standard deviation
SAR drift velocity	9.3 cm/s	6.9 cm/s
AMSR-E drift velocity	8.2 cm/s	6.7 cm/s
velocity difference SAR − AMSR-E	1.1 cm/s	3.4 cm/s
velocity difference |SAR − AMSR-E|	2.5 cm/s	2.6 cm/s
angle difference SAR − AMSR-E	4°	47°
angle difference |SAR − AMSR-E|	29°	38°
correlation coefficient drift velocity	0.87	
linear regression drift velocity	$y = 0.85x + 0.00$	

where, due to the free drift, higher ice drift velocities occur frequently. Another cluster of underestimated AMSR-E ice drift velocities can be observed at about 0.25 m/s, where the SAR drift reaches values of up to 0.45 m/s.

The mean angle difference between SAR and AMSR-E drift is 4°±47°and the mean absolute angle deviation is about 29°. This large standard deviation (47°) and absolute deviation (29°) is mainly caused by the observations at ice drift velocities below 0.1 m/s. As can be seen in the right scatterplot in Figure 4.7 for drift velocities below about 0.05 m/s the angle gets indefinite with angle differences up to ±180°. These large angle differences for low drift velocities are caused by the grid resolution of 6.25 km for the AMSR-E data, which is coarse compared to that of the SAR data. A tracked ice feature has at least to drift this 6.25 km in 2 days (≈ 0.04 m/s) to be detected and in this case the drift direction only can be determined in 90°steps, starting from a drift of 8.84 km (0.05 m/s) at least in 45°steps (diagonal drift). These differences are therefore not surprising and inherent to the used method. For ice drift velocities higher than 0.2 m/s the angle of the SAR and AMSR-E drift agree well (see Figure 4.7).

Ezraty et al. (2007a) compare 2-, 3-, and 6-daily AMSR-E ice drift with buoy ice drift for the complete Arctic. Their mean difference for all three datasets is near zero. The standard deviations they found for the 2-, 3-, and 6-daily datasets are 3.6, 2.6, and 1.6 cm/s, respectively, which agrees well with our standard deviation of 3.4 cm/s found for a mixture of the three datasets (see third column of Table 4.1 on page 54). We therefore can not state from our limited comparison that the AMSR-E ice drift has larger errors in the dynamic Fram Strait region than can be found for the complete Arctic.

The goal of the comparison was to quantify the mean AMSR-E ice drift error in the Fram Strait region in respect to achieve an accurate ice volume flux retrieval in the following. The found standard deviation of 3.4 cm/s could be used as an error estimate. Additionally, there is the systematic shift of about 1 cm/s between the SAR and AMSR-E ice drift velocities. This was not found in the AMSR-E – buoy comparisons performed by *Ezraty et al.* (2007a) and might be attributed to the done inter- and extrapolation. Nevertheless, a similar interpolation for the ice also has to be done to retrieve the sea ice volume flux. Therefore, for the volume flux calculation in Chapter 6 we stick to the error

estimated of 5.1 cm/s (4.4 km/day) already used in *Spreen et al.* (2006), which agrees well with the results found here, taking into account both the standard deviation (3.4 cm/s) and mean difference (1 cm/s). However, even this higher drift error of 5.1 cm/s can not explain the volume flux differences found in Section 6.5.1 on page 114 using the AMSR-E (*Ezraty et al.*, 2007a) and QuikSCAT (*Haarpaintner*, 2006) ice drift. Thus it can not be excluded that for other time periods not covered by the comparison done here the error might be larger. As mentioned before and also can be seen in Figure 6.9 on page 112 April 2003 was a period of rather low mean ice drift (in Figure 6.9 the variability of the ice volume flux is mainly determined by the ice drift velocity at least for the same season).

4.4 Sea Ice Drift Summary

- Sea ice drift can be obtained from AMSR-E 89 GHz vertically and horizontally polarized brightness temperature maps on a daily base.
- Daily brightness temperature maps are used to track ice features from one day to the next one by applying a cross-correlation technique. The final sea ice drift map has a spatial resolution of 31.25 km.
- For AMSR-E ice drift validation in the Fram Strait region a set of 37 higher resolving SAR scene pairs from April 2003 is used.
- The ice drift was extracted visually from the SAR scenes by tracking ice features from scene to scene. The high quality of this method was confirmed by comparison to sea ice drift buoys.
- The comparison of the obtained 3843 SAR ice drift vectors with the AMSR-E ice drift resulted in a mean ice drift velocity difference of about 1 cm/s with a standard deviation of 3.4 cm/s. The mean difference is larger than what was found in another study for the central Arctic comparing AMSR-E with buoy ice drift data (*Ezraty et al.*, 2007a). The standard deviation is similar for both studies. For the sea ice volume flux calculation we will assume a mean ice drift error of 5.1 cm/s. The mean angle difference between SAR and AMSR-E ice drift is $4^\circ \pm 47^\circ$ and the large standard deviation can be mainly attributed to direction uncertainties for low ice drift velocities.

Chapter 5

Sea Ice Thickness

Measurement of sea ice thickness from space was for a long time and in parts still is the largest challenge for sea ice satellite remote sensing. While monitoring of sea ice cover and sea ice motion is routinely done since the 1970s from satellites, the thickness always stayed a difficulty. This is due to the fact that a) no robust and widely applicable relationship between sea ice surface properties, like roughness obtained by radar backscatter measurements, and sea ice thickness could be found and b) the sea ice freeboard, the part of the sea ice sticking out of the water and hence could be measured by satellite altimetry, is only roughly one tenth of the complete sea ice thickness (*Onstott and Shuchman*, 2004; *Wadhams and Comiso*, 1992). Nevertheless, in 2003 *Laxon et al.* (2003) published the first Arctic sea ice thickness map from European Remote-Sensing Satellite (ERS) radar altimeter data. These estimates are hampered by the high inclination of 98.5°of the ERS satellites, which limit the observed latitudes to 81.5°North and that only mean winter ice thicknesses could be derived. *Hvidegaard and Forsberg* (2002) measured the first sea ice thicknesses by airborne laser altimetry. Further first investigations for sea ice thickness retrieval with ICESat data were performed by *Kwok et al.* (2004b, 2006). Very recently, after conducting this study *Kwok et al.* (2007) and *Zwally et al.* (2008) published sea ice freeboard maps for the Arctic and Antarctic derived from ICESat data.

Here a new method to retrieve the sea ice thickness from ICESat data is presented. In our method the SSH, which is needed in high accuracy to obtain the ice thickness, is determined from the ICESat GLAS measurements itself, similar but more advanced as it was applied before for to airborne laser altimetry (e.g. *Hvidegaard and Forsberg*, 2002). First results using this method are published in *Spreen et al.* (2006). For this study several aspects of the method presented in *Spreen et al.* (2006) were improved, e.g. two ice density classes are now discriminated by QuikSCAT measurements (Section 5.2.1) and the minimum elevation algorithm uses a more flexible iterative approach to correctly identify the SSH (Section 5.1.2). The details of the sea ice thickness retrieval from ICESat GLAS measurements are presented in the following.

5.1 Sea Ice Freeboard

A prerequisite to obtain the sea ice thickness from altimeter data are sea ice freeboard heights. In this study the freeboard height, hereafter termed freeboard F, is defined as the part of the sea ice including the snow looking out of the water (Figure 5.1 on the next page). This definition is chosen as the laser reflection origins from the air-snow interface. For e.g. radar altimeter applications the freeboard is often defined as only the ice part without snow looking out of the water, as the radar signal originates from

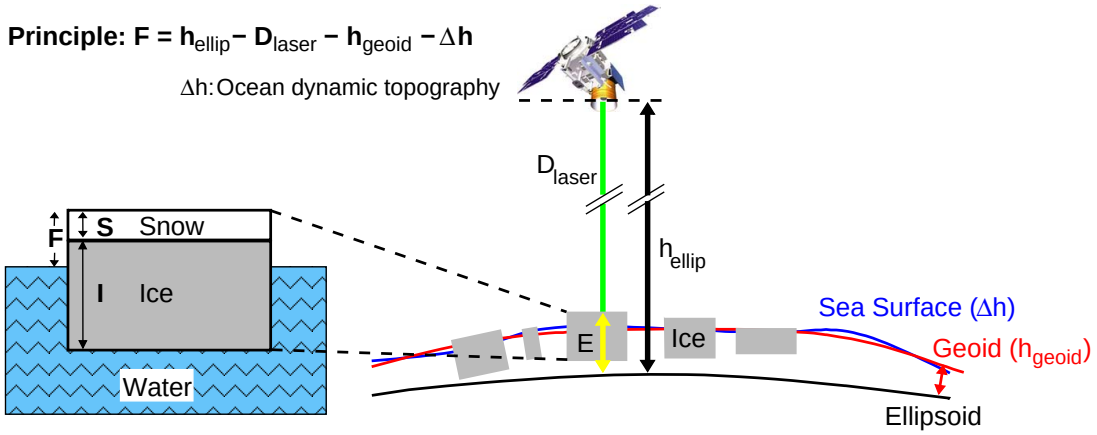

Figure 5.1: Schematic diagrams showing on the left side the interrelation of ice freeboard, F, snow depth, S, and sea ice thickness, I (left) and on the right side an artist's view of ICESat above the three involved surfaces: reference ellipsoid (black), geoid (red), and sea surface (blue). Figures are not to scale.

the snow-ice interface (*Tonboe et al.*, 2006a; *Beaven et al.*, 1995). Under assumption of isostatic balance of the ice floes in the water and knowledge of all involved densities and snow depth the freeboard heights can be converted to ice thickness, which is described in Section 5.2.

The first and so far only satellite laser altimeter is the GLAS instrument aboard the ICESat satellite. GLAS permits to observe the sea ice up to 86° North. This is 4.5° further north than traditional radar altimeters like on ERS or Environmental Satellite (Envisat), but still a not observed hole of 4°(≈ 894 km Ø) around the pole remains. ICESat is in a low inclination orbit of 94° to observe the high latitudes (see Table 2.2 on page 19). As input data for the freeboard calculation the 'GLAS/ICESat L2 Sea Ice Altimetry Data'-product (GLA13) (*Zwally et al.*, 2003) is used. For this product the processing of the waveform and the location of the included data is adapted for sea ice. A detailed description of the satellite and the GLAS instrument is given in Section 2.2.1 on page 17. In total, nine ICESat measurement periods between 2003 and 2006 are used. Table 2.3 on page 20 summarizes all ICESat measurement periods and indicates which are used in this study.

By measuring twice the laser pulse travel time at 1064 nm (near infrared) wavelength between the sensor and the surface, the height of the sensor, D_{laser}, above the surface is obtained for a footprint of 64 m diameter every 172 m along track (see Figure 5.1 and *Zwally et al.* (2002)). ICESat's orbit and thus its height above a reference ellipsoid, h_{ellip}, is determined by a GPS receiver system with an accuracy of 5 cm. The difference E between h_{ellip} and D_{laser}, called surface elevation, is released in the GLA13 data set and used here as starting point. Additional to the above mentioned orbit determination accuracy errors caused by atmospheric delay, atmospheric forward scattering, and range and pointing determination influence the precision of the elevation measurement E. Assessment of the mean total error budget for a single GLAS measurement (one laser shot) results in an error estimate of 13.8 cm (see Table 2.4 on page 22 and *Zwally et al.*

(2002)). Under ideal conditions (cloud free, no detector saturation) ICESat elevation precision was found to be $< 3\,\text{cm}$ over the *salar de Uyuni* salt flat in Bolivia. But in cases of detector saturation and strong atmospheric forward scattering single shot errors can rise up to 1 m (*Fricker et al.*, 2005). From these error values it becomes clear that a single GLAS measurement can not be used to measure the sea ice freeboard accurately because its values and the error budget have the same order of magnitude (several decimeters). Under the presumption of a Gaussian error distribution sea ice freeboard only can be obtained by averaging several GLAS measurements in space and time. For all following error calculations the above mentioned error of 13.8 cm is used for a single GLAS measurement.

By subtracting D_{laser} from h_{ellip} the mean surface elevation E in the footprint above the reference ellipsoid is obtained. By subtracting the geoid height, h_{geoid}, and the contribution to SSH due to the ocean and atmosphere dynamics, Δh, an estimate of the sea ice freeboard height, F, can be obtained (see Figure 5.1). Δh contains contributions caused by ocean and earth tides h_{tides}, atmospheric pressure loading h_{atm}, and ocean currents and other second-order terms like steric SSH changes h_d. Accordingly, the ice freeboard F is given as

$$\begin{aligned} F &= h_{ellip} - D_{laser} - SSH \\ &= h_{ellip} - D_{laser} - h_{geoid} - \Delta h \\ &= h_{ellip} - D_{laser} - h_{geoid} - h_{tides} - h_{atm} - h_d\,. \end{aligned} \tag{5.1}$$

The ICESat surface elevations E as released in the GLA13 data product already include tide corrections h_{tides} (see Section 2.2.1 on page 19):

$$E = h_{ellip} - D_{laser} - h_{tides}\,.$$

The freeboard F in equation 5.1 thereby can be expressed as

$$F = E - h_{geoid} - h_{atm} - h_d\,. \tag{5.2}$$

The influence of geoid height h_{geoid} and atmospheric pressure loading h_{atm} can be corrected for. The remaining ocean dynamic part h_d is not known with sufficient accuracy and has to be eliminated by an alternative approach described in Section 5.1.2 on page 68.

5.1.1 Geoid

Similar to all altimeter studies, an accurate geoid is a necessary prerequisite to estimate the ice freeboard. In a preliminary study *Spreen et al.* (2005) found, that using the project-provided geoid (Earth Gravitational Model 1996 (EGM96)), causes unrealistically large variations of the SSH (several meters) in some regions of the Greenland Sea. Figure 5.2 on the next page shows the difference between ICESat surface elevations E for 2003-03-12 and the EGM96 geoid height h_{geoid} as provided with the ICESat data. Calculation of this difference is the first step to get realistic ice freeboards (equation 5.1). Ellipses in Figure 5.2 on the next page mark region of unrealistically high positive (red) and negative (blue) differences which stay constant through the entire ICESat measurement period and can be attributed to an inaccurate geoid.

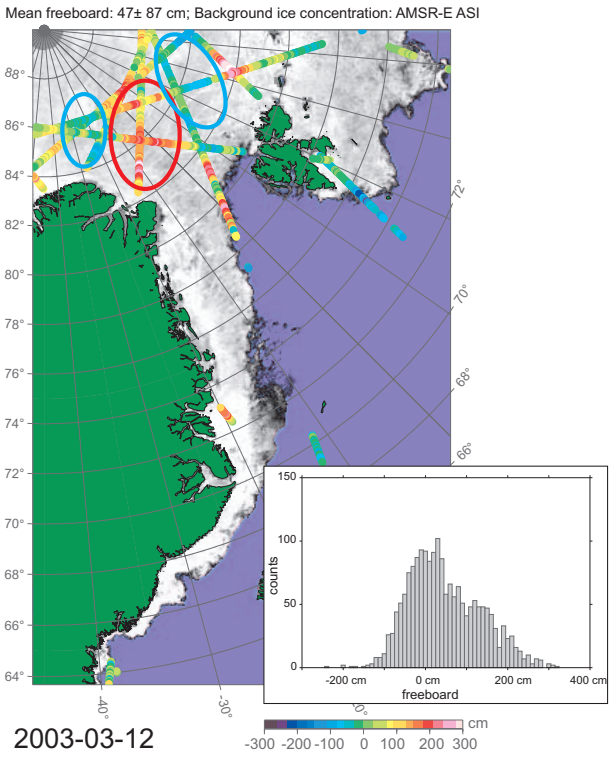

Figure 5.2: Difference between the EGM96 geoid and ICESat elevation measurements (color-coded discs) for 12 March 2003, which is the first step towards ice freeboard measurement. Background is a map of ASI algorithm AMSR-E ice concentration (blue: open water, white 100% ice, medium gray: 50% ice) for the same day. The ellipses mark regions of pronounced under- or overestimation of this simple ice freeboard which stay stable for the considered ICESat period and are mainly caused by inaccuracies of the EGM96 geoid. The insert shows the histogram of all ICESat sea ice freeboards. Size of discs showing the freeboard is not to scale, i.e does not resemble the footprint size of the GLAS sensor.

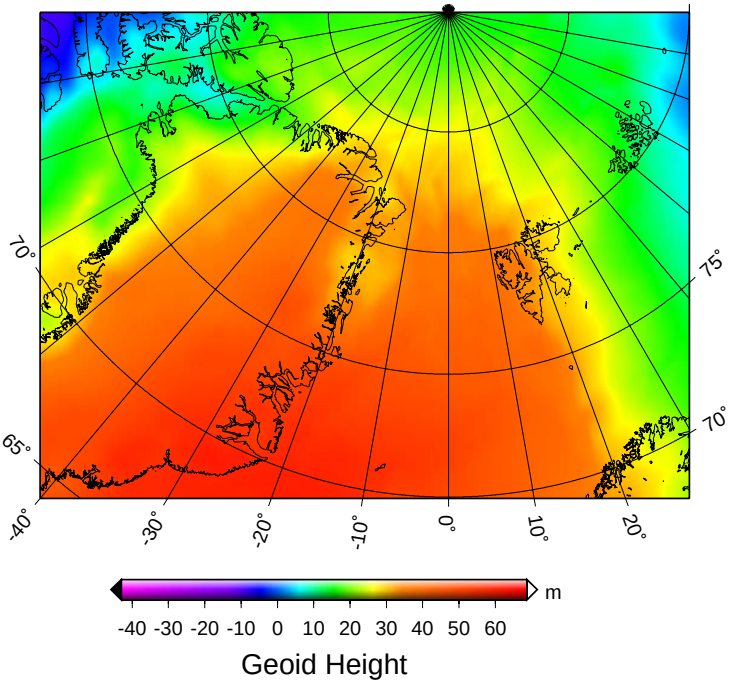

Figure 5.3: Geoid heights h_{geoid} from the Arctic Gravity Project (ArcGP) in reference to the WGS84 ellipsoid.

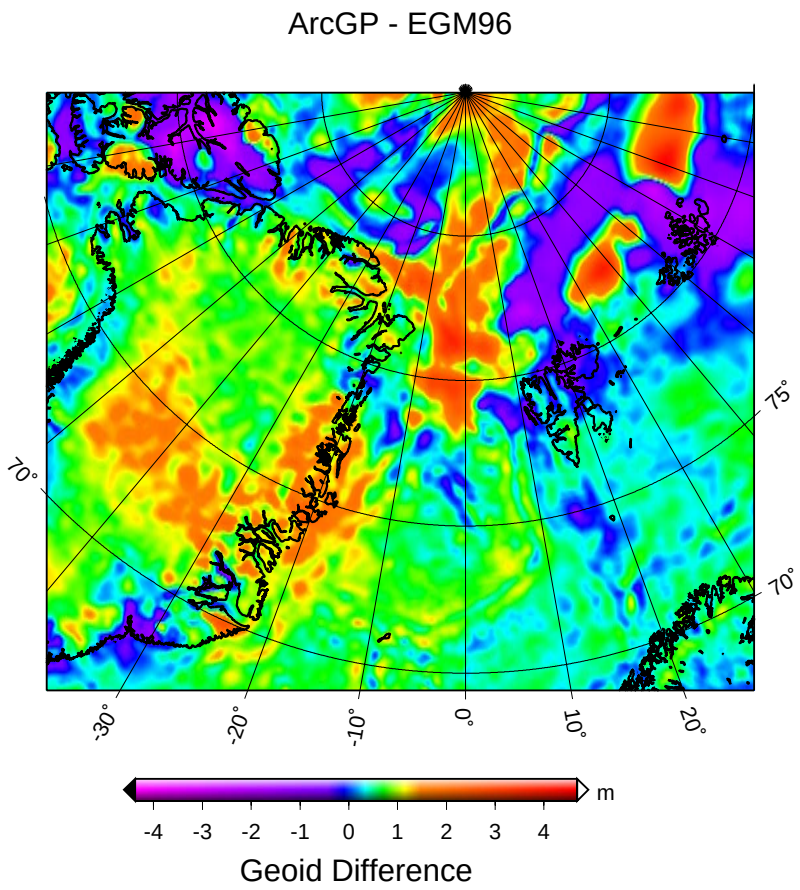

Figure 5.4: Difference between the more accurate ArcGP and the standard EGM96 geoid, distributed with the ICESat data. Differences of ±4 m can be observed in the Fram Strait region.

Therefore a more recent gravity field compiled by the Arctic Gravity Project (ArcGP) and shown in Figure 5.3 is used. It represents today's best geoid north of 64° latitude and combines gravity data from several airborne surveys, surface measurements (ground, helicopter, marine), submarine data, satellite altimetry and Gravity Recovery and Climate Experiment (GRACE) data on a 5'x5' grid (*Forsberg and Kenyon* (2004); *Forsberg and Skourup* (2005)). The latest available version from February 2006 is used (`http://earth-info.nga.mil/GandG/wgs84/agp/index.html`). The Greenland Sea is one of the places with the worldwide highest geoid undulations. Geoid heights of up to 50 m occur in this region. It becomes clear that an accurate geoid is necessary to interpret ICESat elevations, which are referenced to the earth ellipsoid. Figure 5.4 demonstrates the significant improvement of the ArcGP geoid in comparison to the EGM96 geoid. In the Fram Strait differences of ±4 m between the two geoid models become apparent which compares well to the above mentioned discrepancies in the SSH marked with ellipses in Figure 5.2.

The ArcGP geoid is referenced to the WGS84 earth ellipsoid (equatorial radius $a_{WGS} = 6378137.0$ m, polar radius $b_{WGS} = 6356752.314245$ m). ICESat elevations are referenced

to the TOPEX/Poseidon ellipsoid (equatorial radius $a_{TOPEX} = 6378136.3\,\text{m}$, polar radius $b_{TOPEX} = 6356751.600563\,\text{m}$). Both ellipsoids are vertically offset by approximately 0.71 m in our study region. Thus the ArcGP geoid heights first have to be converted to heights in reference to the TOPEX/Poseidon geoid before they can be subtracted from the ICESat elevations. The horizontal changes in latitude caused by the different ellipsoids are below $|1.23 \cdot 10^{-7}|^\circ$ or $|1.37|\,\text{cm}$ and therefore can be neglected. The vertical difference Δ_{ellip} depends on the latitude φ and can be calculated by

$$\Delta_{ellip} = (a_{WGS} - a_{TOPEX})\cos(\varphi)^2 + (b_{WGS} - b_{TOPEX})\sin(\varphi)^2\,.$$

Furthermore the ICESat data is referenced to a geoid in a mean-tide system while the ArcGP data are given in respect of a tide-free geoid. A tide-free geoid would exist for a tide-free Earth with all (direct and indirect) effects of the Sun and Moon removed, while a mean-tide geoid would exist in the presence of the Sun and the Moon with no permanent tidal effects removed. The difference between the two systems can be calculated after *Ekman* (1989) by

$$\Delta_{tide} = (1 + k)\left(9.9 - 29.6\sin^2\varphi\right)\ \text{cm}$$

where k is a Love number here taken as 0.3, as it is common for the earth. Δ_{ellip} and Δ_{tide} then are added to the original ArcGP geoid heights to obtain geoid heights in reference to the geoid used for the ICESat elevations. The sum of Δ_{ellip} and Δ_{tide} amounts to approximately 50 cm (53 cm at 64° N and 46 cm at 90° N) which compares well with the mean difference between ICESat and ArcGP of −0.52 cm found by *Forsberg and Skourup* (2006) for the latitude band 80–81° N. After this conversion the ArcGP geoid heights are interpolated bi-linearly onto the locations of the ICESat measurements before they are subtracted from the surface elevation data.

5.1.2 Lowest-Level Elevation Method

As explained in Figure 5.1 on page 64, the dynamic part, Δh, of the ocean has to be removed next from the remaining SSH field before an estimate of the ice freeboard can be obtained. No measurements or models exist to date, which would provide an accurate estimate of the dynamic SSH field with the temporal and spatial resolution required here. For example one would have to know the deflection of the SSH caused by time varying ocean currents and eddies (*Stammer*, 1997). Instead, Δh has to be inferred from the ICESat data itself. For that purpose a "lowest-level elevation method" is used. A similar but in its implementation different method was used for airborne laser measurements by *Hvidegaard and Forsberg* (2002). This method was later, parallel to this work, also adapted to ICESat data for sea ice freeboard retrieval (*Forsberg and Skourup*, 2005; *Skourup and Forsberg*, 2006). Also Zwally and Yi presented a similar method for sea ice freeboard retrieval at the 1st CryoSat Workshop (2005, `http://earth.esa.int/workshops/cryosat2005/`), and IGARSS'05 (July 25-29, Seoul, Korea).

Openings and leads in the sea ice with open water or thin ice are prevalent in the Arctic ice cover. Their size range goes from a few meters to several hundred meters or even kilometers, but openings with sizes larger than 70 m make up a main part of the size distribution. With a pulse repetition frequency of 40 Hz and a laser footprint diameter of 64 m at the surface ICESat's GLAS measurements frequently originate from

such openings for one overflight. This minimum elevation measurements have to be identified and then can be taken as base for a SSH model. The difference between this SSH and the remaining valid ICESat measurements is the ice freeboard.

The ICESat elevation measurements from the used "GLAS/ICESat L2 Sea Ice Altimetry Data" product (GLA13) already contain some corrections which are important for an accurate SSH estimate. In particular these are the tide (ocean and solid earth), troposphere and saturation correction (see Section 2.2.1 on page 19). Starting from these GLA13 elevations our method for SSH and freeboard determination works as follows:

Separate Orbits One GLA13 dataset contains all data of 14 ICESat orbits (approximately 22.5 hours in total). The single orbits are separated and only data in the region 60° N to 90° N and −50° E to 50° E are considered. All following calculations are done on a single orbit base.

Data Quality Only elevation measurements with positive data-quality flag are used (only shots with valid i_ElvuseFlg in GLA13 dataset). For the surface type (i_surfType in GLA13) only data with sea ice surface flag but not with land or ice sheet flag are selected. This removes data near the land and glaciers in Greenland. The ICESat surface mask is shown in Figure 2.6 on page 20. Only data from the light grey class "sea ice + ocean" is used. As a next first quality check elevations above 100 m are sorted out, as they are clearly above the expected geoid heights shown in Figure 5.3 on page 66.

Correct Inverse Barometer Effect The sea surface is responding to atmospheric pressure changes, which is known as the Inverse Barometer Effect (IBE). The difference between the local pressure P_{surf} to the global mean surface pressure over the ocean $\overline{P_M}$ is causing the SSH change h_{atm} in equation 5.2 on page 65. High pressure loading causes a negative h_{atm}:

$$h_{atm} = -11.2 \, \frac{\text{mm}}{\text{hPa}} \, (P_{surf} - \overline{P_M}) \, .$$

The proportionality constant −11.2 mm/hPa was taken from *Kwok et al.* (2006), where two 8 day exact ICESat repeat cycles in the Arctic are compared. They also show that taking the IBE into account is reducing the variability of ICESat elevation data. As our study is also situated in the Arctic region we chose the same −11.2 mm/hPa proportionality constant for our application. A traditional value for the mid latitudes is −9.948 mm/hPa (*Wunsch*, 1972), which is also used for the Jason mission. *Skourup and Forsberg* (2006) use a slightly higher value of −13.1 mm/hPa for the Arctic. The global mean ocean surface pressure is a time varying variable $\overline{P_M} = \overline{P_M(t)}$ and for an exact calculation of h_{atm} the instantaneous $\overline{P_M}$ must have been taken (*Wunsch and Stammer*, 1997). However, as very high accuracy is not needed for our application the constant $\overline{P_M} = 1013.3$ hPa is used, as is done for the Jason mission (*Picot et al.*, 2004) and by *Skourup and Forsberg* (2006). In the ICESat GLA13 data product surface pressures P_{surf} are distributed for every 40th laser shot, which are used here as surface pressure for all 40 shots. The obtained h_{atm} is subtracted from the elevations E (see equation 5.2).

Subtract Geoid and Smooth SSH Now the ArcGP geoid heights h_{geoid} are subtracted from the elevation measurements E, leaving back elevations which are already close to the SSH:

$$E_{geoid} = E - h_{atm} - h_{geoid}\,.$$

Only the dynamic part h_d of the SSH is still unknown (see equation 5.2). First the large-scale dynamic variability of the SSH is removed by highpass filtering, as the long wavelengths are not important for the freeboard determination. The elevations E_{geoid} are smoothed with a 50 km boxcar moving average and afterwards this smoothed elevations E_{smooth} are subtracted from the original, unsmoothed ones:

$$E_{res} = E_{geoid} - E_{smooth}\,. \tag{5.3}$$

Only the small scale SSH variability including the freeboard should be left in the residual elevations E_{res} now.

Outliers Two filters for data outliers are used. 1.) The standard deviation of E_{res} is calculated. Data laying outside the interval of three standard deviations are discarded. Assuming the data to be distributed Gaussian, only 0.3% of the data should lay outside this interval and thus are removed incorrectly. The majority of data outside this interval are outliers caused by measurement errors.
2.) As a second filter data with high local variance of E_{geoid} are removed. High variance values have been found to origin from large open water areas with swell or the open sea. Like the boxcar moving average a boxcar moving local variance $Var_{50km}(E_{geoid})$ of 50 km size is calculated for every E_{geoid} data point. In E_{geoid} all variability, also the longscale one, is still included. Where this local variance is three times larger than the variance of the complete overflight $Var(E_{geoid})$ the data is discarded, removing most open sea measurements but keeping all sea ice measurements.

Reflectivity Only data with an uncorrected reflectivity between 0.1 and 0.9 are used. Uncorrected means, that atmospheric attenuation is not taken into account. The uncorrected reflectivity is not limited to 1, e.g. specular reflection can cause reflectivity values above 1. Also the GLAS detector amplifier sometimes saturates during fast dark-to-bright transitions, causing overshoots in both positive and negative direction (*Kwok et al.*, 2004b, 2006). Natural surfaces, even dark water and bright snow, should lay in the 0.1 to 0.9 reflectivity range. For this reasons data with reflectivity outside this range is removed.

Ice Concentration Filter AMSR-E ASI sea ice concentration data (see Chapter 3) is used to remove all elevation measurements in areas with ice concentration lower than 30% (including open water). In areas with low ice concentration the ocean waves are dominating the ICESat elevation measurements causing false ice freeboard determination. The ICESat elevation positions are converted to the polar stereographic coordinate system of the ice concentration data and the according ice concentration value for every ICESat measurement is selected. 30% is the lowest justifiable limit. In areas with lower ice concentration waves are definitely contaminating the ICESat measurements, but even in areas with higher ice concentration

there might be still some contamination left depending on the distance to the actual ice edge. Some of this contamination was already removed by the second outliers filter discussed above.

Minima Identification The lowest 2% of the data points in the residual elevations E_{res} from equation 5.3 are identified by calculating the histogram of E_{res} and selecting the lowest 2%. These minima assumed are to represent areas of open water or young, thin ice. This assumption is reasonable, because such areas (leads) are abundant in the study region (sea ice concentrations calculated on a $25\,\mathrm{km} \times 25\,\mathrm{km}$ grid rarely exceed 98% and even then enough thin ice should be abundant to satisfy the 2% assumption), and the combination of the frequent sampling (every 170 m along track) and the small footprint size (64 m) of the GLAS ensures that several leads are hit during one ICESat overpass. It should be mentioned that this 2%-rule certainly results in an underestimation of open water areas in the MIZ.

Linear Fit A linear fit $s(t) = A + B\,t$ through the identified minima is calculated using a robust least absolute deviation method to account for remaining trends in the elevations after boxcar averaging. An example of the residual elevation E_{res} including the 2% minima and the resulting fit is shown in Figure 5.5 on the next page. If the slope B of the fit s is below $2\,\mathrm{mm/sec} \approx 0.3\,\mathrm{mm/km}$ the fit s is taken as SSH and subtracted from the elevations E_{res} to obtain the freeboard heights F for the orbit:

$$F(t) = E_{res}(t) - s(t)\,. \tag{5.4}$$

At this point of the calculation F is still a time t dependent variable, but with associated longitude and latitude coordinates for every measurement. All remaining negative freeboard heights are set to zero.

Recalculation Scheme If the condition slope $B < 2\,\mathrm{mm/sec}$ is not met, it is assumed that a too strong trend remained in the filtered elevations E_{res} to use the 2% minima as reference for the complete orbit. This is mainly the case if the 2% minima are concentrated in one part of the orbit transect. The dataset is then split in two halves and the linear fitting is performed again for the first half. This scheme is pursued iteratively until either $B < 2\,\mathrm{mm/sec}$ is met or the length of the used orbit transect becomes shorter than $10\,\mathrm{sec} \approx 69\,\mathrm{km}$. The same is done for the second half of the orbit. If more than one iteration was necessary for the first half the remaining part of the first orbit half is concatenated to the second one before the fitting is applied to it.
The after n iterations derived fits $s_n(t)$ are concatenated and afterwards smoothed with a 50 km running mean to get a smoother SSH representation. This smoothed $s_n(t)$ is subtracted from E_{res} to get the freeboard F following equation 5.4.

Figure 5.6 on page 73 shows a flow diagram of the freeboard calculation starting with the minima identification from the residual elevations E_{res}.

An example for a part of one orbit on 23 February 2003 demonstrating how this method works is shown in Figure 5.5 on the following page. The black line connects the residual GLAS elevations E_{res}. The green line connects the lowest 2% of data points. In red the

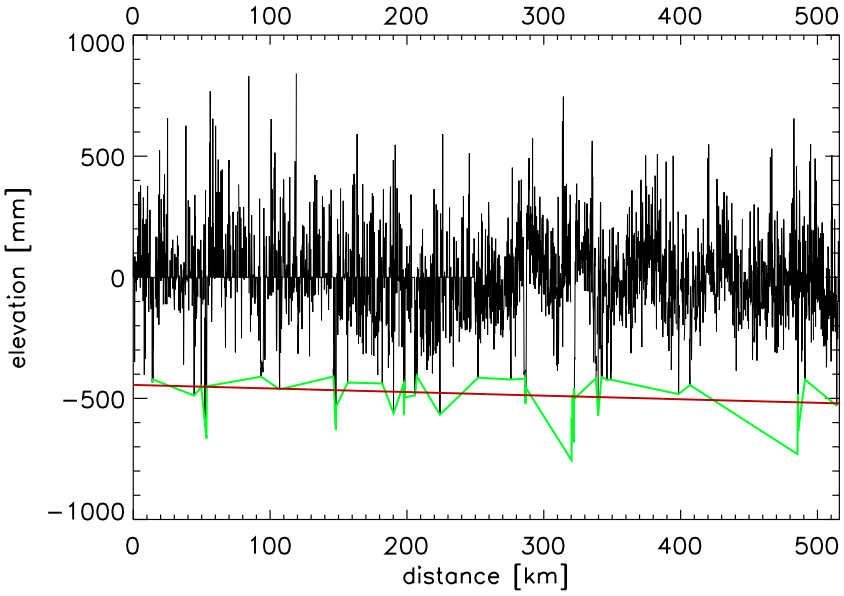

Figure 5.5: Example from 23 February 2003 showing the principle of the lowest-level elevation method. Black: high-pass filtered GLAS elevations E_{res}, green: connected lowest 2% of elevation data; red: the resulting SSH.

finally fitted SSH $s(t)$ is given. In this case no recalculation was necessary. Subtracting the red line from the black elevation and setting all remaining negative values to zero yields the required sea ice freeboard height.

Following this approach, the ice freeboard is sequently calculated for all orbits of one 22.5 h long GLA13 dataset.

5.1.3 Validation

To check if the lowest level elevation method works properly, we compared several Envisat ASAR scenes with our ICESat freeboard heights on a single orbit base. One example of this comparison is shown in Figures 5.7–5.9. More examples can be found in Appendix A.2 on page 141. Figure 5.7 on page 74 top-left shows the complete 400 km × 400 km ASAR image from 2003-03-09, 16:52 UTC. The compared ICESat overflight took place approximately 1 hour before at 15:41 UTC. In Figure 5.7, top-left four zoom regions are marked with red rectangles and numbered 1 to 4. The rest of the Figures 5.7–5.9 are showing these zoom cutouts together with the associated graphs with ice freeboard (black), SAR backscatter (blue, no unit, scaled between 0 and 100 and interpolated to the GLAS measurement positions), and the uncorrected reflectivity (red). The uncorrected reflectivity is the ratio between the received and transmitted laser pulse energy not corrected for atmospheric effects (for details see Section 2.2.1 on page 19). Ideally the darker water with low albedo should show lower reflectivities than the ice and snow with high albedo, if no specular reflection occurs. In a typical winter-time SAR image of the Arctic Ocean sea ice cover the radar backscatter takes high values (grey-white in Figures 5.7–5.9) over multi-year ice and low values (black-dark grey in

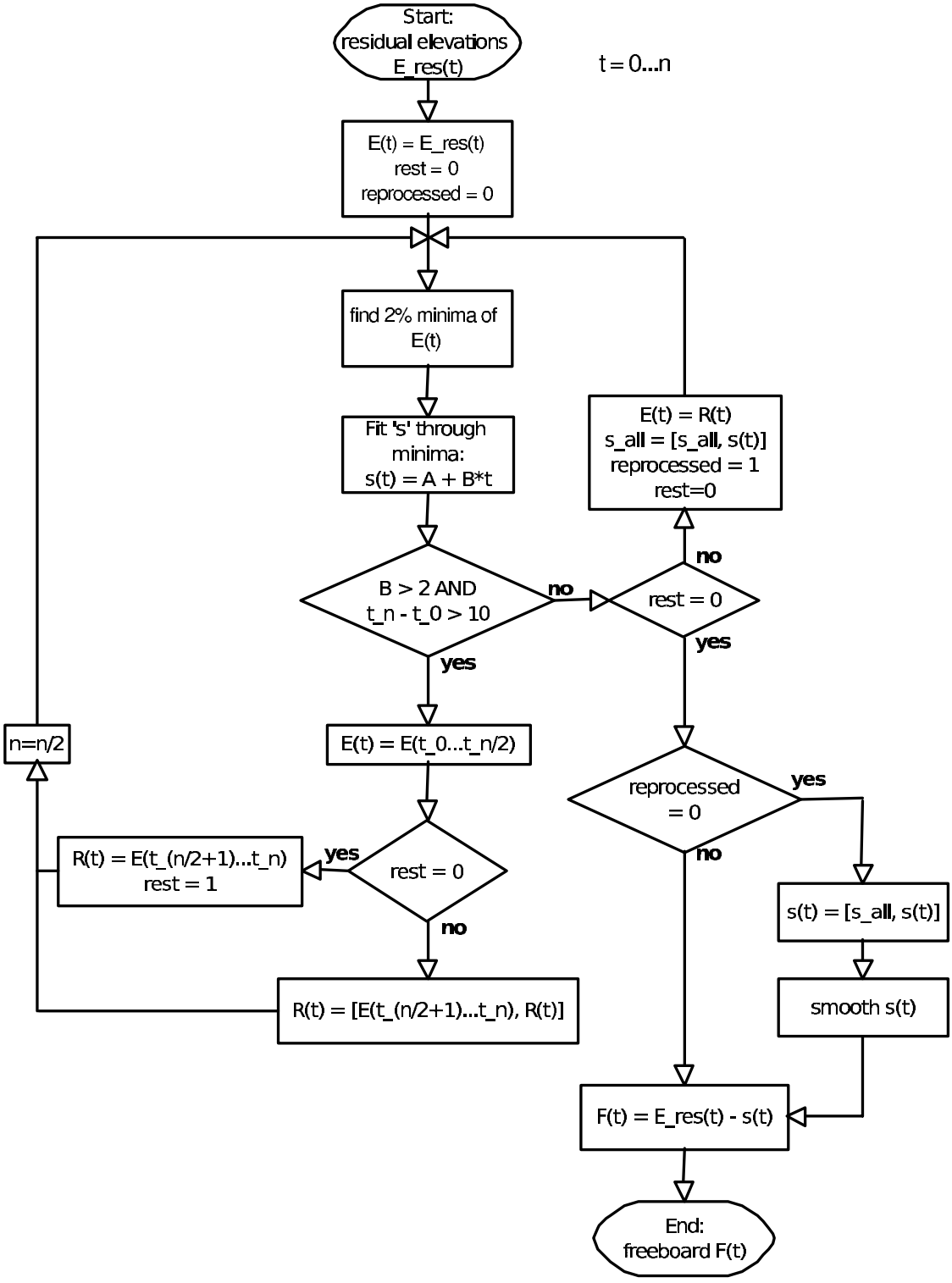

Figure 5.6: Flow diagram of the freeboard F processing starting with the residual elevations E_{res}. F is calculated in dependence of the time t in seconds.

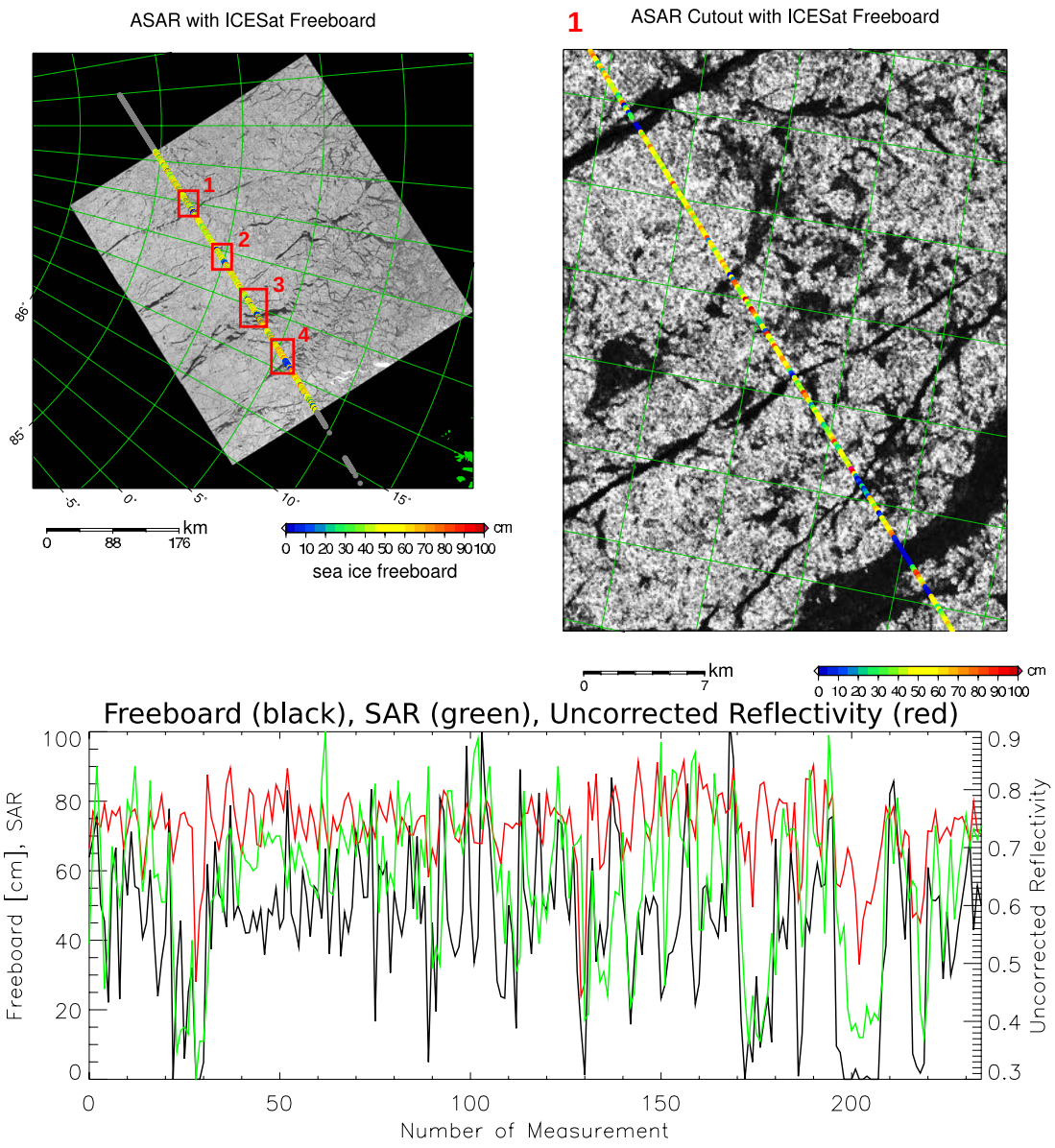

Figure 5.7: Envisat ASAR image from 2003-03-09, 16:52 UTC, overlaid by color-coded sea ice freeboard heights (footprints not to scale) of an ICESat overflight at 15:41 UTC, descending orbit. Top-left: complete 400 km × 400 km ASAR scene north of Svalbard; top-right: blow-up of the red rectangle marked with an 1 in left image; bottom: graphs of the freeboard (black, left y-axis), ASAR backscatter (green, no unit, scaled between 0 and 100), and uncorrected reflectivity (red, right y-axis) along the part of the ICESat transect shown in the top-right image. The measurements on the y-axis are each 172 m apart. In regions where the SAR image shows leads (dark areas in top figures and low backscatter in bottom figure), covered either by smooth first-year ice and/or thin ice and/or calm open water, the ICESat freeboard drops down to values near zero. A slight shift in the location of the leads in the two datasets can be attributed to the ice drift during the 1:10 hour time difference. Blow-ups 2 to 4 are shown in Figures 5.8 and 5.9.

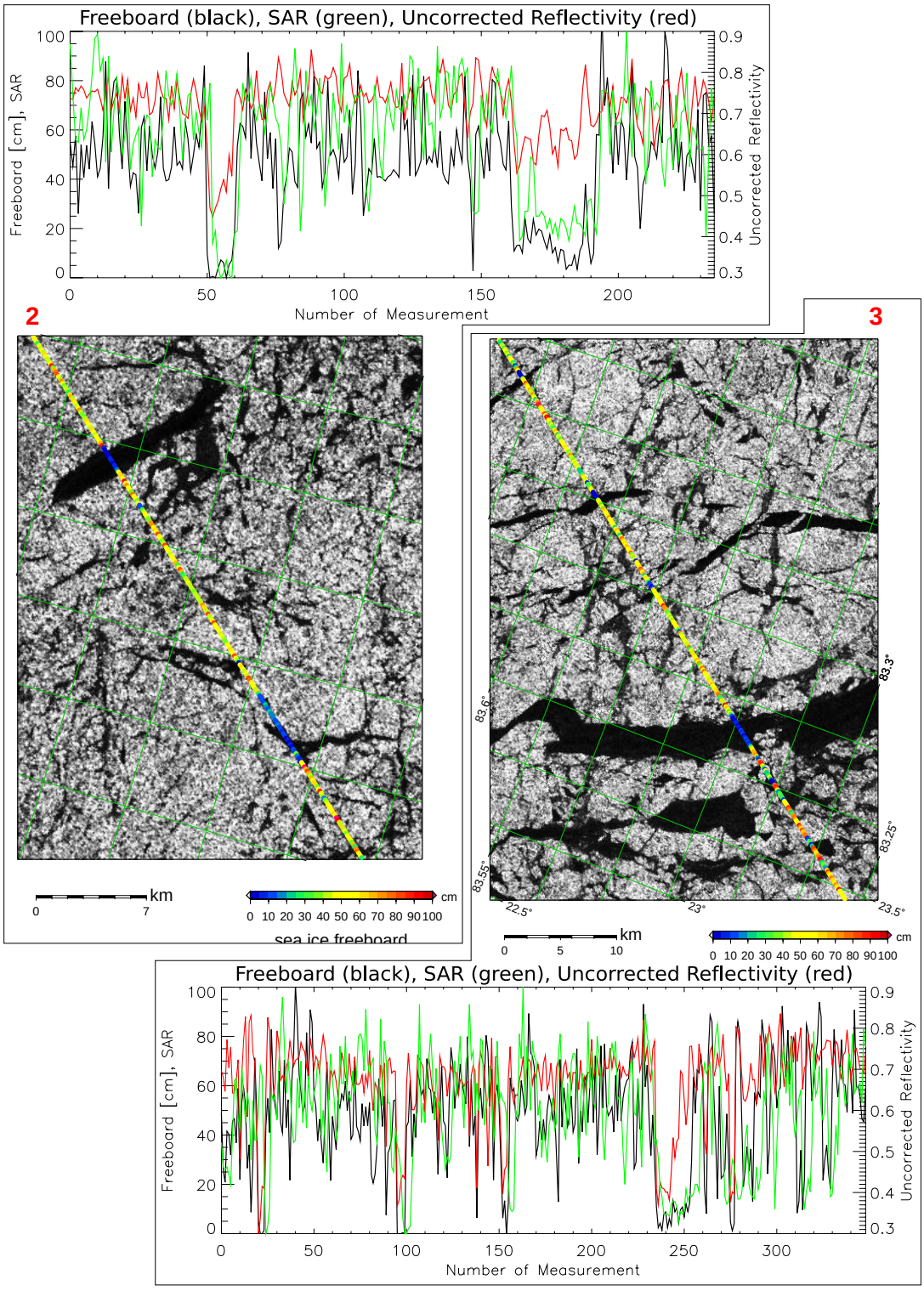

Figure 5.8: Same as Figure 5.7, but for the zoom cutouts 2 (top) and 3 (bottom) marked in Figure 5.7 top-left.

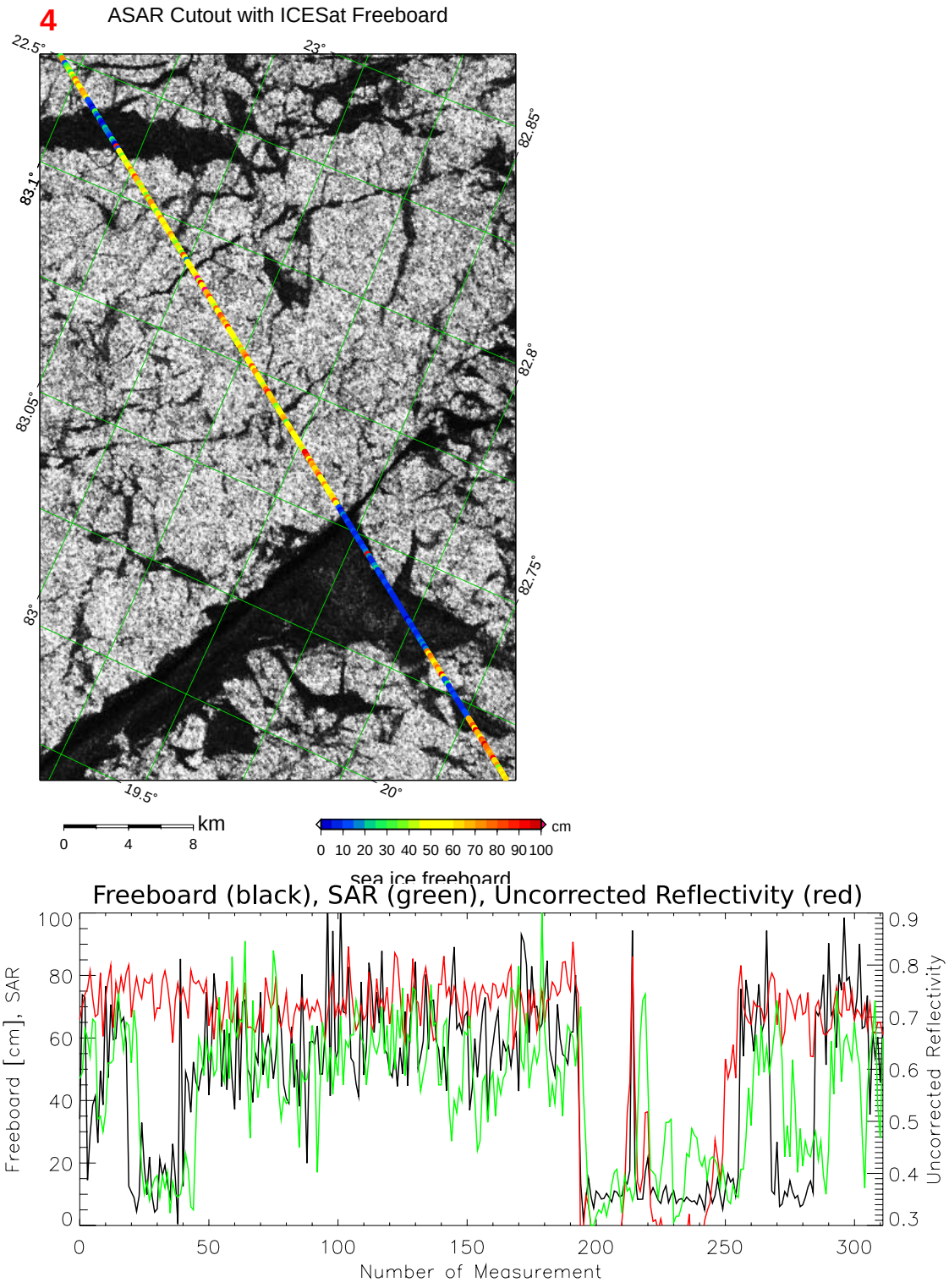

Figure 5.9: Same as Figure 5.7, but for the zoom cutout 4 marked in Figure 5.7 top-left.

Figures 5.7–5.9) over new ice, young ice and calm open water. (Also smooth first-year ice could appear dark, but is not present here.) Over these dark regions the overlaid GLAS freeboard heights drop to zero showing that the algorithm is able to identify the minima correctly. The remaining shift in the location of the open water/thin ice areas identified between both datasets can be ascribed to the ice drift during the acquisition time difference of the two data sets. According to the AMSR-E derived ice drift (lower-left image in Figure A.2 on page 142), the ice should have drifted about 500 m during that 1 hour. This difference causes the biggest problem for comparison of these datasets. If the time difference exceeds 2–3 hours in most cases no agreement between both datasets can be found; otherwise the match between these datasets in general is similar to the example shown here. See Appendix A.2 on page 141 for more examples. Using the 2-daily ice drift derived from AMSR-E or QuikSCAT (Chapter 4) to adjust the two datasets is mostly not solving the problem, as ice drift with high temporal resolution would be needed to correct the datasets successfully, especially in the dynamic Fram Strait region. Additional problems might be caused by an inaccurate geo-location of the datasets.

However, overall the comparisons show good agreement, underlining the feasibility of our approach. Leads can be clearly identified in the freeboard heights. Often, but not always, this is supported by a coincident drop of the reflectivity. This is expected for thin ice or open water, which have a lower albedo than the surrounding thick sea ice. In some cases, for example the northern lead in Figure 5.9 where both SAR and freeboard show a clear signal, the reflectivity is not affected by the open water/thin ice area and stays at a high value of about 0.75. There are multiple possible explanations for this insensitivity. (1) Specular reflection of the laser beam can occur over quite open water or flat ice areas. This would cause a very high reflectivity (theoretically and not taken the atmosphere into account even higher than 0.75). (2) Strong scattering in the atmosphere caused by clouds can also result in a high uncorrected reflectivity value. The exact reason for the individual is unknown. From this considerations it can be concluded that the uncorrected reflectivity could be used as a supporting criterion for the minimum elevation determination (e.g. as a future enhancement of this algorithm) but not as an exclusive criterion.

With this SAR comparison it is not possible to validate the absolute freeboard values, but it has been shown that our method identifies most of the SSH minimas correctly.

5.1.4 Gridded Freeboard

All freeboard data is mapped onto a polar stereographic grid (see Section 2.2.5 on page 25) with 25 km grid size. First the freeboard data of all orbits of each GLA13 dataset (covering approximately one day) is gridded using a "drop in the bucket" method and not interpolating empty grid cells. The mean of all freeboard height measurements in one grid cell is taken as freeboard value F_i for the dataset i.

Afterwards the freeboard heights for each ICESat measurement period are calculated. The freeboard heights F_i of each GLA13 dataset are weighted with the number of measurements n_i in each grid cell and the mean of all measurements in the period is calculated

$$F = \frac{\sum_{i=1}^{m} n_i F_i}{\sum_{i=1}^{m} n_i}, \tag{5.5}$$

where m is the number of available GLA13 datasets for the period, F_i and n_i are the according freeboard heights and number of measurements per grid cell for one GLA13 dataset. The standard deviation of the sample is given by

$$\sigma_F = \sqrt{\frac{1}{j-1}\left(\sum_{i=1}^{m} n_i F_i^2 - \frac{1}{j}\left(\sum_{i=1}^{m} n_i F_i\right)^2\right)}, \tag{5.6}$$

with $j = \sum_{i=1}^{m} n_i$ as number of all measurements per grid cell (*Blobel and Lohmann*, 1998). The variability of the freeboard heights is naturally very high in one 25 km×25 km grid cell. Sea ice conditions are changing during the about one month long periods and even for one overflight ice floes with different freeboard heights are measured. The standard deviation σ_F therefore is not a valid error estimation for the mean freeboard height F. Instead either the standard deviation of the mean $\overline{\sigma_F} = \sigma_F/\sqrt{j}$ or the error $\varepsilon = 13.8\,\mathrm{cm}/\sqrt{j}$ caused by the single measurement uncertainty of 13.8 cm (*Zwally et al.*, 2002) is taken as freeboard error ε_F for one grid cell, depending on which of both is larger. This error estimation likely is an underestimation of the real error, as systematic errors are not taken into account. Systematic errors probably exist, but can not be quantified due to a lack of validation data. E.g., we cannot be sure, that the 2% rule of the minimum elevation algorithm picks up all open water measurements and that the SSH is represented well by the linear fit. In particular, the 2% rule and subsequent SSH determination first is applied to that section of each ICESat overpass which crosses our region of interest. Only if the gradient of the linear fit is larger than a certain threshhold (2 mm/sec) the overpass is split up in smaller parts (see Section 5.1.2 on page 68). However, if the minimum elevation determination fails measurements of a complete overflight might have an offset in freeboard height. Also ocean swell can cause additional inaccuracies for the SSH determination, particularly in the MIZ. Therefore the above error estimate can be seen as a lower margin.

The freeboard height results for the nine used ICESat periods between 2003 and 2007 are shown in Figures 5.10 and 5.11.

The mean ice freeboard for all periods in the study region is summarized in Table 5.1 on page 81 together with the error estimation of the freeboard in every grid cell. A map of the error estimate for every grid cell and the number of measurements per grid cell is shown in Figure 5.12 on page 82 for ICESat period 3b (2005-02-18—2005-03-23). Not surprising the number of measurements shows a strong north–south gradient with more than 5000 measurements per grid cell in the north and only about 100 measurements per grid cell in the south of the study region, which likely are caused by only one valid ICESat measurement overpass during the complete period. With a measurement distance of 172 m one overpass would result in approximately 150 measurements per grid cell if all measurements are valid. The cyan values about 30 in the open ocean are caused by the utilization of the AMSR-E ice concentrations for open water cases, which are counted as one measurement per day. The distribution of the freeboard error estimate in every grid cell in Figure 5.12, right reflects the distribution of the number of measurements with lower errors in the north, where a lot of measurements contributed to the mean freeboard, and higher values to the south (see dependence on number of measurements j in equation 5.6). The maps of number of measurements and error estimate for the other

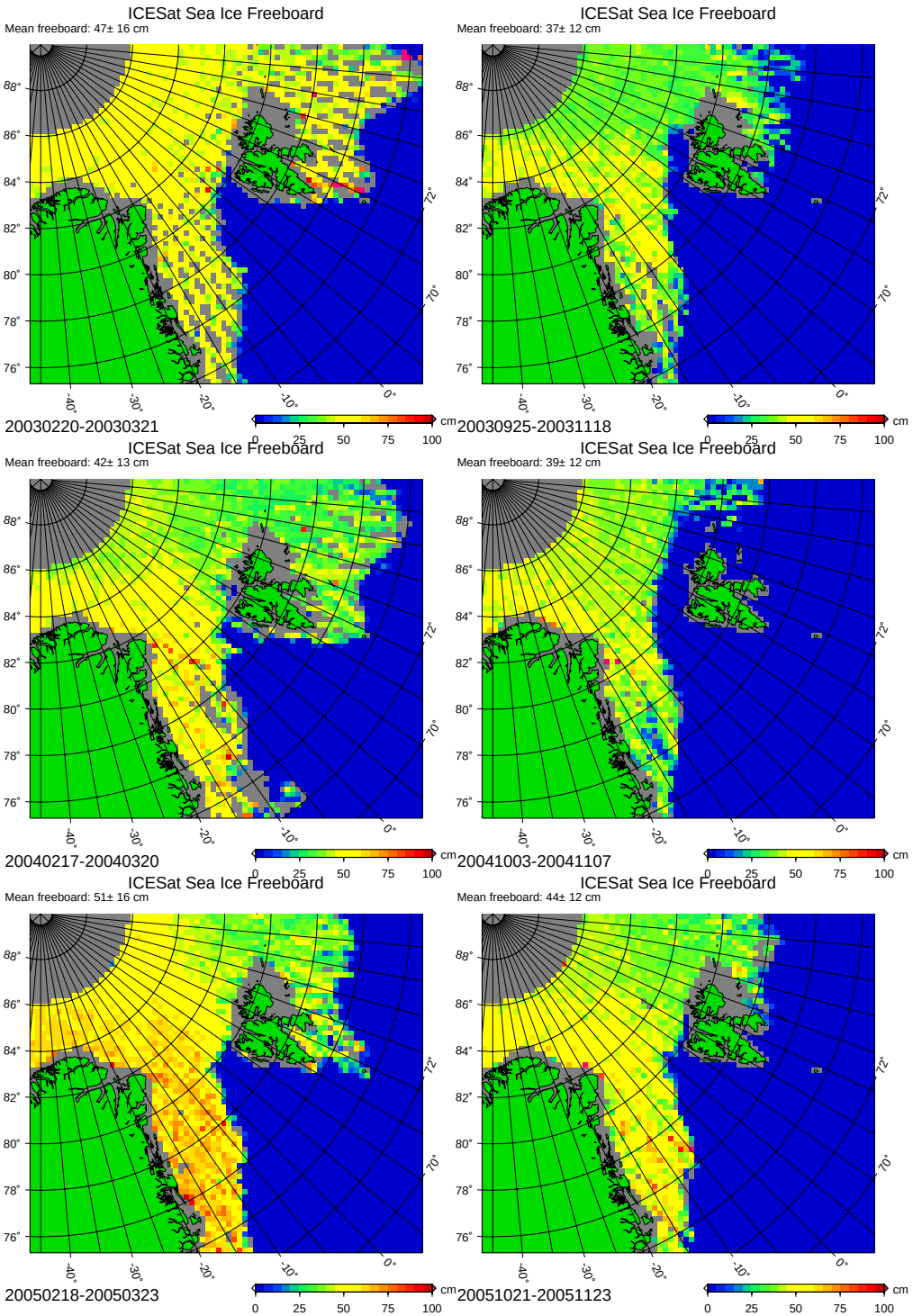

Figure 5.10: Sea ice freeboard for ICESat periods 1 (top-left), 2a (top-right), 2b (middle-left), 3a (middle-right), 3b (bottom-left), and 3d (bottom-right). Figure and caption are continued in Figure 5.11.

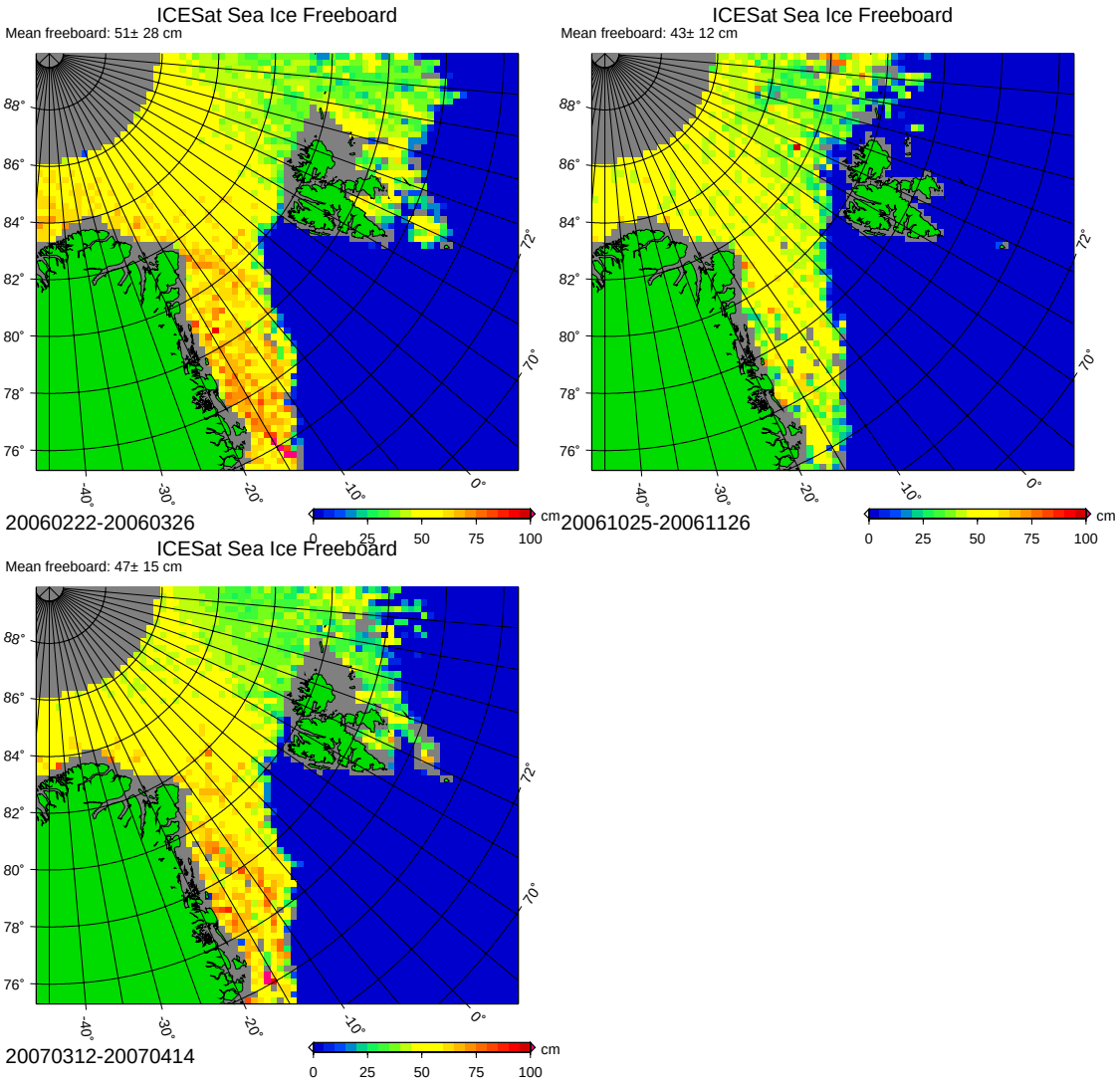

Figure 5.11: Continuation of Figure 5.10. Sea ice freeboard for ICESat periods 3e (top-left), 3g (top-right), and 3h (bottom-left). Dates of periods are given in Table 2.3 on page 20 and coded as yyyymmdd below each subfigure.

Table 5.1: Mean freeboard heights and error estimate per grid cell in the study region for all used ICESat periods. ± values are the standard deviations attributed to the variability in the region.

Period	Dates	Mean Freeboard	Mean Error Estimate
1	20.02–21.03.2003	47 cm ± 16 cm	1.5 cm ± 3.8 cm
2a	25.09–18.11.2003	37 cm ± 12 cm	1.1 cm ± 1.1 cm
2b	17.02–20.03.2004	42 cm ± 13 cm	1.7 cm ± 1.8 cm
3a	03.10–07.11.2004	39 cm ± 12 cm	1.2 cm ± 1.2 cm
3b	18.02–23.03.2005	51 cm ± 16 cm	1.8 cm ± 1.8 cm
3d	21.10–24.11.2005	44 cm ± 12 cm	1.5 cm ± 1.4 cm
3e	22.02–27.03.2006	51 cm ± 28 cm	1.6 cm ± 1.6 cm
3g	25.10–27.11.2006	43 cm ± 12 cm	1.6 cm ± 1.4 cm
3h	12.03–14.04.2007	47 cm ± 15 cm	1.7 cm ± 1.7 cm
Total Mean		45 cm ± 5 cm	1.5 cm ± 0.6 cm

ICESat periods look similar and therefore are not shown.

5.1.5 Outlook: Freeboard

The sea ice freeboard determination algorithm is working stable and only few data is discarded completely (see Appendix A.1 on page 139). In Section 5.1.3 it was shown that open water or thin ice areas are identified with the algorithm.

Nevertheless, a validation of the absolute freeboard values has not been done and can not be done today, as no suitable comparison dataset exists. The only known accurate method is the in-situ measurement of the freeboard with a ruler stick in a borehole. Here the poor sampling in space and time hampers comparison. We do not have and do not know of any in-situ freeboard borehole dataset in the Fram Strait region, which is coincident to ICESat measurements.

ICESat freeboard heights can be compared with freeboards, derived from airborne lidar measurements with a similar technique but higher spatial resolution. *Skourup and Forsberg* (2006) did this for two ICESat tracks north of Greenland. They found an offset of approximately 35 cm between the two freeboard height datasets with the airborne ones higher than the ICESat ones. They used almost the same algorithm for both datasets and attributed the difference mainly due to the absence of larger leads. It would be a helpful validation to get the airborne lidar dataset at hand and to compare it with the freeboard heights derived by the algorithm discussed here.

Another but also indirect validation dataset could be the ice draft derived from ULS data. One ULS operated by the Norwegian Polar Institute (NPI) was measuring in the Fram Strait during several ICESat periods. Unfortunately this data is not processed and available so far. However, ULS ice draft data would be a more meaningful comparison dataset for the complete sea ice thickness discussed in the remaining part of this chapter.

Anyhow, even without more suitable validation datasets than the used SAR data a few concepts can be suggested to improve the algorithm in future.

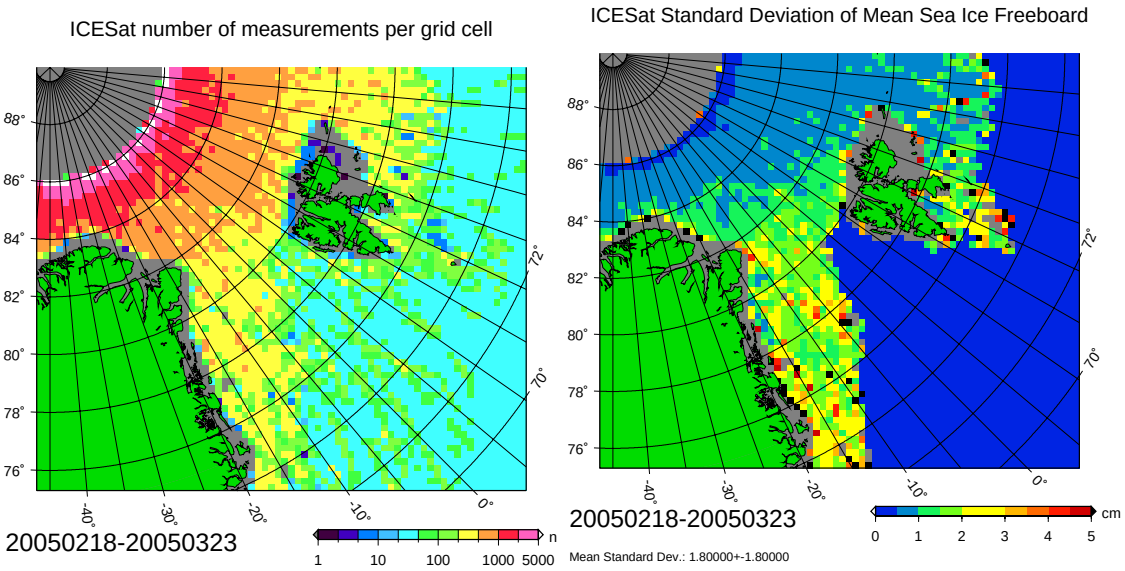

Figure 5.12: Maps of the number of used ICESat measurements per grid cell (left) and the freeboard error estimate per grid cell for ICESat period 3b (2005-02-18—2005-03-23)). Respective maps for the other periods look similar.

- Usage of the uncorrected reflectivity as additional constraint for the minima detection of open water and thin ice. Despite the noisy appearance of the reflectivity data, mainly caused by detector saturation and specular reflection, it should be possible, after some filtering, to use low reflectivity values as further open water and thin ice indicator (*Kwok et al.*, 2004b). Both surface types are darker than the surrounding snow and ice. In the examples shown in Figures 5.7–5.9 and Appendix A.2 the reflectivity often, but not always, drops down over open water/thin ice areas. Maybe also the for atmospheric attenuation corrected reflectivity (Section 2.2.1), which is only available as a mean for 40 laser shots, can be used to in parts correct the uncorrected reflectivity for atmospheric effects.
- Another possible indicator for open water/thin ice is the sea ice surfaces roughness calculated from the shape of the backscattered laser waveform.
- A constant value of 2% of the measurements is used for the minima identification. This value could be defined more flexible and adapted in dependence of e.g. the sea ice concentration.

5.2 Conversion of Freeboard to Ice Thickness

To retrieve ice thickness, I, from the ice freeboard, F, prior information about snow thickness, S, and the densities of ice, ρ_I, of snow, ρ_S, and of water, ρ_W, have to be known (see Figure 5.1 on page 64). As the ice density changes with the ice age, different ice densities ρ_{MY} and ρ_{FY} are applied to multi-year and first-year ice, respectively.

The freeboard F calculated by equation 5.5 on page 77 in Section 5.1 is the mean freeboard of the existent ice in the respective grid cell without the open water. In order

to obtain the mean freeboard $\overline{F}$ and its error $\varepsilon_{\overline{F}}$ for the complete grid cell including the open water parts, the freeboard F has to be scaled with the ice concentration C:

$$\begin{aligned} \overline{F} &= F\,C\,, \\ \varepsilon_{\overline{F}} &= \sqrt{C^2\varepsilon_F^2 + F^2\varepsilon_C^2}\,. \end{aligned} \tag{5.7}$$

The second term is small compared to the first term if $C > 50\%$ and $F < 80\,\text{cm}$. The freeboard error ε_F defined in Section 5.1.4 and a constant ice concentration error of $\varepsilon_C = 0.05$ (5%) is used. An error of 5% for the ASI ice concentration is at the upper limit in the solid ice cover and at the lower end for the MIZ (*Kern et al.*, 2003; *Spreen et al.*, 2008). Before this calculation is done, the ASI sea ice concentrations C (Chapter 3) are sampled down to the 25 km grid used for the ice freeboard F and ice drift D (e.g. shown as background of Figure 4.1 on page 52). Henceforth, this mean freeboard $\overline{F}$ including the open water part is used for all calculations and is called F again ($F = \overline{F}$).

Assuming free floating ice with the above mentioned parameters the ice thickness I can be calculated from the ice freeboard F according to the Archimedes principle as:

$$I = \left(\frac{C_{MY}}{\rho_W - \rho_{MY}} + \frac{C_{FY}}{\rho_W - \rho_{FY}}\right) \frac{F\,\rho_W + S(\rho_S - \rho_W)}{C}\,. \tag{5.8}$$

C, C_{MY}, and C_{FY} are the total, the multi-year, and the first-year ice concentration in each grid cell, respectively. The error of the ice thickness ε_I, calculated by Gaussian error propagation from the input variables and their errors ε, can be defined as:

$$\begin{aligned} \varepsilon_I = \Bigg[& \left(\frac{C_{MY}}{\rho_W - \rho_{MY}} + \frac{C_{FY}}{\rho_W - \rho_{FY}}\right)^2 \frac{\rho_W^2\,\varepsilon_F^2 + (\rho_S - \rho_W)^2\,\varepsilon_S^2}{C^2} \\ & + \left(\left(\frac{C_{MY}\,(S\,(\rho_{MY} - \rho_S) - F\,\rho_{MY})}{C\,(\rho_W - \rho_{MY})^2} + \frac{C_{FY}\,(S\,(\rho_{FY} - \rho_S) - F\,\rho_{FY})}{C\,(\rho_W - \rho_{FY})^2}\right)\varepsilon_{\rho_W}\right)^2 \\ & + \left(\frac{C_{MY}\,(S\,(\rho_S - \rho_W) + F\,\rho_W)}{C\,(\rho_W - \rho_{MY})^2}\,\varepsilon_{\rho_{MY}}\right)^2 \\ & + \left(\frac{C_{FY}\,(S\,(\rho_S - \rho_W) + F\,\rho_W)}{C\,(\rho_W - \rho_{FY})^2}\,\varepsilon_{\rho_{FY}}\right)^2 \\ & + \left(\left(\frac{C_{MY}}{\rho_W - \rho_{MY}} + \frac{C_{FY}}{\rho_W - \rho_{FY}}\right)\frac{S}{C}\,\varepsilon_{\rho_S}\right)^2 \Bigg]^{1/2}\,. \end{aligned} \tag{5.9}$$

The errors of the multi-year and first-year ice concentration are not considered, which might cause an underestimation of the ice thickness error (see Sections 5.2.1 and 6.5.2). The error ε_C of the total ice concentration C is already considered for the mean freeboard calculation in equation 5.7. In Table 5.2 on the next page all parameters used for the freeboard to ice thickness conversion are summarized. The following sections describe how they are found and why the respective values are used. First the used multi-year sea ice concentration algorithm is explained.

5.2.1 QuikSCAT Multi-Year Sea Ice Concentration

The density of sea ice mainly depends on the age of the ice, especially in the upper few decimeters. Old multi-year sea ice has a lower density than young, newly formed ice.

Table 5.2: Parameters used for the freeboard to ice thickness conversion (see equation 5.8 on the preceding page). Winter periods are ICESat periods 1, 2b, 3b, 3e, 3h; fall periods are 2a, 3a, 3d, and 3g (see Table 2.3 on page 20). ε values give the assumed error amount for each parameter used for the ice thickness error calculation (equation 5.9).

Name	Variable Name	Winter Periods	Fall Periods
multi-year ice density	ρ_{MY}	$887\,\mathrm{kg/m^3}$	$887\,\mathrm{kg/m^3}$
multi-year ice density error	$\varepsilon_{\rho_{MY}}$	$20\,\mathrm{kg/m^3}$	$20\,\mathrm{kg/m^3}$
first-year ice density	ρ_{FY}	$910\,\mathrm{kg/m^3}$	$910\,\mathrm{kg/m^3}$
first-year ice density error	$\varepsilon_{\rho_{MY}}$	$20\,\mathrm{kg/m^3}$	$20\,\mathrm{kg/m^3}$
snow density	ρ_S	$330\,\mathrm{kg/m^3}$	$280\,\mathrm{kg/m^3}$
snow density error	ε_{ρ_S}	$15\,\mathrm{kg/m^3}$	$20\,\mathrm{kg/m^3}$
ocean water density	ρ_W	$1023.9\,\mathrm{kg/m^3}$	$1023.9\,\mathrm{kg/m^3}$
ocean water density error	ε_{ρ_W}	$0.5\,\mathrm{kg/m^3}$	$0.5\,\mathrm{kg/m^3}$
snow depth (large freeboard)	S for $S \leq 0.8F$	0.20 m	0.12 m
snow depth (small freeboard)	S for $S > 0.8F$	$0.8F$	$0.8F$
snow depth error	ε_S	$0.25S$	$0.25S$
ice concentration error	ε_C	0.05	0.05

The older the ice is getting, the more of the heavy brine drained out of the ice, leaving behind brine channels and a porous ice structure. Especially after the ice survived one melt season and the connected flushing with melt water the ice density strongly changed. QuikSCAT active microwave backscatter data can be used to distinguish between this less dense multi-year and the heavier first-year ice. Two different ice densities ρ_{FY} and ρ_{MY} can be attributed to the two ice classes (FY: first-year and MY: multi-year). This leads with equation 5.8 on the preceding page to a more accurate ice thickness retrieval as if only one density for all ice types would be used. The method proposed by *Kwok* (2004) is used to calculate multi-year sea ice concentrations from the vertically polarized QuikSCAT data (see Section 2.2.3 on page 24). The vertically (VV) polarized backscatter σ_{VV} is used because the incidence angle and swath width is larger than for the horizontally polarized σ_{HH} leading to a smaller area without data coverage around the North Pole. In principle also σ_{HH} could have been used the same way. Figure 6d in *Kwok* (2004) shows an empirical relationship between multi-year sea ice fraction C_{MY} and backscatter σ_0 (in our case $\sigma_0 = \sigma_{VV}$). Multi-year ice fraction of three winter time months (December 1999 to February 2000) derived from RADARSAT data using the RGPS system (*Kwok*, 1998; *Kwok and Cunningham*, 2002) are plotted against QuikSCAT backscatter data. The RGPS discriminates first-year and multi-year ice and releases the fraction of multi-year ice in respect to the total ice cover. An analytical relationship between the two variables, multi-year ice fraction and backscatter, was not given. We digitized the values of this graph and afterwards fitted a seventh order polynomial L_{MY} through the data points using a least-square method (Figure 5.13). The thereby found analytical relationship between multi-year sea ice fraction C_{MY_f} and QuikSCAT backscatter σ_{VV}

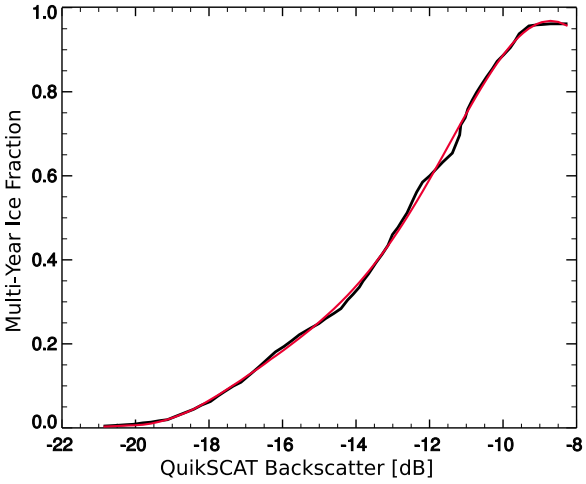

Figure 5.13: Plot of multi-year sea ice fraction (from December 1999 to February 2000 RADARSAT data) versus QuikSCAT backscatter σ_0 in black (digitized from *Kwok* (2004), Figure 6d) and the 7-order polynomial fit L_{MY} to the data in red.

is

$$L_{MY} = 45.4268 + 27.9618\,\sigma_{VV} + 7.08118\,\sigma_{VV}^2 + 0.943513\,\sigma_{VV}^3 + 0.0720040\,\sigma_{VV}^4 + 0.00317470\,\sigma_{VV}^5 + 7.53719 \cdot 10^{-5}\,\sigma_{VV}^6 + 7.46839 \cdot 10^{-7}\,\sigma_{VV}^7\,,$$

$$C_{MY_f} = \begin{cases} 0 & : \quad \sigma_{VV} \leq -21\,\mathrm{dB} \\ L_{MY} & : \quad -21\,\mathrm{dB} < \sigma_{VV} < -9\,\mathrm{dB} \\ 1 & : \quad \sigma_{VV} \geq -9\,\mathrm{dB} \end{cases} \tag{5.10}$$

if σ_{VV} is given in dB. Figure 5.13 shows the original data together with the polynomial of equation 5.10. The relationship in Figure 5.13 was found for the western part of the Central Arctic (Beaufort Sea, north of Greenland and the Canadian Archipelago), which are the main regions covered with high fractions of multi-year ice. Other surface processes (melting and refreezing, snow with layers etc.) on younger ice may cause similar σ_0 backscatter values and thereby could lead to misclassification (*Voss et al.*, 2003; *Tonboe and Toudal*, 2005). This is especially a problem for the marginal seas in the Eurasian part of the Arctic, where in general no multi-year ice is present. In our study region the Fram Strait and Greenland Sea this is not a severe problem, as multi-year ice is frequent and misclassifications only make up a small part. Equation 5.10 is used to calculate the multi-year ice fraction for all grid cells in the Arctic. Additionally, a mask is applied to exclude multi-year ice in unlikely places (but keeping the often missclassified marginal seas). To obtain the total multi-year sea ice concentration C_{MY} for each gridcell C_{MY_f} is multiplied with the ASI AMSR-E (see Chapter 3) ice concentration C:

$$C_{MY} = C_{MY_f}\,C\,.$$

This is necessary as C_{MY_f} does not include the open water part in the grid cell and to always guarantee $C_{MY} \leq C$. Figure 5.14 on the following page shows an example for C_{MY} for 15 March 2007. Other dates look similar. In the Central Arctic multi-year ice is correctly identified. The additionally shown 14.5 dB σ_{VV} contour in white can be used as a good representative for the multi-year sea ice extent. In the marginal seas like the Chukchi Sea, Barents Sea, and Baffin Bay spurious multi-year ice concentrations occur.

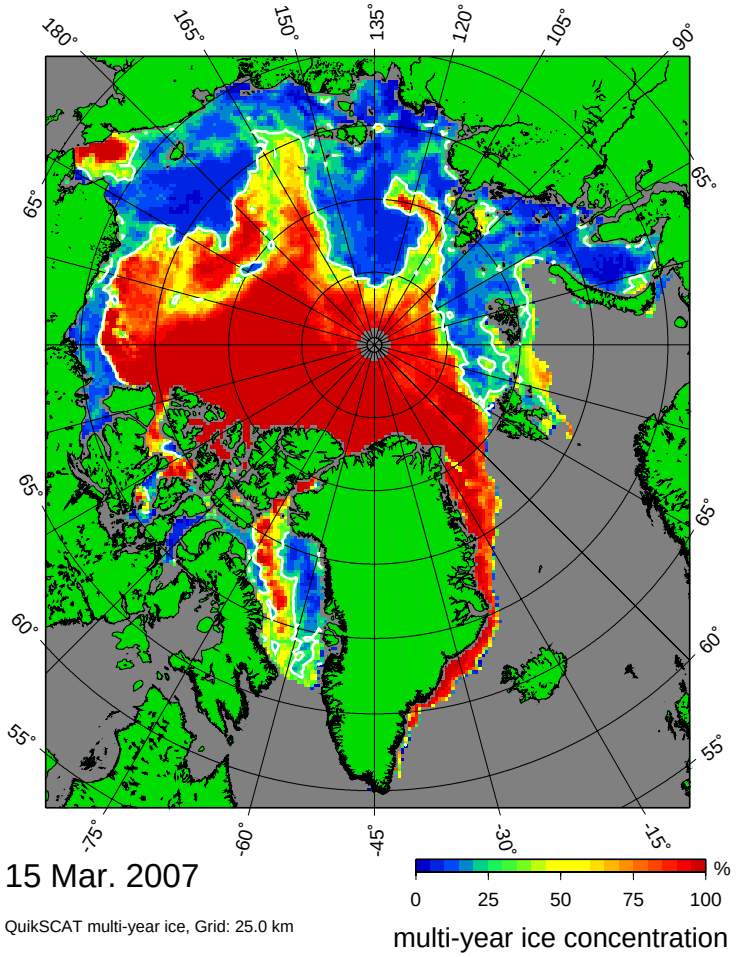

Figure 5.14: Multi-year sea ice concentration C_{MY} calculated from QuikSCAT data (σ_{VV}) on 15 March 2007. The white line represents the 14.5 dB σ_{VV} backscatter contour, which often can be used as a multi-year ice extent definition. In marginal seas, e.g. the Chukchi Sea, spurious multi-year ice concentrations occur.

In the Fram Strait region and Greenland Sea high multi-year ice concentration frequently occur and in general the retrieved multi-year ice concentration values should be accurate. However, as in other marginal seas the multi-year ice concentration is overestimated it can not be excluded that also in the Greenland Sea an overestimation of the multi-year sea ice concentration might occur. For example forming of new ice, deformation processes liking ridging, or refreezing wet precipitation can lead to increased radar backscatter (*Tonboe and Toudal*, 2005; *Voss et al.*, 2003) and thus to an overestimation of the multi-year ice fraction. This can cause an underestimation of the sea ice thickness by several decimeters. See the sensitivity study in Section 6.5.2 on page 116 for a more detailed discussion. Nevertheless, QuikSCAT measurements are the best suited dataset available on a daily base to discriminate between multi-year and first-year sea ice. Further evidence that the detected multi-year ice area in Figure 5.14 consists of thick sea ice is given by comparison to the September 2007 sea ice minimum shown in Figure 3.9 on page 44. Already in mid

of March the white multi-year ice extent contour shows a lot of similarities to the sea ice minimum ice edge in September 2007.

Now, in combination with the ASI total ice concentration C data, also the concentration of first-year ice $C_{FY} = C - C_{MY}$ can be identified for each grid cell and different ice density values ρ_{MY} and ρ_{FY} are assigned to them, respectively. The typical density values $\rho_{MY} = 887\,\mathrm{kg/m^3}$ and $\rho_{FY} = 910\,\mathrm{kg/m^3}$ with an uncertainty of $\varepsilon_{MY} = \varepsilon_{FY} = 20\,\mathrm{kg/m^3}$ are used (*Eicken et al.*, 1995; *Laxon et al.*, 2003).

5.2.2 Snow Thickness and Density

Because no reliable satellite snow depth measurements are available covering the Fram Strait study region, in-situ snow depth and density measurements available in the vicinity of the study area in combination with a snow climatology is used. The snow depth retrieved from AMSR-E data (*Comiso et al.*, 2003) was evaluated and found not to be useful in our study region. Unrealistically large snow depth values and large variability were found in the Greenland Sea and MIZ. The AMSR-E snow depth algorithm was mainly designed for the Antarctic and is still under validation for the Arctic (*Markus et al.*, 2006; *Sturm et al.*, 2006).

Instead snow depth, and snow density measurements from R/V Polarstern, which operated in April 2003, one month after ICESat period 1, north of Svalbard as part of the CryoVEx 2003 campaign (*ARKTIS-XIX/1 and XIX/2 science team*, 2004), are taken as reference for the winter periods 1, 2b, 3b, 3e, and 3h. The observed mean snow thickness, S, was 20 cm (range: 0–70 cm) with a density, ρ_S, of $330\,\mathrm{kg/m^3}$. The uncertainty of $\varepsilon_{\rho_S} = 15\,\mathrm{kg/m^3}$ was estimated from density values after *Warren et al.* (1999) for the adjacent months February and April. The snow depth is assumed to be smaller on thin ice as compared to thick ice. Furthermore, isostatic balance is assumed (on average), i.e. the snow depth on freely floating ice is assumed to be always less than or equal the ice freeboard. This yields the following snow thickness parameterization: If the ratio $S/F > 0.8$ then $S = 0.8F$, otherwise the constant snow depth $S = 0.2\,\mathrm{m}$ is used.

For the end of summer/fall periods 2a, 3a, 3d, and 3g snow parameters can be expected to substantially differ from those of the winter periods (e.g. *Warren et al.*, 1999). In situ measurements representative for snow conditions during these periods are not available to us. Alternatively climatological snow depths (*Warren et al.*, 1999) could be used, revealing values in the range of 19 cm and 32 cm for October and March (resemble the fall and winter periods) for the complete Arctic, respectively. However, these values are based on observations made during 1954 to 1991 predominantly in the central Arctic. Meanwhile the ice age and thickness (*Maslanik et al.*, 2007b; *Rigor and Wallace*, 2004) and presumably also the snow depth has changed but most likely not the seasonal cycle, i.e. the ratio between winter and fall snow depths should be the same. Therefore, we estimated the snow depth of the fall periods by taking the snow depth S measured during CryoVEx as reference, as $S = 19/32 \cdot 0.2\ \mathrm{m} = 0.12\,\mathrm{m}$. After *Warren et al.* (1999) the snow density in the Arctic varies seasonally rather than spatially so that their snow density estimate for October/November of $\rho_S = 280\,\mathrm{kg/m^3}$ is taken for the fall periods. This is supported by their snow density measurements of $325\,\mathrm{kg/m^3}$ for March/April, which match well with the measurements during CryoVEx of $330\,\mathrm{kg/m^3}$. The assumed

uncertainty of $\varepsilon_{\rho_S} = 20\,\mathrm{kg/m^3}$ is the standard deviation of the *Warren et al.* (1999) snow densities for September, October, and November. For small freeboard heights the same parameterization ($S/F > 0.8 \Rightarrow S = 0.8F$) as for the winter periods is used. Due to its variability and the sparse coverage of in situ measurements the uncertainty in snow depth ε_S is considered to be high and a relative uncertainty of $\varepsilon_S = 0.25S$ is used for all ICESat periods.

A water density, ρ_W, of $1023.9\,\mathrm{kg/m^3}$ ($\varepsilon_{\rho_W} = 0.5\,\mathrm{kg/m^3}$) is used for both periods (*Laxon et al.*, 2003), as the temperature of the water below the ice for both period types should be similar.

With these parameters the ice thickness I can be calculated and equation 5.8 on page 83 is yielding the following expression for winter:

$$I = \frac{C_{MY} + 1.20C_{FY}}{C}(7.48F - 5.07S) \tag{5.11}$$

and for fall:

$$I = \frac{C_{MY} + 1.20C_{FY}}{C}(7.48F - 5.43S)\,. \tag{5.12}$$

5.2.3 Sea Ice Thickness Maps 2003–2007

Using equations 5.11 and 5.12 the ice thickness for all periods is calculated from the freeboard heights given in Section 5.1.4. The according errors are calculated following equation 5.9 on page 83.

The ice thickness now is defined for all regions or rather all grid cells where valid freeboard measurements exist. Due to lack of ICESat data or unfavorable conditions, like strong swell, for some grid cells no freeboard data exists in the MIZ (see Figures 5.10 and 5.11 especially period 1), although they are covered by sea ice. To get consistent ice volume flux estimates in the end, the ice thickness has to be defined for all ice covered grid cells. Therefore the ice thickness data calculated from the freeboard heights is inter- and extrapolated to all ice covered grid cells using kriging interpolation (*Isaaks and Srivastava*, 1990). The following interpolation parameters are used: only data within a distance of equal or less than 8 grid cells ($\equiv 200\,\mathrm{km}$) is considered for the interpolation, and a variogram with exponential covariance ($covariance = e^{-3/5d}$, d: distance) is used. These interpolated ice thickness maps for the Fram Strait region are shown in Figures 5.15 and 5.16.

Figure 5.17 on page 91 is showing as an example for a fall and a winter period the ice thickness error ε_I for periods 3a and 3b as calculated with equation 5.9 on page 83. The error distributions of the other periods look similar. Table 5.3 on page 91 gives an overview of the mean ice thickness in the Fram Strait region and the mean error of the ice thickness for all nine used ICESat periods. Only grid cells with an ice thickness $> 10\,\mathrm{cm}$ are used for these statistics. A mean ice thickness uncertainty of 43 cm is estimated. Additionally also the median and mode of the ice thickness distribution in the Fram Strait region is given. The mean and modal ice thickness are mostly 10 cm to 20 cm higher than the mean thickness, as the ice thickness distribution is not Gaussian but containing a larger fraction of small ice thicknesses ($< 50\,\mathrm{cm}$) shifting the mean thickness to lower values. The general distribution of ice thickness in the Fram Strait region for all periods consists of thicker ice ($> 3\,\mathrm{m}$) north of Greenland and in the EGC.

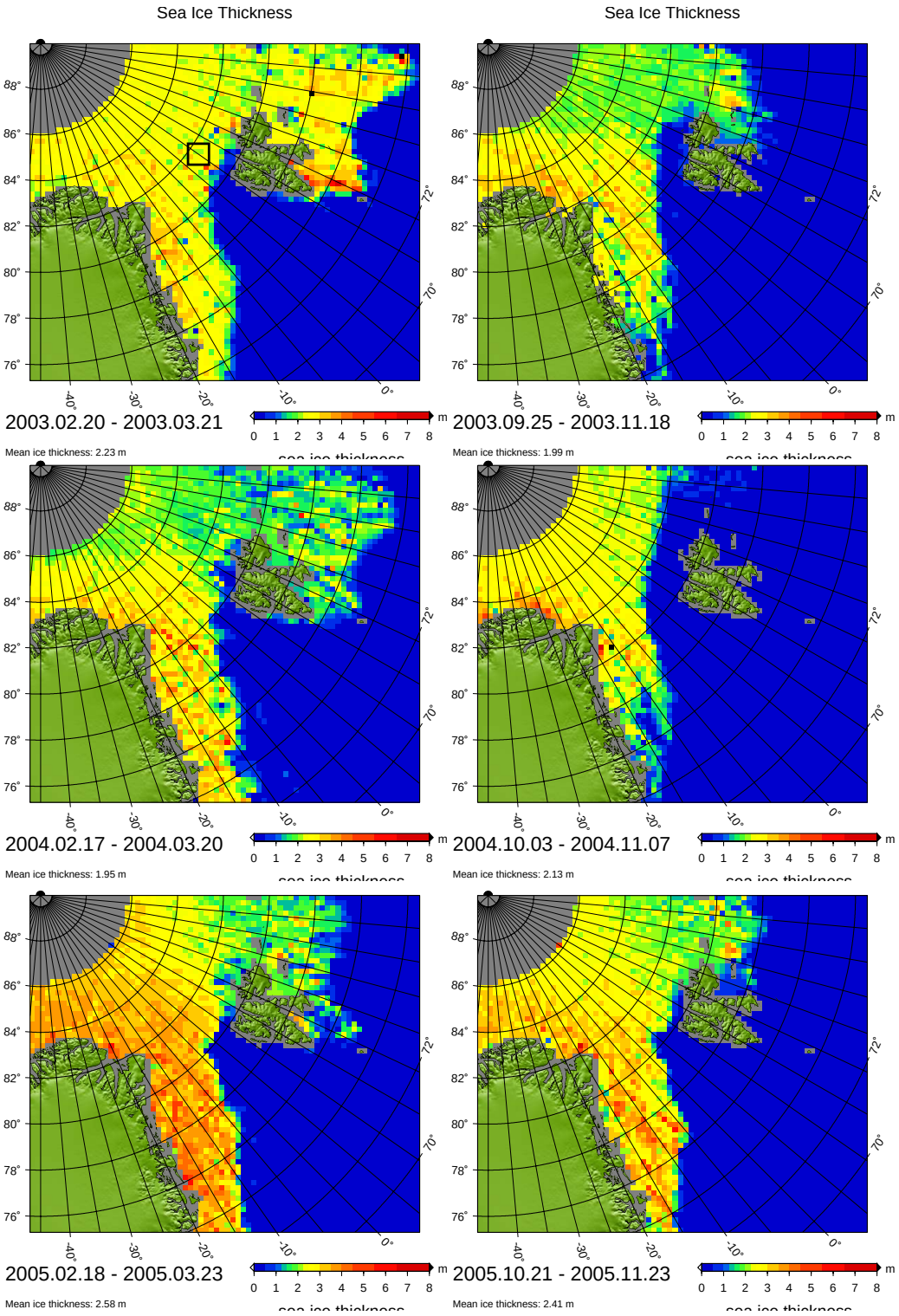

Figure 5.15: Sea ice thickness for ICESat periods 1 (top-left), 2a (top-right), 2b (middle-left), 3a (middle-right), 3b (bottom-left), and 3d (bottom-right). Continued in Figure 5.16.

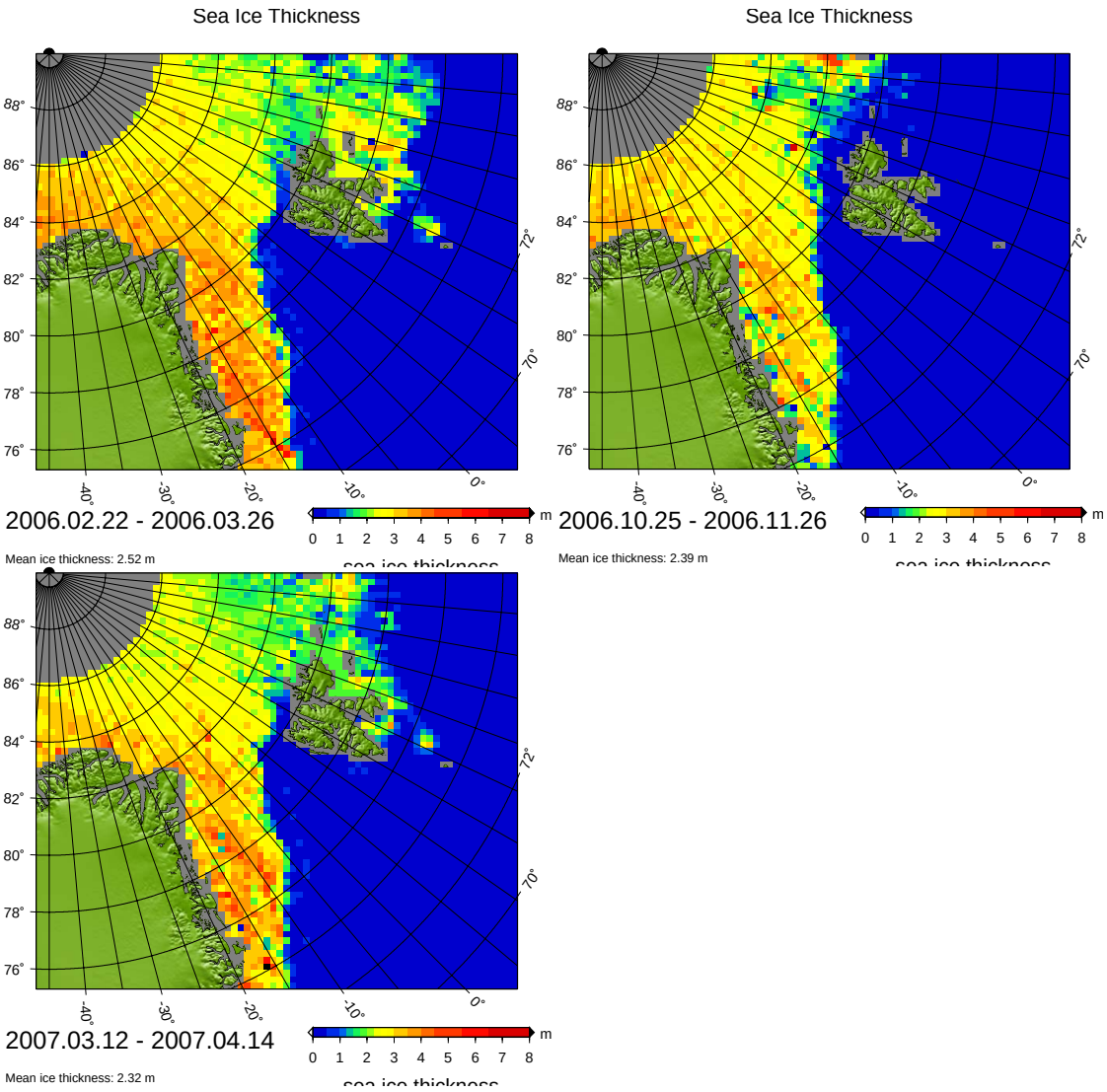

Figure 5.16: Continuation of Figure 5.15. Sea ice thickness maps for ICESat periods 3e (top-left), 3g (top-right), and 3h (bottom-left). Start and end dates of periods are given below each subfigure. Grey areas denote missing data around land or above 86°N.

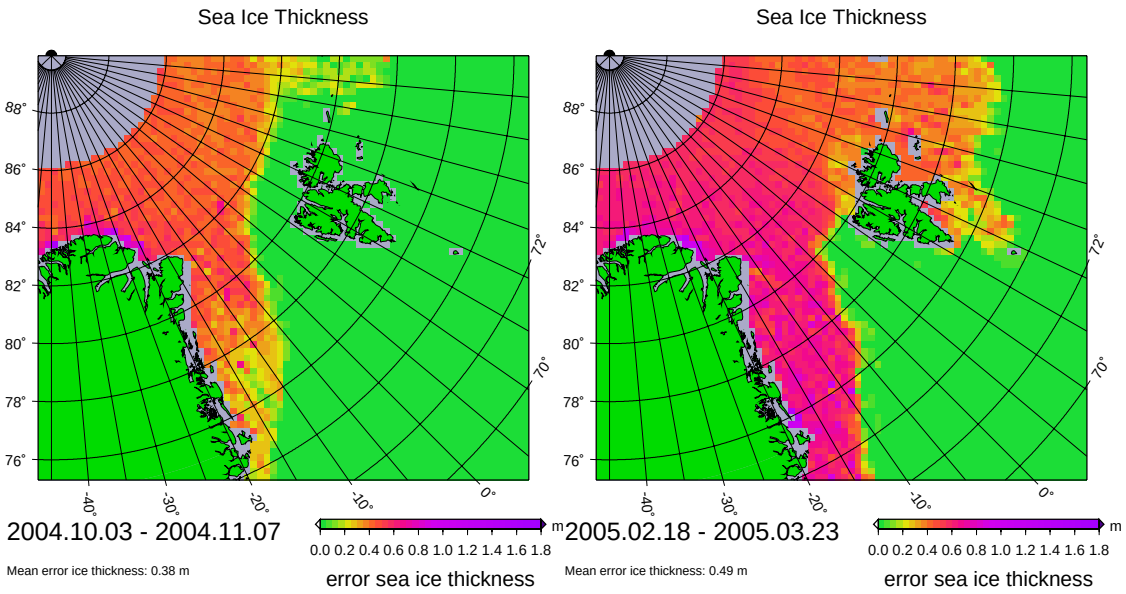

Figure 5.17: Maps of the sea ice thickness error estimate per grid cell for ICESat periods 3a (2004-10-03—2004-11-07, left) and 3b (2005-02-18—2005-03-23, right). Respective maps for the other periods look similar.

Table 5.3: Mean sea ice thickness (column 3), thickness error estimate (column 4), median (column 5) and modal (column 6) sea ice thickness in the Fram Strait region for all used ICESat periods. Column 1 and 2 give the ICESat period name and dates, respectively. Only grid cells with ice thickness > 10 cm are counted. The modal thickness is calculated for 20 cm ice thickness bins.

Period	Dates	Mean Thick.	Error Estim.	Median Thick	Modal Thick.
1	Feb/Mar 2003	2.23 m	0.43 m	2.45 m	2.4 m
2a	Oct/Nov 2003	1.99 m	0.36 m	2.07 m	2.0 m
2b	Feb/Mar 2004	1.95 m	0.41 m	2.00 m	1.8 m
3a	Oct/Nov 2004	2.13 m	0.38 m	2.38 m	2.4 m
3b	Feb/Mar 2005	2.58 m	0.49 m	2.80 m	3.0 m
3d	Oct/Nov 2005	2.41 m	0.43 m	2.54 m	2.4 m
3e	Feb/Mar 2006	2.52 m	0.48 m	2.66 m	2.6 m
3g	Oct/Nov 2006	2.39 m	0.42 m	2.64 m	2.8 m
3h	Mar/Apr 2007	2.32 m	0.45 m	2.40 m	2.2 m
Total Mean		2.28 m	0.43 m	2.44 m	2.4 m

North of Svalbard and in the Barents Sea thinner ice ($< 2\,\mathrm{m}$) is prevailing. But for single periods this general picture can be different. For period 1 in Feb./Mar. 2003, a lot of thick ice can be found in the Barents Sea and almost no west–east gradient in ice thickness can be found as for the other periods. That thick ice existed in the Barents Sea during that period is confirmed by observations from aboard R/V Polarstern during expedition ARK-XIX (*ARKTIS-XIX/1 and XIX/2 science team*, 2004; *Lieser*, 2005). Also in period 3e in Feb./Mar. 2006 some thick ice prevailed in the Barents Sea. In period 3b in Feb./Mar. 2005 the ice, with ice thicknesses above 4 m, is exceptionally thick in the EGC, causing a strong West-East ice thickness gradient. All these examples show the variable nature of the ice thickness, highlighting the importance of its continuous measurement. As later will be seen most of the variability can be attributed to dynamic rather than to thermodynamic causes.

5.2.4 Comparison to Ice Thickness From Helicopter-Borne EM-Sounding

Sea ice thickness is the parameter with the largest uncertainty in this study. We do not have any simultaneous sea ice thickness measurements, which could be used for evaluation, but as mentioned above the R/V Polarstern was in the Fram Strait region one month after ICESat period 1. The mean ice thickness measured between 4 and 19 April 2003 by helicopter-borne EM-sounding (*Haas*, 2004b, 2002) during the expedition in the region marked with a black square in Figure 5.15 on page 89, upper left, was $(2.3 \pm 0.4)\,\mathrm{m}$ (*Lieser*, 2005). Our mean ice thickness estimate from about one month before in that region is $(2.5 \pm 0.3)\,\mathrm{m}$, i.e. both measurements match within the one standard deviation interval. However, the time difference between the data sets of about one month, and the fact that the EM-sounding and the ICESat measurements both cover only a small subsection of the black square in Figure 5.15 can lead to a difference for the ice thickness. We also note, that on average 200–500 single ICESat measurements contribute to the ice thickness in each grid cell in that region, which corresponds to only two to four ICESat overpasses during ICESat period 1. Taking this these natural differences between the two measurements into account the agreement between the two measurements is very good. This is giving confidence in our ice thickness retrieval. Nevertheless, ideally one would combine simultaneous ICESat measurements and EM-sounding. No such coincident dataset exist, and to analyze the quality of the ice thickness results quantifiable, more evaluation datasets are needed. But together with the good agreement found between freeboard heights and SAR data in Section 5.1.3 it can be stated that the ICESat ice thickness retrieval works within the given error estimates.

5.3 Sea Ice Thickness Conclusion

- A method to retrieve sea ice freeboard heights in the Arctic from ICESat GLAS laser altimeter measurements was developed.

- The ICESat surface elevation measurements are accurate within a few centimeters. Key problem is the correct determination of the SSH. The best available geoid, ArcGP, is used. The Inverse Barometer Effect and tides are corrected for. The

remaining uncertainties in the SSH are reduced using an adaptive fit to the lowest elevations as SSH reference points.

- Comparison to SAR radar backscatter data show that leads with open water or thin ice are correctly identified in the freeboard data.
- Freeboard heights are converted to ice thickness by using a monthly snow climatology and in situ measurements for the snow depth. Regarding the sea ice density two different density values for multi-year and first-year ice are used. The multi-year and first-year ice classes were separated using QuikSCAT data.
- Mean sea ice thickness maps of the Fram Strait region for nine ICESat measurement periods between 2003 and 2007 were presented.

Chapter 6

Sea Ice Volume Flux: Determination and Physical Interpretation

The ultimate goal of this study is to obtain the sea ice volume flux from satellite measurements. To obtain an estimate of the sea ice volume flux we use all the above information. In the first part of this chapter (Sections 6.1–6.2) the three quantities sea ice concentration (Chapter 3), sea ice drift (Chapter 4), and sea ice thickness (Chapter 5) are combined to obtain the sea ice volume flux. These quantities are exclusively derived from satellite data. Other information from in situ and air-borne sources are only used indirectly, e.g., as geoid model and in form of a prior information on sea ice density and as snow depth and density. Figure 6.1 summarizes the data flow, the involved quantities, and satellite sensors used in a schematic flow diagram.

In the second part of this chapter (Sections 6.3–6.7) the ice volume flux through Fram Strait are calculated and the results are interpreted in respect to model and oceanographic data.

6.1 Sea Ice Volume Flux Calculation

The sea ice thickness calculated in Chapter 5 is the mean thickness for every 25 km×25 km grid cell (see Section 2.2.5 on page 25) including the open water fraction in every grid cell. This was achieved by multiplying the freeboard height F with the ice concentration C (see equation 5.7 on page 83). To get the absolute ice volume flow out of one grid cell the ice thickness I has to be multiplied with the grid size G of 25 km and the absolute value of the sea ice drift D for the respective cell:

$$V = I\,G\,D\,. \tag{6.1}$$

The vectorial x and y components of the volume flux can be calculated accordingly using the respective x and y drift values as the grid size is the same in x- and y-direction.

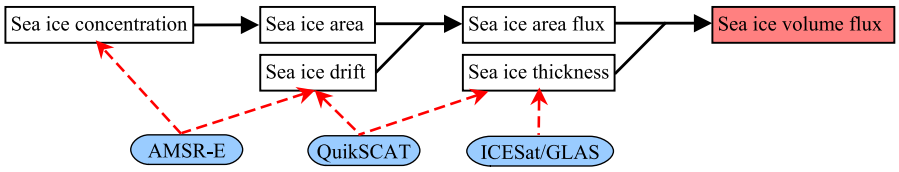

Figure 6.1: Schematic flow diagram of quantities (black boxes) and satellite sensors (blue ovals) involved in the estimation of the sea ice volume flux.

As explained in Chapter 4 two different sea ice drift datasets are used. First, the sea ice volume flux is calculated using the AMSR-E 89 GHz sea ice drift data (*Ezraty et al.*, 2007a) as this drift data is available for all used ICESat periods. For three ICESat periods the duration of the period had to be slightly altered, as AMSR-E drift data were not available for the complete period: ICESat period 2a changed to 2003-09-29 – 2003-11-18 (complete period: 2003-09-25 – 2003-11-18), period 3a to 2004-10-03 – 2004-11-01 (complete period: 2004-10-03 – 2004-11-07), and period 3g to 2006-10-25 – 2006-11-22 (complete period: 2006-10-25 – 2006-11-26). For these three periods the ice volume flux is calculated for the above given time spans. Accordingly also the mean sea ice thickness datasets had to be adapted to the new time length on these three periods. The sea ice thickness shown in Figures 5.15 and 5.16 on page 90 for periods 2a, 3a, and 3g are exchanged with the very similar thicknesses for the new periods with adjusted time spans shown in Figures A.5, A.6, and A.7 in Appendix A.3 on page 145. The mean ice thicknesses given in Table 5.3 on page 91 changed to 2.03 m for period 2a (complete period: 1.99 m), 2.16 m for period 3a (complete period: 2.13 m), and 2.19 m for period 3g (complete period: 2.15 m). The error estimates given in Table 5.3 did not change significantly. For all other ICESat periods the full period time spans are used for the volume flux calculation. But there are 36 days during different ICESat periods where due to data errors no AMSR-E ice drift is available. They are summarized in Table A.2 on page 140 in Appendix A.1. The actual dates for all sea ice volume flux periods can be found in Table 6.1 on page 100. As the length of all periods is different and in particular does not cover a complete calendar month all volume flux estimates are referred to a day. All fluxes calculated are the mean daily volume flux during the accordant time period and given in km^3/day or additional for comparison in Sverdrup ($1\,Sv = 10^6\,m^3/s = 86.4\,km^3$/day). Note that Sverdrup as it is used here is taken as volume measurement and ice flux values are not referenced to ocean water of a certain density and thus are not directly comparable to ocean freshwater fluxes.

The spatial distribution, mean amount and direction of the sea ice volume flux in the Fram Strait region estimated with equation 6.1 on the preceding page using the AMSR-E drift is shown in Figures 6.2 and 6.3 for all nine ICESat periods. Figure 6.4 on page 99 shows an example of a fall (period 3a) and a winter (period 3b) period's ice volume flux error ε_V. These two periods are also reflecting a period with low (3a) and high (3b) error estimates (see Table 6.1 on page 100). The error distributions of the other periods look similar. In general, the error estimate amounts to approximately one quarter of the value of the volume flux. But errors are higher in the Fram Strait region and EGC. The respective error maps for the ice thickness are shown in Figure 5.17 on page 91. The volume flux errors are calculated by error propagation from equation 6.1 on the preceding page with

$$\varepsilon_V = G\sqrt{I^2\varepsilon_D^2 + D^2\varepsilon_I^2}\,. \tag{6.2}$$

For the ice thickness the error ε_I from equation 5.9 on page 83 is used. *Ezraty et al.* (2007a) state that the uncertainty in ice drift speed D is 2.6 cm/s (2.2 km/day). However, this is the mean drift error for the complete Arctic derived by comparison to IABP buoy drift speeds. *Haarpaintner* (2006) stated that the ice drift error is larger in dynamic regions such as Fram Strait. Therefore we doubled the single measurement ice drift error to $\varepsilon_{D_n} = 4.4$ km/day. For the the mean ice drift error ε_D of an ICESat period this leads

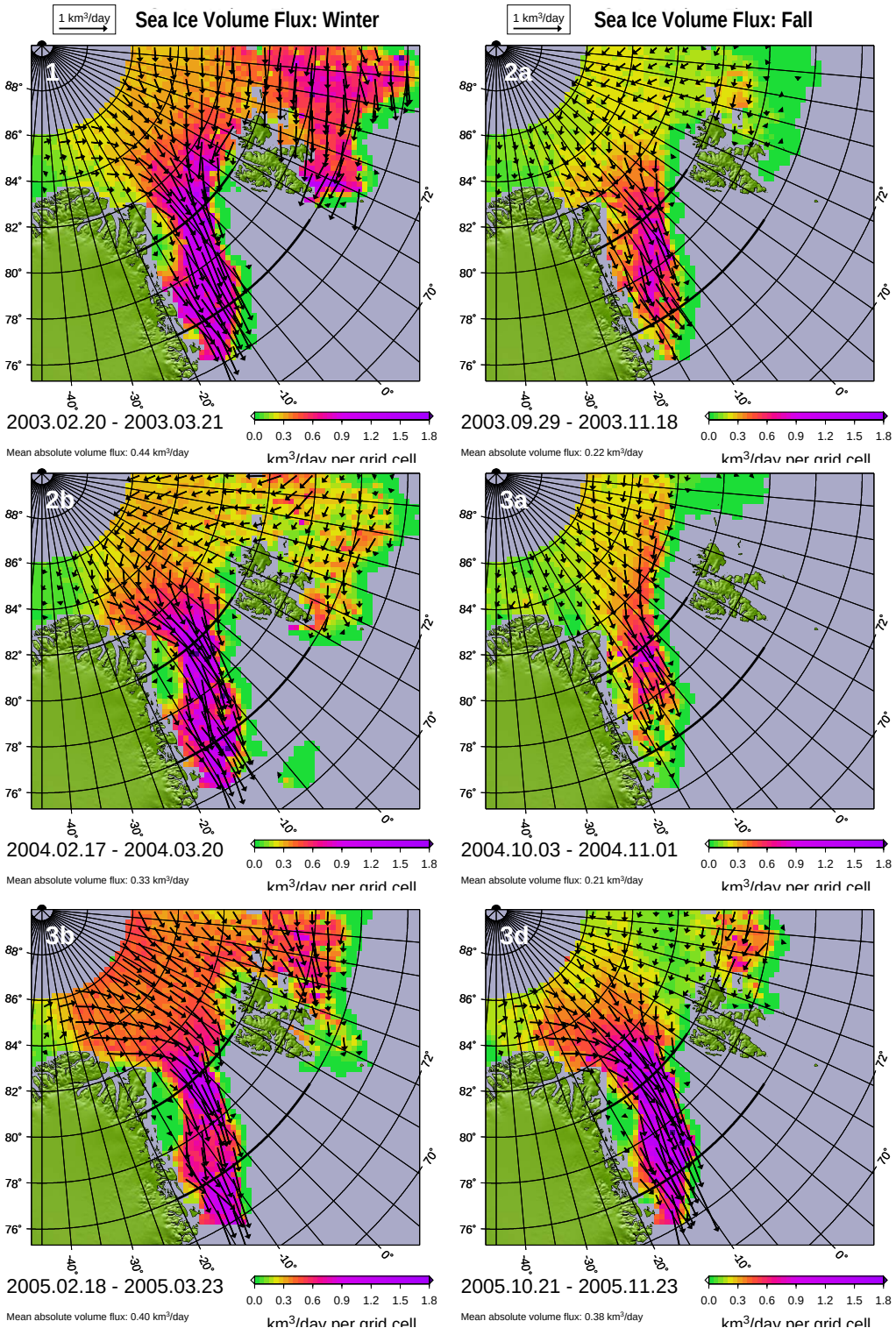

Figure 6.2: Sea ice volume flux in the Fram Strait region for ICESat periods 1 (top-left), 2a (top-right), 2b (middle-left), 3a (middle-right), 3b (bottom-left), and 3d (bottom-right). For full caption and continuation see Figure 6.3.

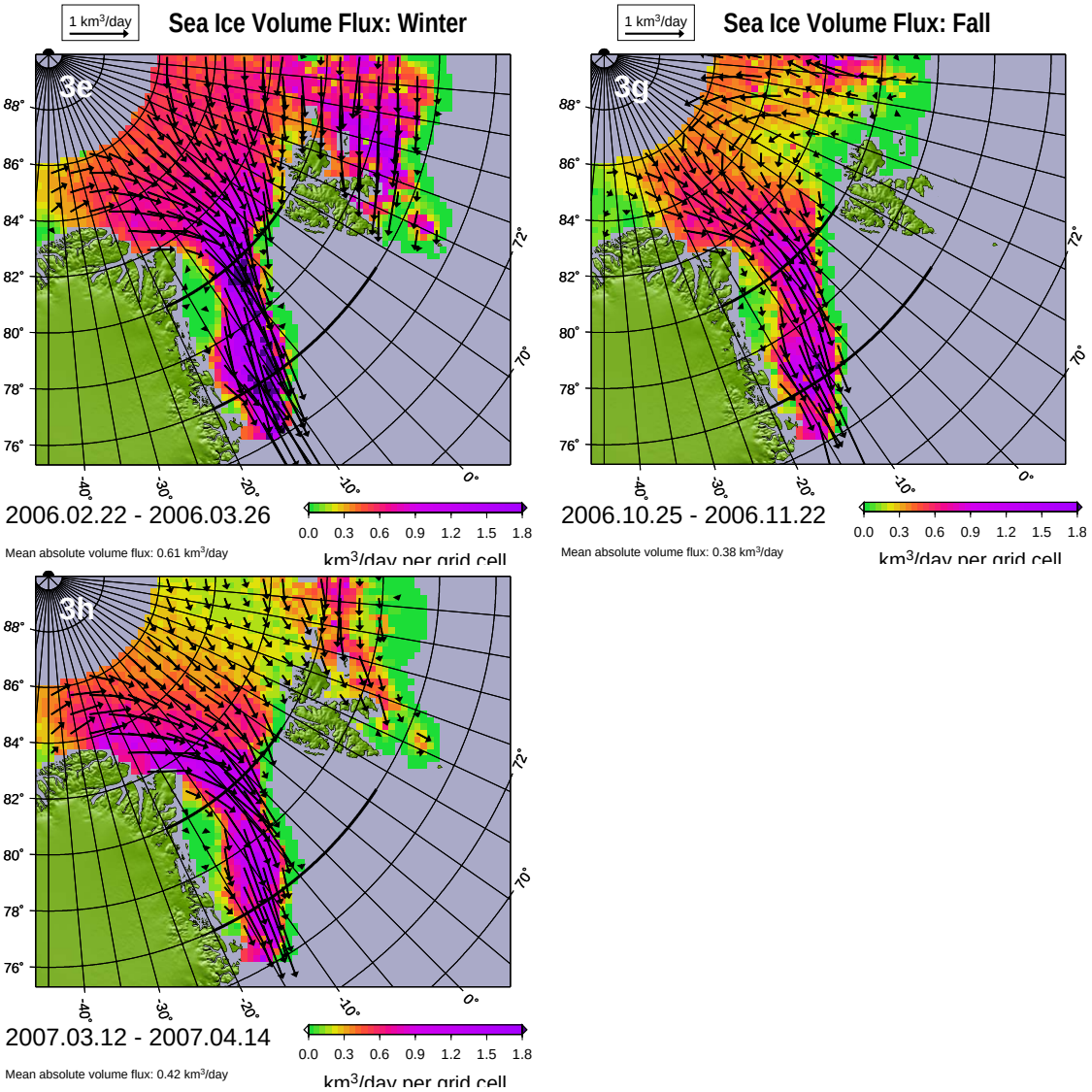

Figure 6.3: Continuation of Figure 6.2. Sea ice volume flux maps for ICESat periods 3e (top-left), 3g (top-right), and 3h (bottom-left). Start and end dates of periods are given below each subfigure. Grey areas denote either missing data around land, south of 74°N or north of 86°N, or open ocean without ice. The absolute volume flux out of each grid cell is colorcoded and given by the length of the black vectors, which also indicate the volume flux direction. Flux vectors are drawn for every third grid cell. Grid size is 25 km. The black lines indicate the transects at 80°N and 76°N used for the Fram Strait volume flux estimates in Figures 6.6, 6.7, and Table 6.2.

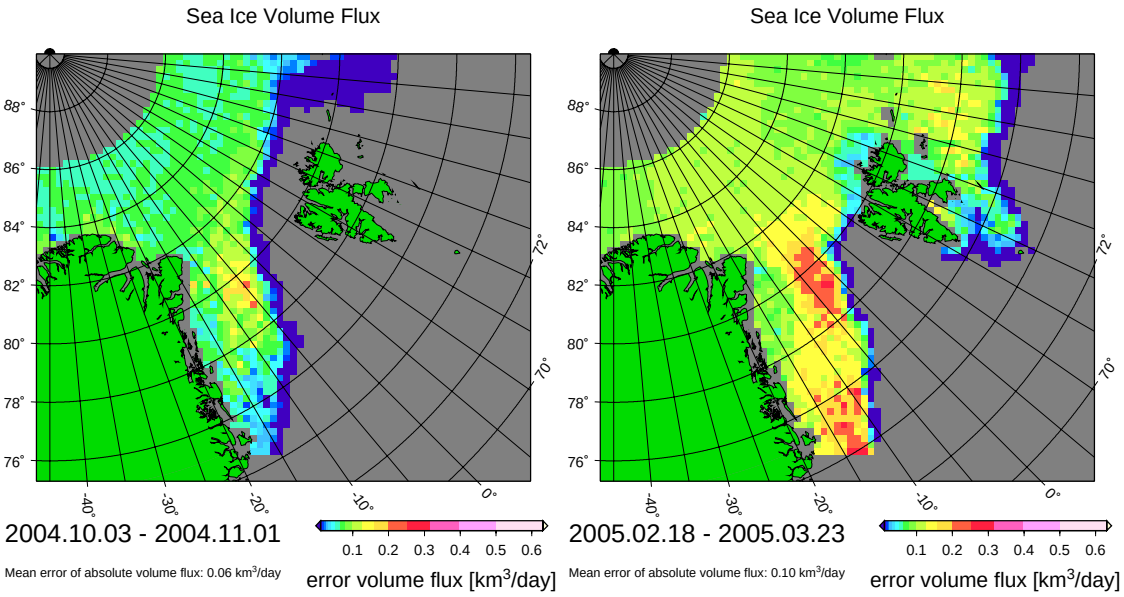

Figure 6.4: Maps of the sea ice volume flux error estimate per grid cell for ICESat periods 3a (2004-10-03—2004-11-01, left) and 3b (2005-02-18—2005-03-23, right). The left map is showing a low volume flux error case, while the right is showing a high volume flux error case. Error maps for the ice thickness of the same periods are shown in Figure 5.17. The error distribution for the other periods look similar, the mean error for all periods is given in Table 6.1.

to

$$\varepsilon_D = \frac{\varepsilon_{D_n}}{\sqrt{n}} \,,$$

with n being the number of valid ice drift datasets in every grid cell during the ICESat period. ε_D is in the order of about 0.8 km/day. The error ε_C of the ice concentration is already included in the ice thickness calculation (see equation 5.7 on page 83). Table 6.1 on the next page summarizes the mean ice volume flux and mean error of the ice volume flux for all nine used ICESat periods.

6.2 Sea Ice Volume Flux Discussion

Figures 6.2 and 6.3 show that the spatial distribution of the sea ice volume flux can be retrieved exclusively from satellite remote sensing data. The provided result demonstrates how new geophysical parameters can be derived by combining several remote sensing datasets. To recapitulate, the following satellites and sensors were used to achieve this goal (see also Figure 6.1 on page 95): sea ice area and drift were derived from 89 GHz AMSR-E data flying on NASA's Aqua satellite. Sea ice thickness is derived from GLAS data on ICESat in combination with multi-year sea ice concentrations obtained from SeaWinds measurements from QuikSCAT to distinguish ice with two different densities. A short description of these sensors and satellites was provided in Section 2.2 on page 17.

The maps in Figures 6.2 and 6.3 represent the amount and direction of the mean daily

Table 6.1: Mean absolute sea ice volume flux and its error estimate per grid cell in the Fram Strait region for all used ICESat periods. (Only ice covered grid cells are counted.)

Period	Dates	Mean Absolute Volume Flux	Mean Error Estimate
1	20.02–21.03.2003	$0.44\,km^3/day$	$0.10\,km^3/day$
2a	29.09–18.11.2003	$0.22\,km^3/day$	$0.05\,km^3/day$
2b	17.02–20.03.2004	$0.33\,km^3/day$	$0.08\,km^3/day$
3a	03.10–01.11.2004	$0.21\,km^3/day$	$0.06\,km^3/day$
3b	18.02–23.03.2005	$0.40\,km^3/day$	$0.10\,km^3/day$
3d	21.10–23.11.2005	$0.38\,km^3/day$	$0.09\,km^3/day$
3e	22.02–26.03.2006	$0.61\,km^3/day$	$0.13\,km^3/day$
3g	25.10–22.11.2006	$0.38\,km^3/day$	$0.09\,km^3/day$
3h	12.03–14.04.2007	$0.42\,km^3/day$	$0.10\,km^3/day$
Total Mean		$0.38\,km^3/day$	$0.09\,km^3/day$

outflow of ice volume out of each 25 km grid cell during the measurement period given below each map. Inflow from neighboring grid cells is not considered. The figure clearly exhibit that the ice volume flux through Fram Strait is not evenly distributed in space, but strongly confined to a small band toward its western portion. Near the north-east corner of Greenland the North East Water polynya covered with thin ice or open water is located. Attached to the south along the Greenland coast a region with thick land-fast ice prevails. Accordingly, the ice motion and volume flux in this region tend to be negligible. However, east of this region during all periods the volume flux reaches its highest values, coincident with the East Greenland Current (EGC) axis which supports the transport of thick multi-year ice from the Fram Strait southward. Further eastward the flux values decline towards the open water area. Moreover, also the source regions for the Fram Strait ice transport can be identified.

Two different ice flux regimes can be identified from Figures 6.2 and 6.3 during the nine periods:

1. An east to west ice drift regime north of Svalbard which then turns south-westward north of Fram Strait. This regime can be observed during periods 2a, 2b, 3g, and a bit less pronounced also during period 3a. The ice in Fram Strait is then dominantly originating from the Barents Sea and the transpolar drift with smaller ice thicknesses (see Figures 5.15 and 5.16 on page 90). For identical ice drift velocities this would result in a lower ice volume flux. And indeed, the ice volume flux for the mentioned periods is comparatively small for the respective season. For period 3g, which has the highest volume flux of these periods, also a strong branch of ice flux from north of Greenland with thicker ice can be identified.

2. The second flux pattern originats from north of Greenland and then bends southward through Fram Strait. Periods 3b, 3d and most impressively 3h are examples for this drift regime. Due to the thicker ice north of Greenland this drift regime favors higher ice volume fluxes. Nevertheless, most (90% according to model results from *Thomas et al.* (1996)) of the variability of the Fram Strait sea ice outflow can

be attributed to ice velocity variations and not to ice thickness changes. Therefore, the ice source region plays only a minor role in comparison to the general ice velocity profile across Fram Strait for the ice volume flux amount.

The high ice volume flux variability can also already be seen in the volume flux maps with the mean ice volume flux in fall 2004 (period 3a) being only one third of the mean volume flux during winter 2006 (period 3e) (see also Table 6.1). In general, the ice volume flux is smaller during the fall periods (right column in Figures 6.2 and 6.3) than during the preceding winter periods (left column in Figures 6.2 and 6.3). This can be explained by (1) higher drift velocities (= stronger atmospheric forcing) during the winter February/March periods and (2) by thinner ice thickness caused by melting during the summer months. But there are exceptions like the fall period 3d in 2005 (Figure 6.2, bottom right), when an extraordinary high ice transport occurred through Fram Strait.

In the Barents Sea the sea ice volume flux situation is much more variable than in the Greenland Sea. Common for all periods is that the ice flux has a east to west component. Thus, during the winter periods ice is flowing south of Svalbard from the Barents to the Greenland Sea. The amount of this flux is very variable. While in 2003 during period 1 the ice volume flux between Barents and Greenland Sea was extraordinary large, during the winter periods 2b, 3b, and 3h only little ice volume was transported to the Greenland Sea. Only period 3e showed again an enhanced ice exchange between the two seas. The exchange of ice with the Arctic Ocean via the Svalbard to Franz Josef Land passage is even more variable, as even the sign of the ice volume flux is changing from period to period. During periods 2a, 2b, and 3g ice is exported out of the Barents Sea to the Arctic Ocean and during periods 3b and 3h ice is imported to the Barents Sea. During the remaining periods the ice exchange is more or less neutral, as the ice flux is oriented mainly in east to west direction and only small amounts of ice are exchanged between the Arctic Ocean and the Barents Sea.

The small, one grid cell wide strip of near zero sea ice volume flux (green color in Figures 6.2 and 6.3) along the ice edge is caused by the low ice concentrations in the MIZ. The sea ice volume flux is calculated and interpolated for all grid cells where the ice concentration is not zero and measurements of ice thickness and ice drift are not more than 100 km corresponding to 4 grid cells away. Due to missing ice drift data from AMSR-E the sea ice volume flux in the EGC south of 74°N can not be calculated anymore and is showing up as missing data (grey area) in Figures 6.2 and 6.3.

6.3 Divergence of Sea Ice Volume Flux

To gain further insight into the dynamic processes and quality of the sea ice volume flux vector field the divergence $\nabla \cdot \vec{V}$ of this field is calculated. The derivative of the volume flux field $\vec{V}$ in x and y direction is calculated by use of the Sobel operator $\frac{1}{8}\begin{bmatrix} 1 & 0 & -1 \\ 2 & 0 & -2 \\ 1 & 0 & -1 \end{bmatrix}$ (Chap. 12 in *Jähne*, 2002). The Sobel operator is convoluted with the x and y component

V_x and V_y of the volume flux field to calculate the divergence field

$$\nabla \cdot \vec{V} = \frac{1}{8G} \begin{bmatrix} 1 & 0 & -1 \\ 2 & 0 & -2 \\ 1 & 0 & -1 \end{bmatrix} * V_x + \frac{1}{8G} \begin{bmatrix} 1 & 2 & 1 \\ 0 & 0 & 0 \\ -1 & -2 & -1 \end{bmatrix} * V_y.$$

G is the grid distances in x and y direction of 25 km, and $*$ is the convolution operator. The Sobel operator smoothes the field perpendicular to the derivation direction. The resulting divergence maps for all nine ICESat periods are shown in Figure 6.5.

In Figure 6.5 changing divergence or convergence patterns can be identified. On short time scales the ice volume is conserved, neglecting deformation processes. Sources or sinks in the volume flux field can only be caused by time dependent dynamic processes during the time span of the considered period, i.e. (a) thermodynamical growth or melting of sea ice, and (b) redistribution of the ice volume during that time span. Inflow and outflow at the borders of the map and from north of 86°N to the south are not considered here. Additionally, inaccuracies in the ice volume flux field might cause spurious divergence/convergence patterns.

The divergence maps in Figure 6.5 have in common that for all periods divergence patterns occur in the Greenland Sea along the ice edge. They are more pronounced during the winter periods 1, 2b, 3b, 3e, and 3h (red annotation) than during the fall periods (white annotation). This divergent zone along the ice edge is often interrupted by smaller convergent zones, causing an oscillating divergent-convergent appearance. This phenomenon is most pronounced during periods 1, 2b, 3d, and 3e. Another maximum of both convergence and divergence patterns often occurs in the Barents Sea, e.g. during periods 1, 3b, and 3e. Also for all periods the absolute amount of divergence is decreasing towards North. These patterns can have different origins:

The Greenland Sea and Barents Sea are the most dynamic sea ice areas of the study region: (1) Cyclones pass the ice edge and redistribute the ice. The sequence of divergent and convergent zones along the ice edge are likely imprints of cyclones passing along the ice edge. On the front side of the cyclone the ice movement is accelerated causing a divergent ice flux and behind the cyclone the ice is getting compressed causing a convergent ice flux regime. The number of divergent-convergent oscillations should give the number of large cyclones passing by the ice edge during the observation period and the amount of divergence and convergence should be correlated with their strength and how far they passed the ice edge. Also changes in the ice thickness influence the divergent and convergent volume flux zones. When the ice is getting compressed, it starts to raft and builds ridges, which is increasing the ice thickness. This would counteract the divergent and convergent patterns caused by the ice drift. But due to the sparse data coverage in time and space of the ICESat measurements these processes can not be resolved with the ice thickness data and therefore are not reflected in the ice volume flux measurements. (2) Ice growth rates are highest in the Greenland and Barents Sea. In the MIZ more open water areas are exposed to the cold atmosphere, causing ice growth. Ice growth is much faster for thin than for thick ice. Therefore, ice growth rates in the MIZ are much higher than in the thick, solid ice pack in the Arctic Ocean. Because of these two processes the observed stronger divergence/convergence zones are in accordance with expectations.

Most pronounced in Figure 6.5 is a zone of high divergence along the ice edge in the Greenland Sea. It can be observed in all ICESat periods and is not completely

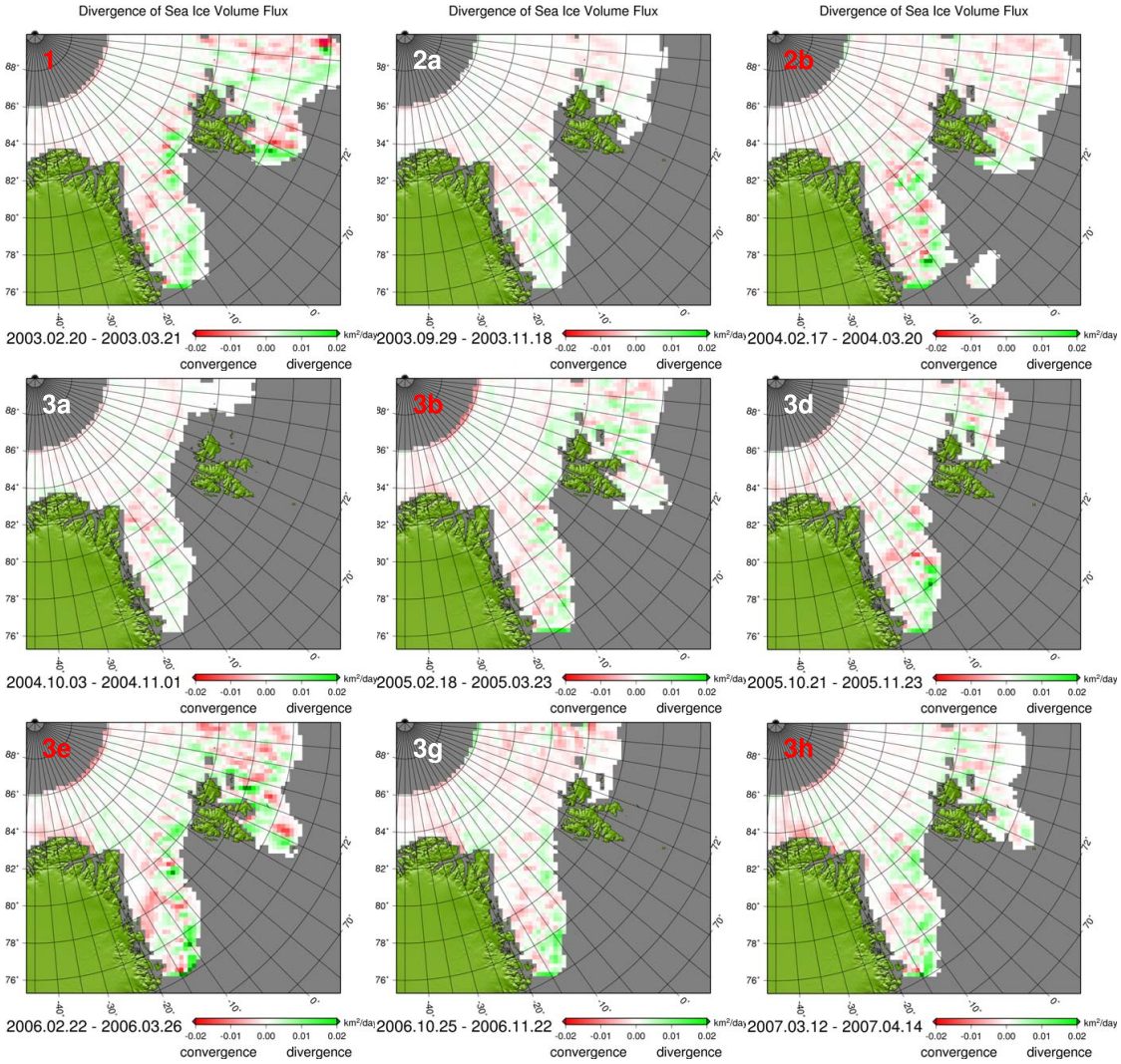

Figure 6.5: Maps of divergence of sea ice volume flux for all 9 ICESat periods shown in Figures 6.2 and 6.3. The period names are given at the top left corner of every map in red for winter periods and white for fall periods. The time span of each period is given below each map. Divergent regions are shown in green and convergent regions in red.

balanced by surrounding convergent zones: the divergence in general is higher than the convergence in the Greenland Sea. This suggests that sea ice is exported from the compact ice cover in the EGC to the open Greenland Sea, where it diverges and melts. If sea ice becomes detached from the compact ice cover in the MIZ it gets lost for the volume flux observation, as only ice covered regions with ice concentrations higher than 30% are considered for the ice thickness measurements (see Chapter 5). Therefore, regions of high divergence near the ice edge, which are not directly matched by nearby convergent zones, can be identified as sources for ice loss to the open ocean. During the observed time periods this ice loss in general is higher during winter than during fall. This can be caused by stronger atmospheric forcing along the ice edge, e.g. through more frequent and stronger cyclones (*Brümmer et al.*, 2000). Also, ice growth contributes to the divergence zones along the ice edge, but to a lesser extent.

Strong melting, which cause a significant reduction of the sea ice thickness, should not have occurred during our about one month long winter and fall measurement periods. Therefore, convergent zones are caused by redistribution of sea ice during the measurement period and should be compensated by divergent zones elsewhere. Indeed, eight of the nine periods show a mean positive divergence in the study region and only the fall period 3g has a slight mean negative divergence of $-0.1 \cdot 10^{-3}\,\mathrm{km}^2/\mathrm{day}$, which can be explained by convergence patterns along the eastern border of our study region. The total mean divergence of all nine periods is $(0.18 \pm 0.16) \cdot 10^{-3}\,\mathrm{km}^2/\mathrm{day}$. And in accordance with the above found higher divergence during winter in the Greenland Sea, also the mean divergence of the winter periods is with $(0.26 \pm 0.14) \cdot 10^{-3}\,\mathrm{km}^2/\mathrm{day}$ much higher than for the fall periods with $(0.07 \pm 0.12) \cdot 10^{-3}\,\mathrm{km}^2/\mathrm{day}$. Therefore, no larger scale sea ice melting can be observed during our measurement periods.

6.4 Fram Strait Sea Ice Volume Flux

The Fram Strait is the main outflow pathway for sea ice out of the Arctic Ocean. Approximately 10% of the overall Arctic sea ice is exported via Fram Strait with a mean amount of approximately $2500\,\mathrm{km}^3$/year (80 mSv) (*Kwok et al.*, 2004a; *Vinje et al.*, 1998; *Dickson et al.*, 2007). The outflows at the other existing pathways of the Arctic are one magnitude smaller ($\sim 130\,\mathrm{km}^3$/yr Nares Strait outflow; 220 to $870\,\mathrm{km}^3$/yr Davis Strait outflow (including Nares Strait), but quite uncertain (*Kwok*, 2005); $40\,\mathrm{km}^3$ Barents Sea mean winter (Oct.–Mar.) outflow, but with very high annual variability ($-280\,\mathrm{km}^3$ to $340\,\mathrm{km}^3$ (*Kwok et al.*, 2005); $-130\,\mathrm{km}^3$/yr Bering Strait inflow to the Arctic Ocean (*Woodgate and Aagaard*, 2005)). Model studies suggest that at least half of the sea ice entering the Greenland Sea through Fram Strait is melting there, the rest is exported through Denmark Strait into the Irminger Sea and is melting there (*Karcher et al.*, 2005). The exact amount of sea ice exported through Denmark Strait is fairly unknown.

6.4.1 Fram Strait Sea Ice Volume Flux for ICESat periods 2003–2007

For recent years no Fram Strait sea ice volume flux estimates from measurements exist. Here the meridional ice volume flux across transects at 80°N and 76°N latitude are calculated for the nine ICESat measurement periods used in this analysis. In Section 6.4.2 this is extended to a monthly winter (October to April) time series between January

2003 and April 2007. The two shown transects at 80°and 76°N are marked in Figures 6.2 and 6.3 on page 98 with thick black lines. Both transects start at 20°W and end at 12°E. While the 80°N transect is situated at Fram Strait smallest width, 76°N is the lowest latitude, where suitable ice drift and ice thickness measurements are available. Further south the ICESat data coverage gets sparse. Nevertheless, one has to keep in mind that already at 76°N the data coverage for ice drift and ice thickness is much worse than at 80°N (e.g. Figure 5.12 on page 82 and Chapter 4). Consequently, ice volume flux estimates at 76°N rely on only few data points requiring a considerable amount of interpolation and thus causing an unknown but probably higher error.

The meridional sea ice volume flux through the transects is calculated by averaging the ice volume flux data of three grid cells around the latitudes of the transects (approximately one north, one at the latitude and one south). The length l_m of the accordant grid cell perpendicular to the meridional flux is calculated by

$$\begin{aligned} l_m &= G/\cos(\lambda + 45^\circ) && \text{for} \quad \lambda \leq 0^\circ \\ l_m &= G/\sin(\lambda + 45^\circ) && \text{for} \quad \lambda > 0^\circ \,. \end{aligned}$$

G is the grid cell size of 25 km for the volume flux maps and λ denotes the longitude of the respective grid cell. The value of +45° is caused by the 45° rotation of the map grid used with respect to the zero meridian (see Section 2.2.5 on page 25). The meridional volume flux V_v is then calculated following equation 6.1 on page 95 by

$$\begin{aligned} V_v &= I\, l_m\, (\sin(\lambda + 45^\circ) D_x - \cos(\lambda + 45^\circ) D_y) \,. \\ V_v &= I\, l_m\, D_v \end{aligned}$$

I is the ice thickness and D_x and D_y are the x and y components of the ice drift in the used grid. Southward fluxes into the Greenland Sea are counted positive here. And accordant to equation 6.2 on page 96 the error of V_v is given as

$$\varepsilon_{V_v} = \sqrt{(I\, l_m)^2\, \varepsilon_D^2 + (D_v\, l_m)^2\, \varepsilon_I^2} \,. \tag{6.3}$$

Figure 6.6 on the next page shows the meridional ice volume flux distribution along both transects for the nine used ICESat periods. The top panel shows the transect at 80°N and the bottom panel the one at 76°N. In Figure A.8 on page 147 in Appendix A.4 the same transects are shown separately for each ICESat measurement period together with the estimated error bars. First thing to recognize in Figure 6.6 on the next page is that the longitude range of maximum ice transport stays almost constant throughout the years. The volume flux rises at about −10°E at 80°N and −17°E at 76°N, and falls again at 4°E for the 80°N and at −6°E for the 76°N transect. The maximum of the volume flux lies in between −2°E and 2°E for the 80°N transect, and in between −15°E and −8°E for the 76°N transect. The mean width of the volume flux stream at 0.8 km^3/day is about 200 km at both transects. Also the volume flux maps in Figures 6.2 and 6.3 on page 98 suggest that the width of the EGC sea ice stream stays fairly constant. In contrast, the amplitude of the volume flux is highly variable both annually and interannually. This can further be seen when integrating the complete volume flux along the transect. Figure 6.7 on page 107 shows the time series of the total Fram Strait sea ice volume flux for the nine measurement periods between February 2003 and April 2007. As black

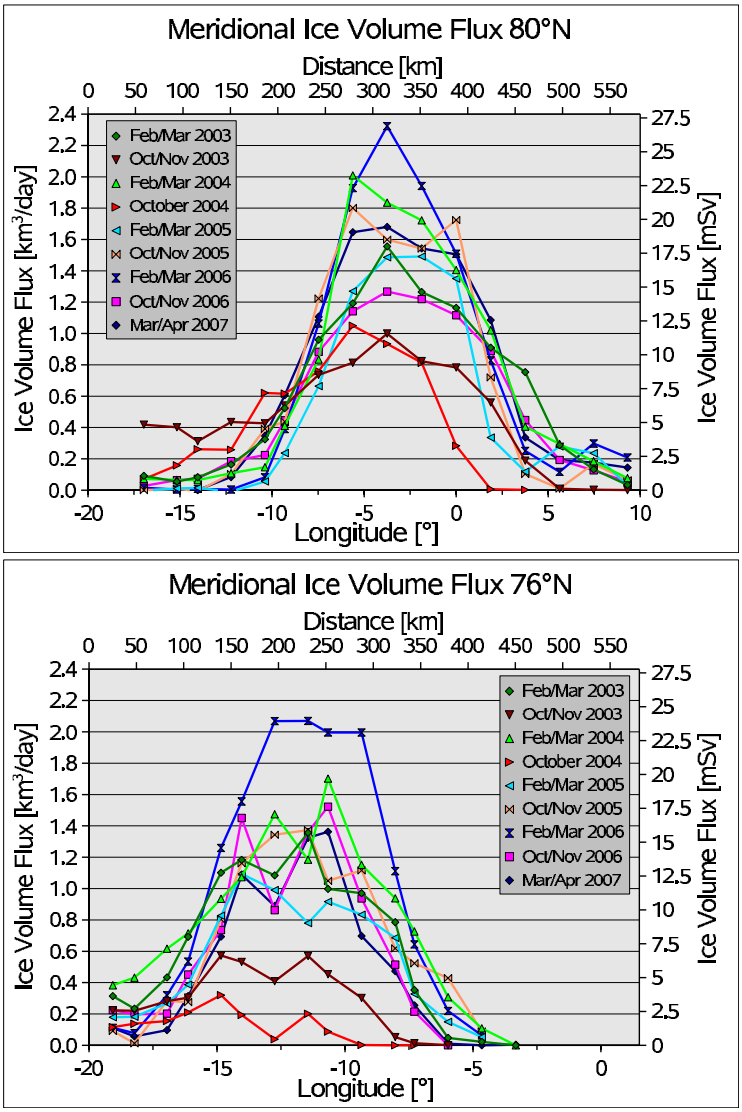

Figure 6.6: Transects of the meridional sea ice volume at 80°N in the Fram Strait (top panel) and at 76°N in the Greenland Sea (bottom panel). Ice fluxes for nine ICESat periods are shown. Fluxes are counted positive towards south. Red to orange colors represent fall fluxes (Oct/Nov) and green to blue colors winter (Feb/Mar) fluxes. The bottom x-axis gives the location in longitudes. Note the different scale in both panels. The top x-axis shows the distance in km and is almost identical for both panels. Volume fluxes are given in km^3/day on the left y-axis and in mSv on the right y-axis.

squares and connected by a line the 80°N outflow is shown and as blue triangles the 76°N one. Red bars at the zero line visualize the difference between the two transects. In Table 6.2 the values of the respective total sea ice volume fluxes are summarized. Error estimates were calculated from the errors ε_{V_v} of the individual grid points in equation 6.3 on the previous page. Gaussian error propagation requires linear independent errors of the single components. This is definitively not given when summing the volume flux along a transect. Errors of neighboring grid cells are likely correlated. To account for that errors calculated by Gaussian error propagation are doubled to get a more realistic error estimation ε_{V_t} for the total volume flux through a transect:

$$\varepsilon_{V_t} = 2\sqrt{\sum \varepsilon_{V_v}^2}\,.$$

Both, the 80°N and the 76°N, time series in Figure 6.7 show high variability. But the standard deviation of the 76°N time series is with 3.8 km^3/day twice as large as the 80°N standard deviation with 1.8 km^3/day. For the 80°N transect the volume flux during the

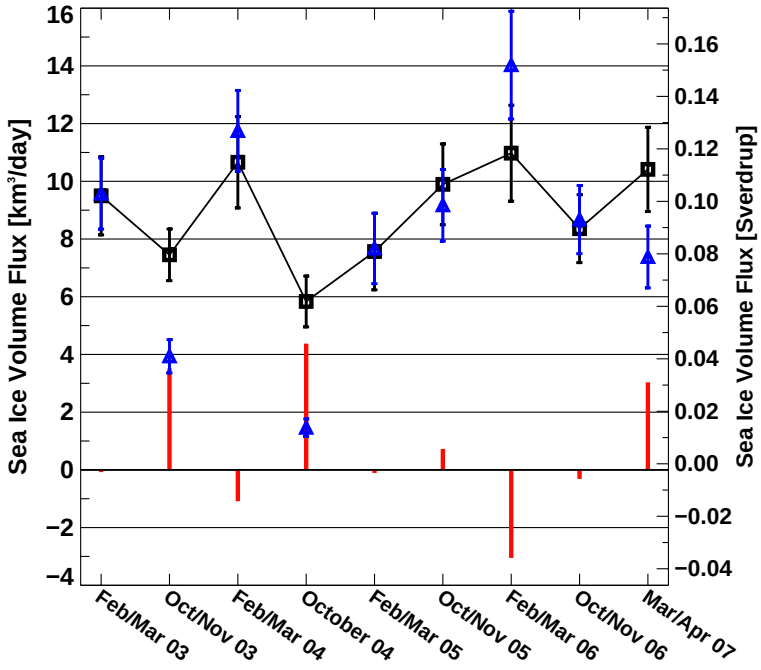

Figure 6.7: Time series for nine ICESat periods of the total amount of sea ice volume flux through Fram Strait at 80°N shown as black lines with squares. Fluxes are counted positive towards south. Blue triangles denote the total volume flux at 76°N in the Greenland Sea and red bars at the zero axis show the difference between the 80°N and 76°N volume flux. Additionally, the error estimates for the individual total fluxes are indicated by error bars.

Table 6.2: Total sea ice volume flux for all nine ICESat periods through transects at 80°N and 76°N in Fram Strait and the East Greenland Current, respectively. ± values give the respective error estimates.

Period	Dates	Volume Flux 80°N	Volume Flux 76°N
1	20.02–21.03.2003	(9.5 ± 1.4) km^3/day	(9.6 ± 1.2) km^3/day
2a	29.09–18.11.2003	(7.5 ± 0.9) km^3/day	(3.9 ± 0.6) km^3/day
2b	17.02–20.03.2004	(10.7 ± 1.6) km^3/day	(11.7 ± 1.4) km^3/day
3a	03.10–01.11.2004	(5.8 ± 0.9) km^3/day	(1.5 ± 0.3) km^3/day
3b	18.02–23.03.2005	(7.6 ± 1.3) km^3/day	(7.7 ± 1.2) km^3/day
3d	21.10–23.11.2005	(9.9 ± 1.4) km^3/day	(9.2 ± 1.2) km^3/day
3e	22.02–26.03.2006	(11.0 ± 1.7) km^3/day	(14.0 ± 1.9) km^3/day
3g	25.10–22.11.2006	(8.4 ± 1.2) km^3/day	(8.7 ± 1.2) km^3/day
3h	12.03–14.04.2007	(10.4 ± 1.5) km^3/day	(7.4 ± 1.1) km^3/day
Mean		(9.0 ± 1.3) km^3/day	(8.2 ± 1.1) km^3/day

fall (Oct/Nov) periods, after the melting during summer, is lower than the one of the preceding winter period, except for 2005: the winter period (Feb/Mar) in 2005 is the lowest winter period of the complete time series and the 2005 fall period is the highest one out of the fall periods. The lowest volume flux at both transects occurred during fall (October) 2004. In general, the shape of the volume flux series at the two transects follows each other and has a correlation coefficient of 0.88.

The difference in sea ice volume flux between the two transects shown as red bars in Figure 6.7 on the previous page can be attributed to both thermodynamical and dynamical reasons. Also the travel time of sea ice from the northern to the southern transect has to be taken into account as we are looking at approximately monthly means. If the sea ice volume flux could react instantaneous between the two transects, the difference in ice volume flux between the transects could be completely attributed to (1) ice melting/freezing between the two transects, and/or (2) accumulation and release (convergence/divergence) of sea ice between the transects, respectively. As sea ice concentration in general is high in the EGC, accumulation could only be achieved by broadening of the ice stream between the two transects. The ice would than accumulate at the eastern border of the EGC towards the Greenland Sea. Alternatively sea ice can be transported out of the EGC to the open Greenland Sea, where it consecutively would melt at the latitudes between the shown transects. The pronounced divergence patterns along the ice edge as shown in Figure 6.5 on page 103 can be attributed to this process. For a larger export of ice at 76°N than is imported at 80°N (divergent flux field shown as negative red bars in Figure 6.7 on the previous page) the situation is reversed. If no ice is formed by freezing, the additional export of ice at 76°N is taken from the reservoir of ice in the EGC between the two transects. The EGC consequently would have to narrow or would be made up of a loser ice cover with lower ice concentration. The bottom panel in Figure 6.15 on page 127 in Section 6.7 shows a time series of the amount of ice volume between the two transects, which illustrates these processes.

But as these are not instantaneous processes and the ice volume flux estimates are approximately monthly means also the elapsed time plays a role. Assuming an average meridional ice drift velocity of 0.2 m/s, sea ice passing the transect at 80°N would take 26 days to travel the 445 km to the second transect at 76°N. Therefore, if the volume flux increases at the northern transect during the observed period this can only be seen approximately one month later at the southern transect. The largest positive differences for the used periods in Figure 6.7 on the previous page are found in October/November 2003 and 2004 (periods 2a and 3a). Here both, melting of ice in the more southern part of the Greenland Sea and a stronger increase of volume flux at the northern transect in comparison to the southern one, likely played a role. In October at the end of the summer no or only fragments of ice are left at 76°N and the ice first has to be transported there during the time span of the period.

The largest negative difference occurred during the February/March 2006 period 3e, when the difference reached more than -3 km^3/day. During February/March likely no ice melting occurred in the EGC and the difference can only be attributed to dynamic causes or errors. The ice volume flux in the EGC often occurs in a pulse like manner, which is caused by atmospheric cyclones passing by. If a higher number of cyclones reach the ice edge near the 76°N transect and accelerate the volume flux there, this would cause the observed divergent situation with a larger outflow of sea ice at the southern transect,

which is not compensated by ice inflow at 80°N. The exported ice is taken than from the ice reservoir in between the two transects.

Mention that despite the large volume flux difference at the two transects the error estimates are overlapping for period 3e (see Figure 6.7). Thus the difference could also be erroneous, which is also true for the differences of the remaining periods beside the positive difference during period 3h in March/April 2007.

In summary, during the three periods 2a (Oct/Nov 03), 3a (October 04) and 3h (Mar/Apr 07) a significantly higher ice volume transported occurred at 80°N than at 76°N, which for period 2a and 3a can be explained by the end of summer situation. For one period, 3e (Feb/Mar 2006) a large negative differences with larger ice transport at 76°N than at 80°N was observed. These convergent/divergent situation like during periods 3h and 3e can be attributed to dynamic causes, mainly forced by cyclones passing along the ice edge during the period duration. For all other periods (1, 2b, 3b, 3d, 3g) the volume fluxes at the two transects agree within their error margins.

6.4.2 Monthly Fram Strait Sea Ice Volume Flux Time Series 2003–2007

So far the sea ice volume flux analysis was limited to two about one month long ICESat measurement periods per year. ICESat is only measuring up to three times per year (see Table 2.3 on page 20) during February/March, May/June and October/November. The three May/June measurement periods from 2004, 2005 and 2006 are not used here as (1) data gaps and errors due to cloud contamination are larger, (2) no IFREMER ice drift data (Chapter 4) exist for these periods, and (3) the data of these periods only became very recently available. The sea ice volume flux is highly variable already at short time scales of days. This is caused by the variability of the ice drift, which is mainly driven by air pressure gradients, which change on synoptic time scales. Therefore, no estimates can be deduced directly from the volume flux during the ICESat measurement periods for the adjacent months or even longer time scales. But the ice thickness is much less variable than the ice drift. Based on this a method is developed to derive the monthly winter (Oct. to May) sea ice volume flux by using the ice thickness obtained from ICESat measurements as supporting points in combination with the daily available ice drift and area measurements.

According to *Vinje et al.* (1998) the sea ice thickness at 79°N and 5°W is showing the seasonal cycle given in Figure 6.8 on the next page. The shown thicknesses were inferred from six years of ULS measurements at about 79°N, 5°W in the Fram Strait between 1990 and 1996. The bars in the graph in Figure 6.8 show the mean ice thickness of the six years as given in the table and the grey lines show the maximum and minimum ice thickness occurred during the six years for the respective month. From this thickness data set the seasonal cycle is used in the following, making two reasonable assumptions:

1. The amplitude of the seasonal cycle measured during the nineties is still valid for the ice thickness between 2003 and 2007. (The absolute value of the ice thickness is allowed to have changed since then.)

2. The seasonal cycle measured at 79°N, 5°W is valid for all longitudes between 20°W and 12°E at 80°N.

	Jan	Feb	Mar	Apr	May	Jun	Jul	Aug	Sep	Oct	Nov	Dec
I [m]	2.68	2.74	3.18	3.26	3.23	3.21	3.10	2.41	2.25	2.72	2.83	2.78

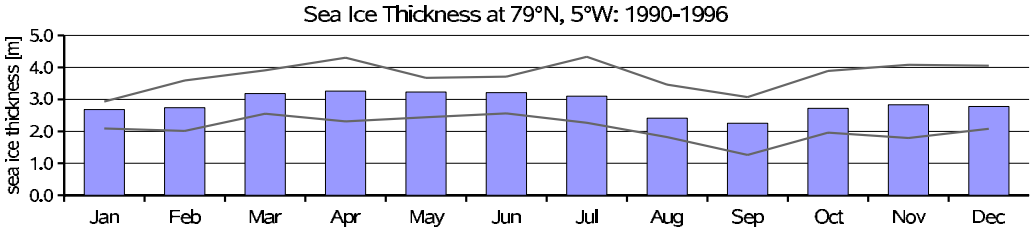

Figure 6.8: Mean monthly ice thickness measurements at about 79°N, 5°W from Upward Looking Sonar (ULS) data for the six years between 1990 and 1996 (*Vinje et al.*, 1998). Blue bars in the bottom graph visualize these mean ice thicknesses. Additionally, the maximum and minimum mean ice thickness that occurred during the six years in each month are shown as grey lines.

The maximum and minimum values of the ice thickness during these six years are showing a significant spread (grey lines in Figure 6.8), therefore absolute values can not be inferred from the time series. But if one looks in the individual time series of each year they show a similar seasonal behavior.

Using the seasonal cycle given in Figure 6.8 monthly ice thickness maps are calculated from the ice thickness maps of the nine ICESat periods (shown in Figures 5.15 and 5.16 on page 90) for the entire period January 2003 to April 2007, i.e. also for the summer months. To additionally account for changes in the sea ice area also monthly mean ASI ice concentration maps are calculated and incorporated in the ice thickness calculation. The ULS-based ice thickness data is used to obtain a pair of factors, which carries the information about how the ice thickness varies seasonally between the ICESat measurement periods. These factors derived solely on the basis of the ULS data are then used to obtain ice thickness values for the period between adjacent ICESat measurement periods, which are based solely on ICESat measurements. The following steps are involved:

1. For each of the nine ICESat data periods its middle date t_p is calculated.

2. ULS-based ice thickness values I_s (see Figure 6.8) of the two months adjacent to each ICESat measurement period are taken and interpolated to get an estimate of the ice thickness (based on ULS-data) at time t_p: I_p. Now for all calendar months and all ICESat periods ULS-based ice thicknesses I_s and I_p are on hand respectively.

3. For each month m of the period January 2003 to April 2007 those two ICESat measurement periods are identified which lie closes in time to the center date t of month m. The time differences between t and t_p of these two periods are calculated: Δt_1 and Δt_2.

4. Using the ULS ice thickness value of month m I_s and the ULS ice thickness values

of the identified ICESat measurement periods, I_{p1} and I_{p2}, the ratios

$$r_1 = \frac{I_s}{I_{p1}} \text{ and } r_2 = \frac{I_s}{I_{p2}}$$

are calculated. These ratios form the pair of factors mentioned above and describe the amount of change in ice thickness between month m and t_{p1} and t_{p2} according to the seasonsal cycle given be the ULS-based ice thickness data.

Now these ratios can be applied to ice thickness data obtained from ICESat, involving the following steps:

5. For each month m the mean ASI sea ice concentration C_m is calculated on a 25 km grid.

6. The ice thickness distributions measured during ICESat periods t_{p1} and t_{p2}: I_1 and I_2 (for this application not scaled with the ice concentration, see equation 5.7 on page 83), are inter- and extrapolated to all ice covered areas of month m using an inverse distance interpolation. These two interpolated ice thickness datasets are multiplied with the ice concentration C_m of month m and the two ice thickness distribution I_{n1} and I_{n2} are obtained. I_{n1} and I_{n2} are similar to the original ICESat ice thickness distributions I_1 and I_2 but carry the information of the ice covered area and ice concentration distribution of month m.

7. The final ice thickness distribution I_m of month m is calculated by applying the ratios r_1 and r_2 to I_{n1} and I_{n2} according to

$$I_m = \frac{\Delta t_2(r_1 I_{n1}) + \Delta t_1(r_2 I_{n2})}{\Delta t_1 + \Delta t_2}\,.$$

The influence of I_{n1} and I_{n2} on the final ice thickness I_m is weighted accordant to their time differences Δt_1 and Δt_2 to the desired month. $r_1 I_{n1}$ and $r_2 I_{n2}$ are the from the ICESat data interpolated ice thicknesses using the seasonal cycle.

Using the above scheme interpolated ice thickness values I_m for all months between January 2003 and April 2007 are calculated.

IFREMER AMSR-E ice drift data is only available for the winter period, which is at least lasting from October to April (in 2003 also data for May is available). The average monthly ice drift is calculated for all winter months between January 2003 and April 2007 from the 2-daily ice drift datasets (see also Chapter 4).

Using the same method as described in Section 6.4.1 to calculate the meridional sea ice volume flux through a transect at 80°N a monthly Fram Strait ice volume flux time series is obtained. The left panel of Figure 6.9 on the following page shows the derived monthly values as black squares, the accordant ice volume flux values are given in Table 6.3 on page 113. Additionally, as green line in Figure 6.9 the 30-day running mean of the ice volume flux is shown. The running mean is calculated by using the same method as described above, but instead of calendar months 30-day boxes centered around each individual day between January 2003 and April 2007 are used for the I_m determination. Clearly the high variability of the ice volume flux even on intra-seasonal scales and in-between the monthly values can be seen in the time series. As already mentioned this is

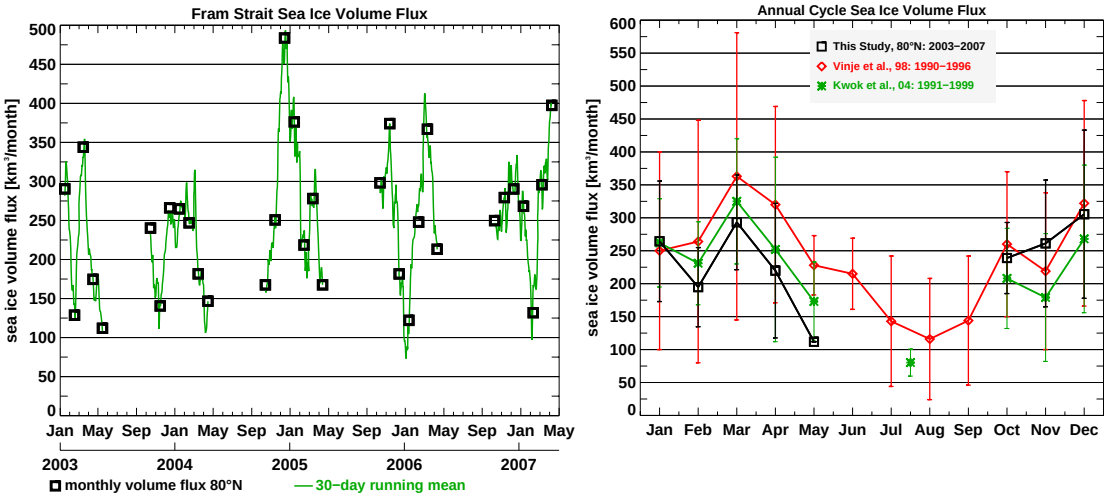

Figure 6.9: Left: Time series of monthly winter sea ice volume flux through Fram Strait at 80°N for the time period January 2003 to April 2007 from solely satellite measurements. Black squares show the monthly ice flux values and the green line the 30-days running mean values. Due to missing ice drift data no values are given for summer months. Right: Seasonal cycle of monthly Fram Strait sea ice volume flux from this study (years 2003–2007) shown in black, from *Vinje et al.* (1998) (years 1990–1996) shown in red, and from *Kwok et al.* (2004b) (years 1991–1999) shown in green. Error bars denote plusminus one standard deviation.

due to the influence of the fast changing atmospheric forcing. From the figure we need to conclude that from the volume flux of one month no implications of the values of the adjacent months can be inferred. In Table 6.3 additionally to the 80°N volume flux also the 76°N volume flux is given, but the uncertainty of these values is expected to be large. The seasonal cycle derived from the ULS measurements of the ice thickness might only be valid for latitudes close to 79°N. At 76°N the seasonal cycle might have changed and due to the sparse coverage with ice drift data the uncertainty of the volume flux at 76°N already is larger than at 80°N. However, following up the discussion from the last section about ice volume flux differences between 80°N and 76°N, Table 6.3 shows that the magnitude of the 80°N to 76°N ice volume flux difference is largest in April ($-64\,\mathrm{km}^3$/month) and October ($+86\,\mathrm{km}^3$/month), the months with the largest possible amount of melt influence. While in October the explanation for the positive difference is clear: ice is just starting to build up at 76°N while at 80°N a constant ice stream is already prevailing, the explanation for the negative difference in April is more uncertain. Melting has not extensively started but it seems that ice which has accumulated during winter in the northern part of the Greenland Sea is faster transported further south towards Denmark Strait than ice is transported into the Greenland Sea at 80°N. Also the preceding winter months January, February, and March show negative 80°N minus 76°N volume flux differences, which indicates that during winter sea ice forms in the Greenland Sea between 80°N and 76°N.

In the right panel of Figure 6.9 the seasonal cycle of the monthly sea ice volume flux is shown and compared to findings by *Vinje et al.* (1998) (VNK98 hereafter) and *Kwok*

Table 6.3: Summary of monthly sea ice volume flux. Upper part: volume transports derived in this study for 80°N/76°N, respectively. Bottom part: mean monthly volume fluxes from *Vinje et al.* (1998) and *Kwok et al.* (2004a) used for comparison. "S. D." is the standard deviation of the measurements in the accordant column. All volume fluxes are given in km^3/month.

Year	Jan.	Feb.	Mar.	Apr.	May	Oct.	Nov.	Dec.
2003	290/293	129/118	344/380	175/171	112/135	240/141	141/211	266/321
2004	265/444	247/326	182/214	147/326		168/68	251/263	484/360
2005	376/326	219/178	278/305	168/297		298/200	374/379	182/204
2006	122/177	248/288	367/461	213/343		250/205	279/288	290/206
2007	268/343	132/198	296/229	397/284				
Mean	264/317	195/221	293/318	220/284		239/153	261/285	305/273
S. D.	91/96	60/84	72/104	102/67		54/64	96/70	128/80
1990–1996 (Vinje et al., 1998)								
Mean	250	264	363	322	228	260	219	322
S. D.	150	184	218	149	45	110	119	156
1991–1999 (Kwok et al., 2004)								
Mean	262	231	325	252	173	208	179	268
S. D.	67	63	95	140	60	76	97	97

et al. (2004a) (KCP04 hereafter), both estimated for the nineties. The work in KCP04 is a continuation of *Kwok and Rothrock* (1999). The black line shows the seasonal cycle at 80°N of this study based on the five years 2003 to 2007 for the months January to April and on the four years 2003 to 2006 for the months October to December. Additionally, the one ice volume flux estimate for May from 2003 is shown. Error bars denote ± one standard deviation interval. VNK98's (red) and KCP04's (green) volume flux estimates are also based on satellite data for the ice drift and area but use ULS data at one single point at about 79°N, 5°W for the ice thickness estimation. VNK98's study covers the six years between August 1990 and July 1996 and KCP04's one covers the eight years between October 1991 and September 1999. While VNK98 published a monthly time series for the complete year shown as red curve in Figure 6.9, right panel, KCP04 published monthly volume fluxes for October to May. For June to September they estimated an accumulated volume flux value for each year.

Despite the different time period covered by the three studies their seasonal cycle agrees well in terms of amplitude and phase and the ice volume flux values vary mainly inside the one standard deviation envelop. For the February to May period the ice transport estimates from VNK98 and KCP04 are about 50 km^3/month higher than the ones from this study, during the rest of the overlapping months the values from this study lay inbetween the two other studies.

The ice volume flux is highest during March therafter it decreases towards summer. In fall it increases again until another high volume flux peak in December. The large standard deviations of all three time series demonstrate the high inter-annual variability

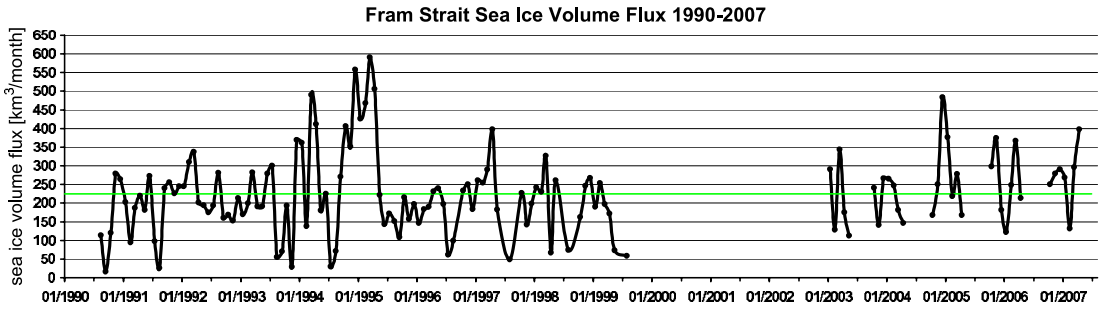

Figure 6.10: Time series of the monthly sea ice volume through Fram Strait between August 1990 and April 2007 (black line). The green line marks the mean value of 225 km3/month. Gaps are due to missing data. The data on the right side after 2003 is new data from this study.

of the ice volume flux.

The monthly time series presented here can be used to continue the former time series from the nineties. Unfortunately, there is a more than three years long gap between September 1999 and January 2003. This gap only could be closed if the existing ULS data during that time would be exploited. However, Figure 6.10 shows the complete available Fram Strait sea ice volume flux time series between 1990 and 2007. Where the VNK98 and KCP04 time series overlap the mean of both is taken. The green line marks the overall monthly volume flux mean of 225 km^3/month. No adaptions were applied to the slightly different flux gates used for the three studies. The monthly Fram Strait sea ice volume flux values of the complete time series shown in Figure 6.10 are given in Table A.3 on page 148 in Appendix A.5. Compared to the high ice volume fluxes between September 1994 and March 1995 the volume flux of the recent years seems to be moderate. This extraordinary high volume flux during 1994/1995 can also be found in the time series shown in *Widell et al.* (2003) and *Vinje* (2001) and mainly cause the above mentioned positive difference of 50 km^3/month during February to May between the time series of the nineties and our volume flux dataset. Also the lowest values during the nineties are not met during our time series, which is due to the missing summer months, where the volume flux often was minimal during the nineties.

6.5 Error Evaluation and Comparison to Alternative Methods

6.5.1 Comparison to Volume Flux Obtained Using QuikSCAT Ice Drift

From the three for the volume flux calculation needed quantities sea ice concentration, drift, and thickness, the sea ice drift is the one with the largest variability. Errors in the ice drift derivation contribute strongly to the final ice volume flux error. An alternative, independent ice drift dataset is used, to get an estimate of the influence which the used sea ice drift dataset has on the final ice volume flux result. In comparison to the passive microwave radiometer AMSR-E the scatterometer SeaWinds on QuikSCAT (referred to as QuikSCAT hereafter) is an active instrument (see Section 2.2.3 on page 24). QuikSCAT emits electromagnetic waves at the microwave frequency 13.4 GHz. The ra-

Table 6.4: Comparison of sea ice volume flux estimates using sea ice drift data derived from AMSR-E and QuikSCAT measurements together with the error estimates of the ice volume flux obtained via error propagation of the input parameters.

ICESat Period	AMSR-E [km^3/day]		QuikSCAT [km^3/day]		Difference [km^3/day]	
	80°N	76°N	80°N	76°N	80°N	76°N
1 : Feb/Mar 2003	9.5 ± 1.4	9.6 ± 1.2	7.4 ± 1.1	8.5 ± 1.1	2.1	1.1
2a: Oct/Nov 2003	7.5 ± 0.9	3.9 ± 0.6	4.7 ± 0.6	4.1 ± 0.6	2.8	−0.2
2b: Feb/Mar 2004	10.7 ± 1.6	11.7 ± 1.4	6.0 ± 1.0	10.0 ± 1.2	4.7	1.7
Mean	9.2	8.4	6.0	7.5	3.2	0.9

diation is reflected and scattered at the Earth surface, and this backscattered radiation is measured again by QuikSCAT. In *Haarpaintner* (2006) and *Haarpaintner and Spreen* (2007) a method is presented how to derive the sea ice drift from enhanced-resolution QuikSCAT data. For the sea ice drift determination from QuikSCAT data a similar cross-correlation method as described in Chapter 4 for AMSR-E data is used. The QuikSCAT ice drift data is available on the same 25 km grid as used for the AMSR-E ice drift on a daily base. The time gap for the cross-correlation is with two days identical. Like the AMSR-E method ice drift determination does not work for surface melt conditions during summer. QuikSCAT sea ice drift data available for this study are the first three ICESat measurement periods 1, 2a, and 2b in 2003 and 2004 (the QuikSCAT sea ice drift data was provided by Jörg Haarpaintner).

Table 6.4 shows the integrated meridional sea ice volume flux through transects at 80°N and 76°N for these three ICESat periods. The sea ice volume flux using the AMSR-E ice drift and using the QuikSCAT ice drift is given together with the difference between the two datasets. The sea ice volume flux using the QuikSCAT ice drift in general is smaller than the one using the AMSR-E ice drift. At 80°N the difference amounts to about 3 km^3/day and at 76°N to about 1 km^3/day. At 80°N the mean difference value accounts for about 35% of the AMSR-E ice volume flux value and reaches up to 45% for period 2b. These differences are large and fall outside the error estimates of about 1 km^3/day for the sea ice volume flux. The reported accuracy of both sea ice drift products is with 2.2 to 3. km/day similar (*Ezraty et al.*, 2007a; *Haarpaintner*, 2006). For the volume flux error estimates this ice drift error was increased to 4.4 km/day to account for larger errors in the dynamic Fram Strait region. Still this error can not explain the large differences in sea ice volume flux using the two different ice drift datasets.

Likely explanations for the large volume flux differences are:

Differences caused by the interpolation of sea ice drift data To calculate the ice volume flux, sea ice drift data has to exist for all ice covered grid cells in the study region. But especially in the dynamic Fram Strait region and also in the Barents Sea the correlation technique of both sea ice drift datasets fails to find sea ice drift speeds for all grid cells. In general, the number of grid cells with valid sea ice drift measurements is higher for the QuikSCAT than for the AMSR-E sea ice drift dataset (*Haarpaintner and Spreen*, 2007). Both ice drift datasets have to be inter-

and extrapolated (up to a distance of 100 km, i.e. 4 grid points) to ensure that ice drift estimates are available for the entire ice covered areas. The fact that the datasets used as input exhibit a different data density might introduce significant differences between the two datasets after interpolation.

Not captured high ice drift speeds in the EGC High ice drift speeds are likely not well captured by the sea ice drift datasets using a two day time gap to correlate the brightness temperature (AMSR-E) and radar backscatter (QuikSCAT) maps, respectively. The maps are getting decorrelated too fast due to the high ice drift speeds. In *Haarpaintner and Spreen* (2007) it was shown that sea ice drift speeds derived from QuikSCAT data when using a one day time gap instead of a two day one are significantly higher in the Fram Strait region. In Section 4.3 on page 58 it was shown that the AMSR-E drift dataset is underestimating the ice drift velocity by about 0.01 m/s in comparison to SAR drift data. Thus both ice drift datasets likely are not capturing high ice drift speeds well but might behave different in this respect.

Both causes likely contribute to the ice drift speed difference in the two datasets. A more detailed explanation and quantifiable values for the difference are subject of ongoing research.

The comparison is limited to three ICESat measurement periods, which is too short to give a solid estimate of the ice drift uncertainty, and it is unsure, which of the two ice drift datasets is reproducing the true ice drift speed best. We therefore keep the sea ice volume flux error estimates based on the 4.4 km/day sea ice drift uncertainty, which in Section 4.3 was shown to be at the upper bound expected for the AMSR-E drift error in the Fram Strait region. However, the comparison shows that the real error could be larger.

6.5.2 Sensitivity Study

A sensitivity study was carried out in order to examine the systematic error on ice thickness and volume flux that could be caused by a systematic bias in the input parameters. The used uncertainties for the sea ice thickness determination are summarized in Table 5.2 on page 84. The used uncertainty for the ice drift has a value of about 0.8 km/day (mean for a complete ICESat period). The influence of the input parameters ice concentration, snow density, snow depth, ice density, and drift speed are investigated.

The influence of the about 5% large total ice concentrationon error on both the ice thickness and the ice volume flux is small. Therefore variations in total ice concentration were not used for the sensitivity study. For the multi-year and first-year ice concentrations the conditions are different. As discussed in Section 5.2.1 on page 86 there is a possibility that the multi-year sea ice concentration in some cases is overestimated in the Greenland Sea by the used retrieval method using QuikSCAT data. This would cause an underestimation of the ice thickness. For example, the sea ice thickness is underestimated by about 20 cm if a multi-year ice concentration of $C_{MY} = 0.9$ is used instead of the true multi-year ice concentration of $C_{MY} = 0.5$ and by 50 cm if the true multi-year ice concentration only would by $C_{MY} = 0.1$. The respective relative ice thickness errors are 7% and 17%. A high ice concentration of $C = 0.95$ and an ice freeboard height of

$F = 50\,\text{cm}$ was used for this calculation. The relative ice thickness errors stay similar for other ice concentration and freeboard values.

As with regard to the ice thickness I (equation 5.8 on page 83) the systematic error caused by a bias in snow density ρ_S of $\pm 30\,\text{kg/m}^3$ was found to be negligible (below 0.05 m) compared to the one caused by a bias of $\pm 10\,\text{cm}$ in the snow thickness S, which results in an ice thickness change of about 0.2 m. The error caused by a bias in the ice densities ρ_{MY} and ρ_{FY} of $\pm 30\,\text{kg/m}^3$ is largest, it increases with freeboard height and is larger for an under- than for an overestimation of the real ice densities. This error takes a value of 0.5 m (1.5 m) for an ice thickness of 2 m (5 m), if the real ice densities are underestimated by $30\,\text{kg/m}^3$.

Regarding the ice volume flux V (equation 6.1 on page 95) the systematic error in the ice volume flux caused by a bias in the ice density ($\pm 30\,\text{kg/m}^3$) or the ice drift speed ($\pm 2\,\text{cm/s}$) depends on ice thickness and drift speed and takes values of, e.g., 0.08–$0.13\,\text{km}^3$/day and 0.15–$0.26\,\text{km}^3$/day at an ice thickness of 3 m and ice drift speeds of 6 cm/s and 12 cm/s, respectively. The systematic error caused by the same biases (see above) is negligible in case of the snow density ($\pm 30\,\text{kg/m}^3$), and is $< 0.1\,\text{km}^3$/day in case of the snow depth ($\pm 10\,\text{cm}$) and therefore is not negligible but smaller than the other contributions (see above) for an ice thickness above about 2 m. The uncertainty of the snow depth is unknown, it might be even larger than 10 cm. Thus it can be concluded that biases in ice drift speed, ice density and snow depth may have an equally large impact on the estimated ice volume flux.

We note here that these systematic errors are not influenced by an improvement of the SSH estimation, which leads to the conclusion that future work should focus equally on this improvement and on the validity of the input parameters, especially ice drift speed, ice density and snow depth.

6.5.3 Volume Flux from Single Point (ULS) and Spatial Distributed (ICESat) Ice Thickness Measurements

In Section 6.4.2 the studies of *Vinje et al.* (1998) (VNK98) and *Kwok et al.* (2004a) (KCP04), who derived the sea ice volume flux through Fram Strait during the nineties, were used for comparison. Both studies used ice drift estimates from satellite passive microwave sensors (SSM/I) in combination with ice thickness estimates obtained from ice draft (part of the ice inside the water) measurements by Upward Looking Sonar (ULS) at near 79°N, −5°E. In contrast to our approach, their ice thickness, and thus the ice volume flux, includes the snow cover cumulatively. For their analysis, the general ice thickness distribution along the transect at 79°N has to be parameterized, as it is not measured. Afterwards this distribution is scaled with the single point ice thickness estimate determined from ULS sea ice draft observation. Our method has the advantage that the ice thickness distribution along the transect is directly measured by ICESat and does not rely on a single point measurement. The relative uncertainty for the total ice volume flux through the 80°N transect for the nine ICESat measurement periods found in this study lies between 12% to 17% (mean 14%, see Table 6.2 on page 107) and is comparable to the uncertainties of 12% to 20% published by VNK98 for their method.

The question arises if we are gaining any advantage by the direct measurement of the ice thickness distribution in comparison to the single point ULS measurements. We

Table 6.5: Sea ice volume flux derived from ICESat and simulated ULS measurements: Total sea ice volume flux through a transect at 79°N using an observed ice thickness profile along the transect (ICESat Volume Flux) and using only one single point measurement together with a thickness parameterization along the transect (Sim. ULS Volume Flux). In contrast to Section 6.4.1 a transect at 79°N is used. The last column shows the difference between the two volume flux estimates with bold values if the difference exceeds the error estimation of the ICESat volume flux (column 2).

ICESat Period		ICESat Volume Flux [km^3/day]	Sim. ULS Volume Flux [km^3/day]	Difference [km^3/day]
1	Feb/Mar 2003	9.7 ± 1.4	9.9	-0.2
2a	Oct/Nov 2003	7.5 ± 1.0	9.1	$\mathbf{-1.6}$
2b	Feb/Mar 2004	10.6 ± 1.6	7.0	**3.6**
3a	Oct 2004	5.3 ± 0.7	6.5	$\mathbf{-1.2}$
3b	Feb/Mar 2005	7.9 ± 1.4	8.1	-0.2
3d	Oct/Nov 2005	9.1 ± 1.3	7.6	**1.5**
3e	Feb/Mar 2006	10.8 ± 1.8	11.6	-0.8
3g	Oct/Nov 2006	7.2 ± 1.1	7.3	-0.1
3h	Mar/Apr 2007	7.2 ± 1.2	7.1	0.1
	Mean:	8.4 ± 1.3	8.2	1.1

therefore first calculate sea ice volume fluxes through a transect at 79°N as were done for 80°N and 76°N in Section 6.4.1. Afterwards we do the same calculation again but use only one ICESat ice thickness measurement: that of the grid cell covering 79°N, −5°E, and the ice thickness parameterization used by VNK98 and KCP04 along the transect. VNK98 and KCP04 use the following parameterization for the ice thickness in dependence of the longitude λ:

$$I(\lambda) = \begin{cases} I_0(-0.127\lambda + 0.37) & : \quad 0^\circ < \lambda < 2.9^\circ \\ 0.68 I_0 & : \quad -5^\circ < \lambda \leq 0^\circ \\ I_0 & : \quad \lambda \leq -5^\circ, \end{cases}$$

where $I(\lambda)$ is the sea ice thickness as a function of the longitude λ and I_0 is the ice thickness at 79°N, −5°E. In our case I_0 is the ICESat ice thickness at that position. Figure 6.11 is showing the 79°N transect for both sea ice volume flux estimates and Table 6.5 summarizes the total sea ice volume flux through that transect for all nine used ICESat periods.

In general the shapes of the two transects in Figure 6.11 show good agreement. Also the total volume fluxes given in Table 6.5 for 5 out of the 9 ICESat periods agree within the error margin of the ICESat derived sea ice volume flux (column 2). The remaining 4 cases (marked bold in the last column) lie outside the error margin and show differences of up to 50% of the simulated ULS volume flux (period 2b). However, in general the ice thickness parameterization used by VNK98 and KCP04 seem to give a valid ice thickness distribution along the transect. One has to keep in mind that the majority of the value of the ice volume flux can be attributed to the ice drift, which is the same for both volume

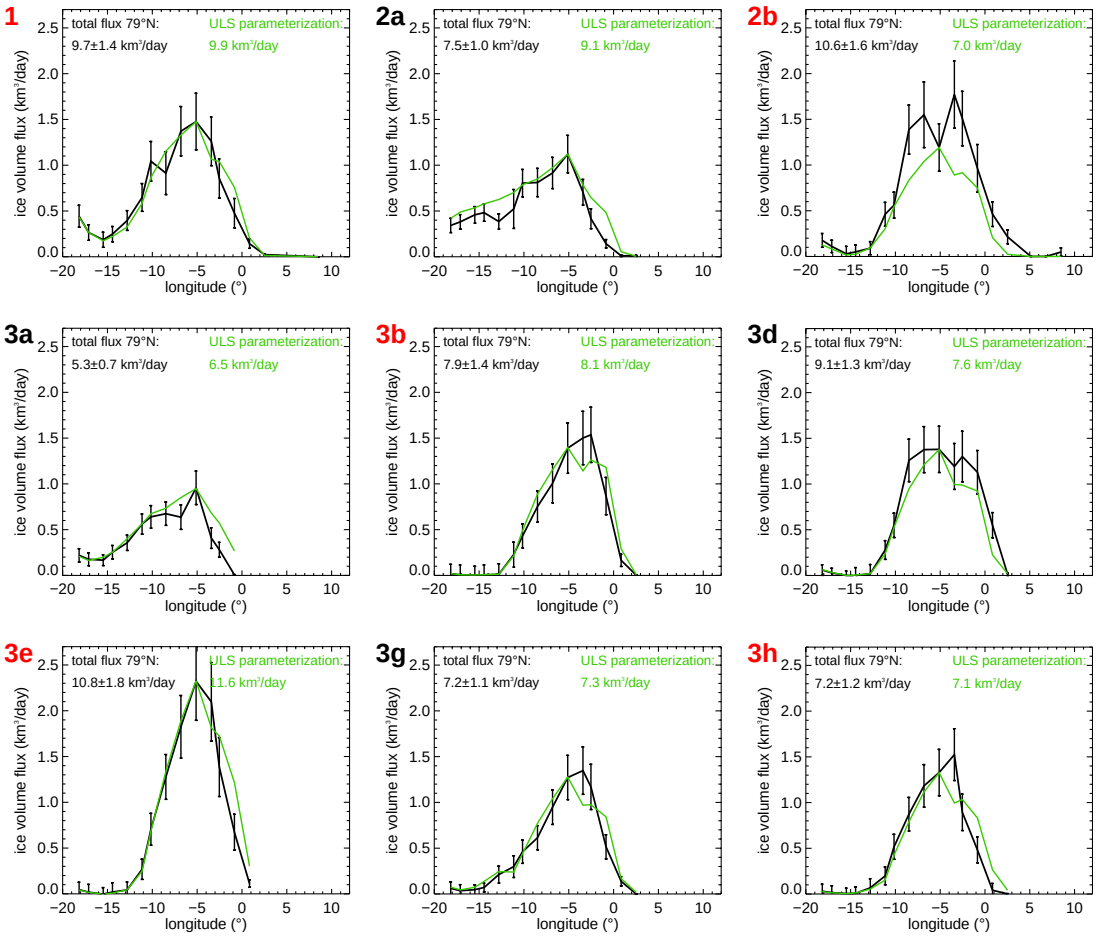

Figure 6.11: Comparison between the sea ice volume flux through a transect at 79°N using an observed (by ICESat) ice thickness profile along the transect (black lines) and using only one single point ice thickness observation (by ICESat) together with a thickness parameterization along the transect (green lines). The green transects simulate how the volume flux transect would have been inferred from single point ULS measurements. Transects are shown for all nine ICESat periods with the ICESat period name given in the upper left corner for winter in red and for fall periods in black (for dates see Table 6.1 on page 100).

flux calculations.

Nevertheless, there are also the cases with large differences between the two volume flux estimates. For example, the ice thickness value of the 79°N, −5°E measurement during period 2b is small compared to the two surrounding ice thickness values (see also Figure 5.15 on page 89). This causes a large underestimation of 3.6 km^3/day for the total ice volume flux derived from the simulated ULS measurement. During period 2a the ice thickness decreases faster towards the East in direction of the open Greenland Sea than predicted by the ice thickness parameterization, which causes an overestimation of the simulated ULS ice volume flux. These two cases lie clearly outside the assumed error margin for our volume flux estimates. Thus in some cases we gain an improvement by measuring the complete ice thickness profile along the transect in comparison to the single point ULS measurement.

On the other hand, the ice thickness derived from ULS measurements can assumed to be more accurate than our ICESat measurements, because the ULS is measuring the ice draft, which makes up about 90% of the ice thickness while ICESat measures only the remaining 10% of the ice thickness, the ice freeboard. The conversion to ice thicknesses is therefore less influenced by errors in ice density, snow depth and density in the ULS case. As on average (see Table 6.5 on page 118) the volume flux using the ULS parameterization agrees well with the ICESat volume fluxes, it can be concluded that we are not gaining improvement in accuracy for the total Fram Strait volume flux by using ICESat instead of ULS measurements. But this is only the case if one is only interested in the total volume flux at one latitude. Our method for the first time offers the possibility to obtain the sea ice volume flux distribution and not only for one transect in the Fram Strait but everywhere in the study region, e.g. the volume flux into the Barents Sea.

Also, as will be seen in Section 6.6, the shape of the volume flux along the transect is important for comparison to model data, which can have different volume flux shapes in the EGC.

As mentioned above a parallel ULS and ICESat sea ice volume flux time series would be of great value to evaluate both methods in more detail. There is hope that in future ULS data in the EGC obtained parallel to ICESat measurements will be released.

6.6 Comparison to Model Data

In this section the sea ice volume fluxes derived from satellite data are compared to sea ice volume fluxes from model data. Two coupled sea ice-ocean models are used for comparison.

The first one is the North Atlantic/Arctic Ocean-Sea Ice Model (NAOSIM) (*Karcher et al.*, 2005, 2003; *Köberle and Gerdes*, 2003; *Kauker et al.*, 2003). The runs used here were performed in the framework of the EU project DAMOCLES (`http://www.damocles-eu.org`, provided by Michael Karcher, unpublished data, 2007). For the model domain, which encloses the Atlantic north of approximately 50°N, the Nordic Seas, and the Arctic Ocean, a rotated spherical grid with 1/4° horizontal resolution is used. The ocean part employs 30 unevenly spaced vertical levels. The sea ice part uses a dynamic-thermodynamic model with viscous-plastic rheology with the prognostic variables ice thickness, snow thickness, ice concentration, and ice drift.

The second ice-ocean model is based on the Massachusetts Institute of Technology (MIT) ocean general circulation model (*Köhl et al.*, 2007; *Marshall et al.*, 1997a,b). The runs were performed in the framework of the German BMBF funded project NORDATLANTIK (`http://www.zmaw.de/NORDATLANTIK.105.0.html`, provided by Nuno Serra, unpublished data, 2008). The model domain comprises the Atlantic region north of 30°S including the Nordic Seas and the Arctic Ocean and uses a curvilinear grid with a horizontal resolution of 1/6°. Laterally, at the borders the model was forced by the optimized solution of the German ECCO (GECCO) 1° resolution model (*Köhl and Stammer*, 2008), which assimilated all available in situ and remote sensing data. It as NAOSIM uses unevenly spaced vertical levels but 50 not 30, which vary from 10 m near the surface to 500 m at depths. The sea ice part is based on the viscous-plastic dynamic/thermodynamic sea ice model by *Zhang and Rothrock* (2000).

Both models were forced at the surface by the atmospheric state obtained from the National Centers for Environmental Prediction (NCEP)-National Center for Atmosphere Research (NCAR) reanalysis project (*Kalnay et al.*, 1996) and bulk formulae. Prior to the comparison, the model data is mapped onto the 25 km polar stereographic grid used for the satellite data (see Section 2.2.5 on page 25). The model data is first compared to the sea ice volume fluxes derived from satellite data for complete ICESat periods (see Section 6.4.1 on page 104). NAOSIM model data has been made available for this study for the eight ICESat periods between 2003 and 2006: 1, 2a, 2b, 3a, 3b, 3d, 3e, and 3g. Therefore, these eight periods are used for comparison for both models. NAOSIM data is available for this study on a weekly basis, MIT model data on a monthly basis. For NAOSIM the mean of all weeks falling inside the respective ICESat period length is calculated for the eight ICESat periods. For the MIT data the months with the largest overlap with the respective ICESat periods are selected for comparison.

Figure 6.12 on the following page shows as example the sea ice volume flux maps for three ICESat periods: 2a (fall 2003), 3b (winter 2005), and 3d (fall 2005). The maps of the remaining ICESat periods are shown in Figures A.9 and A.10 on page 150 in the Appendix. To remove open water areas and ease comparison with the satellite data only volume fluxes above 0.01 km^3/day are shown for the model data. Additionally to the volume flux maps for the satellite (left column), NAOSIM (middle column), and MIT data, plots (inlays) of the sea ice volume flux through a transect at 80°N are shown for the respective periods. Figure 6.13 on page 123 shows the mean volume flux and the standard deviation (error bars) of all eight ICESat periods for the same transect. In Table 6.6 on page 123 the mean and standard deviation of the total sea ice volume flux through Fram Strait as obtained from satellite and model data is given for transects at 80°N and 76°N for the eight ICESat periods.

The NAOSIM model is for four out of the eight ICESat periods overestimating the sea ice volume flux through Fram Strait in comparison to the satellite data. The MIT model is in seven out of these eight cases underestimating the ice volume flux. The mean NAOSIM ice volume flux at 80°N and 76°N is 1.4 km^3/day (16%) and 1.2 km^3/day (14%) larger than the satellite data, respectively. The mean estimated errors for a single ICESat period found in Section 6.4.1 are 1.3 km^3/day and 1.1 km^3/day at 80°N and 76°N, respectively. Thus the NAOSIM volume flux lies slightly outside these error bars. The mean MIT ice volume flux is 2 km^3/day (23%) and 1.8 km^3/day (22%) lower than the satellite volume flux, respectively. Therefore, the MIT results lie clearly outside the

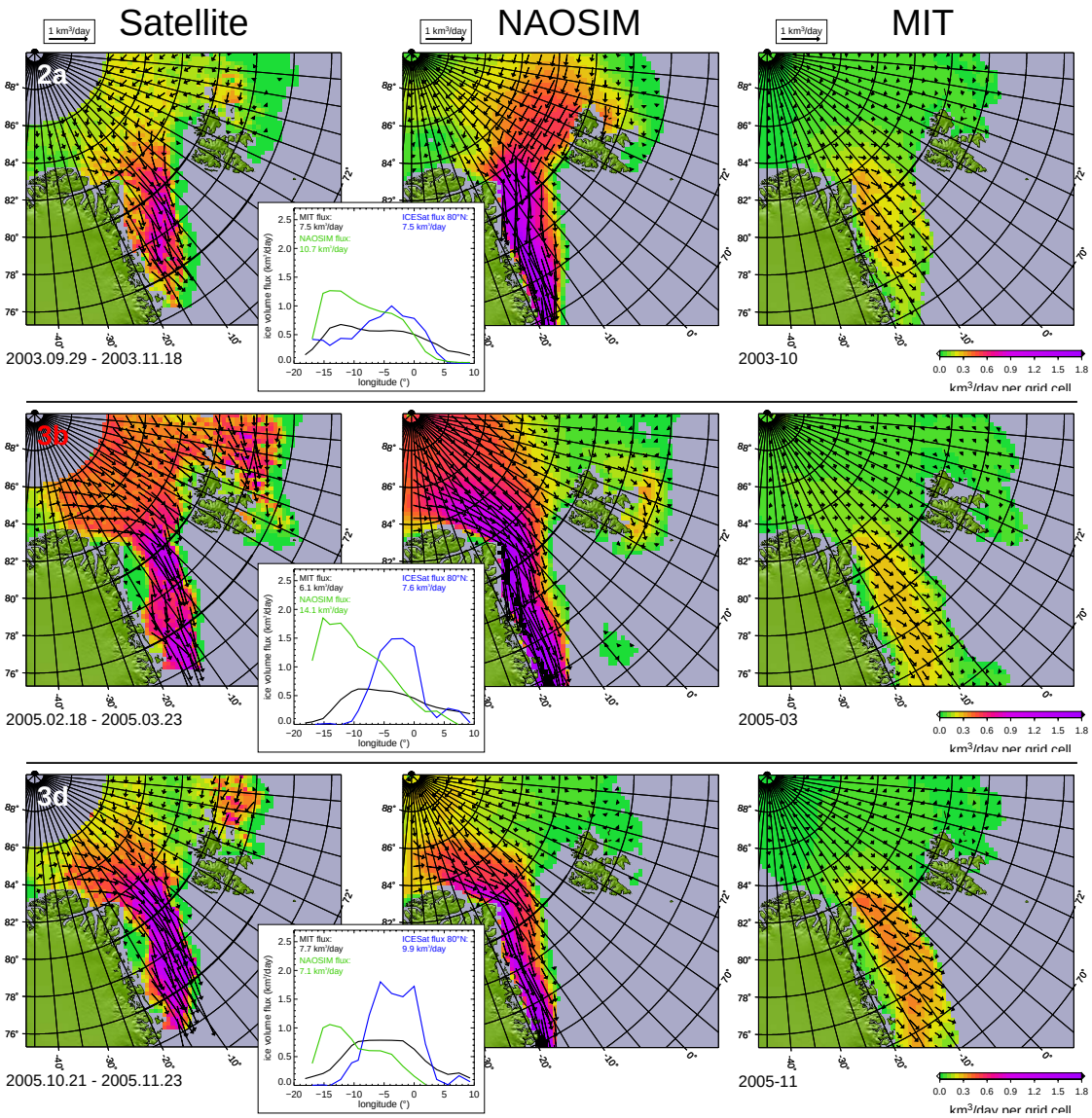

Figure 6.12: Comparison between ice volume flux derived from satellite data (left column) and two coupled ice-ocean models: NAOSIM (middle column) and MIT (right column) for three ICESat periods. The ICESat period name is given in the upper left corner of each row (in white for fall and in red for winter periods), the exact dates of the periods used for the satellite and NAOSIM data is given below each satellite map, the year and month of the MIT data used for comparison is given below each MIT map. The inlay graphs show the ice volume flux through a transect at 80°N in black for MIT, green for NAOSIM, and in blue for the satellite data.

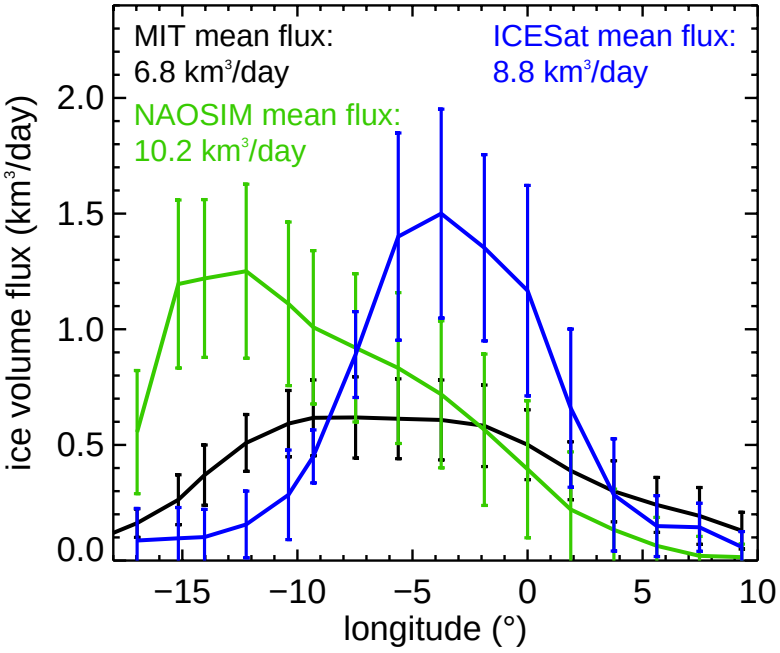

Figure 6.13: Comparison of the sea ice volume flux through a transect at 80°N in Fram Strait derived from satellite data (blue), and from the NAOSIM (green) and the MIT (black) model. Shown is the mean and one standard deviation (error bars) of eight ICESat periods between 2003 and 2006.

Table 6.6: Modeled and measured Fram Strait sea ice volume flux: Mean and standard deviation of the total sea ice volume flux through Fram Strait for eight ICESat measurement periods between 2003 and 2006. Results are given for the ice fluxes derived from satellite data in this study and for the NAOSIM and MIT model for transects at 80°N and 76°N.

	Transect 80°N [km^3/day]	Transect 76°N [km^3/day]
Satellite	8.8 ± 1.1	8.3 ± 1.5
NAOSIM	10.2 ± 1.1	9.5 ± 1.3
MIT	6.8 ± 0.6	6.5 ± 0.8

estimated error margins. But one has to keep in mind that these error estimates do not contain any assumption about systematic errors, which might exist.

More interesting than the differences in the absolute value of the ice volume flux are the differences in the spatial distribution of the volume flux between models and observations and also between the two models. Figure 6.13 and also the examples in Figure 6.12 show that the ice volume flux given by NAOSIM is much more concentrated along the coast of Greenland compared to the satellite data and the MIT model results. The highest volume fluxes in the NAOSIM model occur at about 13°W longitude while the satellite data shows a maximum at about 4°W. The distribution of the MIT volume flux is very broad with highest values between 10°W and 0°E being also only half as large as the values given by the satellite and NAOSIM data. In the NAOSIM model the low volume fluxes in the region of the Northeast Water Polynya and the fastice regions along the Greenland coast are not well reproduced. The MIT model shows a low volume flux region along the Greenland coast but do not reproduce the narrow band of high volume fluxes

which can be found in both the satellite and NAOSIM data (albeit shifted). Also the the mean flux direction in the EGC is shifted westerly towards the open Greenland Sea in the MIT results compared to the satellite and NAOSIM data. This would result in stronger sea ice melting in the open Greenland Sea and less sea ice transport through Denmark Strait out of the Greenland Sea. A correct representation of the shape of the sea ice volume flux distribution in the EGC is of special importance if model data is compared to single-point in situ measurements. If a model would be tuned to represent the ice thickness and ice velocity measured by ULS (see Section 6.5.3 on page 117) and Acoustic Doppler Current Profiler (ADCP) at a mooring at e.g. 79°N, 5°W, the inferred total Fram Strait ice volume flux would be substantial differ from the real one if a wrong zonal flux profile is used.

The representation of the general volume flux distribution in the Arctic Ocean part north of Fram Strait seems to be better in the NAOSIM than in the MIT model data (see Figure 6.12 on page 122). While the direction and amount and also the change of direction of the volume flux north of Fram Strait agree reasonable well between the satellite and NAOSIM data, the MIT data is showing almost the same drift pattern during all eight periods: the ice in Fram Strait originates from the region north of Greenland with almost no contributions from the Transpolar Drift Stream. While the NAOSIM model and satellite data agree well in the Arctic Ocean part of the study region, differences are larger in the Barents Sea. But due to lower data coverage also the error of the satellite data is expected to be larger in the Barents Sea. Again the volume flux distribution of the MIT model agrees less with the two other datasets. The amount and variability of the volume flux of the MIT model seems to be too small in the whole study region, not only in Fram Strait. However, except for the amount, the shape and location of the MIT volume flux in Fram Strait agrees better with the satellite data than the NAOSIM volume flux. For both models and especially the MIT model the ice covered area is too large in the Greenland Sea in comparison to the satellite data, which are very accurate in that respect. This can be seen along the EGC and also around Svalbard.

It is likely that the westward shift of the main ice flux stream, which occurs in the NAOSIM model and to lesser extent also in the MIT model, can partly be attributed to incorrect atmospheric forcing. The location of the mean pressure patterns and the amount of the pressure gradient over Fram Strait might be different in the NCEP-NCAR forcing than in reality. For the MIT model additional model runs using the ECMWF ERA40 reanalysis data as atmospheric forcing were performed (not shown). In this runs which were done on a 1/3° grid the location of the maximum ice volume flux in the EGC is shifted eastwards compared to the results using NCEP-NCAR forcing. It has to be mentioned that already the change of the model resolution from 1/6° to 1/3° for the NCEP forced case causes an eastward shift, but which is less pronounced than it is for the ERA40 forcing. Thus both a higher spatial grid resolution and the NCEP-NCAR atmospheric forcing seem to favor a sea ice volume flux maximum along the Greenland coast.

In Figure 6.14 the monthly interpolated Fram Strait sea ice volume flux derived from satellite data and presented in Section 6.4.2 is compared with the monthly volume fluxes from the NAOSIM and MIT model. The general volume flux curve progression of the three series is similar. The seasonal cycle is well reproduced in all three datasets. The correlation coefficients are 0.60 for the satellite and NAOSIM time series, 0.76 for the

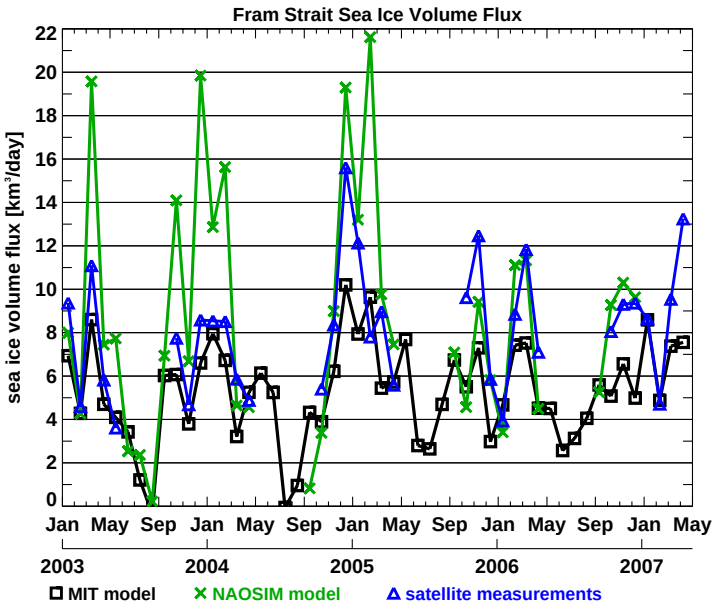

Figure 6.14: Time series of the monthly mean ice volume flux through Fram Strait at 80°N between January 2003 and April 2007. The satellite data from this study is shown in blue (no summer data). Black and green curves show the respective NAOSIM and MIT model ice volume fluxes. The NAOSIM time series ends in December 2006 and has no summer data for 2004 to 2006.

satellite and MIT time series, and 0.81 for the NAOSIM and MIT time series. The correlation between the two model datasets is highest, which might be caused by the identical atmospheric forcing used. The location of the maxima and minima of the volume flux agree well in all three time series. Especially the dip in volume flux in December 2005/January 2006 is very well reproduced by all three time series. Nevertheless, differences in the amount of the volume fluxes are large. The variability of the NAOSIM time series is highest. Followed by the satellite observation, if a small volume flux is assumed during summer months as it occurs in the modeled time series. The variability of the MIT series is lowest. For the NAOSIM time series volume fluxes are much higher during winters 2003, 2004, and 2005 than during 2006 and 2007. This development can not be found in the other two time series. The seasonal cycle of the MIT time series stays almost constant with slightly increased fluxes during winter 2005 and higher summer volume fluxes during 2005 and 2006 than during 2003 and 2004. Also the satellite and NAOSIM time series show an enhanced volume flux during winter 2005. In contrast to the former years also the amount of the volume flux agrees well between the satellite and NAOSIM time series during 2005 and 2006. The linear trends of the three time series are not significant due to the high variances and short time period. The linear trend is with 7%/year largest for the satellite measurements using chi-square error statistics. The MIT model shows with 5%/year the second largest trend, while the NAOSIM time series has no trend during the observed four years. However, as e.g. *Köberle and Gerdes* (2003) pointed out, by looking at a 50 year long model simulation of the Fram Strait sea ice export, trends in the Fram Strait sea ice volume flux are difficult to interpret. The sea ice export shows decadal and multidecadal variability, depending on both thermal and wind stress induced forcing, and therefore long time series are needed to interpret Fram Strait sea ice volume flux trends.

The contrasting behavior of the two models with higher volume fluxes for the NAOSIM data than the satellite data and lower volume fluxes for the MIT data than the satellite

data and the different locations of the main ice volume flux stream show that there are likely still large uncertainties in the model physics and forcing. The satellite data can be useful to get deeper insight in these different behavior, especially in terms of the volume flux distribution and variability.

6.7 Comparison to Oceanographic Measurements

The lateral ice volume flux observations presented in this study offer the possibility to monitor the location where and how much ice melts and forms in the EGC (and also elsewhere) and thereby influences the salinity of the upper ocean mixed layer.

In the context of the German research project *Sonderforschungsbereich 512* an ice strengthened mooring was deployed at 74.5°N, 11.4°W in the East Greenland Current between 2000 and 2006 (*Holfort and Meincke*, 2005). Salinity measurements at the uppermost level of the mooring at about 16 m depth (depending on the tilt of the mooring) are used for comparison to the satellite based volume flux sea ice observations of this study.

The monthly sea ice volume flux time series with interpolated ice thicknesses which was presented in Section 6.4.2 is used for comparison. Additionally to the sea ice volume flux through transects at 80°N and 76°N the total sea ice volume between these two transects is calculated by multiplying the sea ice area and sea ice thickness for each grid cell in the Greenland Sea and than integrating between the two transects. Figure 6.15 shows the measured salinity at 74°N together with the volume flux difference between the 76°and 80°N transects (top) and the total sea ice volume between the two transects (bottom). We do not use volume flux observations closer to the salinity measurements at 74°N because the approach described in this study does not allow reliable volume flux estimates further south than 76°N.

The seasonal cycle of both satellite observations agree well with the seasonal cycle of the salinity measurements. In October, after the melting during summer, the volume flux difference 76 − 80°N is negative with higher fluxes through the northern transect, while at the southern transect almost no ice is left to pass through the transect. From then on the difference is increasing towards a positive maximum during winter, which most often occurred during April at the end of the ice formation season. This agrees well with the lower salinity measured during summer, which from September on starts to increase towards the high salinity values measured during winter.

That the drop in salinity during summer is to a large part caused by melting of ice in the Greenland Sea is even stronger evident in the time series of the ice volume between 76°and 80°N (Figure 6.15 bottom panel). The ice volume data is available all year around, as no ice drift data, which is not available during summer, is needed for its calculation. Both the summertime decrease and the wintertime increase in the observed upper ocean salinity tend to lag the respective decrease and increase of the sea ice volume between 76°and 80°N by about one month. This time gap agrees well with the estimated water travel time of 25 days between 78°N and 74.5°N in the EGC using the mean velocity of 16 cm/s measured by the ADCP at mooring during 2001 and 2002 (*Holfort and Meincke*, 2005).

The salinity during winter 2006 is lower than during the preceding winters. This

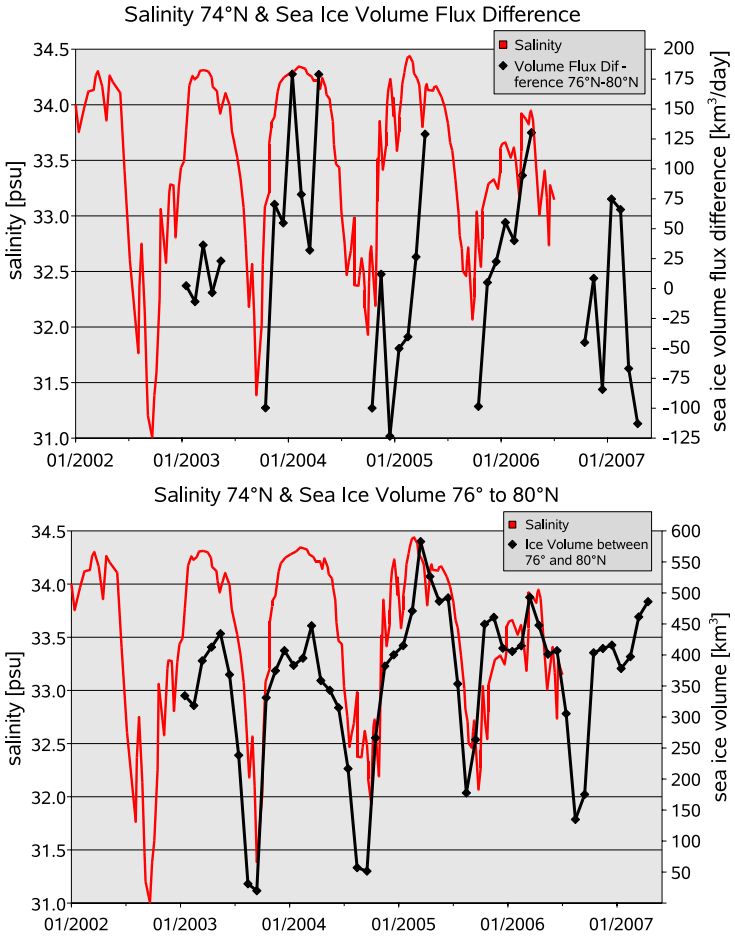

Figure 6.15: Comparison of sea ice volume flux and sea ice volume change with salinity measurements in the upper mixed ocean layer. The salinity measured at a moorring in about 16 m depth at 74.5°N, 11.4°W in the East Greenland Current is shown in red (left y-axis) together with (top) the difference between 76°N and 80°N of the monthly sea ice volume flux (black line, right y-axis), and (bottom) the total amount of sea ice volume between 76°N and 80°N (black line, right y-axis).

inter-annual variability can not be fully explained by the ice volume flux or ice volume observations. On the one hand the ice volume in 2006 is smaller than in 2005, which agrees well with the observed salinity change. On the other hand the ice volumes during 2003 and 2004 are even lower than the one during 2006 without a coincident lower salinity. Also the inter-annual variability of the volume flux difference can not explain the low 2006 salinity. The lowest winter differences occur during 2003 but they are only near zero, which means that no additional ice is formed in the Greenland Sea but also no ice melts between the two transects. During all other years the difference is positive: more ice leaves through the transect at 76°N than enters through 80°N. Therefore ice has to be formed between the two transects. Due to the brine input into the ocean this should lead to an increase in salinity. The ice volume flux difference in winter 2006 is as high as during winter 2005 but the salinity is lower. The cause for the low salinity in winter 2006 therefore has to be found either in the liquid freshwater part in the EGC or in ice volume changes North of 80°N.

In terms of the seasonal cycle our satellite ice volume fluxes agree well with the measured ocean salinities. The drop in salinity during summer clearly can be attributed to a loss of ice volume due to melting between the two volume flux transects. Further insight to the ice-ocean interaction could be gained by examination of additional

oceanographic measurements. For example *Holfort and Meincke* (2005) use ADCP measurements together with salinity measurements of two moorings at the same latitude to obtain the liquid freshwater flux in the EGC during 2001 and 2002 (before our time series starts). Also, if available, the salinity measurements at the mooring at about 79°N in the EGC operated by the NPI could give valuable information for the understanding of the oceanographic processes in that region. *Holfort and Meincke* (2005) state that their liquid freshwater fluxes are of minor value if not the solid freshwater fluxes are available at the same time. Thus in future efforts should be made to obtain both in parallel.

Chapter 7

Conclusion

It was the primary goal of this study to develop an entirely satellite based method to obtain the sea ice volume flux. This goal was successfully achieved and for the first time the spatial distribution of the sea ice volume flux can be directly observed with satellite data.

The sea ice volume flux is an integrative quantity which can be split into the three components sea ice covered area (sea ice concentration, Chapter 3), sea ice drift (Chapter 4), and sea ice thickness (Chapter 5). Figure 1.1 on page 3 shows a scheme how the involved quantities have to be combined and in which chapter they are described.

7.1 Summary

After an introduction to the Arctic climate system and the utilized satellite data and sensors in Chapter 2, the used sea ice concentration data is addressed in Chapter 3. A new sea ice concentration algorithm is introduced and validated. The ARTIST Sea Ice (ASI) algorithm uses microwave radiometer measurements at 89 GHz obtained from the satellite sensor AMSR-E to obtain daily maps of the sea ice concentration with a spatial resolution of about 5 km. This is the highest spatial resolution for global, daily ice concentration data available today. Microwave radiometer measurements are (almost) independent of clouds and daylight. The ASI algorithm was first developed for SSM/I data (*Kaleschke et al.*, 2001), in *Spreen* (2004) it was adapted to AMSR-E data. In this study the algorithm is further validated to ensure that AMSR-E ASI ice concentrations are well suited for the aimed sea ice volume flux retrieval. Parts of the results presented in this study are published in *Spreen et al.* (2008).

AMSR-E ASI ice concentrations were compared to visual sea ice observations made from the bridge of R/V Polarstern during three cruises in the Arctic between 2003 and 2007 (Section 3.5 on page 36). The mean difference between the ASI results and the Polarstern observations for all three cruises was found to be $5\% \pm 16\%$. Comparisons between the Polarstern observations and data from the two "official" AMSR-E sea ice concentration algorithms NASA-Team 2 and Bootstrap show very similar results but these algorithms only offer a spatial resolution of less than 15 km. During the one winter cruise out of the three cruises all three algorithms underestimate the sea ice concentration by about 3% and during the two summer cruises they overestimate the ice concentration by about 9%. The standard deviation stays very constant for all algorithms and seasons at about 16%. The mean bias of about 5% between the AMSR-E ASI and Polarstern observation lays within the assumed error margin of both datasets. The sign of the bias depends on the season. The two alternative AMSR-E algorithms with a lower spatial

resolution show a similar accuracy and bias. Differences between the ASI results and the Polarstern observations are larger for small ice concentrations than for high ones, a result also confirmed in a sensitivity analysis and by error estimation (Sections 3.3 and 3.4). To get further insights into the differences between the different AMSR-E algorithms, the ASI ice concentrations were compared with the NASA-Team 2 and Bootstrap ones for the time period 2002-06-19 to 2006-08-31 (Section 3.6 on page 40). For the northern hemisphere the ASI algorithm on average is underestimating the sea ice concentration by 1.4% and 2% in comparison to the Bootstrap and NASA-Team 2 results, respectively. For the southern hemisphere the ASI results lay in-between the Bootstrap and NASA-Team 2 results with a difference to both of about 1.6%. But for all cases the standard deviation of about 9% is much larger than the mean differences. Differences between the algorithms are in general larger in the Marginal Ice Zone (MIZ), e.g. large differences occur in the Greenland Sea and in the Barents Sea west of Novaya Zemlya. However, the mean differences and standard deviations are comparable to the estimated error of the method of 5% to 10% (for low ice concentrations the error can be higher). As the Bootstrap and NASA-Team 2 algorithms are well validated this good agreement gives also more confidence in the ASI results. We therefore conclude that the AMSR-E ASI ice concentrations are well suited for the sea ice volume flux retrieval. The ASI ice concentrations offer a comparatively high spatial resolution of about 5 km without on average loosing accuracy compared to lower resolving AMSR-E ice concentration algorithms. Nevertheless, under atmospheric conditions with high cloud liquid water and water vapor content the ASI algorithm performs worse than the other two algorithms.

The next component needed to derive the sea ice volume flux is the sea ice drift (see Figure 1.1 on page 3). In Chapter 4 the used sea ice drift dataset is described and validated especially for the Fram strait region. Like the ice concentration, the sea ice drift data used in this study are obtained from the 89 GHz channels of AMSR-E. The ice drift data is provided and processed by IFREMER (*Ezraty et al.*, 2007a). A maximum cross-correlation analysis of the second derivative of two 89 GHz brightness temperature maps with two day time gap is performed to obtain daily sea ice drift maps for the entire Arctic with a spatial resolution of 31.25 km. Previous studies (*Ezraty et al.*, 2007a) assessed the quality of the drift data by comparing them to buoy measurements of the ice drift in the central Arctic. To assure that the accuracy of the ice drift data is also high in the more dynamic Fram Strait region and Greenland Sea, in this study the AMSR-E IFREMER ice drift is compared to ice drift measurements obtained from spatially higher resolving SAR data. An advantage of the validation using SAR data is the better representation of the spatial distribution of the ice drift in comparison to the buoy validation. A set of 37 SAR scene pairs obtained in March/April 2003 was manually analyzed for the sea ice drift. The quality of the SAR ice drift was assured by comparison to ice drift obtained by a drifting buoy array during the same time period, which showed a very good agreement and no bias for the SAR ice drift data. The high resolving SAR ice drift data is used as reference for the AMSR-E ice drift. The mean velocity difference between SAR and AMSR-E ice drift was found to be (1.1 ± 3.4) cm/s. And the mean angle difference between SAR and AMSR-E ice drift amounted to $4° \pm 47°$. For the ice drift velocity the found standard deviation of 3.4 cm/s is very similar to the 3.6 cm/s found by *Ezraty et al.* (2007a) by comparison to buoy data, but in their study they did not find any bias while we found a mean difference of about 1 cm/s. This might be due

to SAR measurements in the MIZ, where often no coincident AMSR-E measurements existed and thus the AMSR-E drift had to be interpolated to those locations. For the sea ice volume flux retrieval the AMSR-E ice drift has also to be interpolated for all ice covered regions. Therefore the sea ice drift differences found for the SAR comparison should be a realistic representation of the AMSR-E sea ice drift accuracy in the Fram Strait region.

As third and last quantity for the sea ice volume flux estimation the sea ice thickness has to be known (see Figure 1.1 on page 3). The retrieval of sea ice thickness from ICESat laser altimeter measurements is the most innovative part of this study (Chapter 5). Unlike the sea ice concentration and drift retrieval no method to measure the sea ice thickness from space existed beforehand. The complete method was a new development and in fact the first published ICESat sea ice thickness maps can be found in *Spreen et al.* (2006), wherein first results of this study were presented. In this study a significantly improved method is presented. The determination of the sea ice thickness can be separated into two parts: (1) the retrieval of sea ice freeboard heights from ICESat measurements (Section 5.1) and (2) the conversion of sea ice freeboard to sea ice thickness (Section 5.2).

ICESat's laser altimeter GLAS measures the distance between the satellite and the Earth surface with centimeter accuracy. Together with the accurate knowledge of the satellite position in space, the elevation of the Earth surface in reference to an ellipsoid is obtained (see Figure 5.1 on page 64). To estimate the sea ice thickness from laser altimetry as first step the sea ice freeboard height, which is the part of the ice above the water line, has to be obtained. For thick sea ice the ice freeboard (including the snow on top) lies in the decimeter range. Therefore, to measure the comparatively small freeboard height, the Sea Surface Height (SSH) of the surrounding water has to be determined with high accuracy. The SSH consists of an (almost) time invariant part, the geoid height, and a time varying, dynamic part, which is caused by tides, ocean currents and surface pressure changes. An accurate geoid therefore is a prerequisite for an accurate SSH determination. In this study the most recent ArcGP geoid is used (*Forsberg and Skourup*, 2005). For the determination of the dynamic SSH part no data with sufficient accuracy exists today. Tides and the atmospheric surface pressure (inverse barometer effect) are partly corrected for, but the remaining dynamic SSH variations have to be inferred from the ICESat measurements themselves. It is a reasonable assumption that the laser footprint of about 67 m hits open water or thin ice areas (leads) in the sea ice pack several times during each overflight. These open water/thin ice measurements are identified using an iterative minimum-elevation method. After the SSH is determined the sea ice freeboard height is derived by subtracting the SSH from the ICESat elevation measurements. All ICESat freeboard measurements of each ICESat measurement period of about one month are binned on a 25 km grid. In total nine ICESat measurement periods between 2003 and 2007 were analyzed.

In a second step the sea ice freeboard has to be converted to sea ice thickness. For free floating ice the ice thickness can be calculated from the ice freeboard following the Archimedes' principle if the densities of ice and water are known. The density of sea water near the freezing point is known with good accuracy but the density of the sea ice is quite variable and changes mainly in dependence of the ice age. We use QuikSCAT satellite radar backscatter data to separate two ice classes with different mean density

values: first-year and multi-year sea ice. Another large uncertainty for the freeboard to thickness conversion is the snow on top of the sea ice. ICESat's near-infrared laser measurements origin from the snow surface. Thus the retrieved freeboard is composed of the snow depth and the sea ice freeboard. As there are no reliable satellite measurements of snow depth for our study region the Fram Strait we use a combination of in situ measurements and a climatological seasonal cycle to estimate the snow depth for the ICESat measurement periods. By applying the snow depth, a fixed snow density, the two ice densities, and the water density, the sea ice thickness can be calculated from the sea ice freeboard for our nine ICESat periods. The mean (modal) sea ice thickness during all nine ICESat periods found in the study region was 2.3 m (2.4 m) with values ranging from 1.9 m (1.8 m) in Feb./Mar. 2004 to 2.6 m (3.0 m) in Feb./Mar. 2005.

The three quantities sea ice concentration, sea ice drift, and sea ice thickness now can be merged to the sea ice volume flux (see Figure 6.1 on page 95). Data from three satellite sensors (AMSR-E, GLAS/ICESat, QuikSCAT) were used to derive this goal. Maps of the sea ice volume flux in the Fram Strait region for the nine ICESat periods were presented (Figures 6.2 and 6.3 on page 98). For the first time the spatial distribution of the sea ice volume flux is directly observed. The sea ice volume flux is showing large variability between the observation periods in both amount and spatial distribution, especially for the northern part of the study region. There the source regions of the ice volume flux are changing between north of Greenland and more easterly from the Transpolar Drift for different ICESat periods. In the Fram Strait itself and further south in the East Greenland Current (EGC) the location of the maximum sea ice volume flux pattern is rather stable and not changing its location much. Nevertheless, the amount of the sea ice volume flux is variable there, too.

The absolute amount of the sea ice transport through Fram Strait into the Greenland Sea is important for water mass modification processes there and further south. Therefore, profiles of the meridional sea ice volume flux through transects at 80°N and 76°N were calculated (Section 6.4.1). Unfortunately, ICESat is only operating for three measurement periods of each about one month length a year at maximum. Therefore there will be always large gaps in the ice volume flux time series. We tried to reduce these gaps by interpolating the sea ice thickness throughout the year. The ICESat ice thickness measurements were used as base points for the accordant months and the ice thickness of the remaining months were interpolated by utilization of a seasonal cycle obtained from ULS ice thickness measurements in Fram Strait. As another difficulty, during summer months the ice drift retrieval using AMSR-E 89 GHz data is hampered if not impossible due to melting conditions which cause a loss of the distinct surface features required for the maximum cross-correlation analysis. Thus for summer months our method would have to use alternative ice drift estimates, e.g. the one proposed by *Kwok* (2008). In this study we keep the gap during summer and do not obtain Fram Strait sea ice volume flux estimates between May and September. However, by using the ice thickness interpolation we derived a monthly Fram Strait sea ice volume flux time series between January 2003 and April 2007 (without the summer months, see Section 6.4.2 on page 109). During this period a mean monthly sea ice volume flux of $(248 \pm 90)\,\mathrm{km}^3$/month was observed for a volume flux transect at 80°N. The lowest volume flux occurred with $112\,\mathrm{km}^3$/month during May 2003 and the highest with $484\,\mathrm{km}^3$/month during December 2004. The Fram Strait sea ice volume flux time series derived from ULS measurements ends in 1999. Our

four and a half year long time series from 2003 to 2007 can be used as an extension of the former time series leaving a gap of three years between 2000 and 2002. The Fram Strait sea ice volume flux time series then spans the time period August 1990 to April 2007 (Figure 6.10 on page 114).

The mean relative error for the sea ice volume flux of each 25 km grid cell was estimated to be about 24% by using Gaussian error propagation for conservative errors of all input variables (Table 6.1 on page 100). The mean relative error for the total volume flux through Fram Strait for one ICESat measurement period was estimated to be about 15% (Table 6.2 on page 107). But a comparison with sea ice volume fluxes calculated with sea ice drift data obtained from QuikSCAT measurements showed that these error estimates might be too optimistic (Section 6.5.1 on page 114). The total Fram Strait volume flux calculated using QuikSCAT ice drift deviates from the volume flux using AMSR-E ice drift by about 35%. This large deviation caused by the two drift datasets might be due to differently interpolated ice drift values for gaps in the ice drift fields and an underestimation of high ice drift velocities. Such differences caused by wrong interpolation are not covered by our Gaussian error propagation. However, the AMSR-E sea ice drift quality assessment in Chapter 4 which also included some possible errors due to interpolation artifacts showed good accuracy for the AMSR-E ice drift data. We therefore assume that a realistic relative error for the total sea ice volume flux through Fram Strait lies somewhere inbetween the 15% found by error propagation and the 35% deviation to the QuikSCAT ice volume flux. A sensitivity study (Section 6.5.2 on page 116) showed that the accuracy of the input variables ice drift, ice density, and snow depth are of equal importance for the quality of our method. The largest improvement for our method is expected to be obtained from a better snow depth representation. Different ice density are already assigned to first- and multiyear ice and the ice drift validation in Chapter 4 showed a good accuracy of the AMSR-E ice drift dataset. The variability of snow depth is so far only represented with a climatological seasonal cycle scaled with the in situ measured snow depths from one campaign. Here is room for improvement. For example, even though it was found that the absolute values of the snow depths retrieved from AMSR-E data seem to be inaccurate for the Greenland Sea, the spatial pattern of the snow depth distribution could be nevertheless used as additional scaling factor for our snow depth estimates. However, with a relative accuracy of at least about 20% to 30% for the total sea ice volume flux through Fram Strait our volume flux estimates can provide valuable geophysical information for the freshwater exchange between the Arctic Ocean and the Nordic Seas.

We note that our approach of estimating sea ice volume transport is entirely satellite based and can therefore be applied to geographical regions other than the Fram Strait and Greenland Sea. We anticipate that our method can easily be adapted to new freeboard measurements like the ones expected to be available from the upcoming CryoSat-II mission in 2009. CryoSat-II will measure continuously and thus the gaps in the time series could be significantly reduced by use of these data.

7.2 Relevance

In summary, a method was developed to directly observe the sea ice volume flux from space by combining data of several satellite sensors. Now, the question arises what is the geophysical relevance of the sea ice volume transport through Fram Strait. Why do we need to monitor the Fram Strait ice volume flux?

The net annual sea ice volume exported through Fram Strait into the Nordic Seas (Greenland, Icelandic, and Norwegian Sea) amounts to about 10% of the total sea ice volume of the Arctic Ocean and is the single largest source of freshwater in the Nordic Seas (*Dickson et al.*, 2007; *Serreze et al.*, 2006; *Aagaard and Carmack*, 1989). Only the liquid freshwater flux through Fram Strait is of the same order. The Fram Strait sea ice export is by far the largest portion of the total Arctic sea ice export. Large parts of the sea ice imported through Fram Strait into the Greenland Sea melt there. The input of fresh or dense water to the ocean enhances or hampers ocean stratification, respectively. Fresh or dense water input to the Greenland Sea corresponds to melting and forming of sea ice there or an enhanced or reduced Fram Strait sea ice volume flux relative to the climatological mean. Anomalies in the sea ice transport through Fram Strait therefore result in a major change in the surface salt content of the Greenland Sea and can modify convective overturning and major water mass formation processes there. This in turn can result in significant changes in the export of dense water from the Nordic Seas into the Atlantic Ocean and then impact the global ocean thermohaline circulation (*Dickson et al.*, 1988, 2007; *Karstensen et al.*, 2005). For those reasons monitoring anomalies and trends in the Fram Strait sea ice volume flux is an important task for better understanding the hydrological cycle of both the North Atlantic and globally. For example, the largest known fresh water anomaly event in the North Atlantic during the last century was the "Great Salinity Anomaly" from the late 1960s to the early 1980s (*Dickson et al.*, 1988), which probably was due to an increased ice transport through Fram Strait.

In Section 6.7 on page 126 a first attempt was made to look into such sea ice – ocean exchange processes. The sea ice volume flux difference between the 76°N and 80°N transect (divergence) and the change in total sea ice volume between the two transects were compared to salinity measurements in the upper mixed ocean layer at 74.5°N. The seasonal cycle of the sea ice and ocean salinity time series including the sea ice melting events during summer are in good agreement. Our four and a half year long time series is too short to clearly identify inter-annual changes. However, at least the reduced salinity during winter 2005/2006 is accompanied by a smaller ice volume compared to the preceding winter 2004/2005.

The influence of changes in the Fram Strait sea ice transport on the global thermohaline circulation was also observed in several modeling studies, e.g. *Komuro and Hasumi* (2007); *Stössel et al.* (1998); *Hasumi and Suginohara* (1995). Amongst others therefore in sea ice modeling studies the ice volume or ice mass flux is one of the quantities of the most interest (e.g. *Koenigk et al.*, 2006, 2007). However, it was always difficult to validate the model results with observations. Now, with our method the spatial distribution of the sea ice volume flux can be observed and the retrieved ice volume flux data can be used to validate and better understand model results. In Section 6.6 on page 120 sea ice volume fluxes derived from satellite data are compared to model results from the NAOSIM and MIT model. While the total amount of sea ice volume transported through Fram Strait

agrees reasonable well between observations and model data, the spatial distribution of the volume flux shows large discrepancies. It has to be further evaluated if the reasons for the discrepancies can be attributed to problems with the model physics or the model forcing.

7.3 Outlook

The last paragraph about data and model comparisons already leads to an outlook for further studies. Certainly problems with model forcing and physics should be first understood but another possibility to obtain more realistic model results is the assimilation of observations. It is possible to assimilate our sea ice volume flux observations in models themselves. For each grid cell of our study region also a sea ice volume flux error estimate is available, which is an important prerequisite for the model data assimilation. However, it might be more feasible and would improve the understanding of the model physics to assimilate the different variables of the sea ice volume flux separately. For example one could start to assimilate the sea ice drift, which might strongly improve the model results as problems with the atmospheric pressure forcing are reduced (e.g. *Dulière and Fichefet*, 2007; *Zhang et al.*, 2003).

Regarding the ocean observations it would be of great value to also exploit the measurements of a mooring at about 79°N in the EGC, which operated simultaneously to the mooring at 74.5°N and our satellite observations. The gradient between the 79°N and 74.5°N salinity measurements would allow a much better identification of the source region of salinity anomalies in the EGC. *Holfort and Meincke* (2005) used ADCP and salinity measurements to observe the liquid freshwater transport in the EGC. They already state that the liquid freshwater measurements should be combined with measurements of the solid (ice) freshwater transport. With the development of our method such observations are now available, unfortunately not for their observed case in 2002.

Concerning the satellite based sea ice volume flux retrieval itself there are also several possibilities for future improvements. As mentioned before the accuracy of the sea ice drift, sea ice density, and snow depth cause the largest uncertainties and are of equal importance for an accurate sea ice volume flux retrieval. As we already separate two sea ice density classes not much improvement can be expected in this respect on a larger scale. But as there might be a positive bias in the multi-year ice concentration in the Greenland Sea (see Section 5.2.1 on page 86) it would be of great value to further validate the QuikSCAT multi-year sea ice concentration retrieval method by comparison to SAR data. SAR data could also be used to separate more than two different ice density classes for limited case studies. But, and this might be the larger challenge, the average densities of the different ice classes have to be known precisely. In this respect more in situ data of ice densities for different sea ice classes would be of great value, as already for our two used ice density classes the uncertainty of the mean densities of these two classes is large.

In respect of the AMSR-E sea ice drift the comparison to SAR ice drift (Chapter 4) revealed a good quality of the AMSR-E ice drift dataset even in the dynamic Fram Strait region. The drift data agreed within the stated error margins with the SAR reference. However, the AMSR-E ice drift on average was too small by about 1 cm/s. Unfortunately

during the time period of the comparison in March/April 2003 the observed ice drift velocity on average was small. Therefore, further comparisons of the ice drift during other time periods with higher ice drift velocities could confirm the confidence in the AMSR-E ice drift estimates in the Fram Strait region. This is already planed for the years 2005, 2007, and 2008 where also simultaneous AMSR-E and SAR ice drift datasets exist or are in preparation.

To improve the quality of the snow depth data, further satellite data should be exploited. Despite the problems we found with snow depths derived from AMSR-E data in the Greenland Sea, this dataset should be further evaluated. Even if the absolute value of the snow depth can not be successfully retrieved from AMSR-E measurements, they nevertheless should contain valuable information about the spatial snow depth distribution in the Fram Strait region. The spatial distribution could be combined with in situ measurements to get a better snow depth representation for our sea ice volume flux retrieval method. There is also a chance that ICESat still will be operating in parallel to the upcoming CryoSat-II mission in 2009. CryoSat-II will carry a radar altimeter and the radar return echoes should originate from the snow – sea ice interface. Thus from simultaneous ICESat and CryoSat-II measurements the snow depth could be directly inferred.

Regarding the SSH determination using our minimum elevation method, improved estimates can be expected from an even more accurate geoid and improved information about day-to-day variations in dynamic ocean surface topography, e.g. from models. Both improvements together could allow a more accurate estimation of the sea ice freeboard height. For a more reliable open water/thin ice detection the GLAS reflectivity measurements should be further exploited. A drop in the reflectivity value sometimes but not always seems to indicate open water/thin ice areas. Apart from that, in the presented method all GLAS measurements with physically unrealistic reflectivities above 0.9 are excluded from the sea ice freeboard retrieval. It should be evaluated if these discarded measurements could be included in the ice freeboard retrieval again to increase the number of measurements.

The most important point for future activities should be further validation of the satellite based sea ice thickness against in situ measured ice thicknesses. Especially the measurements of the ULS operating at a mooring at 79°N in Fram Strait would be of great value for an ice thickness comparison. Unfortunately these measurements are not processed up to now and therefore not available. Another validation possibility would be the comparison to sea ice thickness measurements from Ice Mass Balance (IMB) buoys (`http://www.crrel.usace.army.mil/sid/IMB/`). Some IMB buoys also drifted through Fram Strait but if coincident ICESat measurements exist has to be evaluated and as an IMB buoy is fixed to an individual sea ice flow, they do not provide spatial ice thickness information.

At the end we would like to emphasize again that our method to retrieve the sea ice volume flux is not restricted to the Fram Strait region. For the first time it is possible to get estimates of the sea ice volume flux on a global scale. An adaption of the presented method to the southern hemisphere is right now under development. The disadvantage of the only about three months per year long measurement period of ICESat might be overcome with the launch of CryoSat-II in 2009. We anticipate that our method can be easily adapted to CryoSat-II measurements. CryoSat-II will measure continuously and

thus the gaps in the time series could be significantly reduced by use of these data. Also a successor of ICESat, ICESat-II, with an improved laser is under discussion right now and hopefully will come to positive negotiation.

A Appendix

A.1 Unusable and Missing Data

Table A.1: Data not used for the sea ice freeboard calculation due to unrealistically high freeboards (mean > 80 cm) calculated by the algorithm. First column contains the ICESat measurement period. The orbit number in the last column starts with one for every single GLA13 dataset each containing 14 orbits.

Period	Date	Orbit
1	2003-02-24	3
3b	2005-02-18	9
3e	2006-03-01	3
	2006-03-08	9
	2006-03-24	9
3h	2007-03-12	1
	2007-03-19	3
	2007-03-21	6
	2007-03-25	9
	2007-04-14	1
total	10 orbits	

Table A.2: List of days where no AMSR-E 89 GHz sea ice drift data (see Chapter 4) were available during the ICESat measurement periods and which therefore are missing for the volume flux calculation in Chapter 6. First column contains the ICESat measurement period. The second column the date or date period, where no AMSR-E drift data is available. Date here is the start date of the 2-daily drift data. The last column gives the number of missing days covered by the date period in the second column.

ICESat Period	Date(s)	Number of Missing Days
2a	2003-10-28 to 2003-11-05	9
3a	2004-10-21	1
	2004-10-23	1
3b	2005-02-18	1
	2005-02-27 to 2005-03-06	8
	2005-03-10 to 2005-03-13	4
3d	2005-11-15	1
	2005-11-17	1
3g	2006-11-11	1
	2006-11-13	1
	2006-11-16 to 2006-11-19	4
3h	2007-03-12	1
	2007-03-14	1
	2007-04-09	1
	2007-04-11	1
total:		36 days

A.2 Freeboard – SAR Comparison

Additional to the in Figures 5.7–5.9 in Section 5.1.3 presented comparison between ICESat freeboard and ASAR backscatter data here more examples of these data sets with a time difference of less than 3 hours is shown.

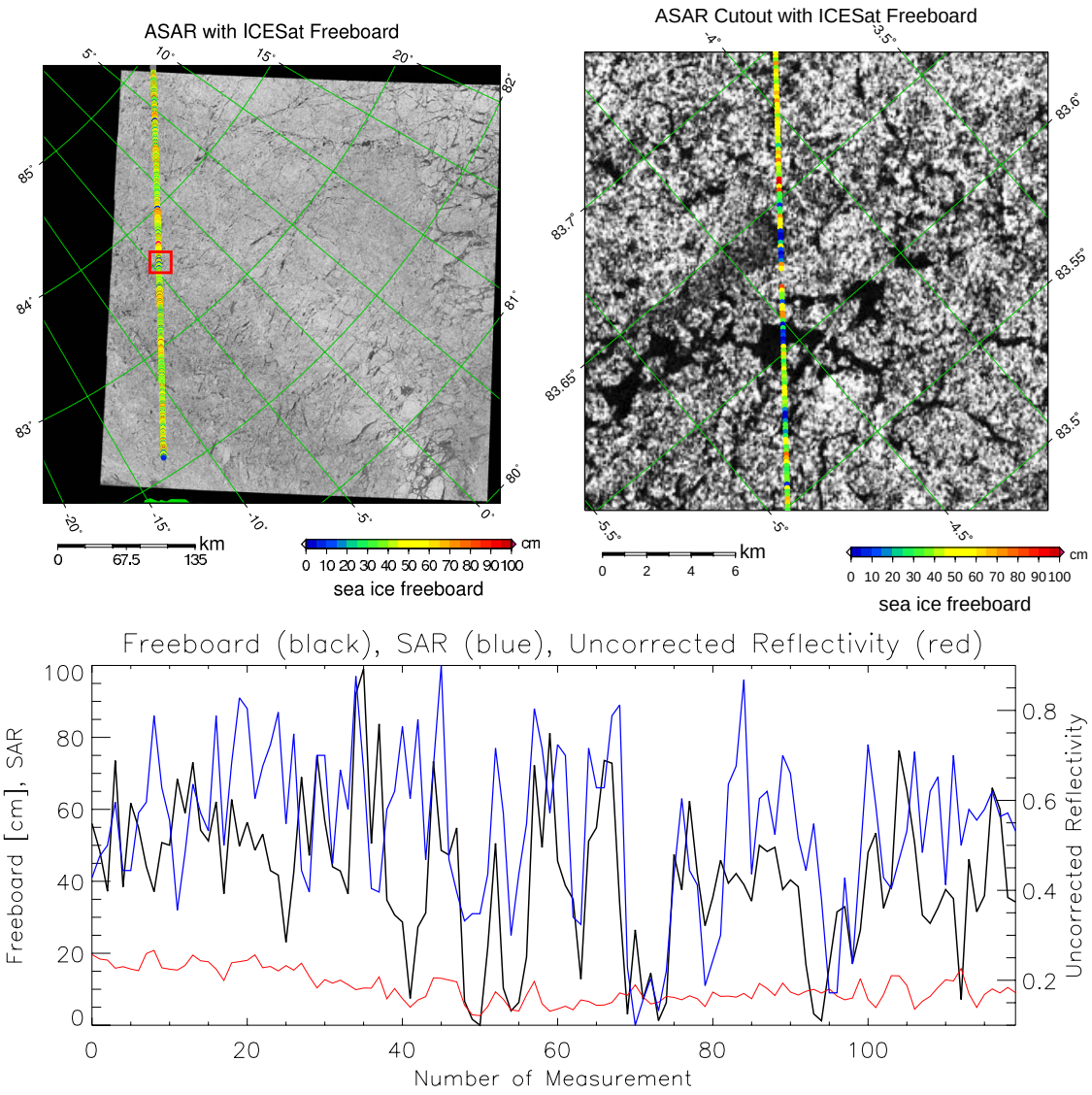

Figure A.1: Comparison ASAR data 2003-02-23, 19:13 UTC with ICESat freeboard 2003-02-23, 18:09 UTC, descending orbit, Δt = 1:04 h:mm. Top-left: complete ASAR scene (400 km × 400 km); top-right: zoom cutout marked with red rectangle in top-left image; bottom: graph with freeboard height (black), ASAR backscatter (blue, scaled between 0 and 100), and uncorrected reflectivity (red), the measurements on the y-axis are each 172 m apart. Dark ASAR areas (top) and low backscatter (bottom) match with low freeboard heights. Ice drift due to time difference not corrected. Note that in this case the uncorrected reflectivity gives no indication of leads.

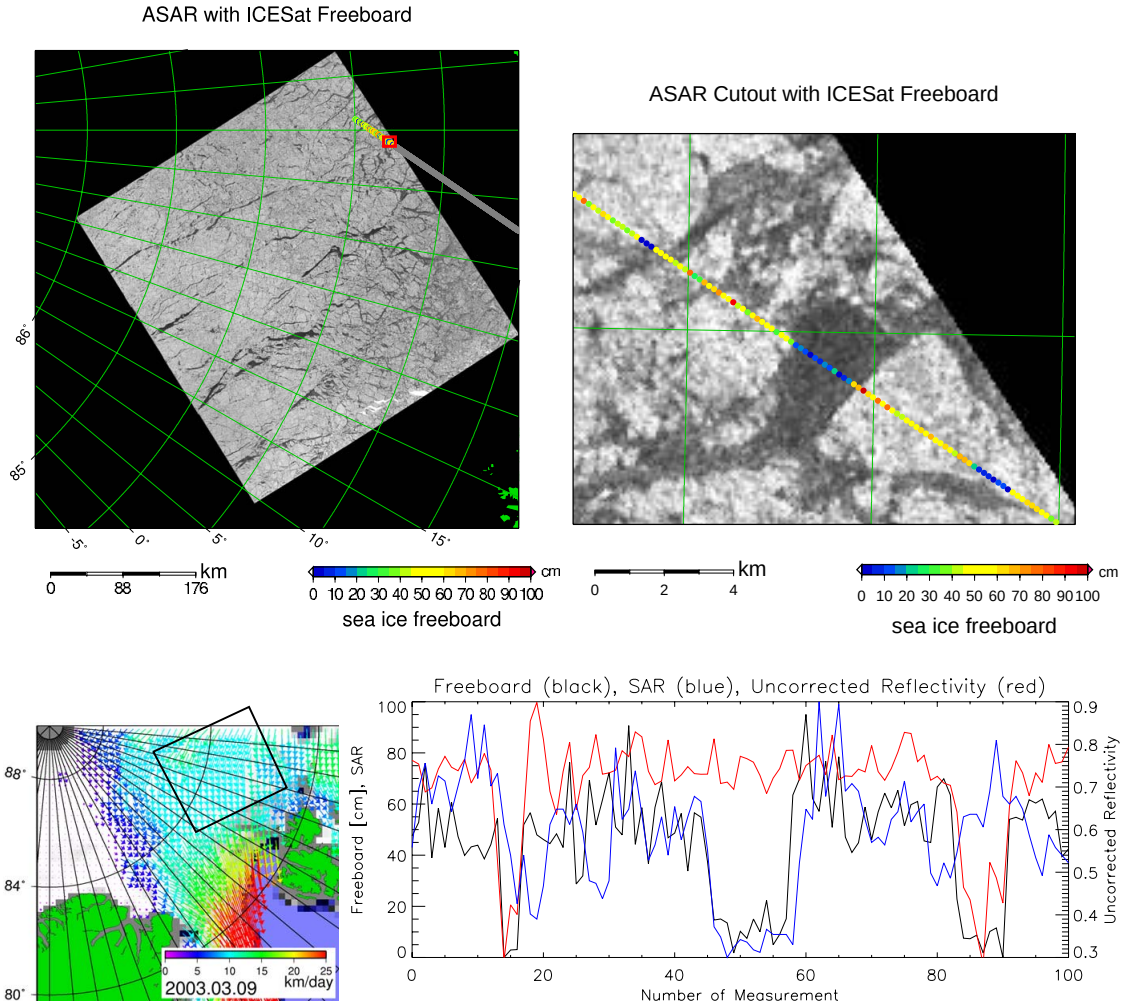

Figure A.2: Comparison ASAR data 2003-03-09, 16:52 UTC with ICESat freeboard 2003-03-09, 14:06 UTC, descending orbit, Δt = 2:46 h:mm. Top-left: complete ASAR scene (400 km × 400 km); top-right: zoom cutout marked with red rectangle in top-left image; bottom-left: AMSR-E 2-day (09–11) ice drift with black outline of ASAR frame; bottom-right: graph with freeboard height (black), ASAR backscatter (blue, scaled between 0 and 100), and uncorrected reflectivity (red), the measurements on the y-axis are each 172 m apart. Ice drift due to time difference not corrected. In the ASAR image region a south-westerly ice drift of around 10 km/day equal to 1.2 km during the Δt of 2:46 h is prevailing. This shift would cause a good match between the leads with low backscatter in the ASAR data with low freeboard heights.

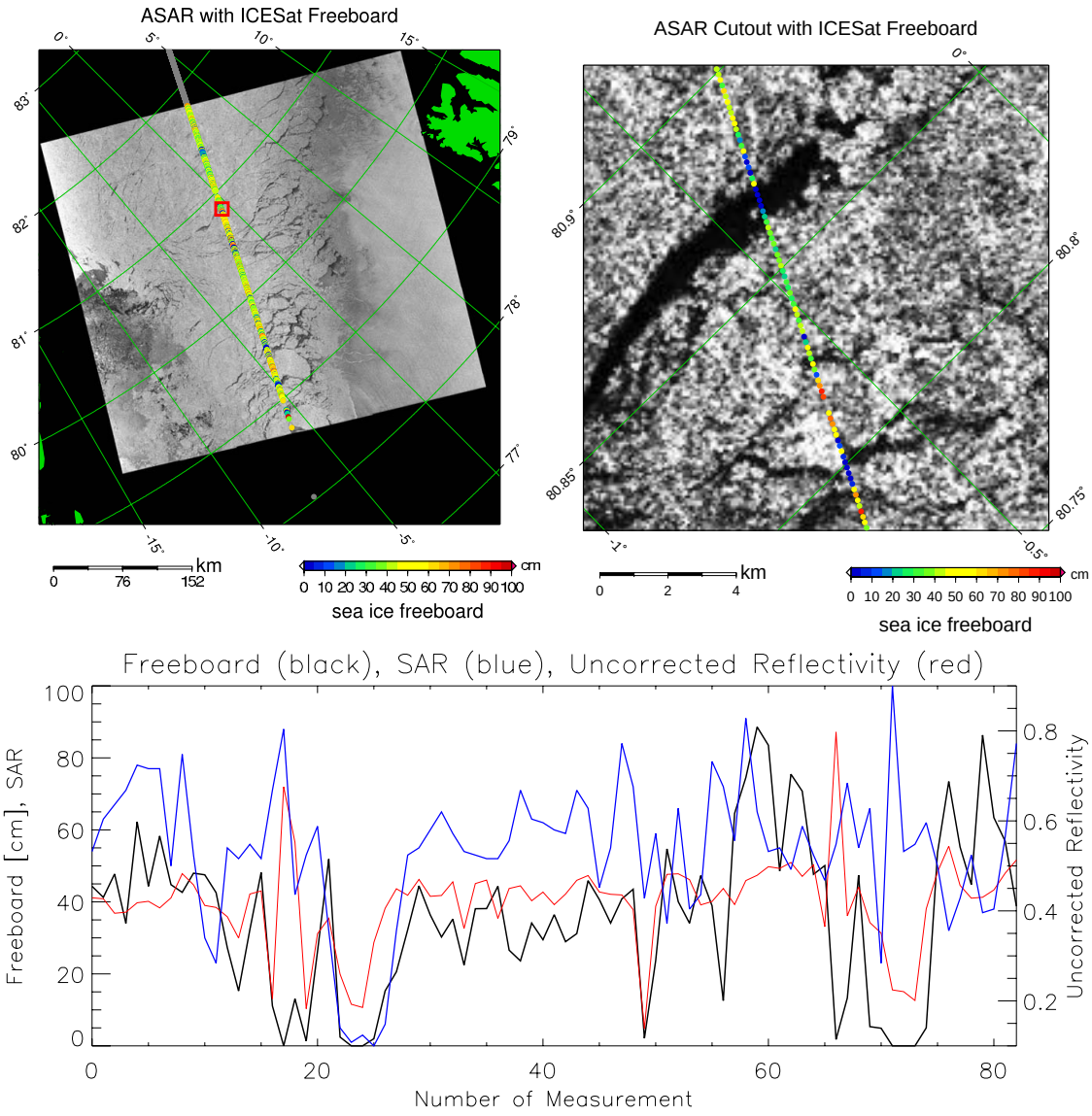

Figure A.3: Comparison ASAR data 2003-10-24, 11:57 UTC with ICESat freeboard 2003-10-24, 09:18 UTC, descending orbit, Δt = 2:39 h:mm. Top-left: complete ASAR scene (400 km × 350 km); top-right: zoom cutout marked with red rectangle in top-left image; bottom: graph with freeboard height (black), ASAR backscatter (blue, called between 0 and 100), and uncorrected reflectivity (red), the measurements on the y-axis are each 172 m apart. Ice drift due to time difference not corrected. The northern lead in the ASAR data is well identified in the ICESat freeboard. For the drop down in freeboards heights in the southern part at least the simultaneous drop down of reflectivity is indicating, that there could have been a lead 2.5 hours before the ASAR acquisition. Ice drift (not shown) was with 0.7 m/s in south-westerly direction low during that period.

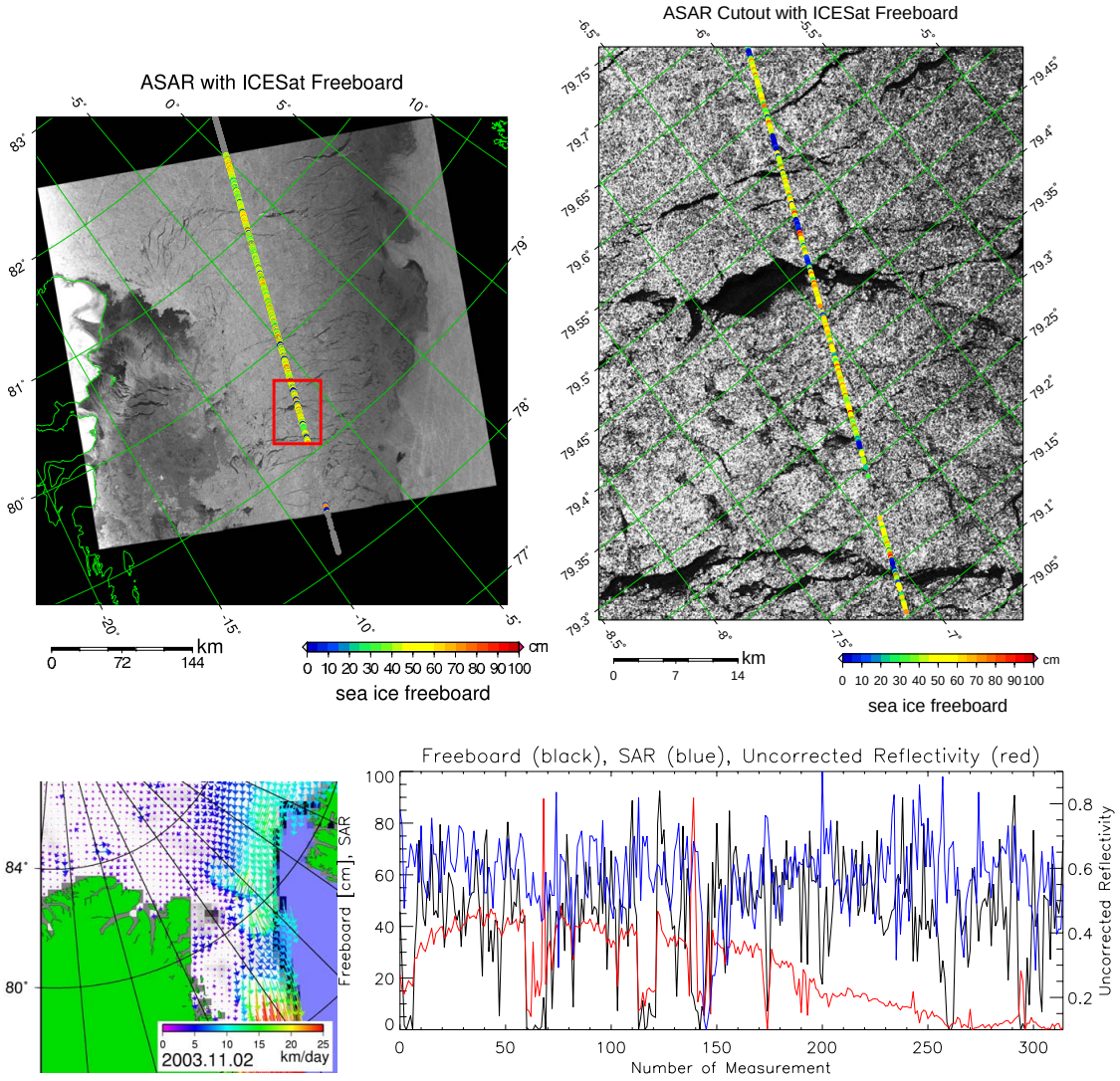

Figure A.4: Comparison ASAR data 2003-11-02, 12:14 UTC with ICESat freeboard 2003-11-02, 09:09 UTC, descending orbit, Δt = 3:05 h:mm. Top-left: complete ASAR scene (400 km × 350 km); top-right: zoom cutout marked with red rectangle in top-left image; bottom-left: QuikSCAT 2-day (02–04) ice drift; bottom-right: graph with freeboard height (black), ASAR backscatter (blue, scaled between 0 and 100), and uncorrected reflectivity (red), the measurements on the y-axis are each 172 m apart. Ice drift due to time difference not corrected. In the ASAR image region a south-westerly ice drift of around 15 km/day equal to ≈ 2 km during the Δt of 3:05 h is prevailing. This shift would cause a good match between the leads with low backscatter in the ASAR data with low freeboard heights. Also the to low freeboards coincident drop down of reflectivity in the northern part of the transect is indicating a good lead identification.

A.3 Additionally Used ICESat Ice Thickness Data

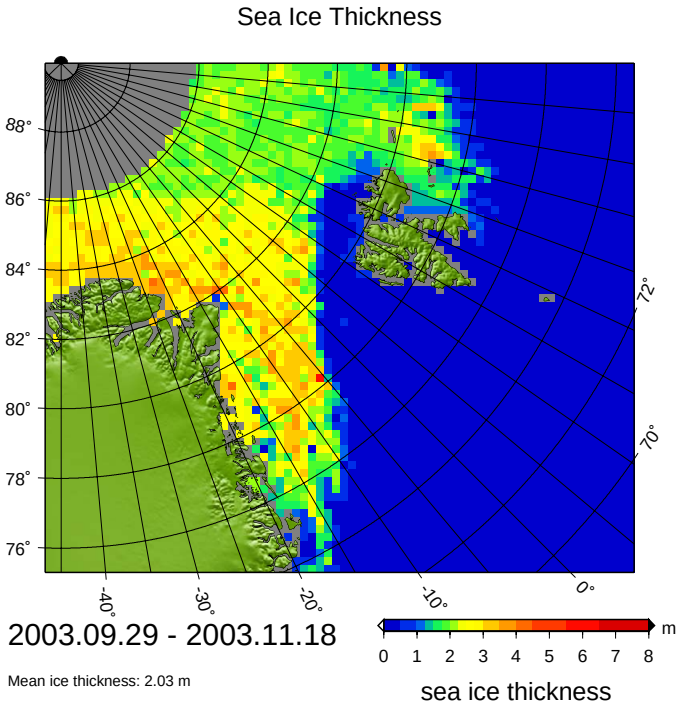

Figure A.5: Map of sea ice thickness for the time overlap 2003-09-29 to 2003-11-18 between ICESat measurement period 2a and the 89 GHz AMSR-E ice drift dataset. This ice thickness is used to calculate the sea ice volume flux in Chapter 6.

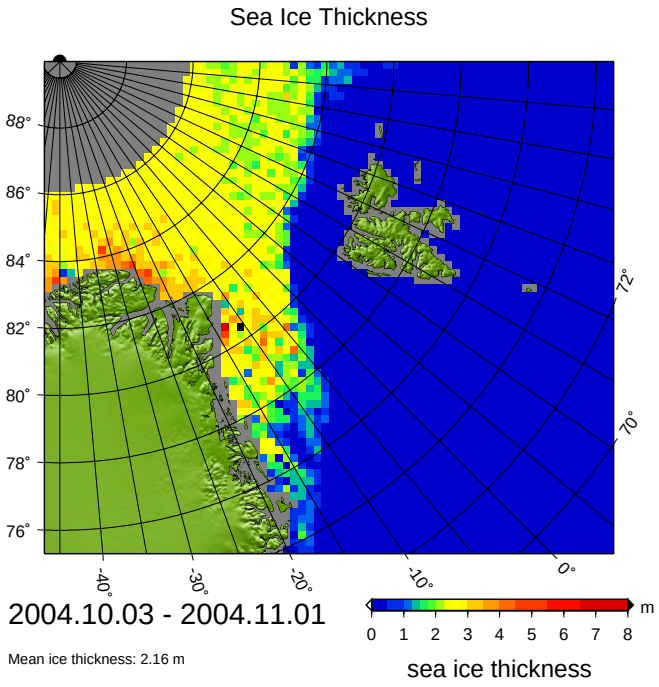

Figure A.6: Map of sea ice thickness for the time overlap 2004-10-03 to 2004-11-01 between ICESat measurement period 3a and the 89 GHz AMSR-E ice drift dataset. This ice thickness is used to calculate the sea ice volume flux in Chapter 6.

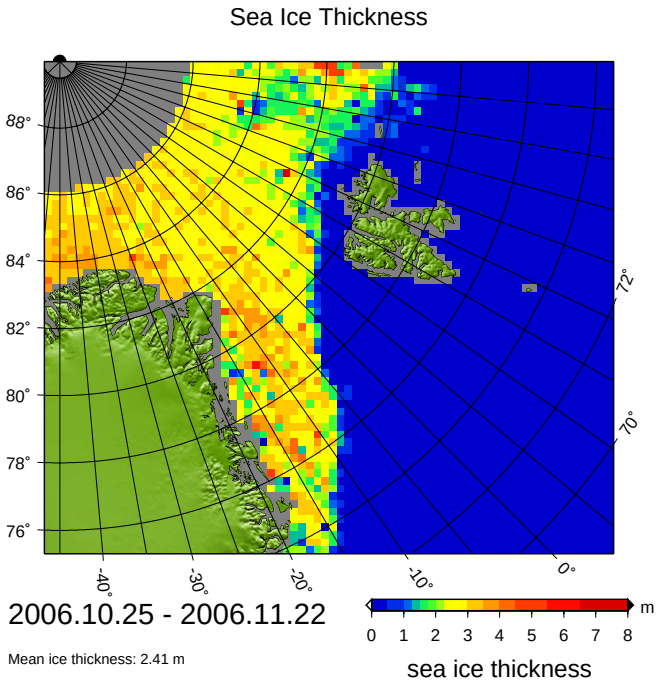

Figure A.7: Map of sea ice thickness for the time overlap 2006-10-25 to 2006-11-22 between ICESat measurement period 3g and the 89 GHz AMSR-E ice drift dataset. This ice thickness is used to calculate the sea ice volume flux in Chapter 6.

A.4 Ice Volume Flux Through Transects

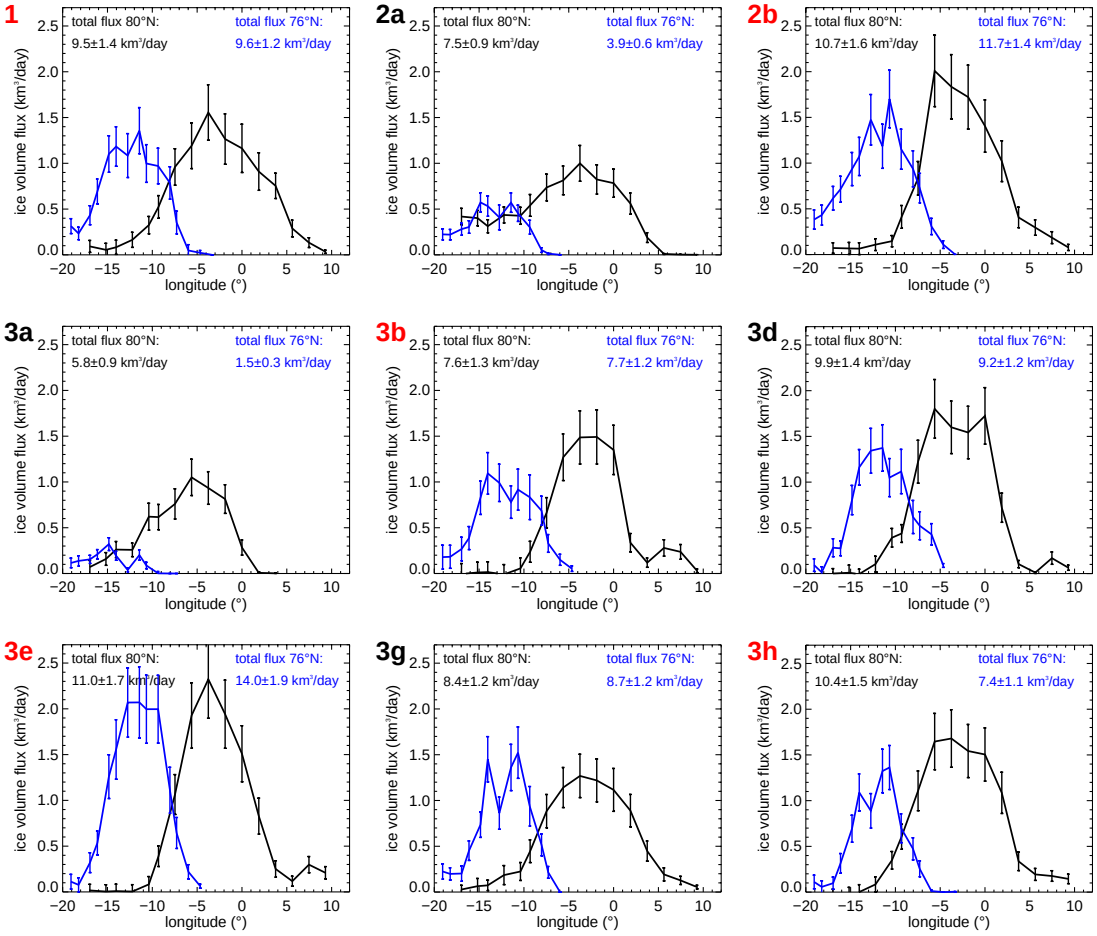

Figure A.8: Transects of sea ice volume flux for all nine ICESat periods at 80°N and 76°N in Fram Strait and East Greenland Current, respectively. Black lines denote 80°N and blue lines 76°N transects. In the upper left corner the ICESat period name (for dates see Table 6.1) is given in red for winter and black for fall periods.

A.5 1990–2007 Fram Strait Sea Ice Volume Flux Data

Table A.3: Monthly Fram Strait sea ice volume flux data for the time series 1990–2007 shown in Figure 6.10 on page 114. Volume fluxes are given in km^3/month (except for summer months 1997-1999). Data from *Vinje et al.* (1998), *Kwok et al.* (2004a), and this study are combined for this time series. For periods where the *Vinje et al.* (1998) and *Kwok et al.* (2004a) time series are overlapping the mean of both is used. For the summer months June to September in 1997, 1998, and 1999 the complete volume flux which occurred during the four months is given.

Year	Jan	Feb	Mar	Apr	May	Jun	Jul	Aug	Sep	Oct	Nov	Dec
1990								113	16	120	279	264
1991	202	94	187	220	181	272	98	25	240	256	226	245
1992	245	310	337	202	194	175	193	281	160	169	153	213
1993	170	200	282	191	191	279	300	55	70	194	29	369
1994	362	138	490	411	181	225	30	71	270	406	352	558
1995	427	468	591	506	222	143	172	152	108	215	157	198
1996	147	183	190	231	240	197	62	99		233	250	183
1997	261	254	290	398	182	|⟵	195		⟶|	227	142	198
1998	242	230	327	67	261	|⟵	297		⟶|	162	246	267
1999	190	253	197	172	73	|⟵	232		⟶|			
2003	290	129	344	175	112					240	141	266
2004	265	247	182	147						168	251	484
2005	376	219	278	168						298	374	182
2006	122	248	367	213						250	279	290
2007	268	132	296	397								
Mean	255	222	311	250	184	164	115	98	114	226	221	286
RMS	88	94	117	126	56	89	89	74	84	72	95	117

A.6 NAOSIM and MIT Ice Volume Flux

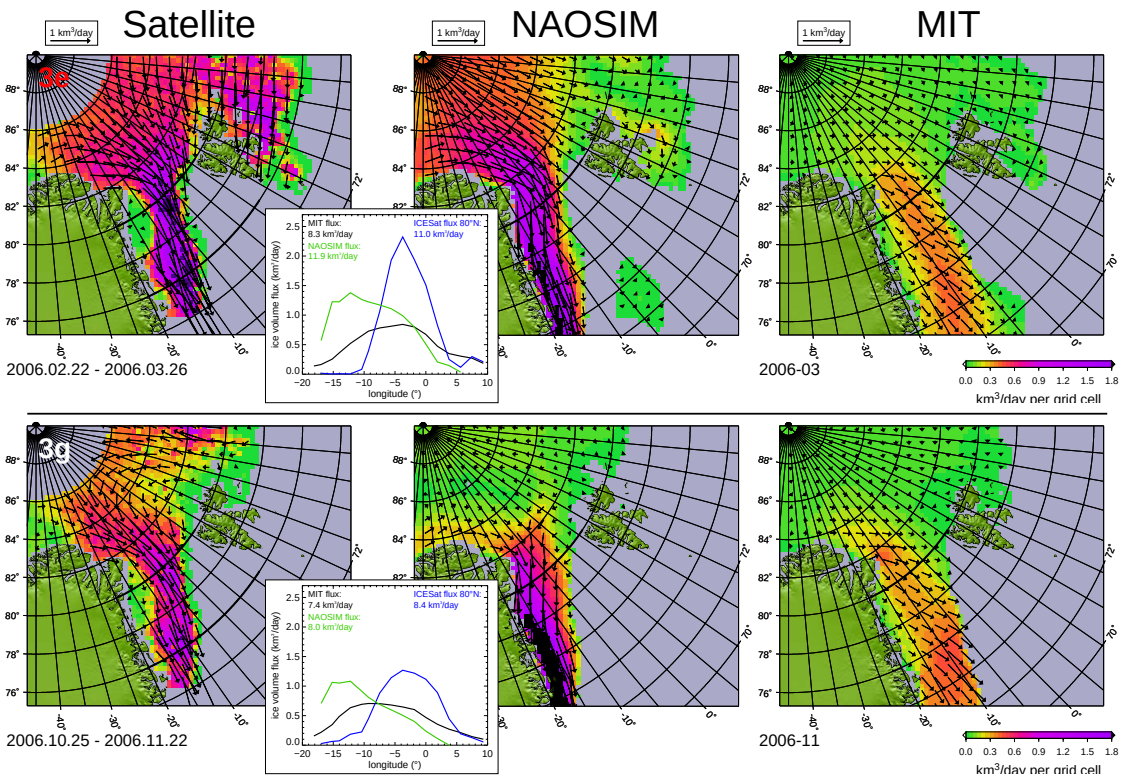

Figure A.9: Addition to Figure 6.12 in Section 6.6 for the ICESat periods in 2006. Comparison between ice volume flux derived from satellite data (left column) and two coupled ice-ocean models: NAOSIM (middle column) and MIT (right column) for the respective ICESat periods given in the upper left corner of each row. The graphs show the ice volume flux through a transect at 80°N in black for MIT, green for NAOSIM, and in blue for the satellite data. Continued in Figure A.10 for the remaining periods between 2003 and 2005.

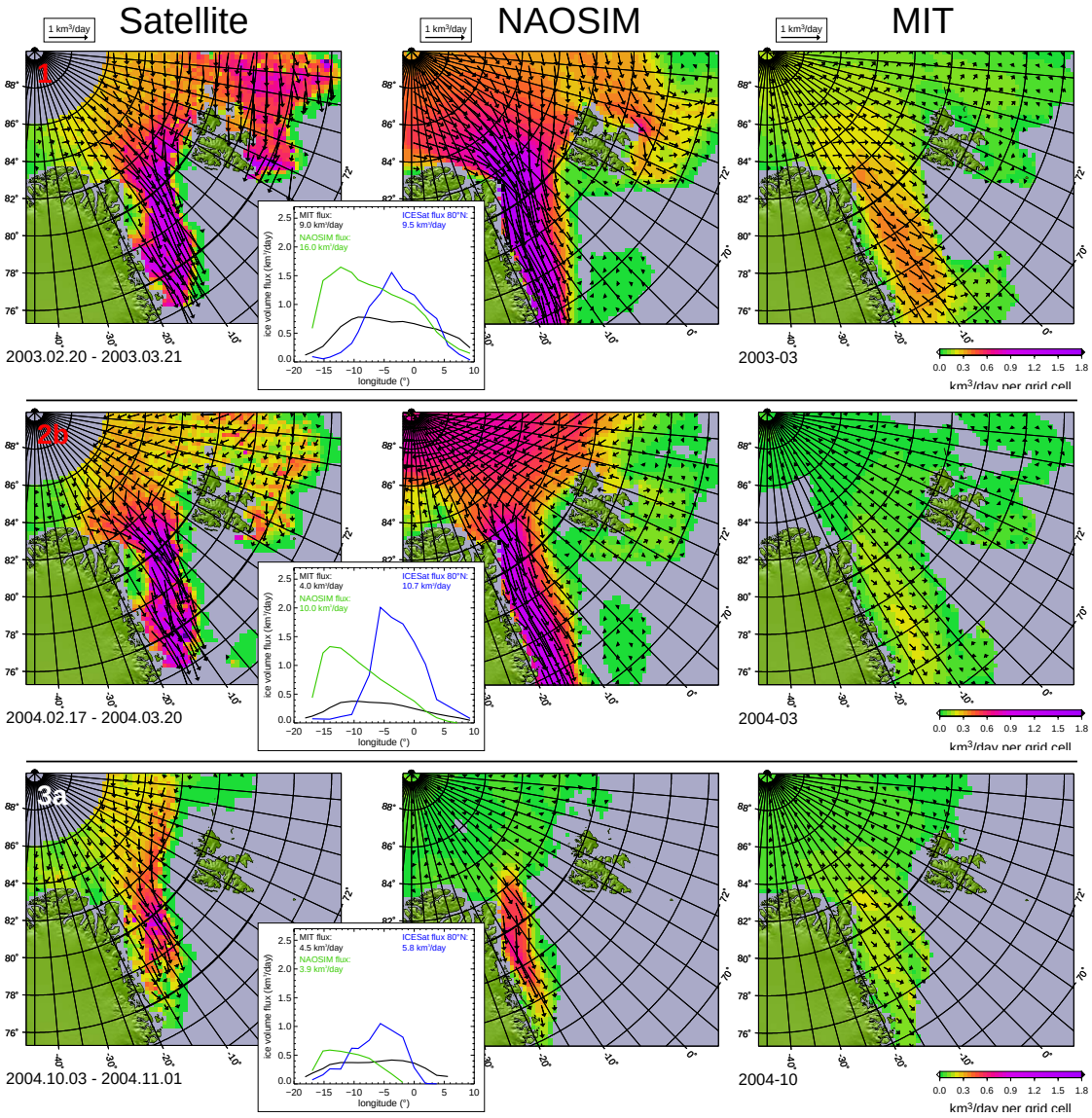

Figure A.10: Addition to Figure 6.12 in Section 6.6 for the remaining ICESat periods between 2003 and 2005. Caption and data for 2006 see Figure A.9.

Acronyms

ACSYS-ABSIS Arctic Systems - Arctic Atmospheric Boundary Layer and Sea Ice Interaction Study

ADCP Acoustic Doppler Current Profiler

AMSR Advanced Microwave Scanning Radiometer

AMSR-E Advanced Microwave Scanning Radiometer for EOS

AO Arctic Oscillation

ArcGP Arctic Gravity Project

ARTIST Arctic Radiation and Turbulence Interaction STudy

ASAR Advanced Synthetic Aperture Radar

ASI ARTIST Sea Ice

ASPeCt Antarctic Sea Ice Processes and Climate

BMBF Bundesministerium für Bildung und Forschung

CSA Canadian Space Agency

CERSAT *Centre ERS d'Archivage et de Traitement*

DAMOCLES Developing Arctic Modeling and Observing Capabilities for Long-term Environmental Studies

ECCO Estimating the Circulation and Climate of the Ocean

ECMWF European Centre for Medium-Range Weather Forecasts

EGC East Greenland Current

EGM96 Earth Gravitational Model 1996

EM electromagnetic

Envisat Environmental Satellite

EOS Earth Observing System

ERS European Remote-Sensing Satellite

ESA European Space Agency

ESMR Electrically Scanning Microwave Radiometer

EU European Union

GLA13 'GLAS/ICESat L2 Sea Ice Altimetry Data'-product

GLAS Geoscience Laser Altimeter System

GPS Global Positioning System

GRACE Gravity Recovery and Climate Experiment

IABP International Arctic Buoy Program

IBE Inverse Barometer Effect

ICESat Ice, Cloud, and land Elevation Satellite

IFREMER *Institut français de recherche pour l'exploitation de la mer*

IMB Ice Mass Balance

IPY International Polar Year

IPCC Intergovernmental Panel on Climate Change

JAXA Japan Aerospace Exploration Agency

LIDAR LIght Detection And Ranging

MIT Massachusetts Institute of Technology

MIZ Marginal Ice Zone

MODIS Moderate Resolution Imaging Spectroradiometer

NAO North Atlantic Oscillation

NAOSIM North Atlantic/Arctic Ocean-Sea Ice Model

NASA National Aeronautics and Space Administration

NCEP National Centers for Environmental Prediction

NCAR National Center for Atmosphere Research

NPI Norwegian Polar Institute

NSIDC National Snow and Ice Data Center

POD Precision Orbit Determination

QuikSCAT Quick Scatterometer Mission

radar (as well: RADAR) Radio Detection and Ranging

RMS root mean square

SAR Synthetic Aperture Radar

SMMR Scanning Multichannel Microwave Radiometer

SSH Sea Surface Height

SSM/I Special Sensor Microwave/Imager

ULS Upward Looking Sonar

UTC Coordinated Universal Time

WGS84 World Geodetic System 1984

WMO World Meteorological Organisation

List of Figures

List of Tables

Bibliography

Aagaard, K., and E. C. Carmack (1989), The role of sea ice and other fresh water in the Arctic circulation, *J. Geophys. Res.*, *94*(C10), 14485–14498.

Abshire, J. B., X. Sun, H. Riris, J. M. Sirota, J. F. McGarry, S. Palm, D. Yi, and P. Liiva (2005), Geoscience Laser Altimeter System (GLAS) on the ICESat Mission: On-orbit measurement performance, *Geophys. Res. Lett.*, *32*(21), L21S02, doi:10.1029/2005GL024028.

ACIA (2004), *Impacts of a Warming Arctic: Arctic Climate Impact Assessment*, 140 pp., Cambridge University Press.

ACIA (2005), *Arctic Climate Impact Assessment—Scientific Report*, 1042 pp., Cambridge University Press.

Agnew, T. A., H. Le, and T. Hirose (1997), Estimation of large-scale sea-ice motion from SSM/I 85.5 GHz imagery, *Ann. Glaciol.*, *25*, 305–311.

Andersen, S., R. Tonboe, L. Kaleschke, G. Heygster, and L. T. Pedersen (2007), Intercomparison of passive microwave sea ice concentration retrievals over the high-concentration Arctic sea ice, *J. Geophys. Res.*, *112*(C8), C08004, doi:10.1029/2006JC004033.

ARKTIS-XIX/1 and XIX/2 science team (2004), *The Expedition ARKTIS XIX/1 a, b and XIX/2 of the Research Vessel Polarstern in 2003*, *Berichte zur Polar- und Meeresforschung (Reports on Polar and Marine Research)*, vol. 481, 194 pp., Alfred-Wegener-Inst. für Polar- und Meeresforschung, Bremerhaven.

Bamber, J., et al. (2004), *Mass Balance of the Cryosphere*, 662 pp., Cambridge University Press, doi:10.2277/0521808952.

Beaven, S. G., G. L. Lockhart, S. P. Gogineni, A. R. Hossetnmostafa, K. Jezek, A. J. Gow, D. K. Perovich, A. K. Fung, and S. Tjuatja (1995), Laboratory measurements of radar backscatter from bare and snow-covered saline ice sheets, *Int. J. Rem. Sens.*, *16*(5), 851–876.

Bettadpur, S. V., and R. J. Eanes (1994), Geographical representation of radial orbit perturbations due to ocean tides: Implications for satellite altimetry, *J. Geophys. Res.*, *99*(C12), 24883–24894.

Blobel, V., and E. Lohmann (1998), *Statistische und numerische Methoden der Datenanalyse*, B. G. Teubner, Stutgart; Leibzig.

Brümmer, B., S. Thiemann, and A. Kirchgäßner (2000), A cyclone statistics for the Arctic based on European Centre re-analysis data, *Meteor. Atmos. Phys.*, *75*(3-4), 233–250.

Brümmer, B., G. Müller, and H. Hoeber (2003), A Fram Strait cyclone: Properties and impact on ice drift as measured by aircraft and buoys, *Journal Of Geophysical Research-Atmospheres*, *108*(D7), 4217, doi:10.1029/2002JD002638.

Brümmer, B., D. Schröder, G. Müller, G. Spreen, A. Jahnke-Bornemann, and J. Launiainen (2008), Impact of a Fram Strait cyclone on ice edge, drift, divergence and concentration: Possibilities and limits of an observational analysis, *J. Geophys. Res.*, p. accepted.

Cavalieri, D., and J. Comiso (2004), AMSR-E/Aqua daily L3 12.5 km Tb, sea ice conc., & snow depth polar grids, *digital media V001*, National Snow and Ice Data Center, Boulder, CO, USA, 2004, updated daily.

Cavalieri, D., T. Markus, J. Maslanik, M. Sturm, and E. Lobl (2006), March 2003 EOS Aqua AMSR-E Arctic sea ice field campaign, *IEEE Trans. Geosci. Remote Sens.*, *44*(11), 3003–3008, doi:10.1109/TGRS.2006.883133.

Cavalieri, D. J., and K. M. St. Germain (1995), Arctic sea ice research with satellite passive microwave radiometers, *IEEE GRS-S Newsletter*, *97*(1), 6–12.

Cavalieri, D. J., K. M. St. Germain, and C. T. Swift (1995), Reduction of weather effects in the calculation of sea-ice concentration with DMSP SSM/I, *J. Glaciol.*, *41*(139), 455–464.

Cavalieri, D. J., C. L. Parkinson, and K. Y. Vinnikov (2003), 30-year satellite record reveals contrasting Arctic and Antarctic decadal sea ice variability, *Geophys. Res. Lett.*, *30*(18), 1970, doi:10.1029/2003GL018031.

Comiso, J. C. (1983), Sea ice effective microwave emissivities from satellite passive microwave and infrared observations, *J. Geophys. Res.*, *88*(C12), 7686–7704.

Comiso, J. C. (1995), SSM/I ice concentrations using the Bootstrap Algorithm, *NASA Reference Publication 1380*, NASA, Goddard Space Flight Center, Greenbelt, Maryland 20771, US.

Comiso, J. C. (2002), A rapidly declining perennial sea ice cover in the Arctic, *Geophys. Res. Lett.*, *29*(20), 1956, doi:10.1029/2002GL015650.

Comiso, J. C., D. J. Cavalieri, C. L. Parkinson, and P. Gloersen (1997), Passive microwave algorithms for sea ice concentration: A comparison of two techniques, *Remote Sens. Environ.*, *60*(3), 357–384.

Comiso, J. C., D. J. Cavalieri, and T. Markus (2003), Sea ice concentration, ice temperature, and snow depth using AMSR-E data, *IEEE Trans. Geosci. Remote Sens.*, *41*(2), 243–252.

Comiso, J. C., C. L. Parkinson, R. Gersten, and L. Stock (2008), Accelerated decline in the Arctic sea ice cover, *Geophys. Res. Lett.*, *35*, L01703, doi:10.1029/2007GL031972.

Dickson, R., B. Rudels, S. Dye, M. Karcher, J. Meincke, and I. Yashayaev (2007), Current estimates of freshwater flux through Arctic and subarctic seas, *Progr. Oceanogr.*, *73*(3–4), 210–230, doi:10.1016/j.pocean.2006.12.003.

Dickson, R. R., J. Meincke, S.-A. Malmberg, and A. J. Lee (1988), The "great salinity anomaly" in the Northern North Atlantic 1968-1982, *Progr. Oceanogr.*, *20*(2), 103–151, doi:10.1016/0079-6611(88)90049-3.

Divine, D. V., and C. Dick (2006), Historical variability of sea ice edge position in the Nordic Seas, *J. Geophys. Res.*, *111*, C01001, doi:10.1029/2004JC002851.

Dulière, V., and T. Fichefet (2007), On the assimilation of ice velocity and concentration data into large-scale sea ice models, *Ocean Sci.*, *3*, 321–335.

Eanes, R. J., and S. V. Bettadpur (1995), The CSR 3.0 global ocean tide model, *Technical Memorandum CSR-TM-95-06*, Univ. of Texas Center for Space Research, Austin, US.

Eicken, H., M. Lensu, M. Leppäranta, W. B. Tucker, and A. J. G. O. Salmela (1995), Thickness, structure, and properties of level summer multiyear ice in the Eurasian sector of the Arctic Ocean, *J. Geophys. Res.*, *100*(C11), 22697–22710.

Ekman, M. (1989), Impacts of geodynamic phenomena on systems for height and gravity, *Bulletin Géodésique*, *63*(3), 281–296.

Ezraty, R., and J.-F. Piollé (2001), *SeaWinds on QuikSCAT Polar Sea Ice Grids – User Manual*, IFREMER, Brest, France, 1.1 ed.

Ezraty, R., F. Girard-Ardhuin, and D. Croizé-Fillon (2007a), *Sea ice drift in the central Arctic using the 89 GHz brightness temperatures of the Advanced Microwave Scanning Radiometer (AMSR-E) – User's manual*, Institut français de recherche pour l'exploitation de la mer (IFREMER), Brest, France, ver. 2.0 ed.

Ezraty, R., F. Girard-Ardhuin, and J.-F. Piollé (2007b), *Sea ice drift in the central Arctic estimated from SeaWinds/QuikSCAT backscatter maps – User's manual*, Institut français de recherche pour l'exploitation de la mer (IFREMER), Brest, France, ver. 2.2 ed.

Ezraty, R., F. Girard-Ardhuin, and J.-F. Piollé (2007c), *Sea ice drift in the central Arctic combining QuikSCAT and SSM/I sea ice drift data – User's manual*, Institut français de recherche pour l'exploitation de la mer (IFREMER), Brest, France, ver. 2.0 ed.

Fofonoff, P., and R. C. Millard Jr. (1983), Algorithms for computation of fundamental properties of seawater, *Unesco Tech. Pap. in Mar. Sci*, *44*, 53 pp.

Forsberg, R., and S. Kenyon (2004), Gravity and geoid in the Arctic region - The northern polar gap now filled, in *Proceedings Second International GOCE Workshop "GOCE, The Geoid and Oceanography"*, ESA-ESRIN, Frascati, Italy, 8-10 March 2004.

Forsberg, R., and H. Skourup (2005), Arctic ocean gravity, geoid and sea-ice freeboard heights from ICESat and GRACE, *Geophys. Res. Lett.*, *32*, L21502, doi: 10.1029/2005GL023711.

Forsberg, R., and H. Skourup (2006), Sea ice thickness, geoid and ocean topography in the Arctic ocean from ICESat and GRACE, in *Arctic sea ice thickness: past, present & future*, *Climate Change and Natural Hazards Series 10*, vol. EUR 22416, edited by P. Wadhams and G. Amanatidis, chap. 15, pp. 165–175, European Commission, Brussels.

Fricker, H. A., A. Borsa, B. Minster, C. Carabajal, K. Quinn, and B. Bills (2005), Assessment of ICESat performance at the salar de Uyuni, Bolivia, *Geophys. Res. Lett.*, *32*, L21S06, doi:10.1029/2005GL023423.

Gascard, J.-C., et al. (2008), Exploring Arctic transpolar drift during dramatic sea ice retreat, *Eos, Trans. Amer. Geophys. Union*, *89*(3), 21–28.

Geiger, C. A., and M. R. Drinkwater (2005), Coincident buoy- and SAR -derived surface fluxes in the western Weddell Sea during Ice Station Weddell 1992, *J. Geophys. Res.*, *110*(C4), C04002, doi:10.1029/2003JC002112.

Gildor, H., and E. Tziperman (2001), A sea ice climate switch mechanism for the 100-kyr glacial cycles, *J. Geophys. Res.*, *106*(C5), 9117–9133.

Gildor, H., and E. Tziperman (2003), Sea-ice switches and abrupt climate change, *Phil. Trans. R. Soc. Lond. A.*, *361*(1810), 1935–1944, doi:10.1098/rsta.2003.1244.

Gloersen, P., and D. J. Cavalieri (1986), Reduction of weather effects in the calculation of sea ice concentration from microwave radiances, *J. Geophys. Res.*, *91*(C3), 3913–3919.

Gloersen, P., W. Campbell, D. Cavalieri, J. Comiso, C. Parkinson, and H. Zwally (1992), *Arctic and Antarctic sea ice, 1978–1987: satellite passive-microwave observations and analysis*, *Scientific and technical information program*, vol. NASA SP-511, National Aeronautics and Space Administration (NASA), Washington, D.C.

Haarpaintner, J. (2006), Arctic-wide operational sea ice drift from enhanced-resolution QuikScat/SeaWinds scatterometry and its validation, *IEEE Trans. Geosci. Remote Sens.*, *44*(1), 102–107, doi:10.1109/TGRS.2005.859352.

Haarpaintner, J., and G. Spreen (2007), Use of enhanced-resolution QuikSCAT/ SeaWinds data for operational ice services and climate research: Sea ice edge, type, concentration, and drift, *IEEE Trans. Geosci. Remote Sens.*, *45*(10), 3131–3137, doi: 10.1109/TGRS.2007.895419.

Haas, C. (2002), Validation of CryoSat sea-ice products: Instruments and methods, in *2002 IEEE International Geoscience and Remote Sensing Symposium Proceedings*, pp. 1753–1755, IEEE, Toronto, Canada.

Haas, C. (2004a), Late-summer sea ice thickness variability in the Arctic transpolar drift 1991–2001 derived from ground-based electromagnetic sounding, *Geophys. Res. Lett.*, *31*(9), L09402, doi:10.1029/2003GL019394.

Haas, C. (2004b), Arctic sea ice thickness variability in the 1990s retrieved from EM sounding, in *Proceedings of the ACSYS Final Science Conference, St. Petesburg, Russia, 11-14 Nov. 2003*, no. WMO/TD No. 1232 in WCRP-118 (CD), WMO, Arctic Climate System Study (ACSYS). 2004. Progress in Understanding the Arctic Climate System: The ACSYS Decade and Beyond.

Hansen, J., and L. Nazarenko (2004), Soot climate forcing via snow and ice albedos, *Proceed. National Academy of Science*, *101*(2), 423–428.

Hasumi, H., and N. Suginohara (1995), Haline circulation induced by formation and melting of sea ice, *J. Geophys. Res.*, *100*(C10), 20613–20625.

Hendricks, S., S. Kern, V. Leinweber, L. Rabenstein, G. Spreen, and A. Winderlich (2008), Sea ice properties during ARK-XXII/2, in *Cruise Report R/V Polarstern ARK-XXII/2*, edited by U. Schauer, Alfred Wegener Institute for Polar and Marine Research, in press.

Hibler, III, W. D., and G. M. Flato (1992), Sea ice models, in *Climate System Modeling*, edited by K. E. Trenberth, Cambridge University Press.

Holfort, J., and J. Meincke (2005), Time series of freshwater-transport on the East Greenland Shelf at 74°N, *Meteor. Z.*, *14*(6), 703–710, doi:10.1127/0941-2948/2005/0079.

Holland, M. M., C. M. Bitz, and B. Tremblay (2006), Future abrupt reductions in the summer Arctic sea ice, *Geophys. Res. Lett.*, *33*(23), L23503, doi:10.1029/2006GL028024.

Hvidegaard, S., and R. Forsberg (2002), Sea-ice thickness from airborne laser altimetry over the Arctic Ocean north of Greenland, *Geophys. Res. Lett.*, *29*(20), 1952, doi:10.1029/2001GL014474.

IPCC (2007), *Climate Change 2007: The Physical Science Basis. Contribution of Working Group I to the Fourth Assessment Report of the Intergovernmental Panel on Climate Change*, 996 pp., Cambridge University Press, Cambridge, United Kingdom and New York, NY, USA.

Isaaks, E. H., and R. M. Srivastava (1990), *An Introduction to Applied Geostatistics*, Oxford University Press, New York.

Jähne, B. (2002), *Digitale Bildverarbeitung*, 5 ed., 618 pp., Springer, Berlin, Germany.

JAXA (2005), *AMSR-E Data Users Handbook*, Japan Aerospace Exploration Agency (Jaxa), 1401 Numanoue, Ohashi, Hatoyama-machi, Hiki-gun, Saitama, Japan, 350-0302, 3. ed.

Johannessen, O. M., et al. (2004), Arctic climate change: observed and modelled temperature and sea-ice variability, *Tellus A*, *56*(4), 328–341, doi:10.1111/j.1600-0870.2004.00060.x.

Kaleschke, L., C. Lüpkes, T. Vihma, J. Haarpaintner, A. Bochert, J. Hartmann, and G. Heygster (2001), SSM/I sea ice remote sensing for mesoscale ocean-atmosphere interaction analysis, *Can. J. Rem. Sens.*, *27*(5), 526–537.

Kalnay, E., et al. (1996), The NCEP/NCAR 40-year reanalysis project, *Bull. Amer. Meteor. Soc.*, *77*(3), 437–471.

Karcher, M., R. Gerdes, F. Kauker, C. Köberle, and I. Yashayaev (2005), Arctic Ocean change heralds North Atlantic freshening, *Geophys. Res. Lett.*, *32*, L21606, doi:10.1029/2005GL023861.

Karcher, M. J., R. Gerdes, F. Kauker, and C. Köberle (2003), Arctic warming: Evolution and spreading of the 1990s warm event in the Nordic seas and the Arctic Ocean, *J. Geophys. Res.*, *108*(C2), 3034, doi:10.1029/2001JC001265.

Karstensen, J., P. Schlosser, D. W. R. Wallace, J. L. Bullister, and J. Blindheim (2005), Water mass transformation in the Greenland Sea during the 1990s, *J. Geophys. Res.*, *110*(C7), C07022, doi:10.1029/2004JC002510.

Kauker, F., R. Gerdes, M. Karcher, C. Köberle, and J. L. Lieser (2003), Variability of Arctic and North Atlantic sea ice: A combined analysis of model results and observations from 1978 to 2001, *J. Geophys. Res.*, *108*(C6), 3182, doi:10.1029/2002JC001573.

Kay, J. E., T. L'Ecuyer, A. Gettelman, G. Stephens, and C. O'Dell (2008), The contribution of cloud and radiation anomalies to the 2007 Arctic sea ice extent minimum, *Geophys. Res. Lett.*, *35*, L08503, doi:10.1029/2008GL033451.

Kern, S., L. Kaleschke, and D. A. Clausi (2003), A comparison of two 85 GHz SSM/I ice concentration algorithms with AVHRR and ERS-2 SAR imagery, *IEEE Trans. Geosci. Remote Sens.*, *41*(10), 2294–2306, doi:10.1109/TGRS.2003.817181.

Kern, S., G. Spreen, L. Kaleschke, S. de la Rosa Höhn, and G. Heygster (2007), Polynya Signature Simulation Method polynya area in comparison to AMSR-E 89 GHz sea-ice concentrations in the Ross Sea and off the Adélie Coast, Antarctica, for 2002-05: first results, *Ann. Glaciol.*, *46*, 409–418.

Köberle, C., and R. Gerdes (2003), Mechanisms determining the variability of Arctic sea ice conditions and export, *J. Climate*, *16*(17), 2843–2858.

Koenigk, T., U. Mikolajewicz, H. Haak, and J. Jungclaus (2006), Variability of Fram Strait sea ice export: causes, impacts and feedbacks in a coupled climate model, *Climate Dyn.*, *26*(1), 17–34, doi:10.1007/s00382-005-0060-1.

Koenigk, T., U. Mikolajewicz, H. Haak, and J. Jungclaus (2007), Arctic freshwater export in the 20th and 21st centuries, *J. Geophys. Res.*, *112*(G4), G04S41, doi:10.1029/2006JG000274.

Köhl, A., and D. Stammer (2008), Variability of the meridional overturning in the North Atlantic from the 50 years GECCO state estimation, *J. Phys. Oceanogr.*, in press.

Köhl, A., R. H. Käse, D. Stammer, and N. Serra (2007), Causes of changes in the Denmark Strait overflow, *J. Phys. Oceanogr.*, *37*(6), 1678–1696, doi:10.1175/JPO3080.1.

Komuro, Y., and H. Hasumi (2007), Effects of variability of sea ice transport through the Fram Strait on the intensity of the Atlantic deep circulation, *Climate Dyn.*, *29*(5), 455–467, doi:10.1007/s00382-007-0245-x.

Kowalik, Z., and A. Y. Proshutinsky (1994), The Arctic Ocean tides, in *The Polar Oceans and Their Role in Shaping the Global Environment*, *Geophysical Monograph*, vol. 85, edited by O. M. Johannessen, R. D. Muench, and J. E. Overland, pp. 137–158, Am. Geophys. Union, Washington, D.C.

Kwok, R. (1998), The RADARSAT geophysical processor system, in *Analysis of SAR Data of the Polar Oceans: Recent Advances*, edited by C. Tsatsoulis and R. Kwok, pp. 235–257, Springer-Verlag, New York.

Kwok, R. (2000), Recent changes in arctic ocean sea ice motion associated with the north atlantic oscillation, *Geophys. Res. Lett.*, *27*(6), 775–778.

Kwok, R. (2004), Annual cycles of multiyear sea ice coverage of the Arctic Ocean: 1999-2003, *J. Geophys. Res.*, *109*(C11), C11004, doi:10.1029/2003JC002238.

Kwok, R. (2005), Variability of Nares Strait ice flux, *Geophys. Res. Lett.*, *32*, L24502, doi:10.1029/2005GL024768.

Kwok, R. (2008), Summer sea ice motion from the 18 GHz channel of AMSR-E and the exchange of sea ice between the Pacific and Atlantic sectors, *Geophys. Res. Lett.*, *35*, L03504, doi:10.1029/2007GL032692.

Kwok, R., and G. F. Cunningham (2002), Seasonal ice area and volume production of the Arctic Ocean: November 1996 through April 1997, *J. Geophys. Res.*, *107*(C10), 8038, doi:10.1029/2000JC000469.

Kwok, R., and D. A. Rothrock (1999), Variability of Fram Strait ice flux and North Atlantic Oscillation, *J. Geophys. Res.*, *104*(C3), 5177–5189.

Kwok, R., A. Schweiger, D. Rothrock, S. Pang, and C. Kottmeier (1998), Sea ice motion from satellite passive microwave imagery assessed with ERS SAR and buoy motions, *J. Geophys. Res.*, *103*(C4), 8191–8214.

Kwok, R., G. F. Cunningham, and W. D. Hibler (2003), Sub-daily sea ice motion and deformation from RADARSAT observations, *Geophys. Res. Lett.*, *30*(23), 2218, doi:10.1029/2003GL018723.

Kwok, R., G. F. Cunningham, and S. S. Pang (2004a), Fram Strait sea ice outflow, *J. Geophys. Res.*, *109*(C1), C01009, doi:10.1029/2003JC001785.

Kwok, R., H. Zwally, and D. Yi (2004b), ICESat observations of Arctic sea ice: A first look, *Geophys. Res. Lett.*, *31*(16), L16401, doi:10.1029/2004GL020309.

Kwok, R., W. Maslowski, and S. W. Laxon (2005), On large outflows of Arctic sea ice into the Barents Sea, *Geophys. Res. Lett.*, *32*, L22503, doi:10.1029/2005GL024485.

Kwok, R., G. F. Cunningham, H. J. Zwally, and D. Yi (2006), ICESat over Arctic sea ice: Interpretation of altimetric and reflectivity profiles, *J. Geophys. Res.*, *111*(C6), C06006, doi:10.1029/2005JC003175.

Kwok, R., G. F. Cunningham, H. J. Zwally, and D. Yi (2007), Ice, Cloud, and land Elevation Satellite (ICESat) over Arctic sea ice: Retrieval of freeboard, *J. Geophys. Res.*, *112*, C12013, doi:10.1029/2006JC003978.

Laine, V. (2004), Arctic sea ice regional albedo variability and trends, 1982-1998, *J. Geophys. Res.*, *109*(C6), C06027, doi:10.1029/2003JC001818.

Launiainen, J. (2003), ACSYS-ABSIS campaign 26 March – 21 April 2003, *Cruise report R/V Aranda*, Finnish Institute of Marine Research, Lyypekinkuja 3, 00931 Helsinki, Finland.

Laxon, S., N. Peacock, and D. Smith (2003), High interannual variability of sea ice thickness in the Arctic region, *Nature*, *425*(6961), 947–950.

Lemke, P., et al. (2007), Observations: Changes in snow, ice and frozen ground, in *Climate Change 2007: The Physical Science Basis. Contribution of Working Group I to the Fourth Assessment Report of the Intergovernmental Panel on Climate Change*, edited by S. Solomon, D. Qin, M. Manning, Z. Chen, M. Marquis, K. B. Averyt, M. Tignor, and H. L. Miller, chap. 4, pp. 337–384, Cambridge University Press, Cambridge, United Kingdom and New York, NY, USA.

Lenton, T. M., H. Held, E. Kriegler, J. W. Hall, W. Lucht, S. Rahmstorf, and H. J. Schellnhuber (2008), Tipping elements in the Earth's climate system, *Proc. Natl. Acad. Sci. USA*, *105*(6), 1786–1793, doi:10.1073/pnas.0705414105.

Lieser, J. L. (2005), *Sea ice conditions in the northern North Atlantic in 2003 and 2004 Observations during RV POLARSTERN cruises ARKTIS XIX/1a and b and ARKTIS XX/2*, *Reports on Polar and Marine Research*, vol. 504, 197 pp., Alfred Wegener Institute for Polar and Marine Research, Bremerhaven.

Lieser, J. L., and C. Haas (2005), Sea ice conditions in the Fram Strait during Polarstern cruise ARK-XX/2 (AIROTICA), PANGAEA data library, digital media, doi:10.1594/PANGAEA.327055.

Lieser, J. L., C. Haas, and S. Kern (2005), Sea ice conditions in the Svalbard region during POLARSTERN cruise ARK-XIX/1 (CryoVex 2003), PANGAEA data library, digital media, doi:10.1594/PANGAEA.272527.

Lomax, A. S., D. Lubin, and R. Whritner (1995), The potential of interpreting total and multiyear-ice concentration in SSM/I 85.5 GHz imagery, *Remote Sens. Environ.*, *54*(1), 13–26.

Lubin, D., C. Garrity, R. Ramseier, and R. Whritner (1997), Total sea ice concentration retrieval from the SSM/I 85.5 GHz channels during the Arctic summer, *Remote Sens. Environ.*, *62*(1), 63–76.

Markus, T., and B. A. Burns (1995), A method to estimate subpixel-scale coastal polynyas with satellite microwave data, *J. Geophys. Res.*, *100*(C3), 4473–4487.

Markus, T., and D. J. Cavalieri (2000), An enhancement of the NASA Team sea ice algorithm, *IEEE Trans. Geosci. Remote Sens.*, *38*(3), 1387–1398, doi:10.1109/36.843033.

Markus, T., D. Cavalieri, A. Gasiewski, M. Klein, J. Maslanik, D. Powell, B. Stankov, J. Stroeve, and M. Sturm (2006), Microwave signatures of snow on sea ice: Observations, *IEEE Trans. Geosci. Remote Sens.*, *44*(11), 3081–3090, doi:10.1109/TGRS.2006.883134.

Marshall, J., A. Adcroft, C. Hill, L. Perelman, and C. Heisey (1997a), A finite-volume, incompressible Navier Stokes model for studies of the ocean on parallel computers, *J. Geophys. Res.*, *102*(C3), 5753–5766.

Marshall, J., C. Hill, L. Perelman, and A. Adcroft (1997b), Hydrostatic, quasi-hydrostatic, and nonhydrostatic ocean modeling, *J. Geophys. Res.*, *102*(C3), 5733–5752.

Martin, S. (2001), Polynyas, in *Encyclopedia of Ocean Sciences*, edited by J. H. Steele, pp. 2241–2247, Academic Press, Oxford, doi:10.1006/rwos.2001.0007.

Martin, S., R. Drucker, R. Kwok, and B. Holt (2004), Estimation of the thin ice thickness and heat flux for the Chukchi Sea Alaskan coast polynya from Special Sensor Microwave/Imager data, 1990-2001, *J. Geophys. Res.*, *109*(C10), C10012, doi:10.1029/2004JC002428.

Martin, T., and E. Augstein (2000), Large-scale drift of arctic sea ice retrieved from passive microwave satellite data, *J. Geophys. Res.*, *105*(C4), 8775–8788.

Martin, T., and T. Martin (2006), Anomalies of sea-ice transports in the Arctic, *Ann. Glaciol.*, *44*, 310–316.

Maslanik, J., S. Drobot, C. Fowler, W. Emery, and R. Barry (2007a), On the Arctic climate paradox and the continuing role of atmospheric circulation in affecting sea ice conditions, *Geophys. Res. Lett.*, *34*, L03711, doi:10.1029/2006GL028269.

Maslanik, J. A., C. Fowler, J. Stroeve, S. Drobot, J. Zwally, D. Yi, and W. Emery (2007b), A younger, thinner Arctic ice cover: Increased potential for rapid, extensive sea-ice loss, *Geophys. Res. Lett.*, *34*, L24501, doi:10.1029/2007GL032043.

Morales Maqueda, M. A., A. J. Willmott, and N. R. T. Biggs (2004), Polynya dynamics: A review of observations and modeling, *Rev. Geophys.*, *42*, RG1004, doi:10.1029/2002RG000116.

Nansen, F. (1897), *Farthest North: Being the Record of a Voyage of Exploration of the Ship "Fram", 1893–1896, and of a Fifteen Months' Sleigh Journey by Dr. Nansen and Lt. Johansen*, Harper & Brothers, New York.

Nansen, F. (1902), The oceanography of the north polar basin, in *The Norwegian North Polar Expedition 1893–1896, Scientific Results*, vol. 3, p. 427, Christiania : J. Dybwad; London, New York, Bombay: Longmans, Green, and Co.; Leipzig: F. A. Brockhaus.

Nghiem, S. V., I. G. Rigor, D. K. Perovich, P. Clemente-Colón, J. W. Weatherly, and G. Neumann (2007), Rapid reduction of Arctic perennial sea ice, *Geophys. Res. Lett.*, *34*(19), L19504, doi:10.1029/2007GL031138.

NORSEX Group (1983), Norwegian remote sensing experiment in a marginal ice zone, *Science*, *220*(4599), 781–787.

Onstott, R. G., and R. A. Shuchman (2004), SAR measurement of sea ice, in *Synthetic Aperture Radar Marine User's Manual*, edited by C. R. Jackson and J. R. Apel, chap. 3, pp. 81–115, US Dept. of Commerce: National Oceanic and Atmospheric Administration, Washington, DC, USA.

Onstott, R. G., T. C. Grenfell, C. Mätzler, C. A. Luther, and E. A. Svendsen (1987), Evolution of microwave sea ice signatures during early summer and midsummer in the marginal ice zone, *J. Geophys. Res.*, *92*(C7), 6825–6835.

Overland, J. E., and M. Wang (2005), The Arctic climate paradox: The recent decrease of the Arctic Oscillation, *Geophys. Res. Lett.*, *32*(6), L06501, doi:10.1029/2004GL021752.

Parkinson, C. L., D. Rind, R. J. Healy, and D. G. Martinson (2001), The impact of sea ice concentration accuracies on climate model simulations with the GISS GCM, *J. Climate*, *14*(12), 2606–2623.

Pfirman, S., W. F. Haxby, R. Colony, and I. Rigor (2004), Variability in Arctic sea ice drift, *Geophys. Res. Lett.*, *31*(16), L16402, doi:10.1029/2004GL020063.

Picot, N., K. Case, S. Desai, and P. Vincent (2004), *AVISO and PODAAC User Handbook. IGDR and GDR Jason Products*, 2.1 ed., SMM-MU-M5-OP-13184-CN (AVISO), JPL D-21352 (PODAAC).

Polyakov, I. (2007), Observational program tracks Arctic Ocean transition to a warmer state, *Eos, Trans. Amer. Geophys. Union*, *88*(40), 398–399.

Polyakov, I. V., et al. (2005), One more step toward a warmer Arctic, *Geophys. Res. Lett.*, *32*(17), L17605, doi:10.1029/2005GL023740.

Rigor, I. G., and J. M. Wallace (2004), Variations in the age of Arctic sea-ice and summer sea-ice extent, *Geophys. Res. Lett.*, *31*(9), L09401, doi:10.1029/2004GL019492.

Rigor, I. G., J. M. Wallace, and R. L. Colony (2002), Response of sea ice to the arctic oscillation, *J. Climate*, *15*(18), 2648–2663.

Rothrock, D., Y. Yu, and G. Maykut (1999), Thinning of the Arctic Sea-Ice Cover, *Geophys. Res. Lett.*, *26*(23), 3469–3472.

Rothrock, D. A., J. Zhang, and Y. Yu (2003), The arctic ice thickness anomaly of the 1990s: A consistent view from observations and models, *J. Geophys. Res.*, *108*(C3), Art. No. 3083, doi:10.1029/2001JC001208.

Rothrock, D. A., D. B. Percival, and M. Wensnahan (2008), The decline in arctic sea-ice thickness: Separating the spatial, annual, and interannual variability in a quarter century of submarine data, *J. Geophys. Res.*, *113*, C05003, doi:10.1029/2007JC004252.

Schutz, B. (2002), Laser footprint location (geolocation) and surface profiles. GLAS algorithm theoretical basis document. Version 3.0, *Tech. rep.*, Austin, TX: Center for Space Research, University of Texas at Austin.

Schutz, B. E., H. J. Zwally, C. A. Shuman, D. Hancock, and J. P. DiMarzio (2005), Overview of the ICESat mission, *Geophys. Res. Lett.*, *32*(21), L21S01, doi:10.1029/2005GL024009.

Serreze, M. C., M. M. Holland, and J. Stroeve (2007), Perspectives on the Arctic's shrinking sea-ice cover, *Science*, *315*(5818), 1533–1536, doi:10.1126/science.1139426.

Serreze, M. C., et al. (2003), A record minimum arctic sea ice extent and area in 2002, *Geophys. Res. Lett.*, *30*(3), 1110, doi:10.1029/2002GL016406.

Serreze, M. C., et al. (2006), The large-scale freshwater cycle of the Arctic, *J. Geophys. Res.*, *111*(C11), C11010, doi:10.1029/2005JC003373.

Skourup, H., and R. Forsberg (2006), Sea ice freeboard from ICESat – a comparison with airborne lidar measurements, in *Arctic sea ice thickness: past, present & future*, *Climate Change and Natural Hazards Series 10*, vol. EUR 22416, edited by P. Wadhams and G. Amanatidis, chap. 8, pp. 82–92, European Commission, Brussels.

Smith, W. H. F., and P. Wessel (1990), Gridding with continuous curvature splines in tension, *Geophysics*, *55*(3), 293–305.

Snyder, J. P. (1987), *Map Projections - A Working Manual*, U.S. Geological Survey Professional Paper 1395, 385 pp., U.S. Government Printing Office.

Spreen, G. (2004), Meereisfernerkundung mit dem satellitengestützten Mikrowellenradiometer AMSR(-E) – Bestimmung der Eiskonzentration und Eiskante unter Verwendung der 89 GHz-Kanäle, Diplomarbeit (master's thesis), University of Hamburg, prepared at the University of Bremen, Dept. of Physics and Electrical Engineering.

Spreen, G., S. Kern, R. Ezraty, H. Witte, and D. Stammer (2005), Towards remote sensing of the net sea ice volume flux in the Greenland Sea, in *1st CRYOSAT Workshop Proceedings*, ESA, ESRIN Frascati, Italy.

Spreen, G., S. Kern, D. Stammer, R. Forsberg, and J. Haarpaintner (2006), Satellite-based estimates of sea ice volume flux through Fram Strait, *Ann. Glaciol.*, *44*, 321–328.

Spreen, G., L. Kaleschke, and G. Heygster (2008), Sea ice remote sensing using AMSR-E 89-GHz channels, *J. Geophys. Res.*, *113*, C02S03, doi:10.1029/2005JC003384.

Stammer, D. (1997), Global characteristics of ocean variability estimated from regional TOPEX/POSEIDON altimeter measurements, *J. Phys. Oceanogr.*, *27*(8), 1743–1769.

Steele, M., W. Ermold, and J. Zhang (2008), Arctic Ocean surface warming trends over the past 100 years, *Geophys. Res. Lett.*, *35*, L02614, doi:10.1029/2007GL031651.

Stössel, A., S.-J. Kim, and S. S. Drijfhout (1998), The impact of southern ocean sea ice in a global ocean model, *J. Phys. Oceanogr.*, *28*(10), 1999–2018, doi:10.1175/1520-0485(1998)028<1999:TIOSOS>2.0.CO;2.

Stott, L., A. Timmermann, and R. Thunell (2007), Southern hemisphere and deep-sea warming led deglacial atmospheric CO2 rise and tropical warming, *Science*, *318*(5849), 435–438, doi:10.1126/science.1143791.

Stroeve, J., M. M. Holland, W. Meier, T. Scambos, and M. Serreze (2007), Arctic sea ice decline: Faster than forecast, *Geophys. Res. Lett.*, *34*(9), L09501, doi:10.1029/2007GL029703.

Stroeve, J. C., M. C. Serreze, F. Fetterer, T. Arbetter, W. Meier, J. Maslanik, and K. Knowles (2005), Tracking the arctic's shrinking ice cover: Another extreme September minimum in 2004, *Geophys. Res. Lett.*, *32*(4), L04501, doi:10.1029/2004GL021810.

Sturm, M., J. Maslanik, D. Perovich, J. Stroeve, J. Richter-Menge, T. Markus, J. Holmgren, J. Heinrichs, and K. Tape (2006), Snow depth and ice thickness measurements from the Beaufort and Chukchi Seas collected during the AMSR-Ice03 campaign, *IEEE Trans. Geosci. Remote Sens.*, *44*(11), 3009–3020, doi:10.1109/TGRS.2006.878236.

Svendsen, E., K. Kloster, B. Farrelly, O. M. Johannessen, J. A. Johannessen, W. J. Campbell, P. Gloersen, D. Cavalieri, and C. Mätzler (1983), Norwegian remote sensing experiment: evaluation of the NIMBUS 7 Scanning Multichannel Microwave Radiometer for sea ice research., *J. Geophys. Res.*, *88*(NC5), 2781–2791.

Svendsen, E., C. Mätzler, and T. C. Grenfell (1987), A model for retrieving total sea ice concentration from a spaceborne dual-polarized passive microwave instrument operating near 90 GHz, *Int. J. Remote Sens.*, *8*(10), 1479–1487.

Thomas, D., S. Martin, D. Rothrock, and M. Steele (1996), Assimilating satellite concentration data into an Arctic sea ice mass balance model, 1979-1985, *J. Geophys. Res.*, *101*(C9), 20849–20868.

Thorndike, A. S., and R. Colony (1982), Sea ice motion in response to geostrophic winds, *J. Geophys. Res.*, *87*(C8), 5845–5852.

Tonboe, R., and L. Toudal (2005), Classification of new-ice in the Greenland Sea using Satellite SSM/I radiometer and SeaWinds scatterometer data and comparison with ice model, *Remote Sens. Environ.*, *97*(3), 277–287, doi:10.1016/j.rse.2005.05.012.

Tonboe, R., S. Andersen, and L. T. Pedersen (2006a), Simulation of the Ku-band radar altimeter sea ice effective scattering surface, *IEEE Geosci. Remote Sens. Lett.*, *3*(2), 237–240.

Tonboe, R., S. Andersen, L. Toudal, and G. Heygster (2006b), Sea ice emission modelling, in *Thermal Microwave Radiation - Applications for Remote Sensing*, *IET Electromagnetic Wave Series*, vol. 52, edited by C. Mätzler, chap. 4.16, pp. 382–400, The Institution of Engineering and Technology (IET), London, UK.

Trenberth, K. E., et al. (2007), Observations: Surface and atmospheric climate change, in *Climate Change 2007: The Physical Science Basis. Contribution of Working Group I to the Fourth Assessment Report of the Intergovernmental Panel on Climate Change*, edited by S. Solomon, D. Qin, M. Manning, Z. Chen, M. Marquis, K. B. Averyt, M. Tignor, and H. L. Miller, pp. 235–336, Cambridge University Press, Cambridge, United Kingdom and New York, NY, USA.

Tucker, W. B., J. W. Weatherly, D. T. Eppler, L. D. Farmer, and D. L. Bentley (2001), Evidence for rapid thinning of sea ice in the western Arctic Ocean at the end of the 1980s, *Geophys. Res. Lett.*, *28*(14), 2851–2854.

Vinje, T. (2001), Fram Strait ice fluxes and atmospheric circulation: 1950-2000, *J. Climate*, *14*(16), 3508–3517.

Vinje, T., N. Nordlund, and Å. Kvambekk (1998), Monitoring ice thickness in Fram Strait, *J. Geophys. Res.*, *103*(C5), 10437–10449.

Voss, S., G. Heygster, and R. Ezraty (2003), Improving sea ice type discrimination by the simultaneous use of SSM/I and scatterometer data, *Polar Research*, *22*(1), 35–42.

Wadhams, P. (2000), *Ice in the Ocean*, Gordon and Breach Science Publisher, London.

Wadhams, P., and J. C. Comiso (1992), The ice thickness distribution inferred using remote sensing techniques, in *Microwave Remote Sensing of Sea Ice*, *Geophysical Monograph*, vol. 68, edited by F. D. Carsey, chap. 21, pp. 375–383, Am. Geophys. Union, Washington, D.C.

Wadhams, P., and N. R. Davis (2000), Further evidence of ice thinning in the Arctic Ocean, *Geophys. Res. Lett.*, *27*(24), 3973–3975.

Warren, S., I. Rigor, N. Untersteiner, V. Radionov, N. Bryazgin, Y. Aleksandrov, and R. Colony (1999), Snow depth on Arctic sea ice, *J. Climate*, *12*, 1814–1829.

Wessel, P., and W. H. F. Smith (1991), Free software helps map and display data, *Eos, Trans. Amer. Geophys. Union*, *72*(41), 441.

Wessel, P., and W. H. F. Smith (1998), New, improved version of the Generic Mapping Tools released, *Eos, Trans. Amer. Geophys. Union*, *79*(47), 579.

Widell, K., S. Østerhus, and T. Gammelsrød (2003), Sea ice velocity in the Fram Strait monitored by moored instruments, *Geophys. Res. Lett.*, *30*(19), 1982, doi:10.1029/2003GL018119.

WMO (1989), WMO sea ice nomenclature, *Tech. Rep. WMO/OMM/BMO 259-TP-145, suppl. 5*, World Meteorological Organization, Geneva, Switzerland.

Woodgate, R. A., and K. Aagaard (2005), Revising the Bering Strait freshwater flux into the Arctic Ocean, *Geophys. Res. Lett.*, *32*(2), Art. No. L02602, doi:10.1029/2004GL021747.

Worby, A. P. (1999), Observing Antarctic sea ice: A practical guide for conducting sea ice observations from vessels operating in the Antarctic pack ice, A CD-ROM produced for the Antarctic Sea Ice Processes and Climate (ASPeCt) program of the Scientific Committee for Antarctic Research(SCAR) Global Change and the Antarctic (GLOCHANT) program, Hobart, Australia.

Wunsch, C. (1972), Bermuda sea level in relation to tides, weather and baroclinic fluctuations, *Rev. Geophys. Space Phys.*, *10*, 1–49.

Wunsch, C., and D. Stammer (1997), Atmospheric loading and the oceanic "inverted barometer" effect, *Rev. Geophys.*, *35*(1), 79–107.

Yi, D., J. Minster, and C. Bentley (1999), Ocean tidal loading corrections. GLAS algorithm theoretical basis document. Version 1.0, *Tech. rep.*, Greenbelt, MD: Goddard Space Flight Center.

Zhang, J., and D. Rothrock (2000), Modeling Arctic sea ice with an efficient plastic solution, *J. Geophys. Res.*, *105*(C2), 3325–3338.

Zhang, J., D. R. Thomas, D. A. Rothrock, R. W. Lindsay, Y. Yu, and R. Kwok (2003), Assimilation of ice motion observations and comparisons with submarine ice thickness data, *J. Geophys. Res.*, *108*(C6), 3170, doi:10.1029/2001JC001041.

Zhang, X., and J. E. Walsh (2006), Toward a seasonally ice-covered Arctic Ocean: Scenarios from the IPCC AR4 model simulations, *J. Climate*, *19*(9), 1730–1747, doi:10.1175/JCLI3767.1.

Zhang, X., J. E. Walsh, J. Zhang, U. S. Bhatt, and M. Ikeda (2004), Climatology and interannual variability of Arctic cyclone activity: 1948–2002, *J. Climate*, *17*(12), 2300–2317.

Zwally, H., R. Schutz, C. Bentley, J. Bufton, T. Herring, J. Minster, J. Spinhirne, and R. Thomas (2003), GLAS/ICESat L2 sea ice altimetry data V028, *digital media*, Boulder, CO: National Snow and Ice Data Center, updated current year.

Zwally, H. J., D. Yi, R. Kwok, and Y. Zhao (2008), ICESat measurements of sea ice freeboard and estimates of sea ice thickness in the Weddell Sea, *J. Geophys. Res.*, *113*, C02S15, doi:10.1029/2007JC004284.

Zwally, H. J., et al. (2002), ICESat's laser measurements of polar ice, atmosphere, ocean, and land, *J. Geodynamics*, *34*(3–4), 405–445, doi:10.1016/S0264-3707(02)00042-X.

Acknowledgements

I would like to thank Prof. Dr. Detlef Stammer for the supervision and constructive discussions during my work. I am grateful for the opportunity to conduct my Ph.D. thesis in his group.

My sincere thanks are given to Dr. Stefan Kern for the continuous scientific but also personal support during my work. I enjoyed the time we had working together both on land and at sea.

I wish to thank Prof. Dr. Lars Kaleschke for the helpful suggestions for my work. Our steady and fruitful discussions about sea ice were of great value for me.

Nina Wilkens and Kirstin Rolle are thanked for the manual extraction of ice drift vectors from SAR data.

I thank Prof. Dr. Burghard Brümmer, Dr. Gerd Müller and Dr. David Schröder for the provision of sea ice buoy data and the good collaboration in the frame of the SFB 512 project. The provision and support of sea ice drift data from AMSR-E by Dr. Robert Ezraty and Dr. Fanny Girard-Ardhuin from IFREMER, Brest, France are gratefully acknowledged. Many thanks to Dr. Jörg Haarpaintner for provision of QuikSCAT ice drift data, and the good collaboration and inspiring discussions. Sea ice model data were provided by Dr. Michael Karcher and Dr. Nuno Serra, and the oceanographic salinity data by Katrin Latarius and Prof. Dr. Detlef Quadfasel. Thomas Busche and Dr. Christian Haas are thanked for the provision of SAR and EM-Bird data. Dr. Leif Toudal Pedersen provided help for the manual extraction of sea ice drift from SAR data. Dr. Rene Forsberg from the Danish National Space Centre, Copenhagen, Denmark provided the ArcGP geoid.

The provision of ICESat and AMSR-E data by the National Snow and Ice Data Center (NSIDC), Boulder, CO, USA is gratefully acknowledged.

Many thanks to all my colleagues in the remote sensing group at the Institute of Oceanography for the discussions and good working atmosphere, and especially to my officemate Nidia Martinez.

This work was supported by the German Research Foundation (DFG) project SFB 512-E1.

Several maps of this work were processed using the open source *Generic Mapping Tools (GMT)* software package (*Wessel and Smith*, 1991, 1998).

Finally, special thanks to my family and to Gabi for their love and encouragement.